Resistive Guiding of Fast Electrons in High-Intensity Laser-Plasma Interactions

Damon Scott Farley

Doctor of Philosophy

University of York

Physics

United Kingdom

March 2020

Abstract

This thesis presents the first experimental investigations into resistive guiding of fast electrons using conically structured targets. Two experiments are presented in which a combination of experimental diagnostics and simulations are used to examine the performance of resistively generated magnetic fields in reducing the fast electron divergence. A critical aspect of this work is the deployment of a novel front surface imaging system to determine the location of the laser-target interaction.

Significant rear surface heating is inferred in both experimental campaigns using shadowgraphy and one-dimensional hydrodynamic simulations in HYADES. Conically structured targets are shown to reach temperatures of up to 200 eV; a significant enhancement at greater depth and reduced laser energies than results reported in the literature. Analysis of the laser focal spot and three-dimensional hybrid simulations in ZEPHYROS show how an astigmatic beam with significant energy outside of the main peak can enhance the confinement of electrons and improve the volumetric heating of the target.

Proton diagnostics are used to determine the performance of conically structured targets. Significantly, an enhancement in peak proton energy is recorded for cones with opening half-angles of approximately 10°. We suggest a mechanism underpinning these results and how the ability of the cone targets to reduce the fast electron divergence is sensitive to the specific target geometries implemented on the experiments.

The fast electron beam that escapes the rear surface is observed to filament using a combination of image plate (IP) and coherent transition radiation (CTR) diagnostics. Three-dimensional hybrid simulations using ZEPHYROS present similar filamentation and show how the observation of the break-up of the electron beam does not significantly inhibit the resistive guiding mechanism.

Role of the author

The vast majority of work presented in this thesis has been conducted by the author. The experimental results are composed of two campaigns undertaken at the Vulcan PW laser facility in 2015 and 2017. The first campaign was conducted before enrolment onto the PhD course, however all analysis from this experiment has been undertaken by the author, who later acted as *Target Area Operator (TAO)* on the 2017 campaign. In addition to playing a significant role in the later experiment, all associated analysis has been carried out by the author, with notable exceptions which are detailed in the breakdown of the results chapters below.

Chapter 4

This chapter is based upon shadowgraphy and hydrodynamic simulations using data obtained from both experiments. The data from the first campaign was obtained by the experimental team before enrolment onto the PhD course. However all analysis has been conducted by the author to determine the rear surface expansion velocity and cut-off density imaged by the probe. In the 2017 campaign, the author played a significant role alongside Zoe Davidson and William Trickey in the implementation of the shadowgraphy probe. Again, all analysis and simulations within this chapter were undertaken by the author. The off-line development of the front surface imaging diagnostic was undertaken by Alana Horne; while the diagnostic was then implemented in-situ by the experimental team and author. This included aligning and focussing the diagnostic, as well as ensuring sufficient white and infra-red lighting and developing a protective shutter mechanism.

Chapter 5

This chapter focusses on proton acceleration from both campaigns. Again, the implementation of RCF on the 2015 campaign was conducted before enrolment onto the PhD course, however all analysis of this diagnostic was later undertaken by the author. However, the design and implementation of the RCF stack on the 2017 campaign was undertaken by the author, in addition to the subsequent data analysis. The specular reflection arguments and hybrid simulations that form the remainder of this chapter are also the author's work.

Chapter 6

This chapter is based upon the analysis of CTR and image plate diagnostics to probe the fast electron beam on the 2017 campaign. During the experiment, the image plate stack was constructed and implemented by the author, while the CTR diagnostic was implemented by William Trickey. The author played a supportive role in aiding this. All analysis detailed in this

chapter, along with hybrid simulations has been undertaken by the author, with the notable exception of determining the weighted-averaged location of the CTR filaments. This location was determined by William Trickey and then handed over to the author to used for the remainder of the analysis.

Contents

List of Tables

List of Figures

Acknowledgements

It's been a pleasure to meet and work with some incredible scientists throughout the PhD, a great number of which need thanking.

First and foremost, I'd like to thank my supervisor Kate Lancaster. I could not have asked for a more supportive and approachable supervisor who has guided me over the last four years of research. For always being on hand to give great advice and guiding me when I was unsure of how to progress.

I'd also like to thank John Pasley for the valuable help, especially when undertaking HYADES simulations, and for providing me with the opportunity to take part in the PowerLaPs training school programme. Also Chris Ridgers for the interesting and detailed physics discussions and guidance with ZEPHYROS simulations. Special thanks to Chris Murphy for the support during experiments and constantly pushing me throughout the last four years of TAP meetings. This has been incredibly useful and allowed me to grow out of my comfort zone.

Thank you to everyone at ILIL in Pisa, notably Petra Koester and Leo Gizzi for providing me with the opportunity to visit and work with the group. Everyone was extremely welcoming and it was a pleasure to work with a group of such dedicated scientists. This was a memorable time during the PhD.

Of course, thank you to everyone at the CLF for the help throughout the numerous experiments undertaken at Vulcan. There's too many to mention, but special thanks to James Green, Rob Heathcote, David Carroll, Nicola Booth, Margaret Notley and Chris Spindloe. I'd also like to thank Adam Higginson for kindly providing the defocus scans and Alana Horne for the offline development of the front surface imaging system. Also to Alex Robinson for the support with ZEPHYROS simulations and implementing the double beam system that has been extremely valuable to this thesis.

It's been great working with everyone that I've met at York and elsewhere. Notably Leo Doehl and James Ellis who have been good friends throughout the PhD, as well as Will Trickey, Chris Baird, Chris Underwood and Zoe Davidson for the fun times on experiments at Vulcan.

Finally, thanks to my partner Rebecca for the continuous support over the years and pushing me forward when things got tough. To my sister, Elisa for constantly reminding me what hard work and dedication can achieve. Last, but certainly not least, special thanks to my mum and dad. None of this would have been even remotely possible without the unwavering love and support.

Declaration

I declare that this thesis is a presentation of original work and I am the sole author. This work has not previously been presented for an award at this, or any other, University. All sources are acknowledged as References.

The following publications have resulted from work conducted by the author:

E. Oks, E. Dalimier, A. Y. Faenov, P. Angelo, S. Pikuz, T. Pikuz, I. Y. Skobelev, S. Ryazanzev, P. Durey, L. Doehl, et al. *In-depth study of intrastark spectroscopy in the x-ray range in relativistic laser-plasma interactions*, Journal of Physics B: Atomic, Molecular and Optical Physics, vol. 50, no. 24, p. 245006, 2017.

J. S. Green, R. Heathcote, N. Booth, D. Farley, C. D. Murphy, J. Pasley, W. Trickey, C. Baird, C. Underwood, P. Koester, A. Horne, Z. E. Davidson, R. Gray, and K. L. Lancaster *A novel in-situ dual channel alignment system for precision alignment of complex targetry*, Central Laser Facility Annual Report 2017-2018.

I. Y. Skobelev, S. Ryazantsev, D. Arich, P. Bratchenko, A. Y. Faenov, T. Pikuz, P. Durey, L. Doehl, D. Farley, C. Baird, et al. *X-ray absorption spectroscopy study of energy transport in foil targets heated by petawatt laser pulses*, Photonics Research, vol. 6, no. 4, pp. 234-237, 2018.

M. Sedov, A. Y. Faenov, A. Andreev, I. Y. Skobelev, S. Ryazantsev, T. Pikuz, P. Durey, L. Doehl, D. Farley, C. Baird, et al. *Features of the generation of fast particles from microstructured targets irradiated by high intensity, picosecond laser pulses*, Laser and Particle Beams, vol. 37, no. 2, pp. 176-183, 2019.

Z. Davidson, B. Gonzalez-Izquierdo, A. Higginson, K. L. Lancaster, S. Williamson, M. King, D. Farley, D. Neely, P. McKenna, and R. J. Gray *An optically multi-plexed single-shot time-resolved probe of laser-plasma dynamics*, Optics express, vol. 27, no. 4, pp. 4416-4423, 2019.

Chapter 1

Introduction

The United Nation's Intergovernmental Panel on Climate Change (IPCC) has reported that warming of the climate is unequivocal and - to 95% certainty - human activity is the dominant cause [1]. In order to combat climate change, the panel suggested in 2018 that global warming be kept 1.5°C below pre-industrial levels [2]. In recent years, climate change and investment into clean, renewable energy sources has moved increasingly onto the public agenda.

One proposed method of generating clean, sustainable energy is through nuclear fusion. This is the process that powers stars across the universe and involves fusing the nuclei of atoms together to generate energy. To achieve this, extremely high temperatures are required to overcome the repulsive forces that act to stop the nuclei joining together.

The most desirable fusion reaction uses two isotopes of hydrogen fuel - *deuterium* and *tritium* to produce a helium nucleus, neutron and a large amount of energy. This reaction is most likely to take place at a temperature of over 100 million °C, at which point the fuel becomes *plasma*, the fourth state of matter. This is a super-heated gas, where enough energy has been supplied to strip the electrons from the atoms and generate a collection of charged electrons and ions that respond to electro-magnetic fields.

For the desired fusion reaction to successfully take place and generate an excess of energy, the fuel needs to reach the required temperature. It also needs to be confined in this state for sufficient time or at a high enough density that enough reactions take place to extract sufficient energy. If these requirements are fulfilled, the stage of *ignition* is achieved. This is the point at which an energy surplus is generated in a reaction, which can then be extracted and used to generate electricity.

A variety of methods are proposed to confine the fuel in the required state to reach ignition. One is *Magnetic Confinement Fusion*, which as the name suggests, uses strong magnetic fields to keep the plasma in place. This scheme aims to work at low-density and long-confinement times to fulfil the requirement of enough reactions taking place. Facilities such as the Joint European Torus (JET) in the UK and the future International Thermonuclear Experimental Reactor (ITER) are investigating this method of plasma confinement.

However, the method relevant to this thesis uses the inertia of the fuel to maintain confinement and achieve fuel ignition; this is termed *Inertial Confinement Fusion* (ICF). In contrast to MCF, ICF aims to work in the regime of high-density and short-confinement time. The fundamental process of ICF involves the fuel capsule being surrounded by an array of laser (or

x-ray) drivers. These are extremely intense and cause a layer of material on the surface of the capsule to ablate, creating an inward force which compresses the fuel to the required temperature and density. The inertia of the fuel keeps it confined long enough for ignition to take place. This specific method is called the *Central Hot Spot* approach. Currently, the National Ignition Facility (NIF) in the USA is the most prominent system being used to investigate laser-based ICF. NIF is the largest and most energetic laser in the world, with 192 beams being directed into a *hohlraum* capsule within which the fuel is suspended. The interaction of the laser beams with the hohlraum walls generates x-rays which then drive the implosion of the fuel capsule in a scheme termed *in-direct drive*. The central hot spot approach to ICF requires a highly symmetrical implosion of the fuel capsule which has proved challenging to achieve.

In 1994, M. Tabak *et al* [3] proposed a method of separating the fuel compression and ignition phases in a method called fast ignition. This offers the potential of reducing the driver energy and relaxing the difficult symmetry requirements found in the central hot spot approach.

In 2001, R. Kodama *et al* [4] introduced a novel scheme of fast ignition which is generally referred to as *cone-guided fast ignition*. This uses a small gold cone embedded inside the fuel capsule. The fuel is compressed using the laser (or x-ray) drivers in the usual manner, however the gold cone offers a path clear of plasma through which a secondary laser pulse is directed. This interacts with the apex of the cone and turns it to plasma. A beam of energetic electrons are then generated and accelerated into the pre-compressed fuel. These *fast* electrons travel at relativistic speeds and deposit energy into the fuel, acting as the *spark* that initiates ignition.

In order to deliver as much energy into the pre-compressed fuel, the electron beam needs to remain collimated across the distance between the end of the cone tip and fuel. However, it has been widely shown that the electron beam diverges as the laser intensity increases towards that required to interact with the gold cone. This divergence has been reported in work including that of J.S. Green *et al* [5] and K.L. Lancaster *et al* [6]. A method of reducing this divergence is required to enable fast ignition to deliver sufficient energy to the fuel and be a viable option of ICF. This is the main focus of this thesis.

In 2003, A.R. Bell and R.J. Kingham [7] showed that as fast electrons travel through a target, they self-induce an azimuthal magnetic field that acts to collimate the beam. The extent of this collimation is dependant upon a variety of laser and target parameters, but is most strongly dependant upon the initial divergence of the electrons. If the beam is already somewhat collimated (low divergence), further collimation is more easily achieved. This work prompted further investigations into methods of reducing the initial divergence of the fast electrons. In doing so, the self-induced magnetic fields would be more easily established and allow self-collimation to then take over.

In 2007, A.P.L. Robinson and M. Sherlock [8] showed how a collimating magnetic field could be generated by structuring the target with materials of different electrical resistivities. At early times, the electrons are forced into the material of higher resistivity. This causes more electrons to enter the region and increase the current density, which in itself causes even more electrons to be confined within the area at later times. Over hundreds of femtoseconds, the magnetic field becomes sufficiently established and acts to confine the electrons within the higher resistivity regions of the target. This technique is termed *Resistive Guiding* and is a proposed method of

reducing the initial divergence of the fast electrons.

In 2009, the first experimental work investigating the resistive guiding technique was recorded. S. Kar *et al* [9] used the Vulcan petawatt laser to irradiate a 12μm thick tin foil surrounded to the left and right by less resistive aluminium slabs. Optical Transition Radiation (OTR) was used to measure the spatial profile of the fast electron beam at the rear surface. Results suggested that the electrons were confined within the high resistivity tin foil and that resisitive guiding in simple target geometries was possible on an experimental setting.

Further experimental work using the Vulcan petawatt laser was reported by B. Ramakrishna *et al* [10] in 2010. A central 25μm diameter cylinder of iron was surrounded by aluminium cladding. Again, the Vulcan laser pulse irradiated the central, high resistivity region and the spatial profile of the electron beam was investigated. Cu-Kα radiation was observed at the rear surface of the target and showed that the cylindrically structured targets generated a smaller emission region compared to planar control foils. This suggested that, for a second time, resistively generated magnetic fields were aiding in the confinement of fast electrons.

In 2013, simulation work continued and A.P.L. Robinson *et al* [11] investigated the use of a relatively high resistivity aluminium wire surrounded by a less resistive cladding material. In this work, the fast electrons were confined within the wire due to the magnetic field generated at the resistivity boundary. Temperatures of over 100 eV (1 million °C) were recorded at a depth of 100μm within the target. The significance of the wire radius - amongst other factors - was investigated, with wider wires reducing the density of fast electrons and thereby generating a weaker confining magnetic field.

The simulation work then progressed to modifying the structure of the high resistivity wire core. In 2015, A.P.L. Robinson *et al* [12] tapered the start of the wire into a conical structure and showed how this caused the electrons to specularly reflect off the magnetic fields at the cone walls and further improve the collimation. After each reflection, the divergence of the electrons was reduced and confinement was enhanced for long, shallower angled cones. In these simulations, the embedded structure followed the complete length of the simulation box.

Recall how in the fast ignition scheme the electrons need to remain collimated across the separation between the gold cone tip and pre-compressed fuel. In 2015, A.P.L. Robinson *et al* [13] investigated this effect by simulating a similar clad conical structure as in [12] but stopped the cone at 57μm depth. Following this was 143μm of hydrogen across which the fast electrons would travel after leaving the cone. This work supported the previous results that shallower angled cones enhanced the collimation, however it was shown that the fast electrons began to diverge once they left the cone.

The combination of experimental and simulation work in the literature shows how the use of a resistivity gradient in a target can generate a collimating magnetic field. The simulations have progressed by modifying the target geometry from the embedded wires proposed in 2007 to conical structures in 2015. The experimental work within this time frame has shown promise of the technique being used in a realistic experimental setting. Here, embedded foils and wires followed the full depth of the target and confined the fast electron beam to the rear surface.

1.0.1 Thesis Outline

This thesis builds upon the foundation of the simulation and experimental work investigating resistive guiding. We implement novel, conically structured targets for the first time in an experimental setting investigating the guiding technique. This is distinguished from the experimental work of S. Kar *et al* [9] and B. Ramakrishna *et al* [10] by not only progressing the target structure to conical geometries, but also by applying a stand-off distance between the end of the cone and rear surface of the target. This allows the transport of the fast electrons to be investigated once they leave the conical structure, with simulations suggesting that they begin to diverge once again.

We report on two campaigns at the Vulcan PW laser facility, with significant results that shed light on implementation of resistive guiding in an experimental setting. An improvement in target heating is reported at significantly lower laser energies and for thicker targets than in the literature. We also show enhancements in proton acceleration for specific cone geometries, and a combination of electron diagnostics and hybrid simulations show how the observation of fast electron beam filamentation does not mean the lack of successful resistive guiding.

The structure of the remaining chapters is the following:

Chapter 2 - Theory

The main theoretical considerations for the thesis are presented in this chapter. These include basic plasma physics, laser-solid interactions, fast electron transport, divergence and collimation techniques. Finally, the driving physics of the fast ignition scheme is presented along with ion-acceleration mechanisms which have been utilised throughout the experiments.

Chapter 3 - Instrumentation and Methods

The relevant instrumentation and analysis methods are detailed in this section, including methods of achieving high-powered lasers and specific components of the Vulcan petawatt laser. The two simulation codes that have been used in this thesis are introduced - HYADES and ZEPHYROS - as well as a novel front surface imaging system. This has been developed and deployed experimentally for the first time and proved invaluable as monitoring device of the laser interaction location on conically structured targets.

Chapter 4 - Inferring Rear Surface Temperature of Conical Structured Targets using Shadowgraphy and Simulation Techniques

This is the first results chapter of the thesis and contains an introduction to the targets and experimental set-up of two campaigns conducted at the Vulcan petawatt laser facility. A combination of shadowgraphy and hydrodynamic simulations are used to infer the rear surface temperature of targets across both campaigns.

Conically structured targets are generally shown to reach temperatures of up to 200 eV. This is a significant enhancement in temperature using thicker targets and lower laser energies than results reported by R.G. Evans *et al* [14], K.L. Lancaster *et al* [15] and M. Nakatsatsumi *et al* [16] using foil targets. ZEPHYROS simulations show that the laser alignment and energy within an astigmatic beam contribute significantly to the ability of conical targets to collimate

the fast electron beam.

Chapter 5 - Ion-acceleration as a Diagnostic of Conical Structured Target Performance

This chapter focusses on proton acceleration from the 2015 and 2017 Vulcan PW experiments. An enhancement in the peak proton energy is recorded for structured targets with cone opening angles of approximately 10°. Significantly, this is recorded in both campaigns, with these targets accelerating protons to higher energies compared to the remaining cones and foil targets.

Specular reflection arguments are invoked along with the P. Mora model of plasma expansion [17] and ZEPHYROS simulations to propose mechanisms behind this observed enhancement. It is shown that the target geometry - such as cone tip width - is a limiting factor to the performance of some cones and is a parameter that needs to be considered for future experimental campaigns.

Chapter 6 - Filamentation of Fast Electrons in Conical Structured Targets

This is the final experimental results chapter and presents investigations into the high energy tail of the fast electron distribution. Using a combination of image plate and CTR diagnostics, I show that the fast electron beam breaks up, with ZEPHYROS simulations also reporting similar filamentation. Significantly, this shows how the observation of filamentation in experimental results does not suggest a lack of successful guiding.

I show how the CTR signal strength and size follows comparable scaling with target thickness as that reported by J.J. Santos *et al* [18] and S. Baton *et al* [19]. I also show how the signal strength is sensitive to the electron areal density of the target.

Chapter 7 - Conclusions and Future Prospects

This chapter shall review the results presented in the thesis and further discuss these in the context of the literature. The two experimental campaigns detailed in this thesis investigate resistive guiding in conically structured targets for the first time. Significant results are established from these campaigns and shed light on the sensitivity of the technique to a range of experimental conditions. I discuss these in detail and propose recommendations for future experiments.

Chapter 2

The Physics of High-Intensity Laser-Plasma Interactions

2.1 Plasma Physics

Plasma is frequently referred to as the *fourth state of matter*, and is created by adding a sufficient amount of energy to a gas so that the electrons are removed from the atoms. This leaves a collection of free electrons and ions that influence each other through the electro-magnetic (EM) fields that they generate.

One property of a plasma is that it is quasi-neutral, i.e. on the macroscopic scale, the system is charge neutral. However, on the microscopic scale, the acceleration of the ions and electrons causes EM fields to be generated on a localised level. This occurs below a certain length scale defined as the distance over which the localised electric field of a particle reduces by a factor of $1/\exp(1)$, where $\exp(1)$ is Euler's number. The distance over which this occurs is termed the Debye Length, λ_D:

$$\lambda_D = \sqrt{\frac{\epsilon_0 k_B T_e}{e^2 n_e}} \tag{2.1}$$

where ϵ_0, k_B and e are the permittivity of free space, Boltzmann constant and electronic charge respectively. T_e and n_e are the electron temperature and density within the plasma.

With each Debye length, the electrostatic effect of a charge carrier is increasingly screened by other charges, hence the net effect of the charge is reduced. This leads to the quasi-neutral description of a plasma where the effects of charge carriers are only significant on the microscopic scale, while the complete plasma is considered electrically neutral.

Another parameter that is used to describe a plasma is the natural oscillation frequency; termed the *plasma frequency*, ω_p. As electrons move on a localised level within the plasma, a charge imbalance is established and induces an electric field. This generates a force on the electrons which subsequently oscillate at a natural frequency relative to the ions.

$$\omega_p = \sqrt{\frac{n_e e^2}{\gamma m_e \epsilon_0}} \tag{2.2}$$

where m_e is the electron rest mass, c the speed of light in vacuum and $\gamma = 1/\sqrt{(1 - v^2/c^2)}$ is the Lorentz factor to correct for relativistic effects of an electron travelling at speed v.

Specifically, ω_p is the frequency of the electron oscillations - sometimes termed the *electron plasma frequency*. Over the short time scales relevant to laser plasma interactions, the ions are considered stationary due to their greater inertia compared to electrons. Therefore, solely the electron contribution to the plasma frequency is significant.

It shall be shown later that the plasma frequency determines how far laser light can penetrate into the plasma.

2.2 Laser-Plasma Ionisation

If a laser pulse has an electric field that is strong enough to overcome the Coulomb force binding an electron to a nucleus, the atoms within the target can be ionised. The Bohr model can be invoked to show that the minimum electric field required to ionise a simple, hydrogenic atom is:

$$I_{ionise} = \frac{1}{2}\epsilon_0 c \epsilon_{atom}^2 \simeq 4 \times 10^{16} \text{ Wcm}^{-2} \tag{2.3}$$

where ϵ_0 and ϵ_{atom} are the permittivity of free space and the binding force of the atom which needs to be overcome.

The Keldysh parameter γ_k determines how a target atom is ionised. This parameter compares the laser field strength to the atomic field binding the electron to the nucleus.

$$\gamma_k = \omega_L \sqrt{\frac{2\epsilon_{atom}}{I_L}} \tag{2.4}$$

where γ_k is the Keldysh parameter. ω_L and I_L are the laser frequency and intensity respectively.

Three main methods of ionisation shall now be discussed and in which intensity regime they dominate.

2.2.1 Multi-Photon Ionisation

When a laser pulse is focussed onto a target, photons of angular frequency ω_L and energy $E_\gamma = \hbar\omega_L$ are supplied to the material. Even if the energy of a single photon does not exceed the ionisation threshold, absorption of multiple photons can excite an electron to higher virtual states, until it is finally ionised from the atom. This is *multi-photon ionisation* and is dominant in the weak field regime of $\gamma_k >> 1$. Once the electron is ionised, it leaves the atom with an energy surplus which can then be deposited into other atoms as it travels through the target. This results in further ionisation in a process called *cascade ionisation*.

2.2.2 Tunnelling Ionisation

For high laser intensities, the laser field has an increased effect on the potential barrier that binds the electron to the atomic nucleus. This effectively distorts the Coulomb potential, reducing the

width of the barrier. In this case, electrons quantum mechanically tunnel through the potential barrier and escape the atom. This is *tunnelling ionisation* and is dominant in the high field regime of $\gamma_k << 1$.

2.2.3 Barrier Suppression

The final mechanism of ionisation occurs when the laser pulse is sufficiently intense that the electric field strength is larger than the Coulomb barrier of the atom. This is termed *Barrier Suppression* and allows the electron to be directly stripped from the atomic field. This mechanism also dominates in the high field regime of $\gamma_k << 1$.

For the laser intensities relevant to this thesis (approximately $10^{20} - 10^{21}$ Wcm^{-2}), multi-photon ionisation is dominant at early times when the intensity is relatively low compared to the main peak. The subsequent cascade ionisation mechanism is also established here. As the main high-intensity peak then reaches the target, tunnelling and barrier suppression then take over.

2.3 Relevant Laser-Plasma Concepts

For the lasers relevant to this thesis, the time-scales across which the pulse is driven into the plasma is of the order of hundreds of femtoseconds to picoseconds. During this time, the ionic response to the laser field is negligible compared to the electrons, therefore the ions may be treated as stationary within the target and solely the electron motion is considered. This section outlines the response of a single electron to a driver laser field.

When a laser pulse propagates into a plasma, the electrons oscillate in the transverse laser electric field. This movement is sometimes referred to as the electron *quiver*, for which the equation of motion is given by the Lorentz force:

$$\gamma m_e \frac{\partial \mathbf{v_q}}{\partial t} = -e\left(\epsilon_\mathbf{L} + \mathbf{v_q} \times \mathbf{B}\right) \tag{2.5}$$

where $\mathbf{v_q}$ is the quiver velocity of the electron in the laser electric and magnetic fields of $\epsilon_\mathbf{L}$ and $\mathbf{B}$ respectively.

Considering solely the electric field component of the laser pulse, integration of Equation 2.5 provides the quiver velocity $\mathbf{v_q}$ of the electron transverse to the laser axis.

$$v_q = a_0 c \sin\left(\omega_L t\right) \tag{2.6}$$

However, if the laser pulse is of relativistic intensity such that $a_0 \geq 1$, the magnetic field becomes significant and acts to accelerate electrons along the direction of laser propagation with a velocity of $v_{e,z}$:

$$v_{e,z} = \frac{a_0^2}{4} \cos\left(2\omega_L t\right) \tag{2.7}$$

These equations result in the electron being accelerated to relativistic speeds along the laser propagation axis twice within a single laser cycle (note the $2\omega_L$ in Equation 2.7). The transverse

quiver causes the electron to trace out a *figure of eight* motion in the plane perpendicular to the laser axis.

The *normalised vector potential* a_0 describes how relativistic the system is by comparing the classical and relativistic momenta.

$$a_0 = \frac{eE_0}{m_e c \omega_L} \tag{2.8}$$

For $a_0 \geq 1$, the electrons within the laser field will quiver at speeds close to the speed of light and the system is considered relativistic.

The laser intensity is related to the vector potential by:

$$I_L \lambda_L^2 = a_0^2 \times 1.37 \times 10^{18} \text{ Wcm}^{-2} \mu\text{m}^2 \tag{2.9}$$

As a laser pulse propagates through a plasma, the following dispersion relation is shown:

$$\omega_L^2 = \omega_p^2 + k^2 c^2 \tag{2.10}$$

where ω_p is the plasma frequency (equation 2.2) and k the wave-vector of the laser of frequency ω_L.

To satisfy the regime of $\omega_L \geq \omega_p$, the wave-vector k of the laser becomes imaginary and the wave is evanescent. For this regime, the laser pulse cannot penetrate into the plasma and is reflected.

The plasma density at which this occurs is termed the *critical density* n_{crit}:

$$n_{crit} = \frac{\gamma \omega_L^2 m_e \epsilon_0}{e^2} \tag{2.11}$$

For plasma densities greater than n_{crit}, the laser pulse is reflected at the critical density.

The refractive index η governs how a laser pulse propagates through a plasma. This is dependant upon the plasma and laser frequencies, or can be considered as a function of the critical density:

$$\eta = \sqrt{1 - \left(\frac{\omega_p}{\omega_L}\right)^2} = \sqrt{1 - \frac{n_e}{n_{crit}}} \tag{2.12}$$

For ultra-high intensity lasers, a mechanism can change the electron density across the laser profile and therefore modify the refractive index. This leads to the laser focussing by different amounts across the radial profile of the beam. The governing mechanism behind this is the *Ponderomotive Force*.

For a realistic laser pulse that has a Gaussian-like intensity in the spatial domain; an electron oscillates between the central regions of high intensity and surrounding lower intensity. Between these regions, the electron experiences a different magnitude of force. If the electron moves radially outwards within the first half of the laser period, the restoring force exerted on the electron in the following half laser period will be less. As such, the electron does not return to it's original position and has experienced a transverse shift in position. Multiple oscillations of the laser pulse subsequently move the electron further out into the lower intensity regions,

with the electron gaining energy from the laser pulse with each oscillation. This can result in an electron density profile across the laser beam which modifies the refractive index and propagation of the beam. The force that governs the radial movement of the electron within the laser field is termed the *Ponderomotive Force* $\mathbf{F_{pond}}$:

$$\mathbf{F_{pond}} = \frac{e^2}{4m_e\omega_L^2}\nabla\mathbf{E}^2 \tag{2.13}$$

where $\mathbf{E}$ is the electric field of the laser.

Equation 2.13 shows how the ponderomotive force exerted on an electron is dependant upon the spatial change of the laser electric field $\nabla\mathbf{E}^2$. As one moves radially from the centre of the Gaussian beam, the laser field strength (and therefore intensity) reduces, hence the electron feels less of the ponderomotive force further from the centre of the laser pulse. This mechanism can shift a large number of electrons and modify the density profile of the plasma. This subsequently changes the refractive index across the laser pulse.

Harmonic emission can be generated up to the critical surface of the plasma via two key mechanisms; *Coherent Wake Emission* (CWE) and the *Relativistic Oscillating Mirror* (ROM).

CWE occurs when the component of the laser electric field directed normal to the target drags electrons from the plasma (see sections 2.4.2 and 2.4.3) and re-injects them into the corona at the front surface of the target. The electrons are accelerated up the plasma density gradient in bunches temporally separated by the laser period; creating plasma density oscillations. These oscillations, at integers of the laser frequency, can resonate and generate harmonic emission from the plasma [20]. Coherent wake emission is dominant between intensities of approximately $10^{16} - 10^{17}$ Wcm^{-2} [21] and relies upon a density gradient at the front surface; it is therefore sensitive to the laser contrast [22, 23].

ROM occurs at the critical density surface of the plasma which oscillates in the laser field. As the critical density surface moves towards the laser during the oscillation, it compresses the pulse and modifies the phase, resulting in harmonic generation. Streeter *et al* [20] show that second harmonic emission becomes dominant at intensities $\geq 10^{18}$ Wcm^{-2} and reaches a maximum at approximately $\geq 10^{20}$ Wcm^{-2}. The emission is also shown to be dependant upon the intensity of the laser such that a higher generation efficiency is observed at the centre of the beam. The dominance of the ROM mechanism at high intensities suggests that it is this mechanism that generates emission observed in experiments using the Vulcan PW laser.

2.4 Laser-Plasma Absorption

After ionisation of the target, the laser transfers energy to the plasma in a variety of mechanisms. The main method of coupling this energy to the target is through the lower inertia electron population which are more responsive to the laser field. Table 2.1 presents each mechanism along with the laser intensities at which they dominate. The direction of electron acceleration is also presented for comparison.

Absorption Mechanism	$\mathbf{I_L}$ **(Wcm^{-2})**	**Acceleration Direction**	**Density Gradient**
Inverse Bremsstrahlung	$\leq 10^{15}$	Un-Directional	$L_s > \lambda_L$
Resonance Absorption	$10^{15} - 10^{17}$	Target Normal	$L_s > \lambda_L$
Vacuum Heating	$10^{15} - 10^{17}$	Target Normal	$L_s < \lambda_L$
$\mathbf{J} \times \mathbf{B}$	$\geq 10^{18}$	Laser Axis	$L_s \approx \lambda_L$

Table 2.1: Laser absorption mechanisms along with the laser intensities I_L at which they dominate. This assumes a $\lambda_L = 1$ μm laser wavelength. Third column is the direction each mechanism accelerates electrons. Final column is the scale length representing the density gradient at which they dominate [24]. References for each mechanism in the relevant sections that follow.

Before reviewing the absorption mechanisms presented in Table 2.1, it is important to first consider a characteristic length scale of the plasma - notably the *skin depth*, l_s [25, 26]:

$$l_s \approx \frac{c}{\omega_p} \tag{2.14}$$

where c and ω_p are the speed of light and plasma frequency respectively.

As a laser pulse propagates into a plasma, it penetrates up to the critical density surface and decays thereafter. This decay is described the skin depth - the distance across which the amplitude of the laser electric field decays by a factor of $1/\exp(1)$ before shielding from the background plasma becomes prominent [25].

2.4.1 Inverse Bremsstrahlung

Inverse bremsstrahlung - sometimes referred to as *collisional absorption* - is a mechanism of photon absorption that is dominant at relatively low laser intensities of approximately $\leq 10^{15}$ Wcm^{-2}. This can be for low intensity lasers or during the early pre-pulse of higher intensity systems. At these intensities, the particles velocities are relatively low and result in an increased collision probability.

As motion is induced through oscillations in the laser field, an electron can travel past an ion and be affected by the Coulomb field. This causes the electron to absorb a laser photon through conservation of energy and damp the laser field. This exchanges energy from the laser pulse to the ions, through the electrons.

Due to the collisional nature of this absorption mechanism, Inverse bremsstrahlung is maximised for a larger density (n_e, n_i), high atomic number (Z) and low temperature plasma (T_e).

2.4.2 Resonance Absorption

Resonance absorption is a collisionless mechanism of coupling energy to electrons when the laser pulse is oblique to the target normal axis. If the laser pulse is incident at an angle θ_L to the target normal, the location of the critical density surface n_{crit} is modified to $n_{crit}\cos^2\theta_L$.

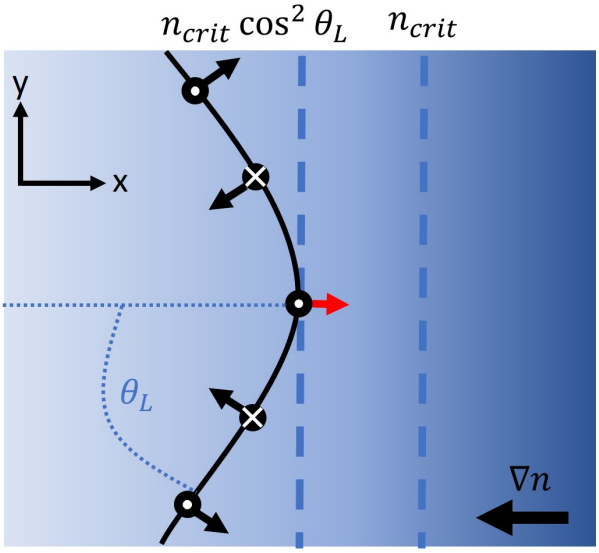

Figure 2.1: Schematic of resonance absorption for a laser pulse incident onto a target surface at angle θ_L. p-polarised laser component (red arrow) excites a resonance wave at the critical surface n_{crit}. Laser pulse penetrates up to $n_{crit}\cos^2\theta_L$ density surface.

When the laser pulse is incident at an angle θ_L to the target normal, the p-polarised component of the electric field is directed into the target and parallel to the density gradient ∇n. This component of the laser field (red arrow in Figure 2.1) can tunnel through the $n_{crit}\cos^2\theta_L$ surface and reach the critical density n_{crit}. Here, n_{crit} and the laser are at identical frequencies and therefore a resonant electron plasma wave is generated. Deeper than the critical density, the electric field is still unable to propagate, therefore electrons that are accelerated past this surface no longer feel a restoring force. This results in damping of the electron plasma wave and energy transfer to the electrons which are accelerated into the target.

The angle of incidence needs to be sufficient such that the laser pulse is reflected deep enough into the plasma while a density scale length needs to be present to allow the mechanism to occur. This is characteristic of relatively long pulse laser systems where the density scale length exceeds the laser wavelength ($L_s > \lambda_L$). Resonance absorption is the dominant mechanism for the intermediate laser intensity range of approximately $10^{15} - 10^{17}$ Wcm^{-2} [27–29].

2.4.3 Vacuum Heating

Vacuum heating is another collisionless mechanism that is also dominant in the $10^{15} - 10^{17}$ Wcm^{-2} laser intensity regime [27–29]. First studied by Brunel [30] in 1987, vacuum heating is often referred to as *Brunel Absorption*. The absorption is similar to resonance absorption where laser energy is collisionlessly coupled to electrons within the plasma, however it occurs for smaller length scale plasmas ($L_s < \lambda_L$). This is characteristic of ultra-short laser pulses.

When the p-polarised component of the laser electric field is directed into the target, it can pull electrons from the skin depth out into vacuum. This occurs over $\frac{1}{2}$ of a laser cycle. In the relativistic regime, the reduced collision rate of the high energy electrons allows them to penetrate deeper into the plasma, causing the skin depth to be slightly increased. The electrons are then re-injected into the target over the remaining $\frac{1}{2}$ of the laser cycle but have gained energy through the oscillation from the laser. The accelerated electrons can collisionally transfer energy to the remaining plasma and heat the target.

2.4.4 J×B

The $\mathbf{J} \times \mathbf{B}$ absorption mechanism [31] arises from the ponderomotive force of the laser and is therefore often referred to as *ponderomotive acceleration*. This mechanism is dominant for relativistic intensities ($\geq 10^{18}$ Wcm^{-2} [28, 29]) where the effect of the magnetic field component of the laser becomes important. In this case, the $\mathbf{v} \times \mathbf{B}$ component of the Lorentz force becomes significant and accelerates electrons along the direction of laser propagation. The oscillatory nature of the laser pulse causes the electrons to be accelerated at the $2\omega_L$ frequency, while some of those electrons that oscillate close to the critical density gain sufficient energy to escape into the over-dense region; taking some of the driver energy.

The force generated through the ponderomotive force and $\mathbf{J} \times \mathbf{B}$ mechanism is detailed by Kruer and Estabrook [31] and exhibits a $2\omega_L$ component showing how electrons are accelerated at twice the laser frequency.

2.5 Fast Electron Transport

2.5.1 Return Current

As the thermalised (fast) electrons travel through the target as a beam, they self-induce an azimuthal magnetic field. This can become sufficient in strength that the Larmour radius of the fast electrons becomes smaller than the beam radius. In this case, the electrons effectively turn back on themselves and no longer propagate in the forward direction. This was formulated by H. Alfvén [32] who determined the current limit at which the fast electrons change direction. This is the *Alfvén Current* or *Alfvén Limit*, I_{max}:

$$I_{max} = 1.7 \times 10^4 \frac{v_z}{c} \gamma \tag{2.15}$$

where v_z is the electron velocity and γ the relativistic Lorentz factor.

The currents generated in high-intensity laser-target interactions regularly exceed the Alfvén limit, but the fast electron beam is still able to propagate. In 1997, A.R. Bell *et al* [33] proposed that a cold return current of electrons is drawn from the target and results in the total current staying below the Alfvén limit. The fast electron $\mathbf{j_f}$ and opposing return currents $\mathbf{j_r}$ locally balance such that:

$$\mathbf{j_r} = -\mathbf{j_f} = \sigma_E \mathbf{E} = \frac{\mathbf{E}}{\eta} \tag{2.16}$$

where $\mathbf{j_r}$ and $\mathbf{j_f}$ are the return and fast electron currents, σ_E the electrical conductivity, η the electrical resistivity and $\mathbf{E}$ the electric field.

While the fast electron and return currents are, on average, equivalent in magnitude, small scale perturbations in the electrons can cause the currents to deviate from Equation 2.16 and generate magnetic fields.

Consider Maxwell's equations where the current under analysis has contributions from the fast electrons and return current such that:

$$\nabla \times \mathbf{B} = \mu_0 \mathbf{j_T} = \mu_0 \left(\mathbf{j_f} + \mathbf{j_r}\right) \tag{2.17}$$

This is Ampere's law where the total current $\mathbf{j_T}$ is composed of fast electron $\mathbf{j_f}$ and return current $\mathbf{j_r}$ contributions.

Recalling from Equation 2.16 that $\mathbf{j_r} = \mathbf{E}/\eta$ and substituting into equation 2.17 gives the electric field:

$$\mathbf{E} = \eta \mathbf{j_r} = \frac{\eta}{\mu_0} \nabla \times \mathbf{B} - \eta \mathbf{j_f} \tag{2.18}$$

The electric field shown in Equation 2.18 can then be applied to Faraday's law to show that a time-varying magnetic field is induced from the currents.

$$\frac{\partial B}{\partial t} = -\nabla \times \mathbf{E} = (\nabla \times \eta \mathbf{j_f}) - \nabla \times \left(\frac{\eta}{\mu_0} \nabla \times \mathbf{B}\right) \tag{2.19}$$

This is Faraday's law describing the time varying magnetic field that is generated from the fast electron current. The first term on the far right hand side generates the magnetic field from the fast electron beam, while the second term is resistive magnetic diffusion.

Magnetic diffusion is negligible over the short time-scales of the laser pulses relevant to this thesis, therefore Equation 2.19 becomes:

$$\frac{\partial B}{\partial t} = -\nabla \times \mathbf{E} = (\nabla \times \eta \mathbf{j_f}) \tag{2.20}$$

This shows that when small perturbations cause the fast electron and return currents to no longer neutralise, the fast electron beam can generate a magnetic field within the plasma. This is azimuthal around the beam and acts to either pinch or break up the beam depending on the resistivity η. The role of this parameter is crucial in determining the transport of the fast electrons and shall be detailed in the following section.

2.5.2 Target Heating and Resistivity

The absorption mechanisms detailed in the previous section deliver laser energy to the electron population at the critical density surface. This is then transferred through the remaining bulk of the target through electron conduction and Ohmic heating.

The fast electrons travel through the target relativistically such that the collision cross-section is low; therefore energy transfer between the fast electron and bulk target via collisions is unlikely. However, the return current drawn from the target is cold and much slower, therefore

collisions with the bulk are much more likely. Hence, it is the return current that drives the energy transfer and heating of the target.

Electron conduction within the target is generally approximated by the classical Spitzer-Härm model. This describes a plasma without magnetic fields or a density gradient and neglects hydrodynamic motion. Naturally this is not applicable to all plasma systems but is a good initial description using a kinetic treatment [34, 35].

$$q_{SH} = -\kappa_{SH} \nabla T \tag{2.21}$$

where q_{SH} and κ_{SH} are the Spitzer-Härm heat flow and conductivity respectively. ∇T is the temperature gradient inside the bulk target.

$$\kappa_{SH} = \frac{4T_e^{5/2}}{Ze^4 m_e^{1/2} \ln \Lambda} \tag{2.22}$$

The target resistivity is also an important parameter to consider. Equation 2.20 showed how the azimuthal magnetic field around the electron beam is dependant upon the resistivity, and determines if the field pinches or causes the electron beam to diverge. Spitzer resistivity η_S is frequently used to describe high temperature plasmas where:

$$\eta_S = Z \frac{\pi e^2 m_e^{1/2}}{(4\pi\epsilon_0)^2 (k_B T)^{3/2}} \ln \Lambda \tag{2.23}$$

Equation 2.23 shows that the Spitzer resistivity η_S is sensitive to the target material (Z) and temperature of the bulk target (T). The target material contribution shall be discussed in detail in a later section showing how structuring the target with different materials can aid collimation of the electron beam. The bulk temperature of the material is time dependant; initially beginning at room temperature and rising in-homogeneously when the laser is incident at the front surface and energy absorbed into the fast electrons.

The Spitzer model is well characterised and suited to the high temperature regime ($k_B T \geq$ 100 eV) found once the target is sufficiently heated. However, before substantial heating has occurred, the resistivity deviates from the Spitzer model presented in equation 2.23 and modifies the magnetic field generation around the fast electron beam. This has been shown to initially cause the electron beam to diverge at early times when the target has not yet reached the substantial heating regime [36, 37].

2.5.3 Fast Electron Filamentation

The fast electron and return currents can be considered as a system of two, counter-propagating beams. This can result in breakup of the fast electron beam through three main mechanisms; *Weibel* filamentation, *Resistive* filamentation and the *two-stream* instability.

2.5.3.1 Weibel Filamentation

Weibel filamentation is a result of the Weibel instability; a collisionless (non-resistive), transverse instability that was identified in 1958 by E.S. Weibel [38]. This work showed how small

perturbations in the density profile of one of the currents results in an increase in the local magnetic field in the transverse direction. This field pinches the electron beam and breaks it into smaller filaments which create further perturbations in the density profile; reinforcing the filamentation mechanism. In 2001, M. S. Wei *et al* [39] first observed the effects of the Weibel filamentation experimentally using the Vulcan PW laser, where the resultant break-up of the fast electron beam was observed as *speckle* features using radiochromic film.

2.5.3.2 Resistive Filamentation

Resistive filamentation is similar to the Weibel instability but considers the collisional (resistive) interaction between the fast electron and return currents. First, consider a small perturbation in the background density profile such as a high density column surrounded by a lower density area. The specific heat capacity within each region is linearly proportional to the density, therefore, the central column will heat up slower than the surrounding low density material. The now hotter annulus becomes less resistive than the central column (see Equation 2.23) and therefore generates a magnetic field that forces electrons into the high density region. This mechanism is well described by A.P.L. Robinson *et al* in [40].

2.5.3.3 Two-Stream Instability

The two-stream instability occurs when two counter-propagating beams of charged particles - such as the fast and return currents - travel through a plasma. In the relativistic regime with low temperature, this situation can be described using the fluid approximation; where the equation of continuity links the velocity of each beam to their densities [41]. When the fast electron beam travels through a potential within a plasma, it is accelerated and results in charge separation between the fast and return currents. This subsequently modifies the beam densities in accordance to the equation of continuity, which itself amplifies the instability.

Bret *et al* [41,42] show how the two-stream instability can combine with the filamentation and Weibel instabilities to generate an intermediate mechanism, resulting in transverse filamentation and density perturbations. The maximum growth rate δ_M of this mode is found to be dependant on the background beam density n_b and relativistic Lorentz factor γ [41, 42]:-

$$\delta_M \simeq \frac{\sqrt{3}}{2^{4/3}} \left(\frac{n_f}{n_b \gamma} \right)^{1/3} \omega_p \tag{2.24}$$

where n_f and n_b are the fast electron and background beam densities, γ is the relativistic Lorentz factor and ω_p is the plasma frequency.

2.6 Fast Electron Divergence

When a high-intensity laser pulse interacts with a solid target, the generated fast electron beam exhibits spatial divergence. K.L. Lancaster *et al* [6] and J.S. Green *et al* [5] present experimental investigations and a literature review of the divergence of the electron beam across a range of laser intensities. A significant figure from [5] is presented in Figure 2.2:

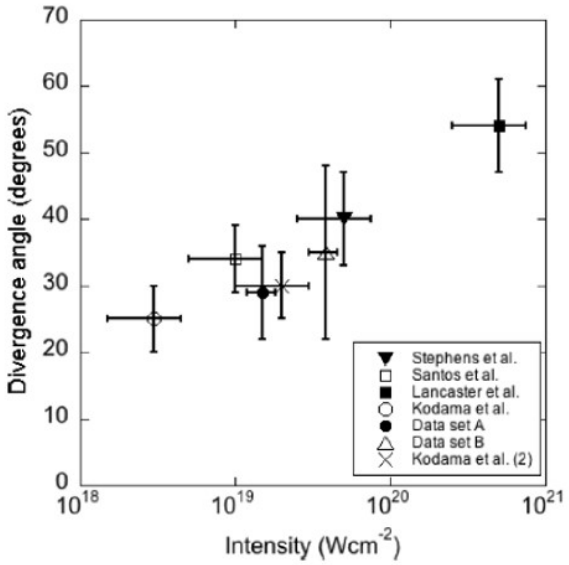

Figure 2.2: Full divergence angle of the fast electron beam for a given laser intensity. Vulcan laser nominally 10^{21} Wcm^{-2} suggesting a divergence angle of approximately 60°. Figure taken from J.S. Green *et al* [5].

A clear increase in divergence is reported as the laser becomes more intense. This increase is attributed to two possible mechanisms: (1) the laser fields around ripples in the density contours at the front surface deflecting electrons (2) deflection from magnetic fields generated by filamentation [5]. Both of these scale with laser intensity.

A. Debayle *et al* [43] used two-dimensional particle-in-cell (PIC) simulations to investigate electron divergence in 30 μm thick gold foils. The laser pulse (5×10^{19} Wcm^{-2}, 125 fs, 12 μm FWHM) was incident along the target normal direction. Again, two mechanisms contributed to the recorded divergence (1) the ponderomotive force caused the electrons to travel down the transverse laser field gradient. This forced electrons radially outwards and thus increased the divergence of the beam. (2) As earlier suggested in [5], the magnetic fields generated by instabilities - namely Weibel - caused the deflection of electrons. Both these mechanisms increase the transverse component of the fast electron velocities and result in a more divergent electron beam.

2.7 Fast Electron Collimation

Many applications of fast electrons require the beam to be collimated; such as the fast ignition scheme in which the electrons from the cone tip need to be highly directional to maximise the energy coupling to the pre-compressed fuel. This will be further discussed in section 2.9.

Self-induced magnetic fields or collimating fields imposed through novel target geometries can be utilised to enhance the fast electron collimation.

2.7.1 Self-Collimation

It has been shown in Equation 2.20 that the fast electron beam self-generates an azimuthal magnetic field as it propagates through the target. The ability of this field to collimate the electrons has been investigated by A. R. Bell and R. J. Kingham [7]. Here, a requirement for successful collimation is presented which applies to the case of substantial ohmic heating where the temperature of the cold, background plasma greatly exceeds the initial temperature. Essentially, this is the same requirement for the Spitzer resistivity to apply ($k_B T_e \geq 100$ eV). For effective collimation to occur, $\Gamma > 1$, where [7]:

$$\Gamma = 0.13 \left(\frac{n_{e,23}^{3/2} \; Z \; \ln\Lambda \; R_{\mu m} \; t_{ps}}{P_{TW}^{1/2} \; T_{f,511keV}^{3/4} \; (2 + T_{f,511keV})^{5/4} \; \theta_{rad}^{5}} \right)^{2/5} \tag{2.25}$$

where $n_{e,23}$ is the electron density in units of cm^{-3}, P_{TW} the power of the fast electron beam of temperature $T_{f,511keV}$. The radius, temporal duration and initial half-angle divergence of the fast electron beam are given by $R_{\mu m}$, t_{ps} and $\theta_{1/2}$ respectively. All units are presented as subscripts for each parameter, for example, $T_{f,511keV}$ is in units of 511 keV.

Equation 2.25 shows that the collimation of the fast electron beam is most sensitive to the initial divergence θ_{rad}. If the electron beam initially injected into the target already holds some degree of collimation such that θ_{rad} is minimised, the parameter Γ and self-collimation will subsequently be enhanced.

Currently, it is difficult to practically achieve a significant reduction in the initial divergence of the fast electron beam through modifying the conditions of the interaction. R.H.H. Scott *et al* [44] detail experimental investigations using two laser pulses to collimate the fast electron beam. The first pulse is reported to inject a population of fast electrons which generate an azimuthal magnetic field; this then acts to collimate the main population of electrons which are accelerated into the target by the second laser pulse. This work shows how the fast electron beam, predominantly measured using Kα emission at the rear surface, is reduced in divergence. However, the effectiveness of this technique is highly sensitive to the interaction conditions; such as the energy and delay between the pulses.

A further technique of collimating the fast electron beam is suggested which does not rely on precisely tailoring the laser conditions [8]. By structuring the target with different materials, this method has been shown to externally collimate the electron beam as it travels through the target. This is termed *Resistive Guiding* and is the main focus of this thesis.

2.7.2 Electrostatic Sheath Confinement

Electrostatic sheath confinement describes the generation of an electric field at the target:vacuum interface that confines the fast electrons within the target. This plays an important role in ion-acceleration at the rear surface which shall be detailed in section 2.8. However, electrostatic sheath confinement can also be used as a method of inhibiting the divergence of the fast electron beam.

R.B. Campbell *et al* [45] used two-dimensional, cylindrically symmetric PIC simulations

(LSP) to investigate electrostatic sheath confinement in a structured target. A 40 μm wide CH core material was surrounded by a 20 μm thick vacuum gap either side. This was then embedded in a CH plasma. A sheath was recorded to form radially at the material:vacuum interfaces with a corresponding electro-static field. This field confined the electrons within the 40 μm core material showing that the generation of an electrostatic sheath can confine electrons within a region, thereby reducing the overall spatial divergence of the beam.

2.7.3 Resistive Guiding

It has been previously shown that the self-generated magnetic field can be used to reduce the divergence of the fast electron beam. However, to achieve substantial collimation, the initial angular divergence of the beam needs to be reduced. Equation 2.20 showed how a magnetic field is generated around the beam due to the $\nabla \times \eta \mathbf{j_f}$ term. The self-generated field is created from the spatial change of $\mathbf{j_f}$, however if a spatial gradient of η is imposed on the target, this can also contribute to the magnetic field generation. This was first described by A. P. L. Robinson and M. Sherlock in 2007 [8].

Equation 2.20 reveals a component of the magnetic field that arises from a gradient in the target resistivity. By invoking a vector identity, this relationship can be clearly shown:

$$\frac{\partial \mathbf{B}}{\partial t} = \eta \nabla \times \mathbf{j_f} + \nabla(\eta) \times \mathbf{j_f} \tag{2.26}$$

The first term on the right hand side of Equation 2.26 generates a magnetic field that forces the fast electrons to areas of higher current density, whilst the second term forces the fast electrons to areas of higher resistivity.

If a high intensity laser pulse interacts with a target containing a resistivity gradient, at early times the fast electrons are forced into the region of the target with the higher resistivity (due to the $\nabla(\eta) \times \mathbf{j_f}$ term). As time progresses and more fast electrons are forced into the higher resistivity material, the current density increases in this region and causes even more electrons to be forced into this region due to the magnetic field generated from the $\eta \nabla \times \mathbf{j_f}$ term. This feedback mechanism results in an azimuthal magnetic field generated around the beam that acts to confine the fast electrons into the region of the target with the higher resistivity.

Implementing a resistivity gradient can be achieved through using materials of different atomic number (Z), however as the fast electron confinement and corresponding heating is improved within the high resistivity region of the target, the resistivity subsequently decreases and results in quenching of the mechanism above a high temperature threshold.

Multiple target configurations are described in the literature [8–13, 46] where two materials of distinct atomic number are used to generate the resistivity gradient.

A.P.L. Robinson and M. Sherlock [8] used the hybrid LEDA code to show how fast electrons could be resistivity guided along a high Z aluminium fibre of 200 μm length, surrounded by a lower Z cladding. The laser was modelled as a 5×10^{19} Wcm^{-2}, 0.5 ps pulse generating a 68° full divergence electron beam. It was shown that the azimuthal magnetic field generated from structuring the target was sufficient to confine the fast electrons along the high Z fibre. A temporal breakdown of the simulations showed that the magnetic field required hundreds of femtoseconds to become established. At 750 fs, the field had extended over 150 μm down the

length of the fibre, with successful guiding being recorded in the fast electron density, as shown in Figure 2.3:

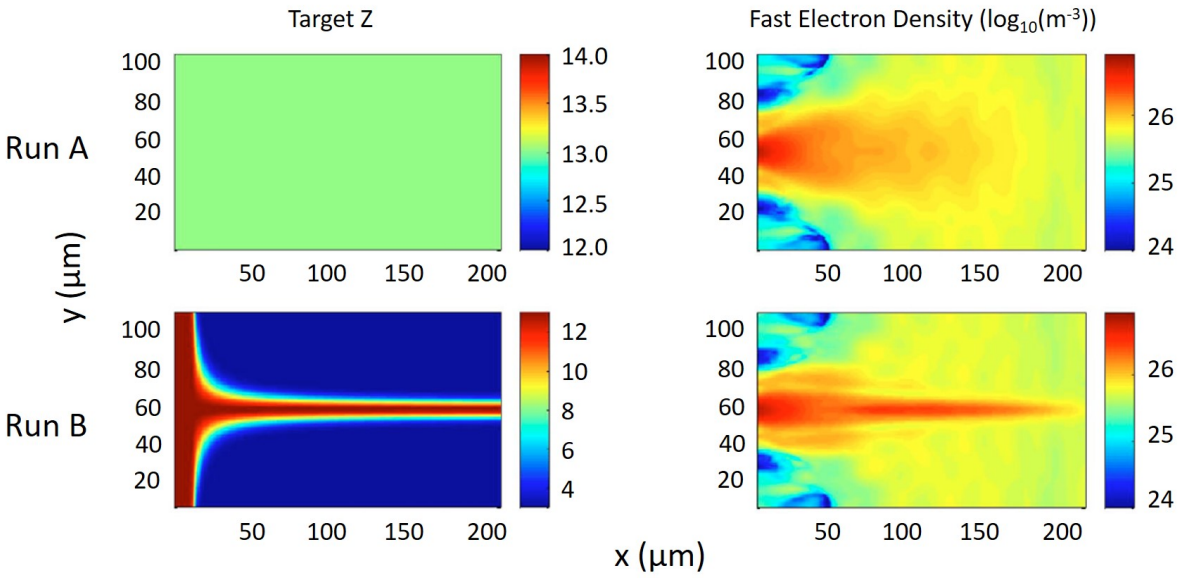

Figure 2.3: Target Z and fast electron density at 750 fs after laser incidence. Run A and Run B are a control foil and structured target respectively. Figure taken from [8].

Results indicate that at low temperatures (approximately 25 eV) cold-target resistivity curves caused the resistivity gradient to be inverted such that the fibre held a lower resistivity than the surrounding cladding. This caused the magnetic field to initially expel electrons from the fibre. However, as the target subsequently heated and moved out of the cold target regime, the resistivity gradient was inverted and the guiding mechanism dominated.

In 2013, A.P.L. Robinson *et al* [11] presented further hybrid simulations using ZEPHYROS to investigate a high Z aluminium wire embedded in a low Z, CH_2 cladding. The fast electron guiding was measured by the effectiveness of heating the target at depth. The wire was 10 μm wide and followed the 300 μm length of the simulation box with laser parameters (1×10^{20} Wcm^{-2}, 1 ps, 10 μm FWHM). Heating to over 100 eV at a depth of 100 μm was visible in the simulations showing the effectiveness of the resistive guiding technique.

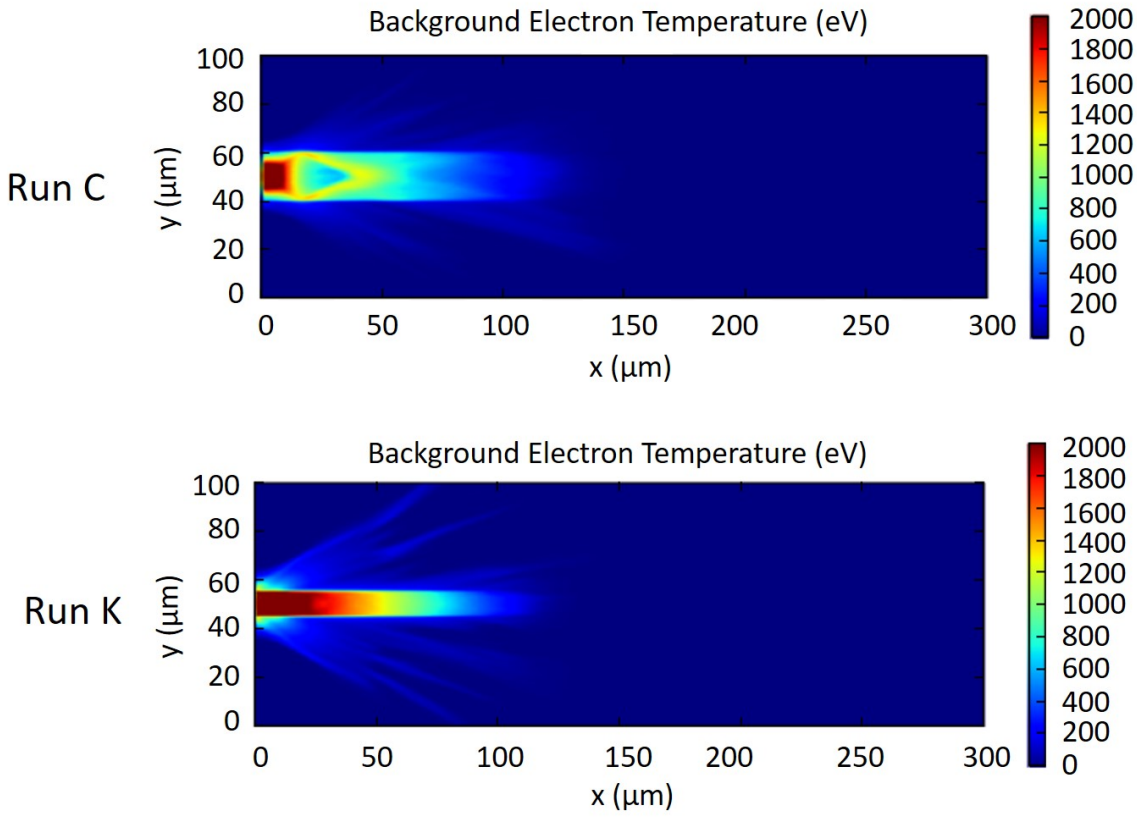

Figure 2.4: Background electron temperature at 1.2 ps after laser incidence. Run C and Run K are identical but with wire radii of 10 μm and 5 μm respectively. Figure taken from [11].

The wire radius - amongst other factors - was shown to be a parameter of importance, where larger radii structures caused the density of fast electrons to reduce as they dispersed across the wider wire. This is presented in Figure 2.4 where improved heating at depth is recorded for the thinner wire in Run K. As shown in Equation 2.26, a reduction in j_f leads to weaker magnetic field generation around the fast electrons, suggesting that the specific target geometry is an important factor to consider.

In 2015, the simulation work progressed to tapering the front structure of the wire to generate a conical guide - sometimes referred to as an *inverse conical taper*. A.P.L. Robinson *et al* [12] implemented ZEPHYROS with a 10 μm wide aluminium guide surrounded by a CH_2 cladding. Across varying lengths, the cone was increased from an initial 5 μm width up to the final 10 μm, resulting in the opening angle of the cone varying between simulations. Through tapering the start of the guide wire, specular reflection arguments show that an electron can bounce off a cone wall and reduce the angular divergence [12]:

$$\theta_1 = 2\alpha_c - \theta_e \tag{2.27}$$

where θ_1 is the angle that an electron specularly reflects off a cone wall of angle α_c. The electron is originally directed towards the cone with initial angle θ_e.

Equation 2.27 considers a single bounce off a cone wall, where the magnetic field generated at the resistivity boundary acts as a rigid reflector. However, considering a distribution of electron angles, [12] shows that the proportion of electrons that undergo at least one reflection is given by P_1:

$$P_1 = \frac{\int_{\alpha_c}^{\pi/2} g\left(\theta_e\right) \sin\theta_e d\theta_e}{\int_0^{\pi/2} g\left(\theta_e\right) \sin\theta_e d\theta_e} \tag{2.28}$$

where P_1 is the proportion of electrons with angular distribution $g\left(\theta_e\right)$ that undergo at least a single reflection. Cone wall opening angle given by α_c.

Equation 2.28 implies - and is borne out in the simulations [12] - that using a low angle (α_c) cone allows a greater proportion of the electron population to have their angular divergence reduced through multiple bounces. The simulation results also show that the implementation of a conical taper enhances the fast electron collimation at depth compared to a straight, embedded wire. This is shown in Figure 2.5 where Run F is a control wire and Runs E and G are tapered wires with opening angles 5° and 10° respectively. Note the improvement in uniform heating for Run E compared to Run G:

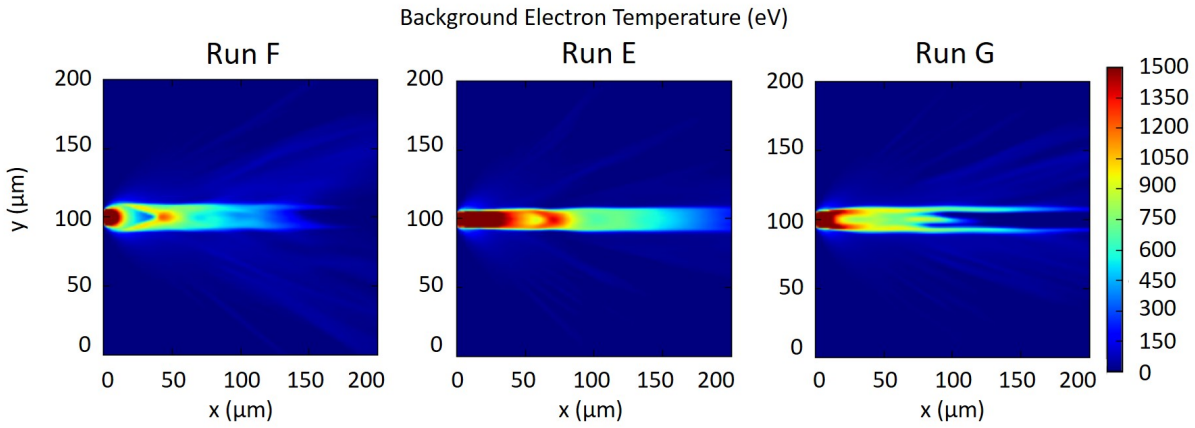

Figure 2.5: Background electron temperature at 1.5 ps after laser incidence. Run F is a uniform control wire and Runs E and G are tapered wires with opening angles of 5° and 10° respectively. Figure taken from [12].

In 2015, A.P.L. Robinson *et al* [13] presented further work using a similar target geometry to [12], but the cone length was restricted to 57 μm, this was then followed by 143 μm of the cladding material. This differentiates from [12] where the embedded conical structure followed the complete length of the simulation box.

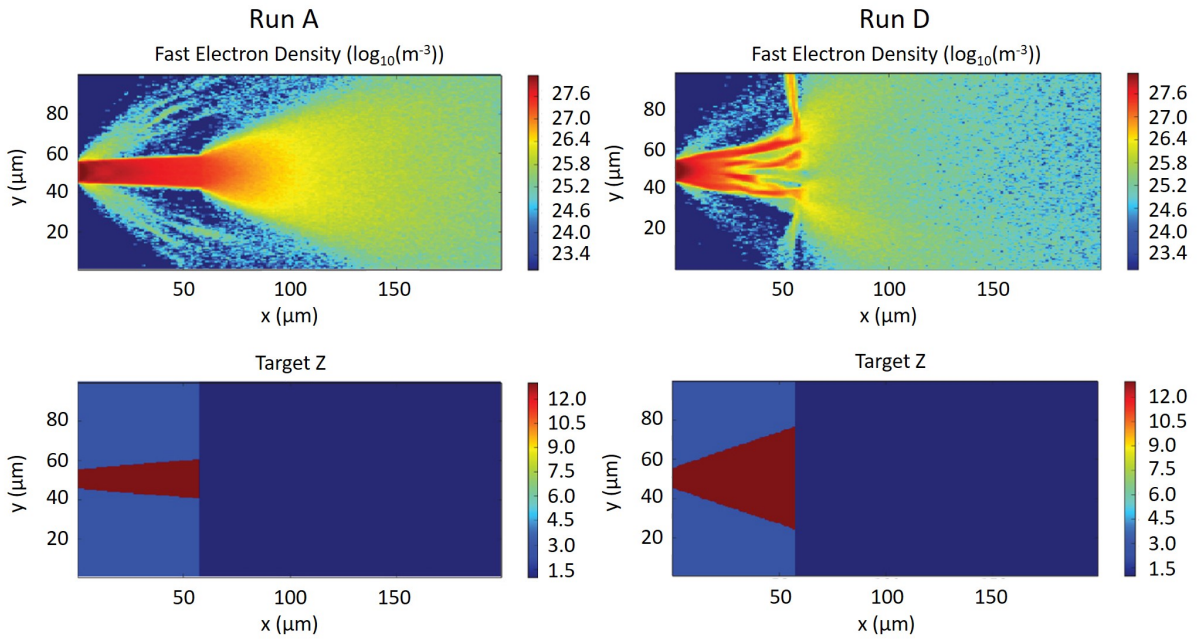

Figure 2.6: Target Z and background electron temperature at 1.4 ps after laser incidence. Runs A and D are conical guides with opening angles of 5° and 20° respectively. Figure taken from [13].

Again, the results suggest that the lower angle cones (5° and 10°) result in an improved angular reduction of the electrons, especially compared to the case of a straight, embedded wire [13]. However as the cone angle is increased (to 15° and 20°), filamentation of the electron beam is visible which acts to inhibit the resistive guiding mechanism. A comparison of the fast electron density and initial target Z for the 5° and 20° cones is presented in Figure 2.6. It is also recorded that as the electrons exit the 57 μm long cone, they begin to diverge again. It shall be shown in section 2.9 that it is advantageous for the electrons to remain collimated once they exit the structured target.

The first experimental evidence of successful resistive confinement of electrons was obtained by S. Kar *et al* [9] in 2009. A 12 μm thick tin (Sn) foil was bounded to the left and right by two aluminium slabs of 200 μm thickness. The Vulcan petawatt laser (1×10^{20} Wcm^{-2}, 1 ps, 20 μm FWHM) in combination with a plasma mirror was focussed onto the Sn component of the target at an angle of 10° to the target normal. Therefore in this configuration, the expected direction of the resistivity gradient in Equation 2.26 is perpendicular to the two Sn:Al boundaries. Optical Transition Radiation (OTR) was used to diagnose the spatial profile of the electron beam at the rear surface, with results showing an aspect ratio of the OTR signal similar to that of the original target. This suggests that confinement of the electrons was successful in the plane perpendicular to the Sn:Al boundary, i.e. in the plane of the resistivity gradient. As expected, the electrons were not confined in the vertical direction due to a resistivity gradient not acting in this direction due to the target geometry.

B. Ramakrishna *et al* [10] progressed the experimental investigations using a cylindrically symmetric target geometry in 2010. An iron (Fe) wire core of 25 μm and 50 μm diameter was surrounded by aluminium cladding to give a total target radius of 250 μm. The thickest target

was 250 μm, each with a copper (Cu) tracer layer at the rear side. Again, the Vulcan PW laser and plasma mirror combination (10^{20} Wcm^{-2}, 0.8 ps, 20 μm FWHM) focussed the laser pulse onto the Fe core at a 5° angle. The main diagnostics used Cu-Kα emission to observe the size of radiation emitted at the rear side of the targets. Results show that the structured targets consistently generated a smaller emission compared to uniform controls, suggesting that the fast electrons were confined within the high Z core.

A combination of simulation and experimental work has been presented in the literature that investigate the effectiveness of structured targets in confining fast electrons. Tapering the start of an embedded wire into a conical structure has been shown to reduce the angular divergence of fast electrons through specular reflection. This thesis focusses on implementing such targets in a laboratory setting, moving the experimental investigations further into the three-dimensional regime.

2.8 Ion-Acceleration

Ion acceleration is routinely recorded in laser-target interaction experiments, however to accelerate ions directly by the laser, intensities $\geq 10^{24}$ Wcm^{-2} are required [47]. Currently, this regime is unattainable, however ion acceleration occurs through the acceleration of electrons and the subsequent generation of a charge separation. This creates a strong electric field which is then capable of accelerating the ion population.

A variety of specific mechanisms accelerate the initial electrons. *Radiation Pressure Acceleration* (RPA), as the name suggests, uses the pressure from intense laser radiation to essentially *push* electrons from the laser focal spot region. The resultant charge separation then generates the ion-accelerating electric field. Esirkepov *et al* [47] shows that RPA becomes dominant for laser intensities exceeding 10^{23} Wcm^{-2} [47]. A further acceleration mechanism is the *Breakout After Burner* (BOA), which is dominant in targets of nm-scale thickness.

This thesis focusses on experiments conducted at the Vulcan PW laser facility [48] which holds nominal intensities of $10^{20} - 10^{21}$ Wcm^{-2}. Clearly, this is below the intensity regime within which direct ion-acceleration dominates. The majority of solid targets irradiated using the Vulcan PW laser in this thesis are approximately 100 μm thick, suggesting that the RPA and BOA mechanisms will not be dominant. This leads onto the final ion-acceleration mechanism that is expected to be found in this laser and target regime: *Target Normal Sheath Acceleration* (TNSA).

2.8.1 Target Normal Sheath Acceleration

A proportion of the most energetic fast electrons can escape from the rear surface of the target before it is sufficiently charged and inhibits the remaining electrons from escaping. A charge separation is induced at the rear surface between the escaped electrons and more massive ions, resulting in a strong TV m^{-1} electric field, capable of ionising atoms on the rear surface of the target. These ions are then accelerated out into vacuum along the target normal direction [49,50]. The acceleration of protons from the rear surface is more easily achieved due the increased charge-to-mass ratios compared to more massive ions. In 2004, Allen *at al* [51] showed that

these protons originate from hydro-carbon impurities on the rear surface of targets.

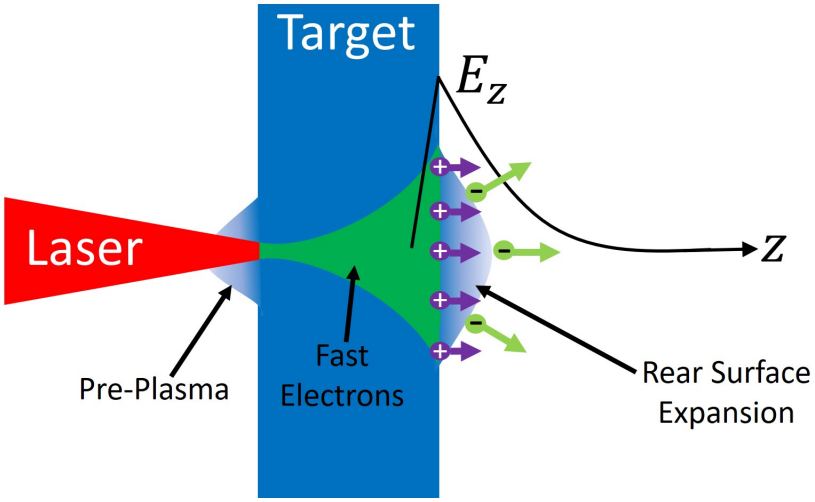

Figure 2.7: Schematic of the TNSA mechanism of ion acceleration. Electrons and ions represented by green and purple circles at the rear surface. Each contain the corresponding charge sign (- or +). Electric field E_z increases to a maximum at the sheath and accelerates ions along the target normal direction. Schematic based on [49].

Figure 2.7 presents a schematic of the TNSA mechanism. The laser pulse is incident from the left and interacts with the pre-plasma and the front surface of the target. The fast electrons are represented by the expanding green feature inside the target and the sheath is visible at the rear surface. Contaminants on the back surface are ionised and accelerated out into vacuum. Note the maximum electric field E_z is located at the rear surface, hence the preferential acceleration of protons from this region.

The 1D P. Mora model of plasma expansion [17] is commonly used to describe the TNSA mechanism. It considers a quasi-neutral plasma at a constant electron temperature and with a fully ionised ion population that is initially cold.

The target is initially (time $t = 0$) considered as a plasma that occupies a 1D space of $x < 0$ with ion density $n_i = n_{i0}$ and electron density $n_e = n_{e0}$. At $x > 0$, the ion density is $n_i = 0$ and electron density follows the Boltzmann distribution.

$$n_e = n_{e0} \exp\left(-\frac{e\phi}{k_B T_e}\right) \tag{2.29}$$

where n_{e0} is the initial electron density inside the target. ϕ is the electrostatic potential, k_B the Boltzmann constant and T_e the electron temperature.

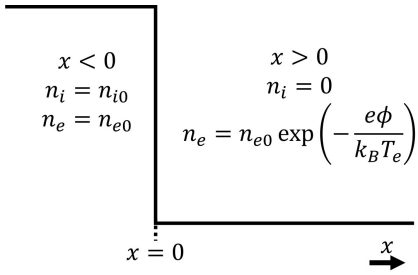

Figure 2.8: Initial set-up of the target at time $t = 0$ in the 1D Mora model [17]. $x < 0$ is inside the target and $x > 0$ outside the rear surface.

The electrostatic potential ϕ follows Poisson's equation and quasi-neutrality applies such that $n_{e0} = Zn_{i0}$. For $t > 0$, the electrons are assumed to be in equilibrium with the electrostatic potential while the equations of continuity and motion describe the ion expansion into vacuum ($x > 0$). The ions expand as a front with velocity v_{front}:

$$v_{front} \simeq 2c_s \ln\left(\tau + \sqrt{\tau^2 + 1}\right) \tag{2.30}$$

where c_s is the ion sound speed $c_s = \sqrt{Zk_BT_e/m_i}$ and $\tau = \omega_{pi}t/\sqrt{2\exp(1)}$.

However, $\omega_{pi}t >> 1$ such that the natural logarithm simplifies to $\ln(2\tau)$. The maximum kinetic energy of the ion population can then be determined from Equation 2.30 and using the substitution for the ion sound speed:

$$E_{max} = 2E_0[\ln(2\tau)]^2 = 2Zk_BT_e[\ln(2\tau)]^2 \tag{2.31}$$

where $E_0 = Zk_BT_e$ and E_{max} is the maximum proton energy.

A full derivation using the Mora model can be found in [17]. However, the above shows how the maximum proton energy is related to the hot electron temperature and the ion plasma frequency. This in itself is dependant upon the ion density and shall be used in Chapter 5 to relate the maximum proton energy to the fast electron population.

Considering the TNSA mechanism, the electrons that escape the target and drive the charge separation and accelerating field are from the relativistic component of the electron spectrum. Therefore, the electron temperature k_BT_e in Equation 2.31 will have a fast electron component such that $k_BT_e = k_BT_f$. For sufficiently high intensities for which the Wilk's Ponderomotive scaling applies ($k_BT_e \propto \sqrt{I_L\lambda^2}$), it can be expected that the maximum proton energy will scale with the square-root of the laser intensity ($E_{max} \propto \sqrt{I_L\lambda_L^2}$).

Experimental work has been conducted on a range of high-intensity laser systems to characterise how the maximum proton energy scales with the driver laser parameters. M. Borghesi *et al* [52] presents a review of such work where the scaling of $E_{max} \propto \sqrt{I_L\lambda_L^2}$ is observed for laser pulse durations relevant to this thesis ($t_L = 0.3 - 1$ ps). It is worth noting that the Vulcan PW laser - which is used in the experiments detailed in this thesis - is recorded to form part of this scaling in [52].

2.9 Inertial Confinement Fusion and Fast Ignition

One scheme of Inertial Confinement Fusion (ICF) uses lasers to compress deuterium and tritium fuel to the required temperatures and pressures for fusion to take place. The central hot spot approach is an isobaric process and aims to use an array of lasers (or x-rays) to compress the capsule of fuel which subsequently reaches ignition. The National Ignition Facility (NIF) is the world's largest and most energetic laser and uses an array of 192 beams to investigate ignition in the *in-direct drive* approach. However, stringent requirements of highly symmetric compression and large driver energies to achieve sufficient gain in the central hot spot approach have led to the consideration of other schemes. One novel technique is fast ignition [53].

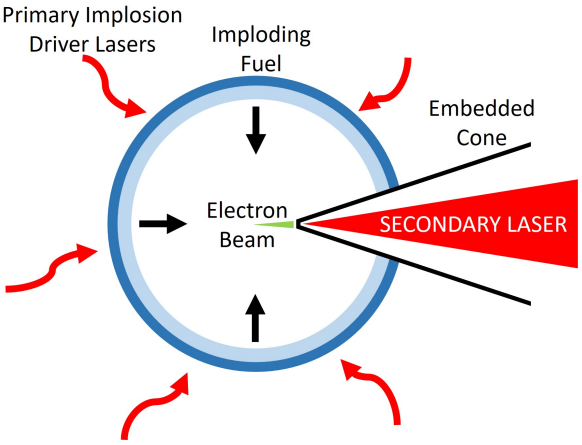

Figure 2.9: Schematic of the fast ignition approach to ICF. Fusion fuel (blue) under compression by primary driver laser beams (red arrows). Embedded cone guides the secondary laser (red) close to the fuel to generate the igniter electron beam (green).

The fast ignition (FI) approach to fusion is an isochoric process and involves two main steps. First, the fuel capsule is irradiated by a driver to initiate the implosion. This is then followed by a secondary stage where a further laser ($\sim$ 10 ps, $\sim$ PW) [53] is used to generate a beam of relativistic electrons that enter and ignite the pre-compressed fuel to initiate the fusion reaction. The cone-guided approach [4] to FI uses a high Z cone (e.g. gold) embedded within the fuel to create a clear channel through which the secondary laser pulse can travel and reach the cone tip. The laser pulse interacts with the tip and generates a fast electron population that is required to travel approximately 50 μm before being rapidly deposited into the fuel. In this scheme, the energy gain is enhanced in comparison to the central hot spot approach allowing for less energetic driver lasers to be used to achieve ignition [53, 54].

Naturally to enhance the energy coupling between the fast electron beam and pre-compressed fuel, the beam is required to stay as collimated into one area as possible. However, the previous sections have shown that the interaction of a high-intensity laser with a solid target results in a divergent electron beam. Investigating methods of reducing this divergence through resistive guiding - with the motivation of fast ignition - is the primary focus of this thesis.

Chapter 3

Instrumentation and Methods

3.1 High Power Laser Physics

The experimental work detailed in this thesis was undertaken using the Vulcan petawatt laser at the Central Laser Facility, UK. The technology of this laser will be detailed in Section 3.2, however it is useful to first outline some important aspects that allow such laser systems to reach the intensities relevant to Inertial Confinement Fusion research and the generation of hot dense matter.

3.1.1 Chirped Pulse Amplification (CPA)

As a high intensity laser pulse propagates through a plasma, the strongest component of the laser electric field is located at the peak of the pulse and can be sufficient in strength to expel electrons from this location through the ponderomotive force. This in turn modifies the refractive index across the transverse laser profile and can cause the laser pulse to focus within the plasma; this is termed *self-focussing*. This can result in the laser focussing to intensities exceeding the damage threshold of optics within the path of the pulse.

The issue of self-focussing initially arose within the radar community where the available circuitry was unable to handle the high peak power signals caused by the effect. This was overcome through a cycle of stretching and compressing the pulse to change the peak power throughout different chains of the system [55].

The general method behind this technique was later applied to high intensity laser physics in 1985 by D. Strickland and G. Mourou [56]. This work is widely known as Chirped Pulse Amplification and shared the award for The Nobel Prize in Physics 2018 [57].

The method involves three main stages of operation. Firstly, a short, low energy pulse is stretched - traditionally by linearly chirping the signal using a pair of diffraction gratings. By temporally stretching the beam, the intensity is reduced to below the damage threshold of the optics and gain medium of the system. The chirped pulse is then passed through the amplification stages of the system, with self-focussing effects minimised due to the reduction in intensity. Finally the amplified pulse is then temporally compressed using a further set of gratings with a reversal dispersion.

The CPA technique transformed high-intensity laser technology, producing intensities of over

10^{15} W cm^{-2} and opening up new frontiers in relativistic laser-plasma experimental research.

3.1.2 Amplified Spontaneous Emission and Plasma Mirrors

Spontaneous emission within the laser cavity can be amplified and observed as a pedestal extending before and after the main pulse. The ratio of the main peak and pedestal is termed the *laser contrast*.

When considering petawatt class systems relevant to this thesis, the energy contrast is typically of the order of 10^{-6} - 10^{-10} and extends nanoseconds before and after the main interaction pulse [58]. A contrast of this size can result in a pedestal of the order of 10^{15} Wcm^{-2} in intensity; more than sufficient to exceed the ionisation threshold of the target and breakdown the front surface before the arrival of the main interaction pulse. This generates *preplasma* on the front surface of the target, and modifies the interaction physics [59–61].

One method of reducing the pre-plasma is the implementation of a plasma mirror [61, 62] in the target chamber, as was done during the 2017 Vulcan PW experiment detailed in Chapters 4, 5 and 6. The device used in this campaign was composed of a BK7 glass substrate coated in an anti-reflective coating [63]. When the low intensity pedestal of the laser pulse is incident upon the device, the BK7 glass and coating are highly transparent and allow the light to travel through the material. However, as the higher intensity component of the pulse follows, the ionisation threshold is exceeded and the surface of the device is ablated. At the critical density, the laser light is reflected and can be directed towards the target.

A further advantage of using a plasma mirror is the ability to direct the laser pulse to the target at normal incidence. This is routinely carried out in simulations in the literature and allows for closer comparison of results. By using a plasma mirror, any direct reflections of laser light from the target surface are stopped, ensuring that they do not travel back through the laser chain and become focussed and damage components of the system.

3.1.3 Optical Parametric Chirped Pulse Amplification (OPCPA)

Originally suggested in 1992 [64] and demonstrated practically in 1997 [65], Optical Parametric Chirped Pulse Amplification (OPCPA) has allowed for focussed laser intensities to progress beyond those earlier opened up by the Chirped Pulse Amplification method.

OPCPA follows the same general process of stretching and compressing the pulse, however varies in the method of amplification. Optical Parametric Amplification (OPA) amplifies the pulse but is not subjected to gain narrowing like the conventional amplification method in CPA. Without the gain narrowing, the pulse bandwidth is no longer reduced and can therefore be compressed to achieve a narrower pulse length.

OPA is based upon the use of non-linear crystals to separate a main pulse into multiple lower frequency pulses and transfer energy between each. In doing so, a final pulse is generated with an amplified signal [64–67]. The gain bandwidth in OPCPA is determined by the crystal length and dispersive properties (as opposed to the specific transition in the gain medium in CPA). This means that the gain bandwidth can be larger than in CPA, and therefore allows for a shorter pulse length to be obtained.

3.2 The Vulcan Petawatt Laser

The experimental work detailed in this thesis was undertaken using the Vulcan petawatt laser (Target Area Petawatt) at the Central Laser Facility, UK.

The short pulse beams of Vulcan petawatt are based on the OPCPA technique of laser amplification, allowing for nominally 500 J of energy to be delivered in a 500 fs pulse.

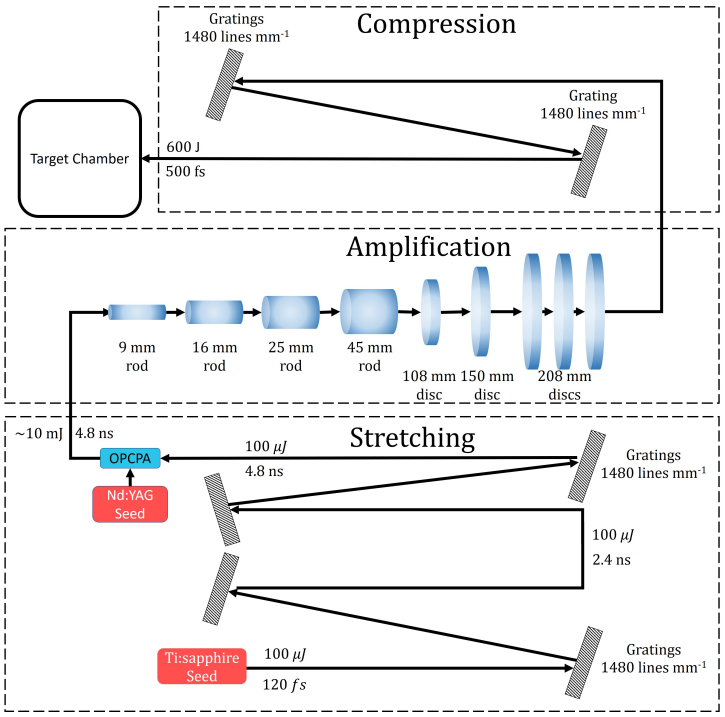

Figure 3.1: The CPA chain for generating the high-power Vulcan petawatt laser beam. Based on the schematic in [68]. The system is seeded by a Ti:sapphire laser shown on the bottom left of the schematic. The chain then stretches, amplifies (with an additional OPCPA chain) and then compresses the pulse before directing it into the target chamber shown at the top left of the image.

The system is seeded by a Ti:Sapphire laser which undergoes a single stage of OPCPA to reach 100 μJ in a 120 fs duration [48, 68, 69]. It is then temporally stretched using a double-decker Offner stretcher - composed of two Offner triplets stacked on top of one another. The seed pulse is injected into the lower Offner triplet and exits into the amplifier chain.

Whilst the Vulcan system is based upon Nd:glass as a gain medium, using solely this material as an amplifier in CPA would result in gain narrowing to a level below the limit required for the desired 500 fs compressed duration [48]. Therefore, a pre-amplification stage is implemented using the OPCPA technique, allowing for the stretched seed pulse to be amplified without the undesired gain narrowing. An Nd:YAG seed is mixed with the previously stretched Ti:sapphire seed pulse and input into an Optical Parametric Amplifier (OPA). This results in a 10-20 mJ pulse, corresponding to a total gain exceeding 10^7 from the OPCPA system [48, 70].

The OPCPA generated pulse is then amplified to approximately 500 J using a series of rod and disc amplifier chains, with the beam increasing in size between each stage to ensure that the energy density is below the damage threshold of the gain media. The rods and discs are

surrounded by an array of flash lamps which emit light, a fraction of which is absorbed by the amplifiers and stored in preparation for the laser beam to extract energy. A mix of 9 mm and 16 mm Nd:Silicate and 25 mm and 45 mm Nd:Phosphate glass rods (diameter) are used in the amplifier chain [68, 69]. The beam is initially injected into a 9 mm Nd:Silicate rod and then progresses through the remaining rods in increasing diameter size, resulting in a 4 J pulse being emitted from the chain.

As the beam and required rod amplifiers increase in radial size, the amplification becomes un-even across the beam. It also becomes technologically impossible to grow rod amplifiers to the required dimensions, therefore a series of disc amplifiers are used. These are 108 mm, 150 mm and (then 3× ex-Nova laser) 208 mm in diameter and are set at the Brewster's angle to allow for perfect transmission of the beam that is ejected from the rod chain [68, 69]. The disc chain amplifies the beam from 4 J to approximately 500 J of energy.

A single pass compressor is then used to temporally compress the amplified pulse to the desired 500 fs duration. This system is located in the target area.

The now amplified and compressed pulse is directed into the target chamber and reflected off a final turning mirror (diameter = 1 m). At this stage, the beam is 600 mm in diameter to keep the energy density below the damage threshold of the final optics.

The beam is then focussed using a 620 mm diameter, F#3 off-axis parabola with a focal length of 1.8 m. The mirror is silver coated with a protective layer to defend against ballistic material ablated from the target. Drive mechanisms on the parabola allow for 3-way motion, namely *yaw*, *roll* and *tilt* to optimise the focal spot to approximately 7 μm in FWHM.

The nature of high intensity laser physics means that experiments are undertaken in extreme environments. Therefore, it is critical for the driver beam to be well characterised in order to understand the data in relation to the environment in which it was obtained. This section details a number of diagnostics located in the Vulcan PW laser system.

3.2.1 Adaptive Optic

Thermal gradients along the large optical path of the Vulcan system, along with inherent optical aberrations, result in distortions to the beam's wave front quality [48, 71]. These need to be addressed before the beam enters the target chamber. This is achieved using a deformable mirror that automatically corrects the wave front of the alignment CW beam. The position of the mirror is then retained for the full energy shot [68, 69].

The deformable mirror, also known as the adaptive optic (AO), comprises of 64 actuators at the rear surface which deform under a low-voltage signal [71]. The extent of this deformation can modify the wave front of the beam to correct for any aberrations that would de-optimise the full energy shot.

3.2.2 Autocorrelator

In order to achieve the 10^{21} Wcm^{-2} intensities required of Vulcan petawatt, obtaining a sufficiently short pulse length and the on-shot monitoring of this is vital. This is performed using a *third order autocorrelator* which uses the input laser pulse to generate an asymmetric third order signal. This can then be used to diagnose the temporal shape of the input pulsed, with

the asymmetry of the signal allowing one to distinguish between temporal activity before and after the main pulse [72, 73].

3.2.3 Defocus Monitoring

During the amplification stages of laser operation, the firing of flash lamps can produce non-uniform heating and thermal gradients in the system. The increase in temperature can be on the order of 10 K and generate deformation of the optics, distorting the pulse as it travels through the amplifier [74]. A defocus aberration can be established in the pulse whereby the position of focus in moved along the laser axis so that the power held within the pulse at the original focal position is spread over a larger area, reducing the intensity of the beam.

When considering the Vulcan petawatt laser system, a Shack-Hartmann wave-front sensor (termed *HASO*, manufactured by *Imagine Optic* [75]) is used to determine the defocus of the beam by monitoring the quality of the wave-front. This is carried out on a shot-to-shot basis.

The principle underpinning a Shack-Hartmann sensor is to measure the local tilt of a distorted wave-front using an array of lenslets. The focal point of each lenslet is compared to a flat profile to determine the overall spatial tilt of the beam.

This information can be fed back into the adaptive optic (Section 3.2.1) which can apply a voltage across the AO actuators to correct for the wave front aberration.

3.3 Front Surface Imaging System

When considering the Vulcan petawatt laser system, an extremely important characteristic is the spatial *jitter* of the beam. This is the movement of the beam between the pre-shot alignment position, and the subsequent location of the main interaction pulse. Contributors to this movement include slight variations in the alignment procedure and temperature profiles along the laser chain that alter the local refractive index and subsequent path of the beam [76]. A further contributing factor relates to the structural integrity of optical components throughout the system and the ability for these to exhibit movement [76].

Considering the Vulcan petawatt system, the spatial jitter is generally considered to be approximately 3 times the size of the laser full-width half-maximum, corresponding to approximately 20 μm. This has been previously measured using Optical Transition Radiation to 17 $\pm$ 14 μm [77]. The spatial jitter becomes significant when implementing targets with small scale features onto which the main beam needs to be precisely aligned. This is the case for targets used in the 2017 experiment detailed in Chapters 4, 5 and 6 where clad conical structures are used to investigate the resistive guiding technique. The main interaction beam was required to interact with the centre of a cone tip, however across the targets under investigation, the dimensions of these structures ranged between 13 - 50 μm in width. The 17 $\pm$ 14 μm spatial jitter of the Vulcan petawatt beam suggested that even if the laser was aligned to the centre of the smallest cone structures, the jitter would inevitably cause the main interaction beam to move from the centre and miss some of the cone tips. Therefore, a mechanism was required to determine the position of the main interaction beam on the target surface in order to fully understand the environment in which the interaction took place. Due to the varying nature of

the spatial jitter, this was needed on a shot-to-shot basis.

In order to diagnose this, a novel front surface imaging (FSI) system was developed and later deployed on the 2017 experimental campaign detailed in Chapters 4, 5 and 6. The system was based upon two aspects: (1) the ability to simultaneously image the target and CW alignment laser to align and take a post-shot image, and (2) to record the time-integrated self emission from the plasma on the front surface of the target, signifying the position at which the main interaction pulse was incident on the target. This made use of the relativistic oscillating mirror (ROM) mechanism of self-emission detailed in section 2.3.

The system was developed off-line by A. Horne [77] to optimise the design and test limitations in the location of optics and signal levels. At this stage, the spatial resolution of the system was found to be 2.2 μm using USAF resolution slides [77]. The system was then deployed in the main target chamber to be used during the experimental campaign; this was undertaken by the author and the experimental team. In-situ, the spatial resolution was found to be slightly reduced to 3 ± 1 μm, measured using the known diameter of an alignment wire imaged using the deployed system [77]. The in-situ layout of the system can be seen in Figure 3.2, while further details can be found in [78].

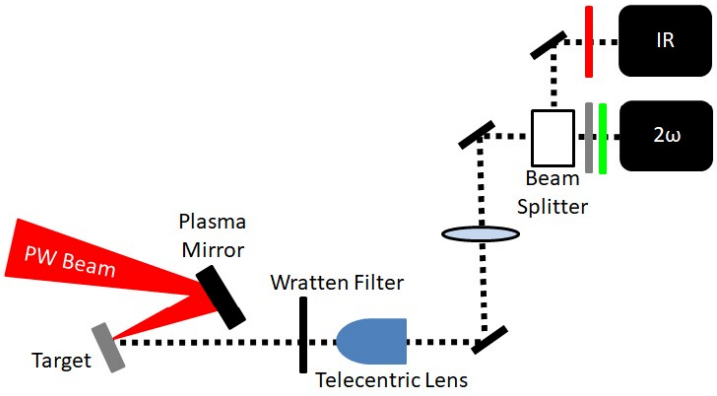

Figure 3.2: Setup of the in-situ front surface imaging (FSI) diagnostic used to determine the position of laser incidence. Target front surface illuminated with an IR diode and white light source. Pre-shot image recorded in an IR channel and a reference and time-integrated self emission image captured in a 2ω channel.

The first optic of the system was an Edmund Optics $2\times$ telecentric lens with a working distance of 75 mm. This was positioned 8.5 cm from the target, to image the front surface. Due to the proximity of the first optic to the target, Kodak Wratten filtering was positioned in front of the optic using an electronic shutter mechanism to protect from debris during the shot. ND filtering (ND3) was also used to reduce signal levels to avoid image saturation.

A 30 cm focal length achromatic lens was positioned 31 cm behind the back of the telecentric lens to further magnify the target image. A cube beam splitter was located 280 cm from target chamber centre to separate the signal into two channels, each incident onto a different camera. Between the telecentric lens and beam splitter was a series of mirrors to direct the image out of the target chamber.

The first channel was the alignment channel used to image the target before the shot and

aid the alignment procedure. To view the Vulcan petawatt alignment beam of wavelength 1053 nm, a Xenic IR CCD camera was utilised, with RG1000 filtering to remove signal outside of this wavelength. In order to sufficiently image the target before the shot, an IR diode of wavelength 1050 nm was positioned to illuminate the target front surface. To increase the brightness of this illumination, a 1 inch lens collimated the light emitted from the diode.

The second channel utilised the self-emission from the plasma to determine laser incidence. This was done using the emission at 2ω frequency, and hence a green image was recorded at a wavelength of 527 nm. This emission is predominantly produced via the *Relativistic Oscillating Mirror* (ROM) mechanism (see Section 2.3), for which the source size strongly correlates to the maximum intensity component of the laser focal region [79]. Therefore, by imaging this self-emission, the position of the maximum laser intensity can be monitored. An Andor Neo CMOS camera was used to image the signal of the 2ω channel, with a 527 nm interference filter combined with ND2 filtering in front of the camera to reduce undesired signal.

The 2ω channel was used to capture the self emission from the plasma, but also recorded a reference image before the shot which could be overlaid to determine the position upon the target from which the emission originated. In order to capture the reference image, the target was illuminated with a white light source directed into the target chamber using an optical fibre.

When in-situ in the target chamber, the resolution of the system was found to be 3 μm with a magnification of approximately $\times 17$. Section 4.3.5 presents images obtained using the FSI diagnostic recording various laser positions on conical structured targets.

3.4 Optical Shadowgraphy

Shadowgraphy has been utilised in order to image the expansion of plasma from the rear surface of the target. This method of optical probing involves parallel rays of laser light incident upon the plasma as it expands from the rear surface of the target into vacuum. When the probing rays interact with a density exceeding that of the critical density, the rays are unable to penetrate the plasma and reach the detector plane, leaving a shadow on the recorded image. This can then be analysed to extract the plasma size and mean expansion velocity.

It takes time for the rear surface to begin expanding after the main interaction laser pulse has reached the front of the target, therefore the probing beam is temporally delayed with respect to the main beam. The experiments detailed in this thesis were undertaken at the Vulcan petawatt facility, therefore it is pertinent to discuss how such a probing system is deployed on this facility.

The probing beam used on Vulcan petawatt is created from a small pick-off from the main interaction beam. A periscope is used as a pick-off from the main beam after the final turning mirror. The probe beam is then frequency doubled and linearly polarised to 45° using a KDP crystal and waveplate respectively [70]. Timing slides are situated before the target to adjust the path length of the probing beam and therefore the delay with respective to the main interaction pulse.

A streak camera was used to determine the timing slide position corresponding to a 0 ps delay, i.e. where the probe and main beams reach the target at identical times. For this, the main interaction beam was lowered in intensity and directed to TCC along with the probe beam. At TCC, a mirrored target was positioned to direct both beams to a Hamamatsu streak camera;

onto which the beams were focussed. The position of the timing slides were then adjusted so that the traces from the two beams were temporally matched. Once this was achieved, the position of the timing slides was recorded and corresponded to the 0 ps delay reference position. The timing slides were then moved from this position to increase the probing beam's path length and generate a temporal delay.

The timing slides have a 10 μm [70] accuracy corresponding temporally to 0.03 ps and were adjusted so that the majority of shots used a probe delay of 200 ps. The Hamatsu streak camera had a resolution corresponding to a temporal accuracy of 10 ps [70], hence the streak camera dominates the error in the temporal accuracy of the probe delay.

When a shot is taken, the probe beam is directed out of the interaction chamber using a combination of lenses and mirrors. It is then focussed onto a CCD camera and filtered using Neutral Density (ND) and Schott KG filter glass. The specific optics, filtering and detection equipment used for the probe diagnostic on each experiment are presented in Chapter 4.

As the rear surface plasma expands, the density profile causes the refractive index to be modified and refract the probing beam. The beam can be sufficiently refracted that it is no longer collected by the imaging optics and therefore appears as a dark region on the shadowgraphy image. Therefore, densities below the critical density can generate dark regions on the recorded image by refracting the beam.

Consider a rear surface plasma expansion with a density gradient perpendicular to the target plane. The probing rays travel along the plane perpendicular to the page, whilst the plasma is expanding from left to right.

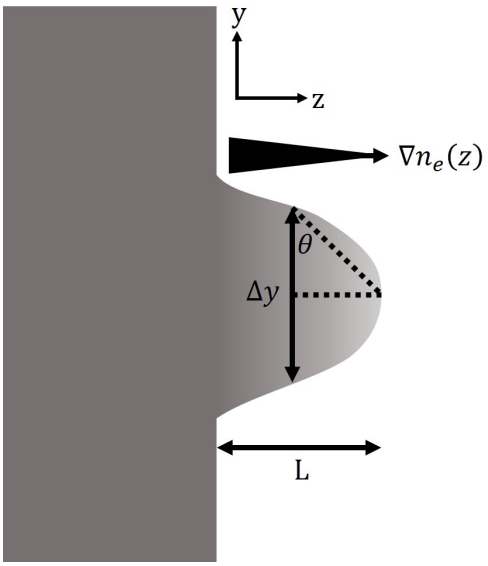

Figure 3.3: Rear surface plasma expansion with density gradient perpendicular to the target plane. Length scale L is the maximum expansion size perpendicular to the target plane. Δy is the full width half maximum of the expansion. Probing rays propagate perpendicular to the page.

If substantial refraction takes place, the probing light is deflected to outside of the detection optics and also exhibits a shadow on the detector. The deflection of the probing rays due to

refraction is detailed by G.J Tallents [80]:

A Boltzmann distribution can be used to describe the electron density at a given distance from the rear surface. Through differentiating the refractive index and implementing this distribution, one can determine the minimum electron density that is able to deflect the probe rays outside of the first collection optic [80]:

$$n_e = 2n_c \frac{\theta_{max}}{\Delta y} L \tag{3.1}$$

Here we can see that due to refraction of the probing beam as it propagates through the plasma, the actual density recorded on the detector image as dark shadows is actual shifted from the critical density by a factor $2\frac{\theta_{max}}{\Delta y}L$.

The work presented in Chapter 4 uses this result to calculate the plasma density that is imaged by the probing optics and then simulate a similar expansion using a radiation-hydrodynamic code (Section 3.8).

3.5 Radiochromic Film

In order to diagnose the proton beam emitted from the rear surface of the target, GAFCHROMIC radiochromic film (RCF) has been implemented extensively throughout the experiments detailed in this work.

3.5.1 Radiochromic Film Stack Design

In general, RCF consists of one or two polymer-based film substrates supporting a thin, active layer (see Figure 3.4). Upon exposure to ionising radiation, energy is transferred from the incident species to crystals of colourless photo-monomer molecules (diacetylene) which undergo a polymerisation process [81–84]. In doing so, a dye is released into the active medium resulting in a visible colour change dependant upon the incident radiation dose [81]. By placing the film closely behind the rear of the target and measuring the extent of the colour change, it is possible to investigate the spectra of protons emitted along the rear target normal direction.

Radiochromic film is used extensively in the medical, quality assurance and dosimetry industries due to a variety of benefits. The film is relatively robust, insensitive to visible light and doesn't requiring chemical processing, meaning that the diagnostic is widely favoured when compared to the traditional silver halide films [83, 84]. The RCF sheets can be prepared, installed and recorded under room lighting, meaning that the diagnostic is relatively simple and effortless to use.

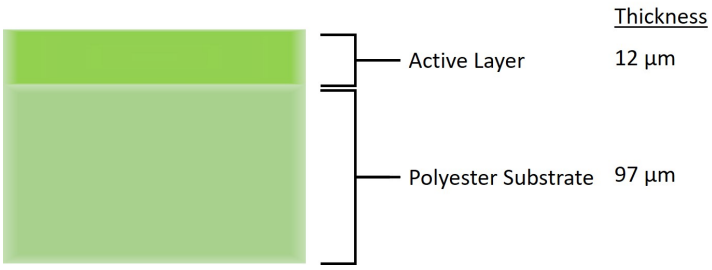

(a) HD-V2 Type RCF

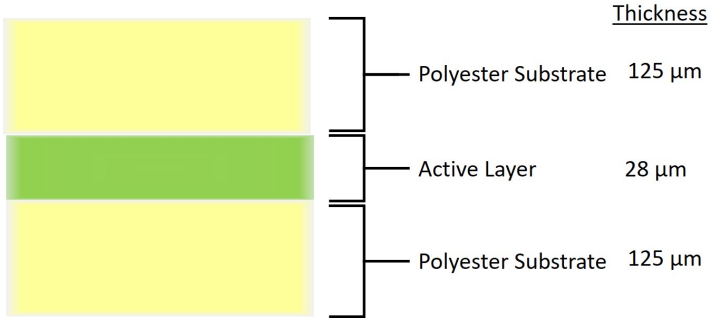

(b) EBT3 Type RCF

Figure 3.4: Structure of the (a) HD-V2 and (b) EBT3 type radiochromic films. Composition and layer thickness values taken from [85] and [86] for the HDV-2 and EBT3 films respectivelly.

As displayed in Figure 3.4, two types of GAFCHROMIC^{TM} film have been utilised in the experiments detailed in this thesis - namely HD-V2 and EBT3. These films are both capable of capturing protons in the 100 keV to MeV energy range [85, 86], but contrast in their dynamic dose ranges and therefore allow an extended dose range to be recorded when used in combination. The HD-V2 film performs best in the 10-1000 Gy range [85] whilst EBT3 response is optimised in the lower range of 0.2-10 Gy [86] due to thicker active layer and substrate.

Considering an arbitrary laser-generated proton spectrum, more protons are generated within the lower energies than in the high energy tail. Therefore, by combining the two types of RCF in a stack (Figure 3.5) containing filtering, the HD-V2 (higher dynamic range) can be placed towards the start of the stack where there are more protons. The EBT3 film with the lower dynamic range is then located further into the stack where the proton signal is reduced.

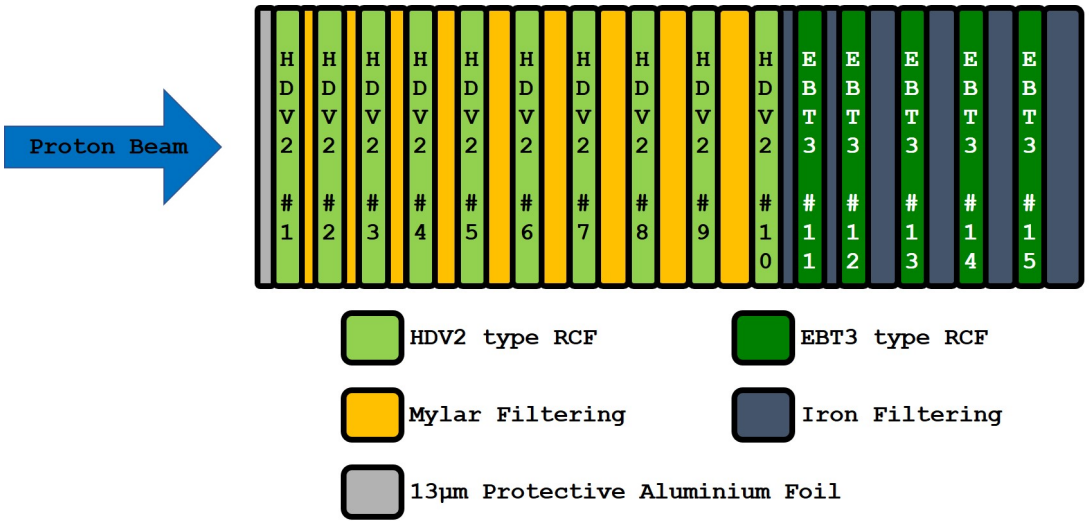

Figure 3.5: Example structure of an RCF Stack. Proton beam incident from left onto a protective aluminium foil. Filtering materials between each RCF sheet. Image plate (IP) stack located after the RCF (see section 3.6).

The thickness of the filters is increased deeper into the stack to increasingly stop the higher energy protons. The thickness of mylar and Fe filters for the example in Figure 3.5 range between 100 - 1200 μm and 250 - 750 μm respectively. A thick plate of 1 cm Fe is placed at the rear of the stack to provide structural support for a pair of screws that apply pressure to the stack to keep it held together. Without this, the screws would damage the final layers of the stack. In between the final RCF sheet and the 1 cm Fe sheet is an image plate (IP) stack to detect high-energy electrons; this is detailed in Section 3.6.

3.5.2 Response Curve Analysis

For the work presented in this thesis, a MATLAB code was implemented to calculate the energy range that the RCF stack captures. This code was created by D. C. Carroll (Central Laser Facility, UK) for the HPL user community and is based upon the SRIM stopping range tables. This method has been used to calculate the proton energies captured for the RCF stacks used in both experiments, with results presented in Chapter 5.

The code requires the user to input a range of proton energies, spatial and energy step sizes and to designate the order and thickness of materials in the RCF stack design under consideration. SRIM stopping data for the filters and RCF are loaded for the materials designated by the user.

For each energy step within the range suggested by the user, the code advances a proton of this energy through the depth of the RCF stack. This is undertaken incrementally for each spatial step provided by the user. The SRIM data files are drawn upon during each spatial step to calculate the energy deposited by the proton to the material at that depth. The proton is advanced until all of its energy is deposited. If the final energy deposition step is too large and the resultant proton energy is negative, this is set to zero.

The code then locates the position of the active layer of each RCF sheet and the deposited energy range that this covers. It then averages this range to give a single energy value for the

whole active layer. This results in a response curve for each RCF sheet, showing which initial proton energy deposits the majority of the energy. An example of this is shown in Figure 3.6.

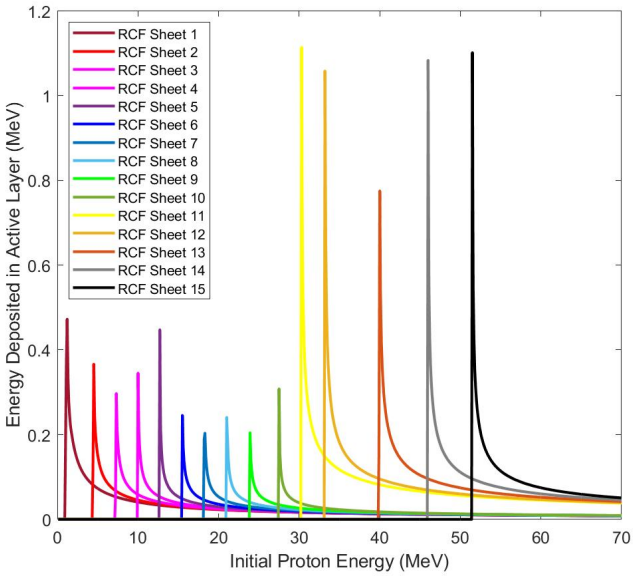

Figure 3.6: Response curves for the RCF stack design shown in Figure 3.5. For each peak, the horizontal location shows the energy of the proton that deposits the majority of it's energy within the active layer of that RCF sheet.

Once the proton beam has irradiated the RCF, the colour change is visible by eye, so prompt analysis can be undertaken to find the deepest RCF sheet that exhibits a colour change. Combining this with the response curves, one can find the maximum proton energy that the RCF stack has captured. However, if the laser pulse is directed along the target normal axis, protons generated by the TNSA mechanism will follow the same axis as the fast electrons generated during the interaction. Therefore, care needs to be taken to differentiate between the colour change generated from the two separate particle populations. Sometimes, this is more easily distinguished by looking at the images of the RCF once scanned using the *Nikon Super Cool Scan 9000 ED Transmission Scanner* located at the Central Laser Facility, UK.

3.6 Image Plate

FUJIFILM image plates (IP) are a radiation detection medium that have been used to detect the electron beam emitted from the rear surface of the laser irradiated targets.

Currently, FUJIFILM manufacture four types of IP that are used by a variety of scientific disciplines to image ionising radiation. These are the BAS-ND, BAS-MS, BAS-SR and BAS-TR, where the acronyms after the hyphen stand for *Neutron Detection*, *Multi-purpose Standard*, *Super Resolution* and *Tritium* respectively. It is the BAS-TR variety of IP that has been used in the experimental campaigns detailed in this thesis, where the *TR (Tritium)* acronym relates to the plate being originally designed to measure low energy beta emission during tritium decay [87].

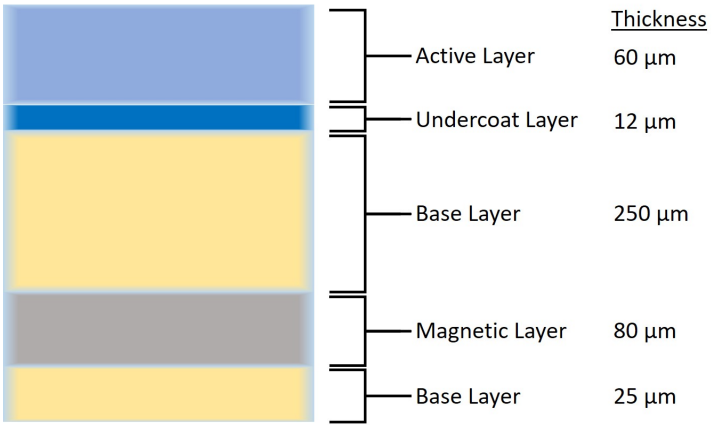

Figure 3.7: Composition of BAS-TR image plate. Composition and layer thickness values obtained from [28, 87].

The radiation is first incident upon the active layer of the BAS-TR image plate which is composed of 5 μm Barium Fluorohalide phosphor crystals ($BaFBr_{0.85}I_{0.15}$) and doped with Eu^{2+} bivalent europium atoms [28, 87–91].

The IP also consists of two base layers composed of mylar plastic ($C_{10}H_8O_4$) to provide structural support to the plate [87,89,91]. A further magnetic layer composed of a ferrite (MnO, ZnO, Fe_2O_3 and plastic) [89, 91] is also present and proves useful for magnetically securing the image plate in position during scanning.

As high energy electrons from the target rear surface - or other ionising radiation sources - are incident upon the image plate, they deposit a proportion of their energy into the phosphor layer. This causes the Eu^{2+} dopant atoms to become excited into the metastable state of Eu^{3+}, which then decays when exposed to laser light [28]. Photoelectrons generated by the excitation of Eu^{2+} become trapped in lattice defects called *colour-centres* [89].

The decay process leads us to the method of scanning and extracting the image from the IP. At the Central Laser Facility where the experiments were conducted for this thesis, the image plates were scanned using a FUJIFILM Fluorescent Image Analyzer FLA-5000, to be referred to as the *FLA-5000* or *IP scanner* for the remainder of this work.

The FLA-5000 uses a variety of solid state lasers and filters to generate light of different wavelengths. Practically, the image plates are positioned onto a cassette and held in place using magnets (note the Ferrite layer inside the IP in Figure 3.7). This is then inserted into the scanner which houses the cassette in a light-tight environment. A red laser of 685 nm wavelength is then scanned across the IP over an area designated by the user using the software loaded onto a connected PC [92].

The red laser is absorbed by the metastable Eu^{3+} states which further excite and rapidly decay, releasing blue light of approximately 480 nm wavelength [28, 93]. This process of light emittance is termed *Photo-Stimulated Luminescence (PSL)* and is collected by the photomultiplier tube (PMT) in the FLA-5000 scanner. Through digitising the light signal, the user is able to obtain a spatial pattern of the trapped photoelectrons within the colour-centres, which can be used to acquire a spatial and intensity profile of the incident ionising radiation.

Other than when subjected to the laser light, metastable Eu^{3+} levels can also decay over time

depending on the temperature. Detailed work of this decay process and corresponding temporal profile ($<10^4$ minutes) of the signal has been presented by [89, 94], in which it is clear that the rate of decay is slowest soon after the IP is irradiated by the ionising source. Therefore during the experimental campaigns detailed in this thesis, the IP was scanned as soon as possible after the laser-target interaction took place (of the order of 10 minutes). Naturally, this was only possible once the IP and RCF stack reached radiation levels suitable for handling.

Once the IP is sufficiently scanned, the signal on the image plate is removed through exposure to a white light source. This allows the image plate to be used multiple times, making it a favourable recording medium for a range of diagnostics.

3.6.1 First Scan Retrieval

If the PSL from the image plate reaches sufficiently high levels, the PMT can saturate and render the extracted image unusable. To avoid this, the IP is scanned multiple times, throughout which a proportion of the metastable Eu^{3+} levels fully decay. Multiple scans are undertaken until enough of the metastable levels have decayed so that the PMT during the final scan is no longer saturated. An image can then be extracted where each pixel shows an unsaturated PSL value.

A method was required to unfold the PSL from multiple scans so that one could determine what the value was on the initial saturated scan. This has previously been undertaken by D. Rusby [28] using MATLAB code and calibrations of the FLA-5000 scanner at the Central Laser Facility. Retrieving the first scan data requires knowledge of how the PSL decays as the IP is scanned an increasing number of times. With this relationship, the first scan PSL can be extrapolated back from the final scan data.

The process uses an IP that has been scanned multiple times but has an area that is unsaturated on the first scan. This is regularly the case outside of the main electron beam signal. The average PSL is calculated within this (rectangular) area across each scan of the IP, maintaining the same location of the region of interest between each scan. This process is then repeated for multiple IPs.

For each IP, the average PSL for each scan is plotted against the value for the first scan. Separate linear fits are then applied to each scan number. This is presented in Figure 3.8 where a number of scans have been undertaken for different IPs; here we refer to the scan number by the parameter n. The different IPs are designated by the vertical dashed-lines.

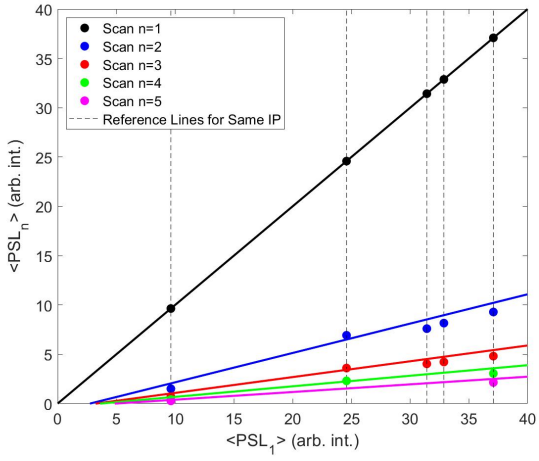

Figure 3.8: Comparison of the average PSL after being scanned n times against the average PSL after being scanned only once ($n = 1$). Linear fits applied across different IPs for the same scan number n. Vertical dashed-lines for reference. Data points lying on the same vertical line are from different scans on the same IP.

The gradients of these linear fits are then recorded and plotted as a function of the scan number that they correspond to.

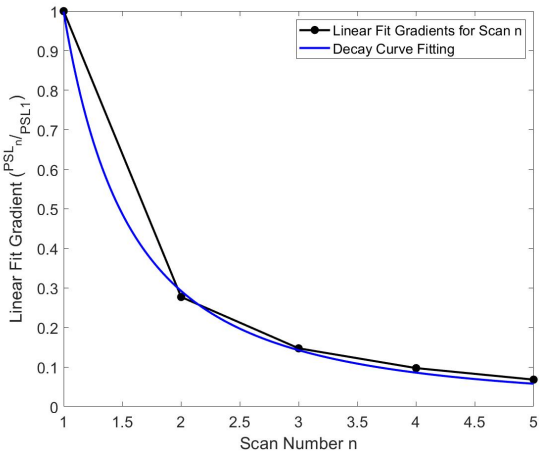

Figure 3.9: Gradient of the linear fits in Figure 3.8 for each scan number n. Used to determine the decay of PSL as the IP is scanned multiple times.

Figure 3.9 presents the decay of the PSL as the IP is scanned multiple times. The decay fit has been applied in the form of:-

$$PSL_n = an^b \times PSL_1 \tag{3.2}$$

where parameters $a = 0.998$, $b = -1.771$ and n is the scan number of the IP. A root-mean-squared (RMS) error of 0.0129 is achieved for the decay curve fitting.

A MATLAB code generated by D. Rusby [28] was then implemented which uses the a and b decay parameters to retrieve the Scan 1 PSL from the unsaturated image after scan n. The user inputs the unsaturated image of the IP and the scan number n. The code then uses the a and b decay parameters in Equation 3.2 and the n value defined by the user. It converts the PSL_n at each pixel on the image to the PSL that would be located at each pixel if the IP was scanned for the first time (PSL_1). The code then outputs the final scanned image with the calculated PSL_1 at each pixel. The code is then implemented for each shot on the experiment.

The method detailed above for extracting the decay curves and the first scan PSL shall be discussed in further detail in Chapter 6.

3.7 Optical Transition Radiation (OTR)

When a charge crosses a boundary between two materials of contrasting optical properties, radiation is emitted [18, 19, 95–98]. This can be collected and imaged in different wavelengths to obtain information regarding the charged population that initially crossed the boundary. This radiation is termed *Transition Radiation* (TR), and when the wavelength of the radiated light is within the optical spectral range, it is then referred to as *Optical Transition Radiation* (OTR).

3.7.1 OTR Mechanism

The filamentation of the fast electron beam has been investigated using the second harmonic (2ω) frequency of OTR radiation. This work is detailed in Chapter 6.

Transition radiation was first proposed in 1945 [95] and a detailed microscopic description is presented by A. P. Kobzev [96]. The radiating mechanism can be described by considering a single fast electron travelling at a constant velocity. In doing so, any radiation due to acceleration can be neglected and solely the OTR is considered [96].

As the electron approaches and passes the atoms at the rear surface of the target, energy is spent by the charge in polarising the surface atoms. This follows the law of conservation of energy and the surface atoms then oscillate freely with a dependency upon the surrounding atoms. Energy is lost during these oscillations and emitted into the vacuum as the transition radiation [19, 96, 98]. A schematic of this can be seen in Figure 3.10.

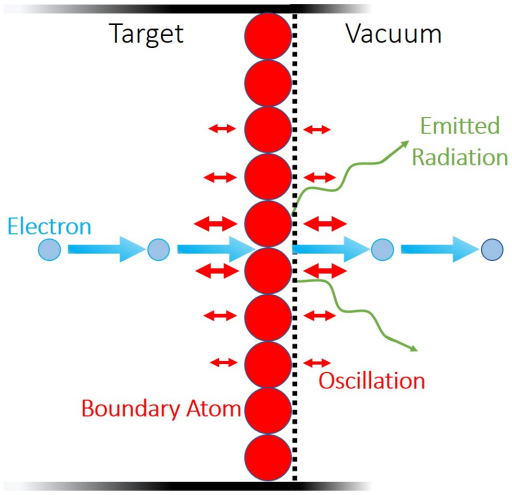

Figure 3.10: Schematic of the OTR mechanism. A single electron (blue) travels through the target and crosses the target:vacuum interface (dashed vertical black line). Atoms (red) at the target rear surface become polarised due to this electron motion and oscillate. These atoms then emit OTR radiation (green) in fulfilment of conversation of energy.

As shown in the Figure 3.10, the transition radiation is emitted from the oscillating target atoms [19, 96, 98], not the electron that leaves the target rear surface.

3.7.2 Coherent Transition Radiation (CTR)

In the work presented in Chapter 6, the OTR under investigation was at the second harmonic (2ω) frequency. This is generated in the identical process as that of OTR, however the electrons that drive the atomic oscillations are micro-bunched in time. This causes the fields generated by the electrons to sum coherently, and therefore the radiation emitted due to the oscillations is also coherent [18, 19]. With the electrons being driven into the target at twice the laser frequency, the transition radiation is therefore centred on the 2ω frequency. In this scheme, the radiation is termed Coherent Transition Radiation (CTR), and it is this variation that the work in Chapter 6 is based upon.

The intensity of the CTR radiation is described by Equation 3.3 [19]:-

$$I(\omega) = \eta(\omega) P^2 |i(\omega)|^2 \frac{sin^2\left(\frac{1}{2}M\omega\delta T\right)}{sin^2\left(\frac{1}{2}\omega\delta T\right)} \tag{3.3}$$

where $I(\omega)$ is the intensity of the coherent transition radiation as a function of angular frequency ω. $\eta(\omega)$ is the radiation intensity generated due to a single electron crossing the boundary and $|i(\omega)|$ is the modulus of the Fourier transform of the electron current due to a single electron bunch. M is the number of identical electron bunches containing P electrons, with each bunch temporally separated by a time δT.

For the sake of continuity, the total number of electrons N crossing the boundary is therefore the product of the number of bunches M and the amount of electrons each bunch contains P:-

$$N = PM \tag{3.4}$$

Therefore, when solely considering a constant number of M electron bunches travelling at the second harmonic frequency 2ω, Equation 3.3 can be reduced to show that the the intensity of CTR radiation is proportional to the square of the number of electrons N^2 crossing the boundary between the rear surface of the target and the vacuum region [98].

$$I(\omega) \propto N^2 \tag{3.5}$$

By collecting the CTR emission from the target, one also captures information about the number of electrons passing through that region. The work presented in Chapter 6 details such a process, as well as comparing the signal strength and the size of the emission region to work reported in the literature. This work is focussed upon the effect of target thickness and laser intensity. A detailed account is presented in Chapter 6, however one can briefly postulate how the CTR emission is related to these parameters by considering the fast electron beam.

Firstly, at greater laser intensities, the ability to liberate a higher number of fast electrons is also increased. So when considering Equation 3.5, one would expect the CTR intensity to also increase; this has been reported by Zheng *et al* [97]. However, it is clear that the divergence of the electron beam also increases with laser intensity, as shown by J.S. Green *et al* [5]. Therefore, the electrons should cross the rear surface over a larger transverse region, resulting in an increase in the CTR emission region. This has been reported by J.J. Santos *et al* [18].

One can also consider the effect of target thickness on the electron beam. As shown by K.L. Lancaster *et al* [6], the electron beam becomes increasingly divergent with target thickness. The increased number of collisions results in the reduction in not only the number of fast electrons reaching the rear surface, but also the collimation of the electron beam. In doing so, the CTR signal should be reduced in strength and spread across a larger transverse region for a target of greater thickness. This has been reported in [18, 19, 97].

3.7.3 CTR Diagnostic Design

In order to collect and image the emission generated from the CTR mechanism, a diagnostic was implemented on the 2017 Vulcan PW campaign. A schematic of this is presented in Figure 3.11:-

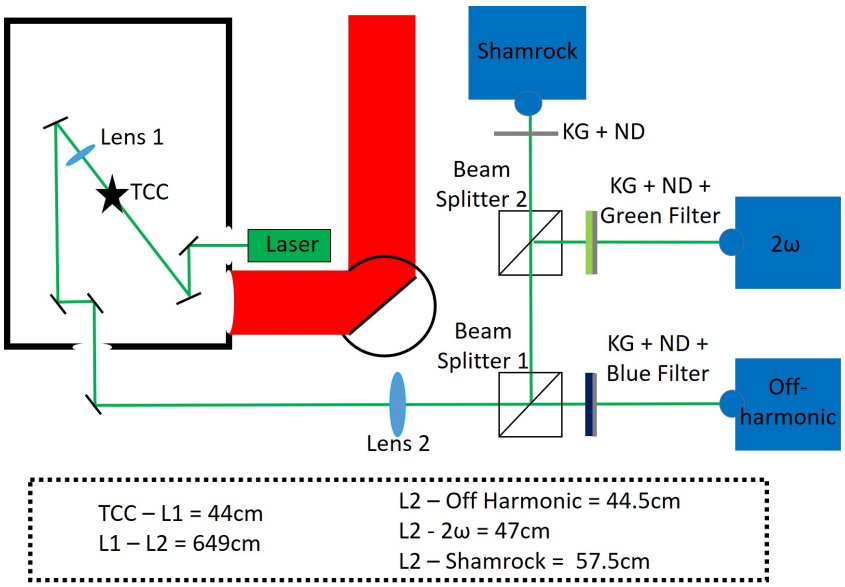

Figure 3.11: Schematic of the OTR layout used during the 2017 Vulcan petawatt experiment. Target chamber displayed as the black rectangle to the top left of the schematic. Red components show the propagation of the Vulcan beam from the compressor into the target chamber. Emission from the target rear surface was collected and directed out of the target chamber into 3 different devices displayed in blue to the right of the figure.

In reference to Figure 3.11, the target is positioned at TCC (Target Chamber Centre) and a 3 inch diameter lens (*L1*) was used to collect the total OTR emission from the rear surface of the target. This optic was located 44 cm behind the target, followed by a system of mirrors to direct the image out of the chamber. This allowed the team to work in a more open area, as well as keeping the cameras outside of the chamber to protect from EMP. A second lens outside of the chamber (L2) began to focus the image in preparation for the system of recording diagnostics. The signal then passed through two beam splitters, allowing the image to be split onto 3 separate recording devices, each operating behind different ND, KG and interference filters.

The device relevant for this thesis is the 2ω camera, which was imaging the CTR radiation, however for completeness, it is worth noting the purpose of the remaining 2 devices. (1) The *Shamrock* was a spectrometer that collected the OTR signal to allow for spectral analysis in further work, while the (2) *Off-harmonic* was an Andor Neo (16.6×14.0 mm CCD) camera that captured the blue spectrum OTR signal from the target. The work detailed in Chapter 6 is based upon the coherent transition radiation (CTR), so only the 2ω system shall be discussed further.

The 2ω camera was also an Andor Neo (16.6×14.0 mm CCD) positioned behind a series of

KG, ND and a green interference filter. These reduced the signal to avoid image saturation, but also excluded wavelengths outside of the 532 nm required for imaging the coherent transition radiation. By solely imaging the CTR, the analysis is centred upon the transport of the fast electrons - bunched at the second harmonic frequency - with sufficient energy to escape the target surface. Without the interference filter, the camera would be recording off-harmonic thermal emission from the lower energy electrons within the target [18].

A detailed account of the analysis method shall be presented in Section 6.3 where the CTR signal strength and emission size have been investigated, along with the filamentation of the electron beam.

3.8 HYADES code

HYADES is a one-dimensional, radiation-hydrodynamic code that has been used to infer the rear surface temperature in combination with shadowgraphy. This work is presented in Chapter 4.

The code is intended for use by experimentalists to design simple laser-matter interaction experiments, in addition to aiding researchers in the high energy density community to understand the interactions between relevant physical processes [99]. The simple one-dimensional nature of the code allows the simulations to be run relatively quickly which makes it ideal for the iterative nature of the method detailed in Chapter 4.

A one dimensional mesh is constructed by the user, within which the code follows the Lagrangian formalism where the mesh is moved with the material. Three fluids are modelled - the electrons, ions and radiation - the former two are coupled by Coulomb collisions modelled by Maxwell-Boltzmann statistics. Dependant upon the situation, the radiation fluid can be treated as a single group (gray-approximation) described by an ideal Planckian, or multi-groups which allow for small deviations from this. The radiation is solely coupled to the electron fluid [99].

Ionisation can be modelled using a variety of inbuilt descriptions, whilst the energy transport is modelled by flux limited diffusion, both of which are determined by the user's input deck. For situations involving large temperature gradients, the predicted heat flow can exceed the free-streaming limit; therefore, a flux limiter is introduced to inhibit this effect and limit the heat flow to a fraction of the free-streaming value [70, 100].

The code solves the conservation equations of mass, momentum and energy, closing the system with an Equation of State (EoS). The Lagrangian nature of the code means that mass conservation is automatically fulfilled. Conservation of momentum is solved by calculating the mesh accelerations from pressure gradients, allowing the velocity and position of each mesh cell to be determined. The final energy conservation is solved using the EoS to relate the change in internal energy to the specific heats of the materials. This final process closes the system. The EoS is derived from realistic models and selected by the user; these are the Sesame EoS Library, QEOS and Ideal Gas model. Magnetic fields and laser deposition can be included in the simulations, however this shall not be detailed here as the work described in Chapter 4 does not model this.

The code houses an inbuilt post-processor capability which has been utilised in this work. A multitude of desired parameters from the output file can be selected using the post-processor

and combined into a single data file. This is ideal for the work presented in Chapter 4 where an iterative method required successive simulations to be run using data from the previous outputs.

3.9 ZEPHYROS code

3.9.1 Outline

The second simulation code used in this thesis is ZEPHYROS [101]. Developed by A.P.L. Robinson from 2009 onwards, ZEPHYROS is a 3D hybrid Particle-In-Cell (PIC) code that is based on the work of J. R. Davies [102]. It is worth noting at this point that the code, and therefore all equations in this section, follow the SI units system unless stated otherwise. However, notable exceptions are the laser intensity (W cm^{-2}), laser wavelength (μm) and temperature (eV).

ZEPHYROS is a *hybrid* simulation code meaning different species within the system are modelled using different descriptions. The fast electrons are modelled by a particle description whilst the background is treated as a fluid, this allows the code to investigate physics on a broader time scale than would be possible with solely a PIC or hydrodynamic code. A specified number of fast electrons are collectively represented by single, computational macro-particles, which then travel through the system following relativistic equations of motion. The fluid description of the background uses a simple Ohm's law to relate the background current density and resistivity to the electric field. This assumes that the background electrons are collisionally dominated and respond instantaneously to fast electron motion. Substituting this into the Ampere-Maxwell law gives the complete description of the electric field:-

$$\mathbf{E} = -\eta \mathbf{j_f} + \frac{\eta}{\mu_0} \nabla \times \mathbf{B} \tag{3.6}$$

The first terms on the right hand side generates the component of the electric field that opposes the fast electron current, whilst the final term describes the separation of fast electron and background currents [102].

The magnetic field is described with slightly more contributing terms and is shown by Faraday's Law below:-

$$\frac{\partial \mathbf{B}}{\partial t} = \eta \nabla \times \mathbf{j_f} + \nabla \eta \times \mathbf{j_f} + \frac{\eta}{\mu_0} \nabla^2 \mathbf{B} - \frac{1}{\mu_0} \nabla \eta \times \mathbf{B} \tag{3.7}$$

The first and second terms on the right hand side of Equation 3.7 are comparable to those governing the resistive guiding technique (Equation 2.26). The first generates a magnetic field due to a gradient in the fast electron current; this governs pinching and filamentation of the beam. The second term generates the magnetic field from gradients in the resistivity - these can be from the resistivity change as the target heats or initially inbuilt into the target structure by using a composition of different materials. The magnetic field generated from this term pushes the fast electron beam either inwards or outwards depending on the resistivity profile. The final third and fourth terms on the right hand side of Equation 3.7 describe magnetic field diffusion and convection respectively [102].

3.9.2 Fast Electron Beam Injection

3.9.2.1 Number of Fast Electrons

The laser-target interaction is not explicitly modelled in ZEPHYROS, instead the laser conditions are defined by the user and a corresponding fast electron population is calculated from this. The fast electrons are assumed to be generated from the background and are injected into the simulation box at each time step. The number of particles injected at each time step follows the relationship [101]:-

$$N_{fast} = \frac{\eta_{abs} I(r) \Delta y \Delta z dt}{\bar{\epsilon}_{fast}} \tag{3.8}$$

where N_{fast} is the number of fast electrons injected in each time step dt, η_{abs} is the fractional absorption to fast electrons from a laser of intensity $I(r)$. The fast electron population holds an average energy of $\bar{\epsilon}_{fast}$ and is injected into a vertical and horizontal space described by Δy and Δz respectively. The injection is directed along the x-axis whilst the radial direction of the laser intensity is r.

3.9.2.2 Spatial Distribution

The temporal profile of the laser pulse is restricted to a top-hat profile, with a maximum duration defined by the user. However, the spatial distribution of the injected fast electron population can be chosen from a number of options including an exponential, top-hat, Gaussian or various super-Gaussian profiles. Excluding the top-hat profile, each of these spatial injections are based upon a characteristic spot size, r_L, defined by the user. The simulations undertaken in this thesis utilise a Gaussian profile for the electron beam, so an example of this relationship is shown below [101]:-

$$I(r) \propto \exp\left[-\frac{r^2}{2r_L^2}\right] \tag{3.9}$$

where $I(r)$ is the laser intensity at a given radial distance r and r_L is the characteristic laser spot size defined by the user.

By setting the left hand side of Equation 3.9 to $\frac{1}{2}$ and $r = r_{HWHM}$, one obtains the relationship between the characteristic laser spot size required by the code to model a laser of desired Half Width Half Maximum (HWHM) radius r_{HWHM}:-

$$r_L = \frac{r_{HWHM}}{\sqrt{2\ln 2}} \tag{3.10}$$

where r_{HWHM} is the HWHM size of the laser pulse and r_L is the characteristic laser spot size required by the code to model such a beam - assuming a Gaussian spatial distribution.

3.9.2.3 Energy Distribution

The fast electrons are also characterised by an energy distribution. This is based upon the temperature of the population which can either be defined by the user, or follows the Wilks-like

scaling relation [101]:-

$$T_{fast} = 2m_e c^2 \left(\sqrt{1 + \frac{I\lambda_L^2}{1.38 \times 10^{18}}} - 1 \right) \tag{3.11}$$

where T_{fast} is the fast electron temperature in units of eV, m_e the electron mass and c the speed of light in vacuo. I is the peak laser intensity is units of Wcm^{-2} and λ_L the laser wavelength in units of μm.

The calculated fast electron temperature is then used to determine the energy distribution of the population. For the simulations included in this thesis, an exponential energy distribution is used.

3.9.2.4 Angular Distribution

The final characteristic of the fast electron population that ZEPHYROS considers is the angular distribution. A wide range of profiles can be selected ranging from a uniform and multiple cosine-power distributions through to an exponential, Gaussian or *Moore* and *Sheng* Energy Dependant models.

The angular distribution model is selected by the user along with a further parameter being defined; namely the half-angle of the profile. For the purpose of this thesis, this parameters shall be referred to as $\theta_{\frac{1}{2}zeph}$. For the uniform angular distribution, the electrons are injected over a solid angle subtended by the half-angle $\theta_{\frac{1}{2}zeph}$ parameter, however for the Gaussian distribution, this parameter refers to the standard deviation σ. As it is the latter angular distribution used in this thesis, the relationship between these two parameters is:

$$\theta_{\frac{1}{2}zeph} = \frac{\theta_{\frac{1}{2}}}{\sqrt{2\ln 2}} \tag{3.12}$$

where $\theta_{\frac{1}{2}zeph}$ is the user defined parameter in radians that represents the a Gaussian angular distribution with HWHM angle $\theta_{\frac{1}{2}}$.

3.9.2.5 Additional Secondary Beam

ZEPHYROS has the capability for a secondary beam to be injected into the simulation. The beam parameters are controlled in the same way as for the main beam, however the additional beam was initially directed from the opposite side of the simulation box. However, A.P.L. Robinson (the code author at The Central Laser Facility, UK) has made a recent modification to ZEPYHROS which allows us to direct the secondary beam from the same side as the primary beam. This has been used to investigate the effect of an astigmatic beam, where the first *Airy wing* of the beam was replicated by the secondary fast electron beam. This work is presented in Chapter 4.

3.9.3 Running ZEPHYROS

In order to understand how the user runs ZEPHYROS and the general process that the code follows, a flow diagram is displayed:-

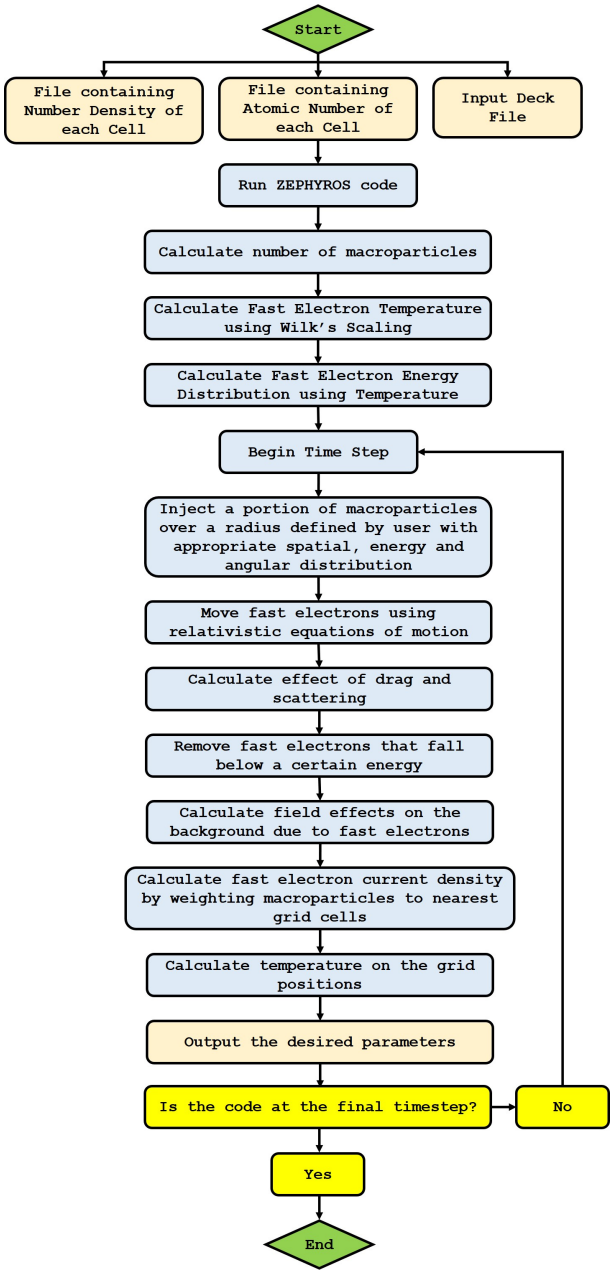

Figure 3.12: Flow chart outlining the method used by the ZEPHYROS code.

As can be seen in Figure 3.12, the user generates the input deck and files containing the number density and atomic number of each cell. The code is then run and macroparticles are generated with parameters corresponding to a fast electron distribution based upon the laser pulse information provided in the input deck. The macroparticles are then injected into the simulation and allowed to move in accordance to the relativistic equations of motion. The effects on the background and the associated energy loss are calculated. The relevant parameters on the grid are also calculated and output as a *.dat* data file. The next time step is then initiated

until the simulation reaches the final time specified by the user.

The data files are then visualised by the user to show the relevant parameters, as can be seen in the work presented in Chapter 4.

Chapter 4

Inferring Rear Surface Temperature of Conical Structured Targets using Shadowgraphy and Simulation Techniques

4.1 Preamble

This thesis presents the first experiments using conically structured targets to investigate the resistive guiding technique. This adds to the previous work by S. Kar *et al* [9] and B. Ramakrishna *et al* [10] which implemented planar and cylindrically structured targets respectively. In this chapter we chronologically present the targetry, diagnostic and laser configurations used in each of the conical target experiments. Results obtained from shadowgraphy and hydrodynamic simulations are used to infer the rear surface temperature of the implemented targets. An enhancement in rear surface heating is reported for a group of targets for which we propose a possible mechanism underpinning this result.

Resistive Guiding is well suited to high intensity, high energy, picosecond pulse length laser systems. Previous simulation and experimental work shows how the technique not only requires hundreds of femtoseconds to establish the confining magnetic fields, but is also dependant upon the fast electron current; which itself depends on the driver intensity [8–13]. Nominally, the Vulcan PW laser is capable of achieving intensities of 10^{21} Wcm^{-2} with a pulse duration of 500 fs, meeting both the intensity and temporal requirements for the technique.

Both of these experiments centred upon using conical structured targets clad in a lower Z material. As displayed in Equation 2.26, the magnetic field is initially generated by the gradient in material resistivity, which is dependant upon the material Z number. Naturally, a variety of control targets, such as planar foils, were also investigated on each experiment.

If one considers the fast ignition scheme of ICF, the cone tip is displaced from the compressed fuel core by a distance of approximately 50 μm. As such, the fast electrons need to remain collimated across this distance to maintain sufficient energy density when they reach the fuel. However, in the case of a short conical guide surrounded by lower resistivity cladding, simulations

show that the electrons diverge after leaving the end of the structure [13]. For resistive guiding to be applied successfully to fast ignition, this divergence needs to be controlled once the electrons leave the guide element.

Therefore, in both experiments detailed in the following chapters, we investigate the electron divergence across this distance by introducing a comparable 50 μm stand-off between the cone base and rear surface of the targets.

4.2 Vulcan Petawatt Campaign 2015

The first experiment was conducted in 2015 before enrolment onto the PhD course. Although not present during the experimental campaign, all of the data analysis presented in this thesis has been carried out by the author.

4.2.1 Targetry

Four categories of targets based on aluminium were implemented on the 2015 campaign. The first were aluminium control foils, the second was a structured control target composed of aluminium and CH glue. The final two categories were variations on conical structured targets. The aluminium control foils ranged in thickness between 10, 50, 75 and 100 μm. The remaining targets were all 100 μm thick.

Target	**Thickness (μm)**	**Purpose**
Control Foils	10, 50, 75, 100	Homogeneous Controls
Structured Control Foil	100	Missed Shot Control
Unclad Cones	100	Electrostatic Confinement
Clad Cones	100	Magnetic Confinement

Table 4.1: Targets used on 2015 Vulcan PW Campaign.

The 100 μm thick control foils also acted as the base structure from which the remaining cone targets were engineered. The first 50 μm depth of the foils was mechanically machined to create the desired conical structures, leaving a further 50 μm of aluminium foil behind. This process continued with a portion of the cone targets being surrounded by a plastic (CH) glue to provide the resistivity gradient between the high Z aluminium and lower Z glue. These targets were termed *clad cones*. The remaining portion of the targets were left without the glue and termed *unclad cones*. These were used to act as control targets for electrostatic sheath confinement; where the electrostatic field generated at the cone:vacuum interface is sufficient to confine electrons as recorded by [103,104]. Further details of this effect are presented in section 2.7.2. A structured foil target was used as a control for the possible situation in which the laser pulse missed the clad cone tip and hit the CH glue to the side. Therefore, this was constructed from 50 μm of CH glue followed by 50 μm of aluminium foil behind. All targets had a 7 μm thick, alignment wire located at the top of the front surface. This was constructed from carbon fibre.

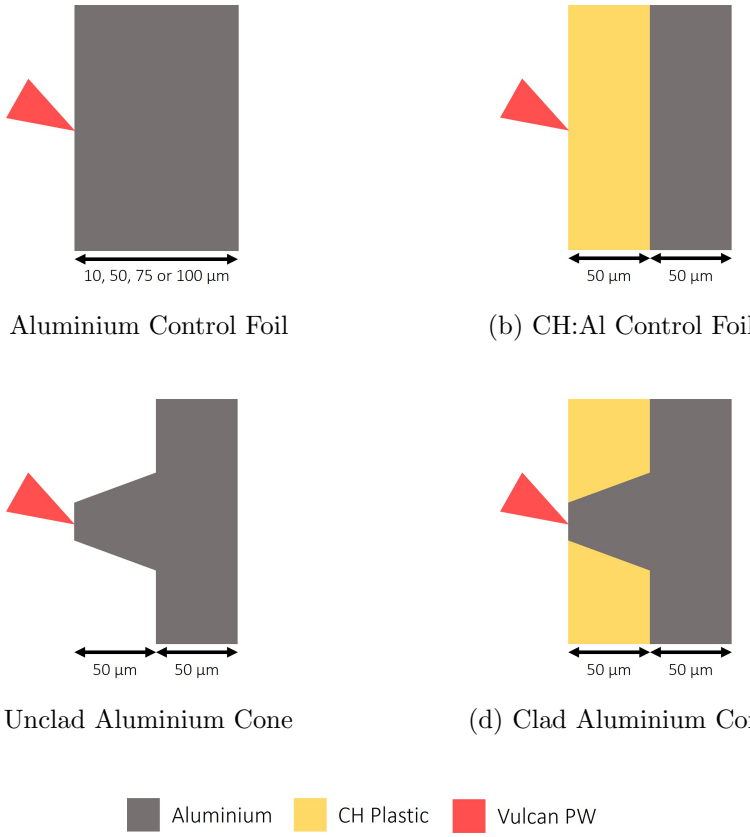

(a) Aluminium Control Foil

(b) CH:Al Control Foil

(c) Unclad Aluminium Cone

(d) Clad Aluminium Cone

Figure 4.1: Targets used on the 2015 Vulcan PW campaign. (a) aluminium foils (b) CH:Aluminium control foil (c) unclad cones used to investigate electrostatic confinement (d) clad cones surrounded by CH glue to provide the resistivity gradient.

Due to the nature of mechanically machining the cone structures from 100 μm thick foils, the tip and base size of the cones varied across the assortment of targets. Naturally this meant that the opening angles of the cones also varied.

Target	$<$**Tip Width**$>$ $\pm$ σ (μm)	$<$ **Base Width**$>$ $\pm$ σ (μm)	$< \alpha_{\frac{1}{2}} > \pm \sigma$ (°)
Unclad Cone	33.7 $\pm$ 13.5	52.9 $\pm$ 15.2	10.8 $\pm$ 3.1
Clad Cone	37.3 $\pm$ 11.8	56.7 $\pm$ 10.6	10.8 $\pm$ 6.4

Table 4.2: Mean tip and base widths and opening half-angle of unclad and clad cone targets used on the 2015 Vulcan PW campaign. Symbols $<>$ and σ denote the mean and standard deviation of values respectively. $\alpha_{\frac{1}{2}}$ is the half angle of the opening of the cone.

Table 4.2 shows that both the clad and unclad cones had an average opening half-angle $< \alpha_{\frac{1}{2}} >$ of approximately 10°. Most of the clad cones ranged between approximately 5° to 15°, comparable to the majority of targets investigated in the simulation literature [12,13]. The widths of the cone tips ranged between approximately 20 μm to 50 μm, significantly larger than those in the literature. However, this still proves to be an issue in the experimental environment

due to the spatial jitter of the laser pulse. This shall be further discussed in the chapter.

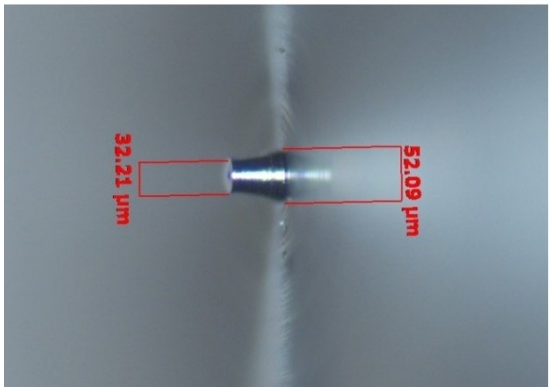

(a) Side photograph.

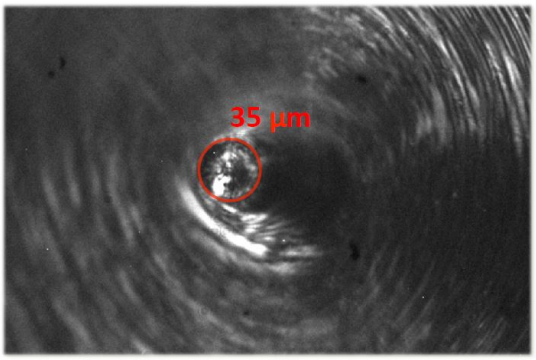

(b) Front surface photograph.

Figure 4.2: Photographs of (a) the side of an unclad aluminium cone (b) the front surface of an unclad aluminium cone. Both used on the 2015 campaign. Note the surface roughness caused by the mechanical machining tool used to create the cone feature.

An effect of mechanically machining away the foil targets to achieve the desired cone features is visible in Figure 4.2b. The machining tool leaves grooves across the target creating a rough front surface. Naturally this will play some role in the laser absorption and scattering; this shall be discussed in detail later.

4.2.2 Experimental Setup

The Vulcan PW laser was focussed onto the front surface of the targets using the 620 mm diameter, F/3 off-axis parabola (OAP) present in the target chamber. The angle of incidence between the laser pulse and target normal axis was 13° in the horizontal plane. This was as close as possible to normal incidence whilst being outside of the angular cone of debris that extends back from the front surface. This was determined using ZEPHYROS simulations by C. Ridgers [105] and S. Doyle [105] prior to the experiment.

The average (± standard deviation) laser intensity upon the target was determined as (3.12± 1.06) $\times 10^{20}$ Wcm^{-2} across the experimental campaign.

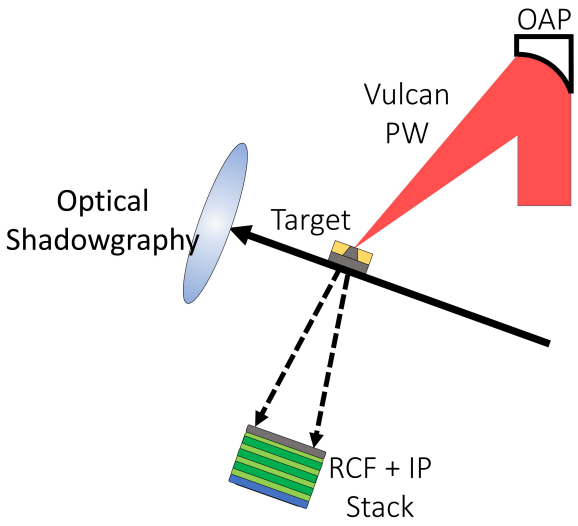

Figure 4.3: Main diagnostics used in the 2015 Vulcan PW campaign. Vulcan PW beam (red) is focussed onto the target using a 620 mm diameter, F/3 off-axis parabola (OAP). Laser incidence angle of 13° to target normal. Radiochromic film (RCF) and image plate (IP) stack located 5 cm normal to the target rear surface. Optical shadowgraphy imaged perpendicular to target normal direction (solid black arrow) to extract plasma expansion information. Schematic not to scale.

The beam was optimised at the start of the experiment using the focal spot camera provided by the facility. An RCF and IP stack was located 5 cm perpendicular to the rear surface of the target to collect the proton beam emitted through the Target Normal Sheath Acceleration (TNSA) mechanism. The specific stack design and analysis of this diagnostic will be presented in Chapter 5. Electrons were captured on the IP (BAS-TR variety [28, 87]).

An optical probe (shadowgraphy) operating at the 2ω harmonic frequency was installed so that images of the full target width and plasma expansion from the front and rear surfaces were obtained. The probe imaging axis was parallel to the target plane and used a pick-off from the main Vulcan beam; this method follows that detailed in section 4.2.4. Across the whole campaign, the delay between the probe and main interaction beam ranged from 100 - 500 ps in 100 ps intervals. A 527 nm wavelength and KG5 Schott filter was used to exclude the majority of signal outside of the 2ω frequency.

4.2.3 Laser Beam Characterisation

The main parameter of the laser pulse to be considered is the intensity incident upon the target; naturally this is comprised of the temporal duration, spatial FWHM of the pulse and the energy contained within this area. Each of these have been characterised to obtain a unique laser intensity for each shot.

The spatial FWHM of the beam was determined at the start of the experiment using a focal spot camera to image the optimised CW alignment beam. A line-out across the focal spot image was then extracted and a Gaussian distribution fitted to the central peak. From this, the FWHM was calculated and converted into microns using the camera's spatial calibration. This

was determined as 5 μm.

Calorimetry was used to determine the transmission of laser energy from the pre-compressor and target locations. An average value of 43% was calculated. For each shot, the energy reading before the compressor was multiplied by this value to provide an energy at the target location after the focussing parabola. To calculate the intensity upon the target, a further 30% of this energy was assumed to be contained within the FWHM. Work presented in section 4.3.4.1 supports this value.

The temporal duration of each laser pulse was determined using traces from the Vulcan PW autocorrelator diagnostic [72, 73]. These images were processed by the user to calculate each pulse length throughout the campaign.

The intensity for each shot was calculated by combining the pulse duration, energy contained within the FWHM of the beam at the target position and finally the size of this area. Across the experiment, the average intensity was found to be $(3.12 \pm 1.06) \times 10^{20}$ Wcm^{-2} (mean $\pm$ standard deviation).

4.2.4 Shadowgraphy

The probe beam was picked-off from the main Vulcan PW interaction beam using a periscope just after the final turning mirror. The beam is low energy (approximately 2 J) and was frequency doubled and linearly polarised using a KDP crystal and wave plate respectively [70]. It was then directed over timing slides to increase the path length and create a delay from the main Vulcan PW beam. This delay varied between 100 - 400 ps in 100 ps increments to determine the most suitable time-scale for a significant amount of plasma to be generated across the image. This was finalised at 200 ps for the majority of shots throughout the campaign. The delay was calibrated using a Hamamatsu streak camera which dominated the temporal error (10 ps) [70].

A periscope lifted the probe beam to the height of the target and then a combination of mirrors directed the beam perpendicularly across the target. Optics before and including the periscope shall be referred to as the *delay system* throughout the remainder of this thesis.

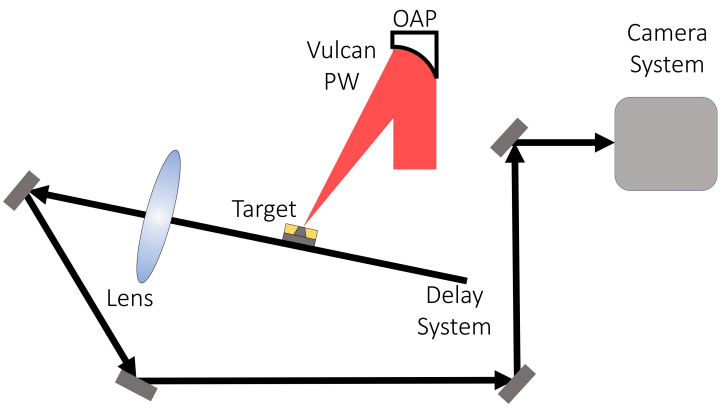

Figure 4.4: Configuration of the shadowgraphy system implemented on the 2015 campaign. Probe beam is picked-off from the main interaction beam and delayed using timing slides. The beam is then directed across the target and focussed using a 7.62 cm diameter lens onto a CCD camera located outside of the chamber. Distance between the target and lens was 46 cm.

A 7.62 cm diameter lens was located 46 cm after the target to focus the image. This was then channelled out of the target chamber where a CCD camera recorded the focussed image of the expansion. The camera was wavelength filtered to 532 nm, with additional KG5 Schott glass and Neutral Density (ND) filtering. The majority of shots used ND 4.0 to reduce the signal strength to appropriate levels to avoid image saturation. The probe configuration resulted in a magnification of $\times 6.6$ and a spatial resolution of approximately 3.5 μm. The limiting f/number of the system was approximately f/5.2.

In order to spatially calibrate the diagnostic, the tip of the 7 μm thick alignment wire on top of a target was imaged in real time. The target was shifted in height and along the target normal direction by known magnescale positions so that the wire tip was recorded at all 4 extremes of the CCD image. The known target displacement and movement across the camera allowed the probe to be spatially calibrated to 0.577 μm/pixel.

4.2.4.1 Calculating the Average Rear Surface Expansion Velocity

A reference image of each target was captured before the shot to determine the location of the unperturbed front and rear surfaces. A further image was then captured after the specific delay from the main interaction beam. The imaged expansion was time-integrated over the 100 ms exposure duration of the camera.

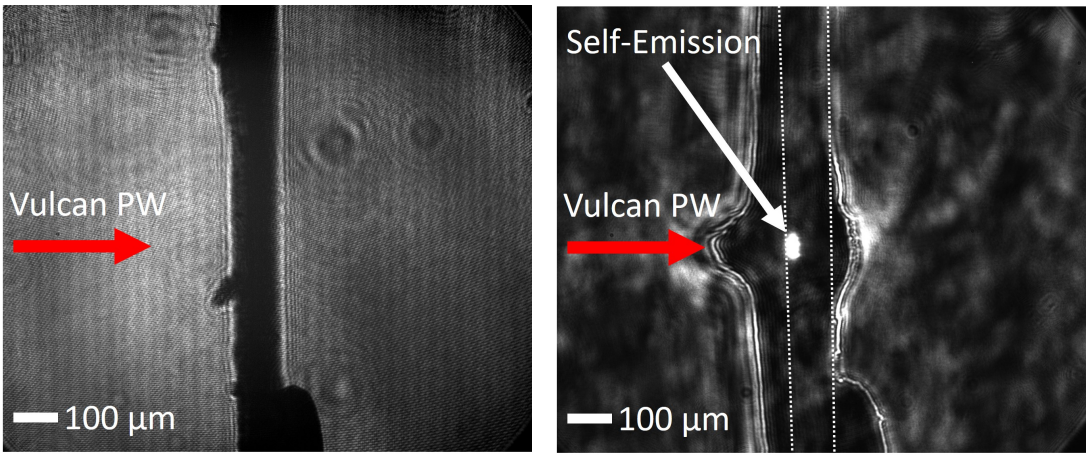

(a) Pre-shot reference image.

(b) Time-integrated post-shot image.

Figure 4.5: Images from 2015 optical probe diagnostic (a) pre-shot reference of clad Al cone target (b) time-integrated (100 ms) image of the same cone target during the shot. White-dashed lines reference unperturbed target surfaces. Probe delayed by 200 ps after main Vulcan beam incident from the right.

MATLAB software was created to analyse the complete set of probe data from the campaign. This extracted the expansion size and calculated the velocity and plasma density that was imaged as dark regions on the probe. The method of extracting the average expansion size and velocity is shown in the following bulleted list. The first two points allow image contrast and magnification alterations to be made to more accurately locate the required features on the image:-

1. The front and rear target boundaries are located on the reference image (respectively left

and right boundaries on Figure 4.5a).

2. The horizontal boundary of the rear surface expansion is located on the post-shot image (right boundary on Figure 4.5b).

3. The difference between this position and the rear surface reference is calculated.

4. This is converted using the calibration factor from pixels to μm. This is the rear surface expansion size.

5. The probe delay is loaded into the software and the rear surface expansion size is divided by this value to calculate the average velocity.

6. The above steps are repeated so that the images are analysed a total of 3 times.

7. This allows the mean $\pm$ standard deviation to be calculated for both the plasma expansion size and velocity.

This method was applied to all of the shots throughout the campaign, with the mean $\pm$ standard deviation expansion velocity being calculated as (3.08 ± 0.21) $\times 10^5$ ms^{-1} across the experiment.

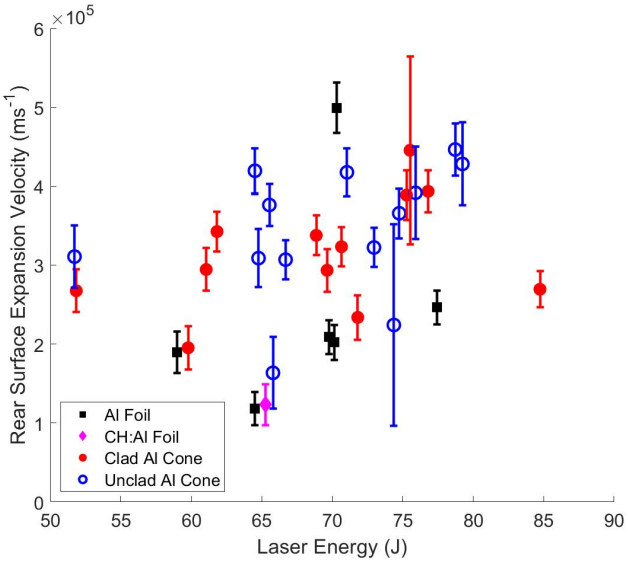

Figure 4.6: Mean rear surface expansion velocity as a function of laser energy for 100 μm thick aluminium targets. Vertical error bars combine the standard deviation between the 3 analysis runs with the system's spatial and temporal delay resolution.

The mean rear surface expansion velocity for each 100 μm thick target is presented in Figure 4.6, where each data point is created by analysing the shadowgraphy image three times. The vertical error bars combine the standard deviation between the three analysis runs with the error due to the system's spatial resolution. The resolution of the streak camera in determining the temporal delay is also incorporated in the error value. The errors for the majority of shots were dominated by the spatial resolution of the system, however for some shots, the standard

deviation between the three analysis runs became dominant. In these cases, determining the precise location of the expansion boundary was difficult and resulted in a large standard deviation in velocity across the three analysis runs. This situation was apparent in shots such as the clad and unclad cones with the large error bars at approximately 75 J laser energy. Structures within the expansion contributed to the difficulty in deciphering the boundary location of the expansion.

In general, the mean expansion velocity of the rear surface increases somewhat with laser energy, however the range of energies is too small to obtain a clear correlation. Excluding the single shot at approximately 5×10^5 ms^{-1}, the aluminium control foil targets consistently create a slower expansion than the cone targets. A low expansion velocity is also generated for the Al:CH structured target that represents the laser pulse being incident on the CH glue. Variation in rear surface velocity is seen across the clad and unclad cone targets, with no clear distinction between the two.

The variable nature of the rear surface velocity across all of the 100 μm thick targets means that observing any effect of resistive guiding is challenging.

4.2.4.2 Determining the Plasma Density

When the probe beam penetrates sub-critical areas of the plasma, refraction can sufficiently bend the beam so that is it no longer collected by the first optic. This is detailed in section 3.4 and results in a dark region being obtained on the shadowgraphy image. The density at which this occurs shall be referred to as the *cut-off density* for the remainder of the thesis.

As shown in Equation 3.1, the cut-off density is related to the maximum collection angle of the first optic (θ_{max}), the size of the expansion perpendicular to the target plane (L) and the FWHM size of the plasma that the probe beam travels through (Δy). The perpendicular expansion size L was already calculated from the previous section using the pre-shot reference and post-shot images. The maximum collection angle of the first optic θ_{max} is determined from the radius of the lens and distance from the target.

$$\theta_{max} = tan^{-1}\left(\frac{r_{lens}}{d_{target \rightarrow lens}}\right) \tag{4.1}$$

where r_{lens} and $d_{target \rightarrow lens}$ are the radius of the first lens and distance between the target and lens respectively. θ_{max} is in units of radians.

The optical probe images the side of the target, therefore the FWHM size of plasma that the probe beam travels through is perpendicular to the page and cannot be extracted. However, if one assumes a spherical expansion, this distance is equivalent to the vertical FWHM of plasma, which can be calculated from the image.

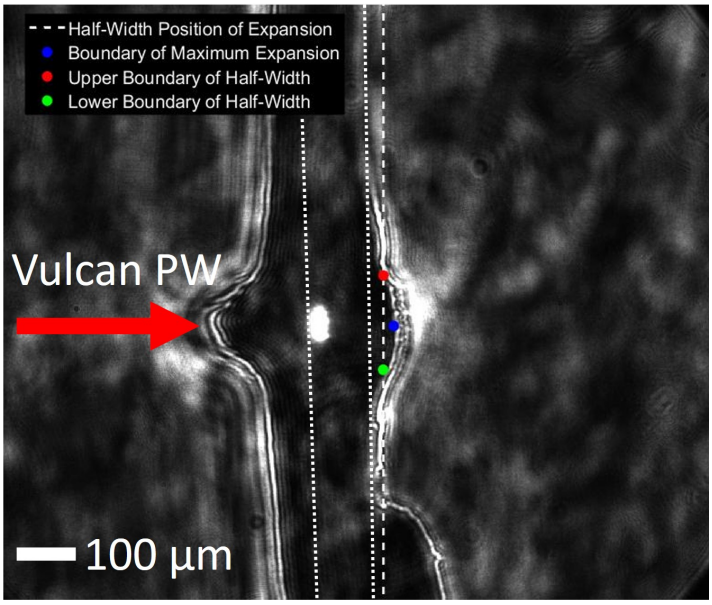

Figure 4.7: Image of plasma expansion on the optical probe. Used to determine the imaged cut-off density. Vertical dashed line placed half-way between the unperturbed position of the rear surface and the most extreme position of the plasma expansion (blue dot). Two white-dotted lines reference unperturbed target surfaces.

The farthest location of the expansion is signified by the blue dot, while the unperturbed rear surface is referenced by the right-most of the two vertical, dotted lines. The half-way location between these two points is the plane that the FWHM lies upon, and is referenced by the vertical, dashed-white line. The FWHM is then the distance between the upper and lower locations that the expansion intersects this line. These are represented by the red and green dots respectively. This distance is converted to microns to become Δy, and is then combined with the maximum collection angle of the first lens θ_{max} and perpendicular expansion size L to calculate the cut-off density.

Across the experiment, the average cut-off density was calculated as $(2.21 \pm 1.66) \times 10^{20}$ cm^{-3} (mean $\pm$ standard deviation). The critical density of the plasma without refraction effects being incorporated is 3.95×10^{21} cm^{-3}. Here one can see how densities less than the critical value can result in dark regions being imaged on the optical probe.

4.2.5 Hydrodynamic Simulations

The cut-off density and rear surface expansion velocity have been used in combination with hydrodynamic simulations to infer the rear surface temperature of the target. This follows a similar method by K. L. Lancaster *et al* in [15] and uses HYADES in a one-dimensional format to simulate the hydrodynamic expansion of each target. Details of the code are presented in section 3.8.

The general principle of this work involves simulating the rear 30 μm of the aluminium targets. The initial temperature of the target is varied until the cut-off density expands at the same velocity as determined by the shadowgraphy. In doing so, the rear surface temperature of the target can be inferred.

The rear 30 μm of aluminium is split into 30 zones on a mesh grid. Each zone is 0.9 the thickness of the previous zone meaning that the final zone width is approximately 3×10^{-4} nm; more than ample to resolve any hydrodynamic features at the rear surface. Feathering the mesh in this way balances computational expense with obtaining sufficient resolution towards the rear surface where the cut-off density is most likely located. The whole target is designated with a mass density, atomic number and atomic mass of 2.7 gcm^{-3}, 13 amu and 26.982 amu respectively [99]. An equation of state (EOS) for aluminium is used from the inbuilt library [99]. The aluminium foils, CH:Al structured foil, clad and unclad cones all share an identical structure for the rear-most portion of the targets. Therefore, setting the HYADES simulations up in this way allows the same input structure to represent all four of these targets.

After the relatively long probe delay, the dense aluminium plasma is likely to be found in local thermal equilibrium (LTE), therefore the inbuilt average-atom ionisation model describes the target. A flux limiter is placed on the ions with a multiplier of 0.05. The radiation uses the multi-group diffusion model and is split into 40 groups with the energies logarithmically interpolated between 1×10^{-6} - 2 keV. Using multi-group diffusion as opposed to single-group allows the system to model the large range of photon mean-free-paths within the dense plasma.

The simulations are implemented using an iterative method to determine the temperature that generates an expansion similar to that recorded by the shadowgraphy. The process is undertaken for each unique shot separately. A flow diagram of this method is presented in Figure 4.8 for reference.

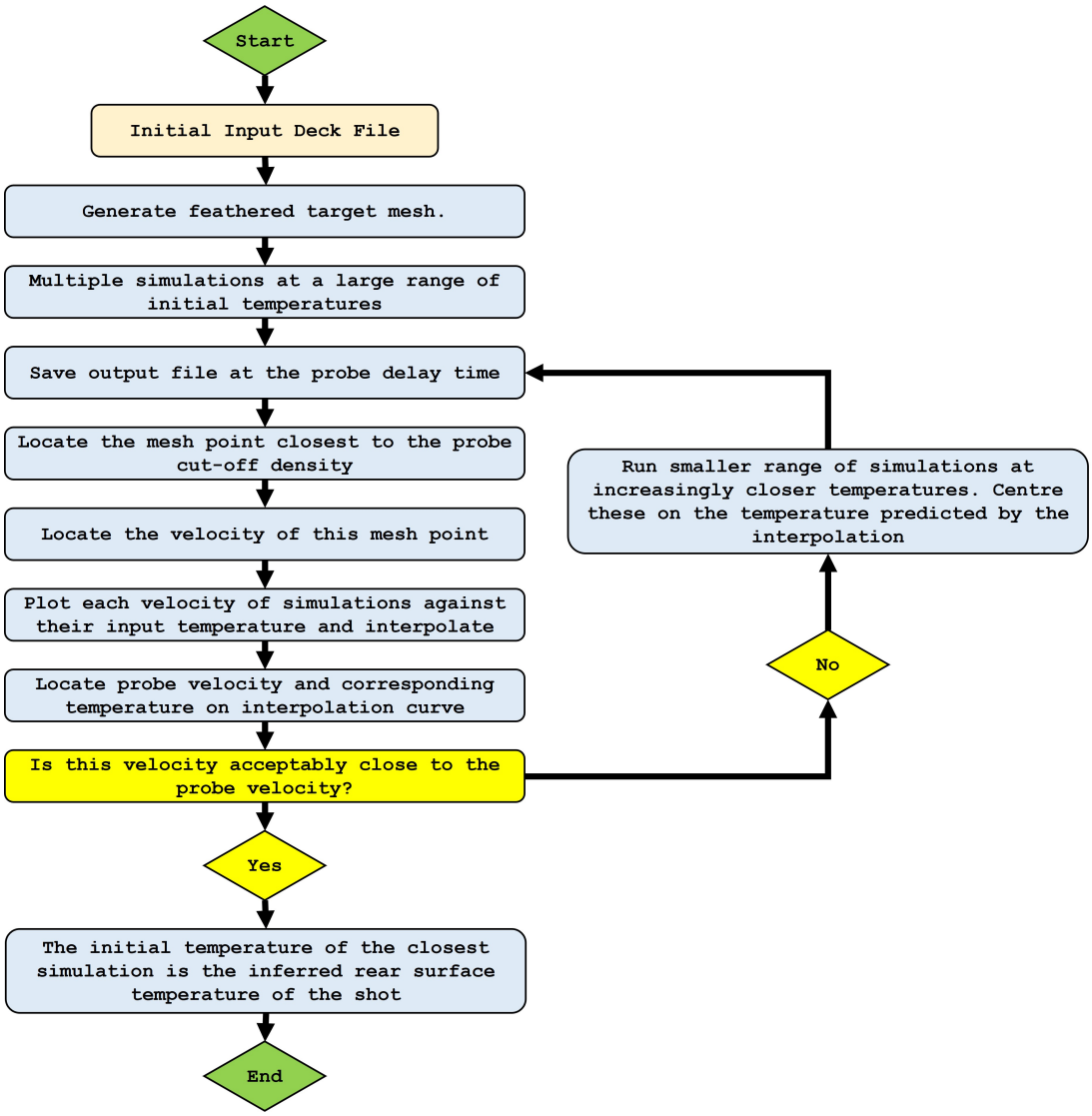

Figure 4.8: General process of using HYADES simulations to infer the rear surface temperature of targets using the expansion velocity determined by shadowgraphy.

The simulation process begins by generating the feathered target mesh and setting this to a homogeneous, initial temperature. The target then hydrodynamically expands for the duration of the probe delay; after which the electron density is plotted as a function of distance. Figure 4.9 presents an example of this plot which shows the electron density at each mesh wall as a function of distance after 200 ps. Each mesh wall is represented by a blue dot.

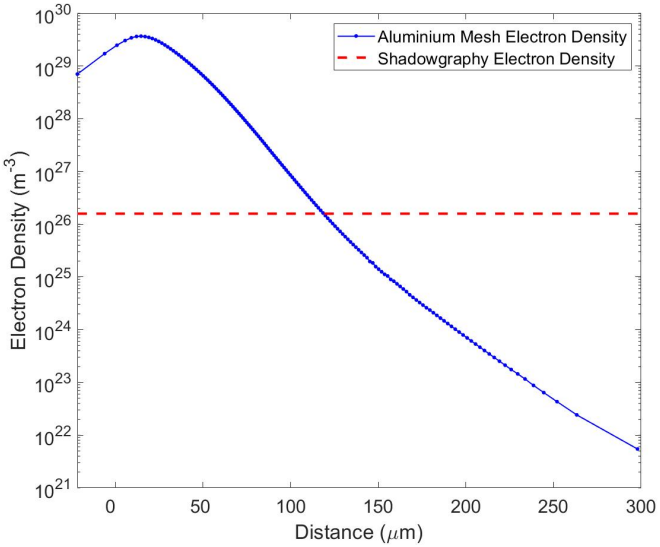

Figure 4.9: Electron density at each mesh wall after 200 ps. Blue dots represent each mesh wall. Red dotted line is the cut-off density calculated in section 4.2.4.2 for the specific shot under analysis.

The cut-off density is represented by the horizontal, dotted red line in Figure 4.9. This is unique for each shot and is the minimum density being imaged as dark regions by the probe. By locating the nearest mesh wall to the cut-off value, one can find the mesh number in the simulation which most accurately represents this density. The velocity of this mesh point is then located in the output data file and directly compared to the expansion velocity calculated from the probe images. Naturally, these velocities did not initially match, therefore the iterative method was implemented to generate a final simulation that best matched the expansion recorded by the shadowgraphy.

The initial simulations were carried out for each unique shot, with target temperatures ranging between $10 - 250$ eV in 10 eV increments. Figure 4.10 shows the velocity of each of these simulations as a function of their initial temperature. These have been spline interpolated so that the rear surface expansion velocity calculated from the shadowgraphy can be located on this curve. The corresponding temperature of this location is then recorded and the next simulations are based around this value.

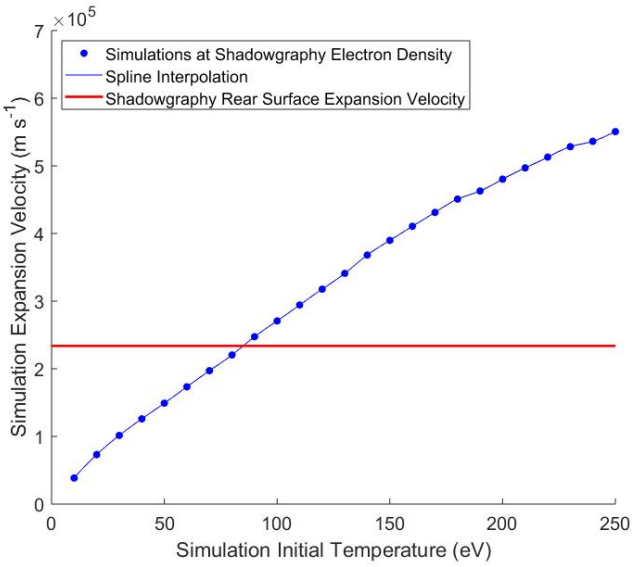

Figure 4.10: Expansion velocity of the mesh number associated with the shadowgraphy cut-off density. Results taken after 200 ps and represented by the blue dots. These are spline interpolated. The red horizontal line is the expansion velocity unique to the shot and determined using shadowgraphy.

It must be noted that the curve and associated data points presented in Figure 4.10 are unique to the shot they are simulating. This is because the velocities have been extracted for the mesh point that corresponds to the specific cut-off density that was calculated using shadowgraphy for that shot. Therefore a similar figure is produced for each shot that corresponds to the unique density that is required.

The temperature is recorded at which the cut-off density and spline interpolation curve intersect. The next round of simulations are then based around this temperature and separated by smaller increments. For example, in Figure 4.10, the rear surface expansion velocity determined using shadowgraphy was 233807 ms^{-1}. This intersects the spline interpolation curve at a temperature of 85.005 eV. Therefore a second round of simulations were undertaken with initial target temperatures of 81, 83, 85, 87 and 89 eV.

The process was then repeated for these simulations and the velocity of the cut-off density calculated and compared to the probe. A final simulation was then run at the corresponding temperature. In all instances, the velocity of this final simulation closely matched that of the probe. For the example under discussion in this section, the final temperature was found to be 85.58 eV and produced an expansion velocity of 233704 ms^{-1} in the simulations. This is only a 100 ms^{-1} discrepancy with the experimental measurements and is negligible when taking into consideration the 1D nature of the simulations. The aim of these simulations is to infer the approximate temperature of the rear surface of the target, not to calculate the temperature to a high degree of precision using expensive computational techniques.

The method detailed above was undertaken for every shot from the campaign. A MATLAB code was generated to quickly extract the data, locate the mesh point of the required cut-off density and the corresponding velocity. This then plotted the results for all of the simulations

for the shot and interpolated the data to produce similar figures to Figure 4.10. The code then generated the input decks with the appropriate temperatures in preparation for the next set of simulations.

Due to the high number of shots and relatively small temperature range across which they are spread, it became clear that the temperatures of the second round of simulations overlapped for multiple shots. This meant that the simulations didn't need to be run multiple times. Instead, the output data files could be used multiple times by extracting the unique cut-off density for the specific shot. This improved the efficiency of the iterative method.

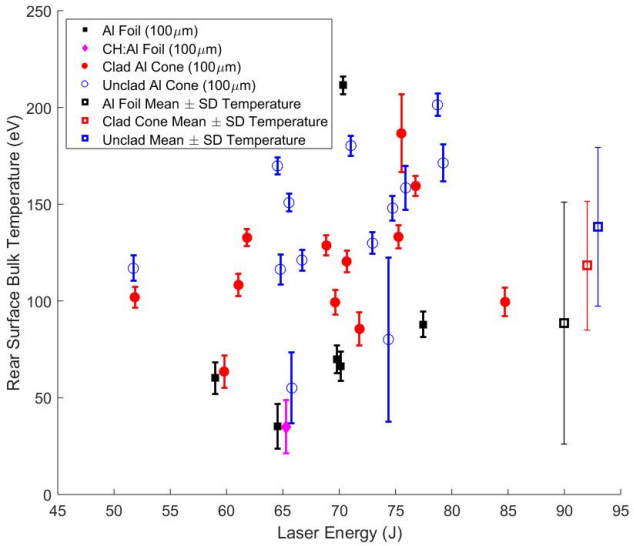

Figure 4.11: Inferred rear surface temperature as a function of laser energy for the 2015 campaign. Results obtained using a combination of shadowgraphy and HYADES simulations. For clarity, temperature mean ± standard deviation (SD) data points are located towards the right of the figure at arbitrary laser energies.

The rear surface temperature has been inferred in Figure 4.11 using a combination of shadowgraphy and hydrodynamic simulations in HYADES. R. G. Evans *et al* [14] shows how the rear surface temperature is highly dependant upon the target thickness, therefore to minimise the effect of this, all of the targets shown in Figure 4.11 are based on 100 μm aluminium.

Qualitatively, one can initially see a degree of variability across all of the targets. This was also recorded for the rear surface velocity measurements in Figure 4.11, however this is to be expected as the velocity roughly scales linearly with the temperature. This dependency is shown in Figure 4.10.

The aluminium foil targets reach a bulk temperature of 88 ± 63 eV (mean ± standard deviation), while the single CH:Al structured foil is recorded at 35 eV. Generally, the clad and unclad cone targets improve on these temperatures; reaching 118 ± 33 eV and 138 ± 41 eV respectively.

M. Nakatsutsumi *et al* [16] reports a reduction in rear surface temperature with increasing areal electron density of the target. For the 100 μm aluminium targets implemented on the 2015 campaign, the areal density is calculated as 7.8×10^{25} m^{-2}, using a mass density of $2.7 \times$

10^3 kgm^{-3} [99] and considering a fully ionised plasma due to the high recorded temperatures. Locating this areal density in the work of M. Nakatsutsumi *et al* corresponds to a temperature of approximately < 50 eV. This is achieved using laser energies exceeding 214 J. Comparing this to Figure 4.11, the temperature of < 50 eV reported in the literature is exceeded even when using the significantly lower laser energies in the 2015 campaign. Comparing this to Figure 4.11, the aluminium foils and cones generally improve on the 50 eV temperature reported in the literature, even when using the significantly lower laser energies in the 2015 campaign.

In the case of the clad cones, the literature reports that the resistively generated magnetic fields aid in confining electrons and improve the heating of the target [11, 12]. The aluminium clad cones provide a resistivity gradient to generate a similar magnetic field geometry, therefore the improvement in rear surface temperature may be due to the resistive guiding mechanism taking place.

The unclad cones do not exhibit the cone:cladding interface, instead a cone:vacuum boundary is found. Electrostatic sheath confinement between a material and vacuum interface has been shown to generate sheath electric fields sufficient to aid the confinement of electrons within the target [103,104]. The improvement in rear surface temperature in the unclad cones compared to the control foils suggests that electrostatic sheath confinement may be occurring. The similar performance of the clad and unclad cones suggests that if these confinement mechanisms do occur, the extent to which the electrons are confined and the subsequent target heating is similar in both cases.

Across each target category, variability in the inferred temperatures is apparent. There is not a clear dependency on the laser energy in Figure 4.11 suggesting that the variation is not accounted for by this parameter. Further investigations were undertaken comparing the temperature to the laser intensity and various target geometry conditions; such as the cone angle. However, these did not successfully provide a justification for the variability. Therefore, this leads one to consider other factors in the experiment.

First, lets examine the targets implemented on the campaign. Figure 4.2b shows the front surface of an unclad aluminium cone, upon which a significant number of spherical indentations are visible. These are created during the manufacturing process of the targets by mechanically machining the cone structures from a 100 μm thick aluminium foil. Not only did these features scatter the CW alignment laser and inhibit the alignment process, but will generally improve the laser absorption into the target [106, 107].

The spatial jitter of the main Vulcan PW beam is also significant when investigating micro-structured targets such as the clad and unclad aluminium cones. Table 4.2 shows that the tip widths of both cone categories were as small as 20 μm in some cases. The spatial jitter of the Vulcan PW beam was later measured as 17 ± 14 μm [77] during a subsequent campaign. This means that even if the CW alignment beam was positioned perfectly central on these narrower tips, the jitter would have inevitably moved the main beam off the structure. This would not have been within the experimental team's control.

A spatial defocus in the laser was discovered after the 2015 campaign. It was determined that this offset would have been present in the earlier 2015 experiment. In section 4.3.4.1, we assess how the energy contained within the FWHM of the laser in a later campaign changes

with defocus. The presence of the offset was not known at the time of the 2015 campaign, so could not be monitored or quantified. Therefore, it is likely that the specific laser energy at which each shot is located in Figure 4.11 will likely change. The extent of this change - caused by the unknown defocus - cannot be quantified and is a possible contributor to the variability of the temperature results.

Finally, the contrast of the laser system is of importance. The inevitable pedestal of the beam that proceeds the main interaction pulse will generate some low density coronal plasma at the front surface [58]. Either a method of diagnosing, or mitigating this effect would be required in order to remove this possible contribution to the variability of results.

From these possible sources of variation, a subsequent campaign was undertaken in 2017 which implemented a variety of control mechanisms to act as mitigation. The 13° angle of laser incidence was also removed to better match the experimental set-up to that of the literature; allowing for improved comparison. This experiment shall now be discussed in detail.

4.3 Vulcan Petawatt Campaign 2017

The sources of variability in the previous campaign established the need for a further experiment using conical structures but with these complications being minimised. This was achieved through a different target manufacturing process, the implementation of a front surface imaging diagnostic, mitigation of the pre-pulse using a plasma mirror, and quantifying the defocus of the beam. In the following section, we present each of these developments along with results from shadowgraphy in a similar arrangement to the 2015 campaign.

4.3.1 Targetry

Four main types of targets were implemented in 2017. These were similar to those used in the first campaign and consisted of homogeneous control foils, a structured control foil, unclad and clad cones. The structured control foil was used to replicate if the laser pulse missed the clad cone structure and interacted with the CH plastic.

Target	**Thickness (μm)**	**Purpose**
Control Foils	50, 100	Homogeneous Controls
Structured Control Foil	92.7	Missed Shot Control
Unclad Cones	100	Electrostatic Confinement
Clad Cones	100	Magnetic Confinement

Table 4.3: Targets used on 2017 Vulcan PW Campaign.

Mechanically machining the cone targets in the 2015 campaign resulted in rough surfaces and varying cone geometries (tip width, opening angle etc). This signified the need for a more controlled method of engineering the targets for the following experiment; this was achieved through a collaboration between Scitech Precision Ltd [108], STFC [109] and The University of York [105] to fabricate novel etched targets using MEMS (Micro-ElectroMechanical Systems)

technology. The technique inherently required the targets to be based on silicon, however this still had a larger Z number compared to the surrounding CH cladding, so the resistivity gradient between the two materials was still present. The MEMS process allowed for a high number of more reproducible targets to be produced for the 2017 campaign.

The cone targets were etched from 100 μm silicon foils to a depth of 50 μm, with a further 50 μm of foil being left behind. For the clad targets, the cones were then surrounded by CH glue to provide the resistivity gradient. The glue had the same chemical structure as that used for the 2015 campaign. A structured control foil was created by applying a layer of CH to the front of a 50 μm silicon foil. The resultant front layer was 42.7 μm thick, meaning a total thickness of 92.7 μm. This target was used to replicate the situation where the laser pulse missed the cone tip and hit the CH cladding to the side, similar to the CH:Al structured foil used in the earlier campaign.

Through using the MEMS technology, highly characterised and reproducible targets could be manufactured, with a large number on each wafer for future experiments. Each cone target was characterised using an electron microscope to determine the width of the cone tips and bases. The targets were tracked throughout the experiment so that the detailed target conditions were known for each shot.

Figure 4.12 presents the general design of the targets used on the 2017 Vulcan PW campaign.

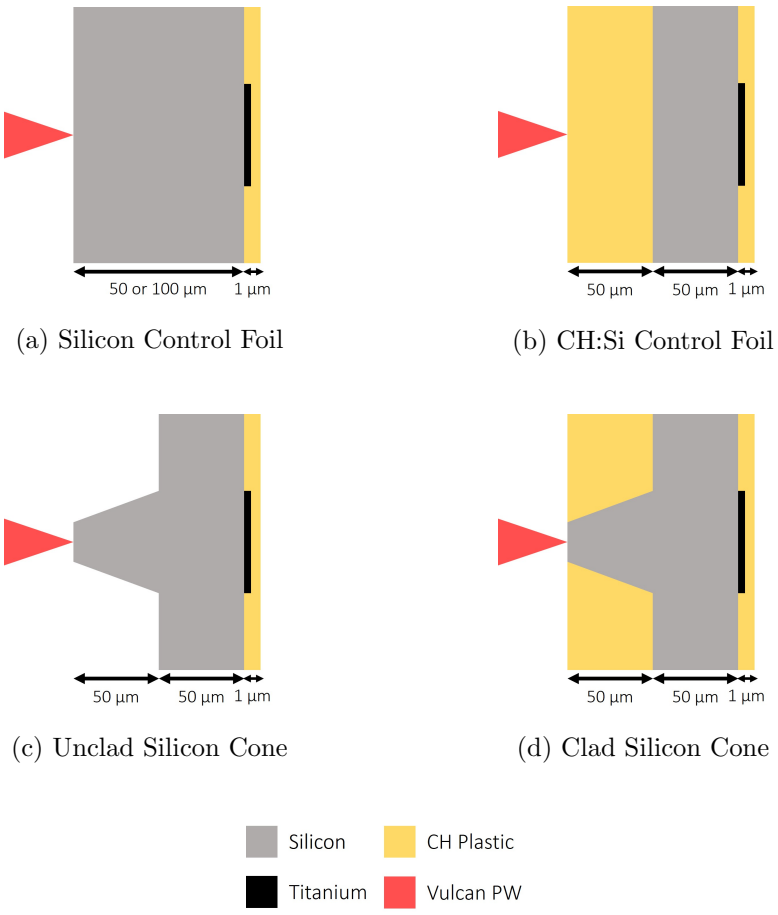

(a) Silicon Control Foil

(b) CH:Si Control Foil

(c) Unclad Silicon Cone

(d) Clad Silicon Cone

Figure 4.12: Targets used on the 2017 Vulcan petawatt campaign. Cones etched using MEMS technology.

At the rear surface of the silicon was a 150 nm thick titanium dot to act as a tracer for x-ray He-α spectroscopy. This was then tamped by a further 1 μm of CH. The titanium dot was applied to the back of the silicon wafer using lithography. A layer of resist was spun on the back of the silicon and exposed to create an area where the titanium dot was to be positioned. This was removed, along with the masking resist, to allow the titanium dot to be applied. The final CH tamping layer was then applied using vacuum deposition [110]. This process, along with the complete engineering of the targets, was undertaken by the target fabrication team [108, 109]. The rear surface configuration was applied to both the foils and cones in order to reduce any form of variation due to rear surface structure. Therefore the rear 51 μm (50 μm Si + 150 nm Ti + 1 μm CH tamping) was identical for all of the targets, regardless of whether foils or cones.

Planar silicon foils (Figure 4.12a) of 50 μm and 100 μm thickness were used as material control targets, with the latter being the same thickness as the cone targets. The unclad cones (Figure 4.12c) were left without CH cladding to investigate the possible confining effect of electrostatic sheath formation on the cone wall:vacuum interface. The clad targets (Figure 4.12d) had CH glue applied around the conical features to provide the resistivity gradient for investigating magnetic confinement. Effectively, this was the same method of applying the CH cladding using small glue applicators as was carried out for the 2015 campaign. Whilst manufacturing the targets, the fabrication team avoided getting CH glue on top of the cones by meticulously using the small glue applicators. Solvent was also used to remove any stray CH that did manage to reach the surface of the silicon cones [110]. The same technique of avoiding CH glue on undesired areas of the targets was also used when applying the CH tamping layer on the rear surface of the silicon wafers. The final target under consideration is the CH:Si foil (Figure 4.12b) used to replicate the target that the laser pulse would see if it missed the cone tip and interacted with the surrounding cladding. For this reason, the front of the target consisted of 42.7 μm of CH glue followed by the 50 μm thick silicon foil behind. The same titanium dot and 1 μm CH tamping was also applied to this target.

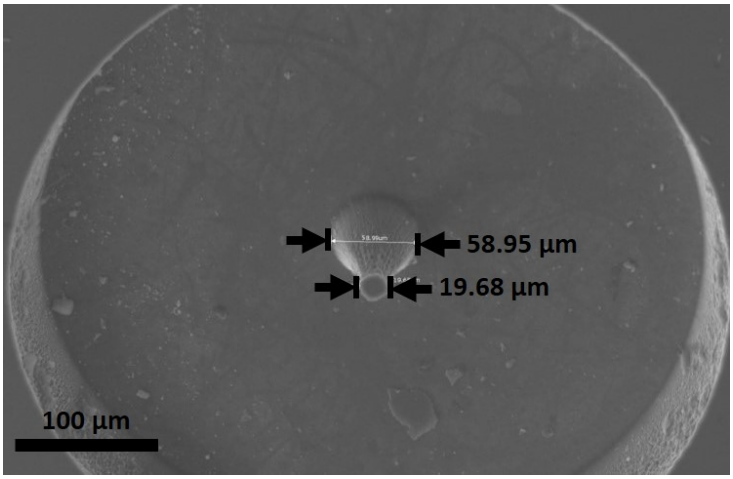

Figure 4.13: Electron microscope image of the front surface of an unclad silicon cone. Tip width = 19.68 μm and Base width = 58.95 μm. Large indented area surrounding the cone is 50 μm deep and filled with CH glue for clad targets. Diameter of this area is approximately 460 μm.

Figure 4.13 presents an electron microscope image of the front surface of an unclad silicon cone. The 19.68 μm wide cone tip is significantly smoother than that seen in Figure 4.2b for the 2015 campaign. This improvement in the surface profile of the cone tip aids to mitigate against the issue of groves being generated by mechanical machining the target surface. This was determined in the 2015 campaign and scattered light during the alignment process. The cone is surrounded by a 50 μm deep *bowl* area which is filled with CH glue for the clad cone targets. This then provides the resistivity boundary between the silicon cone walls and CH cladding to aid the generation of the confining magnetic fields shown in Equation 2.26.

Target	**<Tip Width> $\pm$ σ (μm)**	**< Base Width> $\pm$ σ (μm)**	**$< \alpha_{\frac{1}{2}} > \pm \sigma$ (°)**
Unclad Cone	40.45 $\pm$ 4.78	57.57 $\pm$ 3.41	9.70 $\pm$ 2.14
Clad Cone	29.53 $\pm$ 9.58	56.45 $\pm$ 4.85	14.89 $\pm$ 5.96

Table 4.4: Mean tip width, base width and opening half-angle ($\alpha_{\frac{1}{2}}$) of unclad and clad cone targets used on the 2017 Vulcan PW campaign. Symbols < > and σ denote the mean and standard deviation of values respectively. For each separate cone type (clad or unclad), the mean and standard deviation of each width parameter and angle are calculated separately.

The cone angles are similar to those tested in the simulation literature, allowing for close comparison [12,13]. The reduction in standard deviation for the unclad cones is due to less being implemented on the experiment - these were mainly used for electrostatic confinement control purposes, not to directly implement the resistive guiding mechanism. A crucial aspect to note is the tip widths of the clad cones. A significant proportion of the targets that were implemented during the late stages of the campaign had tips that were much smaller than those used earlier in the experiment. For example, one clad cone tip was only 12.77 μm across. This becomes an important parameter as the tips tend towards this narrow size. Again, this relates to the jitter of the main interaction beam.

The Vulcan PW spatial jitter has been measured in previous work as 17 ± 14 μm [77], which suggests that even if the CW alignment laser was aimed perfectly central to the smallest of cone tips, the jitter would inevitably cause the beam to move off the feature and hit the surrounding area. This signified the need for a method of determining the laser interaction location on the targets. To do this, a novel front surface imaging system was developed and deployed on the 2017 campaign. Details of this are presented in section 3.3 and results will be discussed in section 4.3.5.

4.3.2 Experimental Setup

The Vulcan PW laser pulse was focussed using the 620 mm diameter, F/3 off-axis parabola (OAP) housed in the target chamber. However, unlike the 2015 campaign, a plasma mirror was used to improve the laser contrast. The operation mechanism of a plasma mirror is presented in section 3.1.2, however the main points to take from this are that it reduced the corona

generated on the front surface of the target due to the low intensity pedestal being removed. The device also allowed the laser beam to be directed onto the target at normal incidence. This 0° configuration matches well to the simulation work in the literature [8, 11–13].

Previous experimental work by S. Kar *et al* [9] and B. Ramakrishna *et al* [10] used a laser incidence angle of 10° and 5° respectively. To the knowledge of the author, this is the first time an incidence angle of 0° has been used to experimentally investigate resistive guiding.

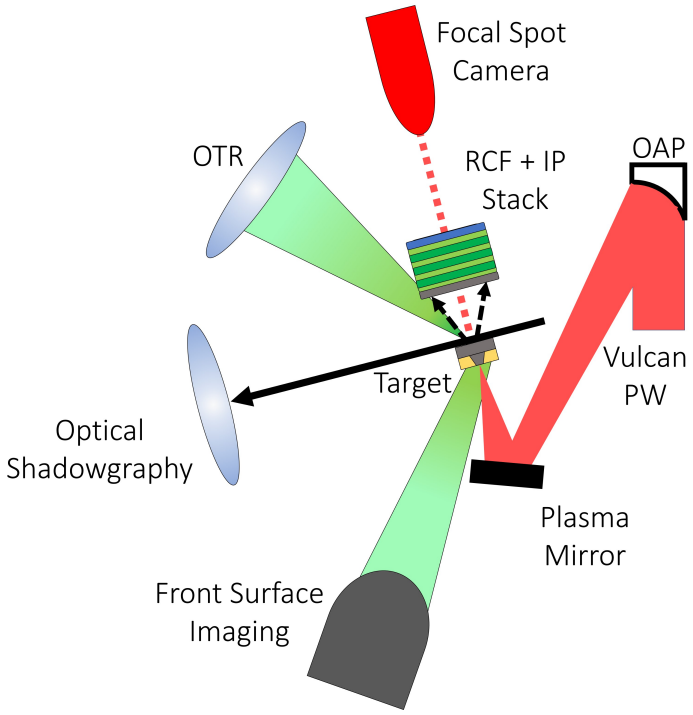

Figure 4.14: Main diagnostics used in the 2017 Vulcan PW campaign. Vulcan PW beam (red) focussed using an off-axis parabola (OAP). Plasma Mirror in-between the OAP and target to reduce the pre-pulse and enable normal incidence configuration. Front Surface Imaging system monitored laser incidence location. Radiochromic film (RCF) and image plate (IP) stack located 5 cm normal to the target rear surface. Optical shadowgraphy imaged parallel to the target plane (solid black arrow) to extract information on plasma expansion. Optical Transition Radiation (OTR) collected out of plane (above the RCF), location is displaced on the image for clarity. Schematic not to scale.

An optical probing (shadowgraphy) system was also deployed to image the front and rear surface expansion from the target. This system was designed with the 2015 configuration in mind, keeping many similar components for comparative purposes. The system between the main beam pick-off and the periscope was identical to that displayed in section 3.4.

The probing beam was picked-off from the main beam and delayed using timing slides. The beam passed parallel to the target plane and then through a 3 inch diameter, 50 cm focal length lens using a glass wedge. A further configuration of mirrors directed the beam to a camera outside of the chamber. For the vast majority of shots, KG5 and ND3 filtering was placed directly in front of the camera to filter background noise and reduce the signal below image saturation. The timing slides were set so that the probe beam was delayed by either 150 ps or

200 ps behind the main interaction beam and the camera was set to an acquisition time of 100 ms. Images were recorded before the shot and then after the delay time to compare the locations of the target surfaces. From this, the size of rear surface expansion was calculated. The probe was spatially calibrated using the same method as in 2015 where a target was moved by known distances across the CCD. This calibration was determined as 0.817 μm/pixel. Section 4.3.6 presents details on the analysis method and results using the system.

A radiochromic film (RCF) and image plate (IP) stack was deployed to investigate the proton and electron beams respectively. Located 5 cm behind the target normal (and therefore laser axis), the stack was designed using filtering materials to grade the energy of the spectrum that each layer responded to the most. A detailed review of RCF and IP is presented in sections 3.5 and 3.6, while the specific stack design implemented on the 2017 campaign and corresponding results shall be presented in Chapter 5.

Optical Transition Radiation (OTR) was investigated and results will form part of this thesis in Chapter 6. The theory underpinning this diagnostic and the specific design that was deployed on the 2017 campaign is presented in Section 3.7. The 2ω frequency of radiation was investigated which is emitted as electrons reflux at the second harmonic laser frequency and cross the rear surface of the target into vacuum. This causes atomic oscillations at the surface boundary and the emittance of radiation.

4.3.3 Laser Alignment Technique

A rigorous alignment procedure was developed to ensure that the Vulcan PW beam was centred on the cone tip features as accurately as possible. This requirement was identified from the 2015 campaign where laser positioning was a likely contributor to the variability of results.

The transparent nature of silicon meant that the targets used on the 2017 campaign couldn't be aligned using the retro-focus camera that is normally used at the CLF. The lack of reflected laser light from the front surface of the silicon meant that a novel technique was required. This combined the use of a focal spot camera, the optical probe, front surfacing imaging diagnostic and the opaque nature of the embedded titanium dot at the rear of the targets.

Alignment wires (7 μm thick carbon fibre) were attached to the top of the front surface of the targets to aid the alignment procedure before each shot. Once the ideal position of the target was determined, the location was marked on the optical probe and FSI (2ω) camera PCs as reference guides for all three dimensions.

To begin aligning the target, the CLF target alignment jig was used to ensure that the target was positioned without rotation about the target stalk. This was then inserted into the target mount inside the chamber. The target holder magnescales were then moved so that the target lined up with the reference marks on the probe and FSI camera PCs. The probe was used to determine the longitudinal position of the target, whilst the FSI looked at the front of the target and could be used to confirm the correct transverse position.

The focal spot camera was moved so that the tip of the 7 μm alignment wire was in focus. At which point, the target was reduced in height and the CW alignment laser was turned on. The off-axis focussing parabola was then adjusted so that the CW beam was in focus on the focal spot camera. This then meant that the focal spot camera, alignment laser and target were

all focussed on the same plane. A reference mark was applied to the focal spot camera PC to indicate the location of the focussed CW beam.

The target was then moved up in height so that the bottom of the alignment wire was in view, any focussing issues due to the target being vertically tilted were corrected by moving the target in the longitudinal direction.

The target was then moved in the transverse direction so that both top corners were found, allowing the central position of the target to be calculated. The target was then displaced so that this top central position was visible on the focal spot camera. This was a contingency as the positioning of the alignment wires was not always central at the top of the target, so could not be used as a central marker.

With back-lighting provided by the CW alignment laser, the target was moved up in height until the embedded titanium dot was found on the focal spot camera. This was relatively simple to decipher due to the opaque nature of titanium, so a clear reduction in CW back lighting was seen in addition to the rounded edges of the dot.

The infra-red (IR) channel of the front surface imaging system was also used to aid the alignment procedure. This used filtering so that the CW alignment laser was visible on the IR camera. The target was also illuminated using an IR diode so that the front surface and conical features were visible. The channel was then used to corroborate the above alignment technique by ensuring that the CW alignment laser was positioned over the tip of the conical feature.

Once the alignment position was determined, the focal spot camera was retracted in the horizontal direction and reduced in height to protect against any stray laser light or debris damage. The electronic RCF mount was driven up in height into position. This was confirmed using an external camera that imaged the top of the RCF stack until it reached the reference position which was earlier determined as the same height as the target. The process of arming diagnostics and requesting the main Vulcan PW beam then commenced.

4.3.4 Laser Beam Characterisation

Characterisation of the main PW beam is vital to understand the environment in which the laser-target interaction took place. This was undertaken for the 2015 campaign however notably, it was not possible to characterise the location of the beam upon the target and the effect of defocus. This section shall detail the methods used to determine the intensity upon the target, including methods of resolving the unknown quantities discovered in the earlier campaign.

4.3.4.1 Defocus and Spatial FWHM Considerations

Once the CW beam was determined to be at optimal focus, an image was recorded using the focal spot camera. This is presented in Figure 4.15. The focal spot was slightly astigmatic due to the use of an OAP (this is inherent to the Vulcan system), so a line-out was taken across the longest side of the beam.

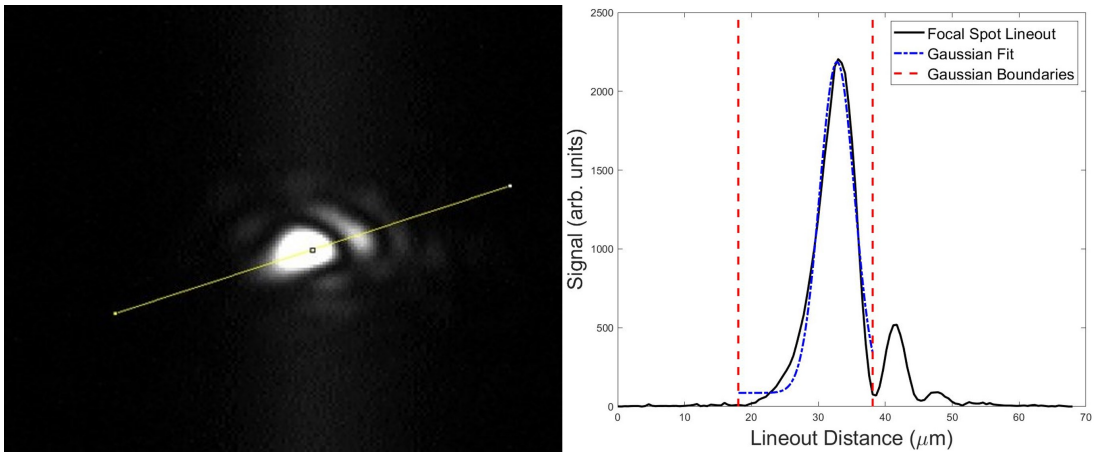

Figure 4.15: Photograph of the CW focal spot from the 2017 Vulcan PW campaign and corresponding line-out. Gaussian fit applied to the main peak in the line-out with FWHM = 6.1 μm. Fit boundaries between 18.03 μm and 38.11 μm.

A Gaussian fit was applied to the line-out and the FWHM calculated as 6.1 μm. However, the existence of a known defocus in the beam modifies the size of the spot depending on it's position from focus. This was characterised for each shot. The calibration of the focal spot camera was calculated as 0.515 μm/pixel.

The characterisation of the defocus in the 2017 campaign was carried out for all shots and related to how this affects the size of the laser FWHM and the energy contained within this area. This work is based upon that by A. Higginson *et al* [29] where defocus scans of the Vulcan beam have been provided. These scans were conducted during a Vulcan PW campaign beginning in February 2016; the major optics were the same and focussing conditions checked between these periods so that the scans were applicable to the 2017 campaign [76].

The Zernike polynomial values from the HASO wave front detector were obtained from the Vulcan PW laser team and converted to a spatial defocus using Equation 4.2 [111].

$$\Delta\delta = \frac{4\lambda_0}{NA^2} Z_3 \tag{4.2}$$

where $\Delta\delta$ is the spatial defocus for a HASO Zernike polynomial Z_3. λ_0 is the laser wavelength of 1.053 μm and NA is the numerical aperture of the beam equivalent to 0.16 for the Vulcan PW beam.

This conversion was possible for the majority of shots throughout the experiment, however the HASO diagnostic did not trigger for approximately 30% of the shots. The relationship between the defocus and a variety of parameters was investigated to attempt to find a clear trend between the two, allowing for the missing defocus values to be approximated from the relationship. This was carried out for the defocus as a function of time of day, day of the experiment and time since the previous shot, however a trend was not found. The shot number of the experiment was then investigated. Again, a relationship was not clear, but the variability in the defocus appeared to be minimised against this parameter, so the analysis progressed using the shot number of the experiment.

The defocus was calculated for each shot using Equation 4.2 and then plotted against the shot number of the experiment. The shots where the HASO diagnostic failed to trigger were then interpolated using the defocus value for the shot either side of the missing value. This can be seen in Figure 4.16.

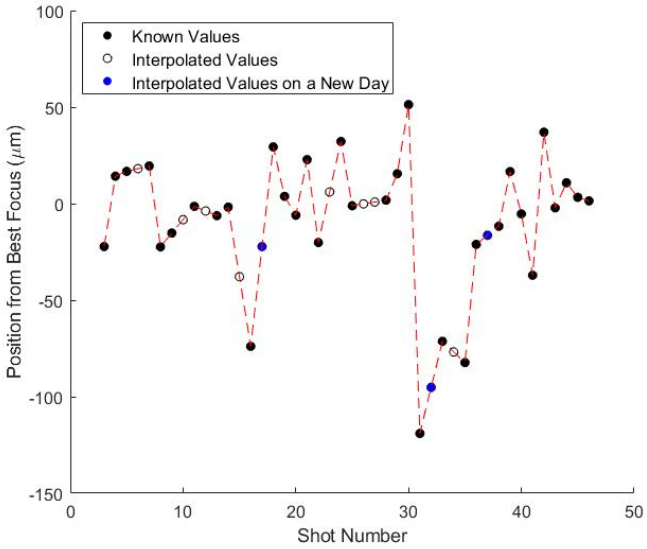

Figure 4.16: Position from focus for each shot calculated using Equation 4.2. Known values correspond to when the HASO successfully triggered. Interpolated values are for when the HASO failed and are calculated by interpolating between the two nearest known values. Solid blue points are interpolated values that have used the two nearest known values, but which are on different days of the experiment

.

As can be seen in Figure 4.16, the position from best focus varies by approximately 170 μm across the whole experimental campaign, significantly more than the Rayleigh range of the Vulcan beam. This demonstrates the importance of fully characterising the defocus of the laser and how this can affect the environment in which the shots take place. Specifically, the defocus has two effects, it changes the size of the beam at the target plane, and with that, the energy contained within this area. These have both been investigated and characterised for the 2017 experiment.

A spatial FWHM defocus scan provided by A. Higginson *et al* was digitised and then interpolated across the 170 μm defocus range for the 2017 experiment. The provided scan ranged between -83.4 μm to 60.3 μm in defocus, whilst the defocus values for the 2017 experiment ranged between -119 μm to 51.3 μm. Therefore, extrapolation outside of the provided defocus range was required so that all of the shots during the 2017 campaign could be characterised. To do this, the MATLAB *interp1* function was employed using the *cubic extrapolation* method. This used a shape-preserving, piecewise cubic interpolation and extrapolation procedure across the desired defocus range. *Linear* and *nearest* techniques were investigated but presented a clear deviation from the provided scan between the known data points. Using the cubic method, interpolated and extrapolated values for the 2-minute shot beam were calculated for the position

from focus for each shot.

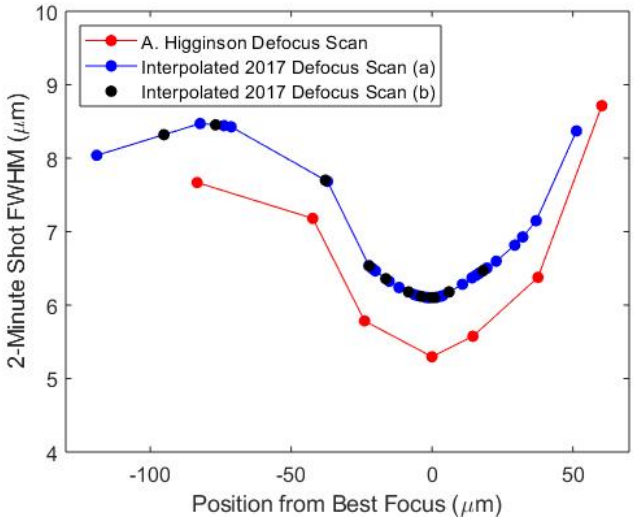

Figure 4.17: 2-Minute shot spatial FWHM across the defocus range calculated for the 2017 campaign (using Figure 4.16). The A. Higginson curve is provided by [111] and the interpolated values are calculated from this curve using the MATLAB inbuilt shape-preserving, piecewise cubic interpolation function. (a) values for the known defocus positions when the HASO triggered (b) values for the interpolated defocus positions when the HASO failed to trigger (calculated from Figure 4.16). Curves (a) and (b) shifted up in FWHM so that the zero defocus position has the best focus FWHM measured on the experiment (6.1 μm).

For the defocus scan provided by A. Higginson *et al*, the FWHM of the 2-minute shot beam at the best focal position was 5.3 μm. However, an image of the optimised focal spot was recorded on the 2017 campaign and suggested a FWHM of 6.1 μm. This meant that there was a discrepancy of 0.8 μm between the two experiments which needed to be corrected for. To resolve this, the scan provided by A. Higginson *et al* was extrapolated across the defocus range from the 2017 campaign. This was then shifted up by 0.8 μm so that the FWHM was 6.1 μm at 0 μm from best focus. This provided predictions for the FWHM of the beam for the shots where the HASO wave-front diagnostic failed to trigger. These are represented by the black data points in Figure 4.17.

4.3.4.2 Energy Considerations

The proportion of energy contained within the FWHM of the beam also varies with the position from focus. To investigate this, a further defocus scan provided by A. Higginson *et al* was used in a similar interpolation method as above. The scan provided the proportion of energy contained within the FWHM of the beam at each defocus position. This was interpolated using the inbuilt Akima Spline technique in *Origin* software using an interpolation defocus range of -119 to 51.3 μm (calculated from Figure 4.16). On this curve, the position from focus was found for each shot during the 2017 campaign, and the corresponding proportion of energy within the FWHM at that position.

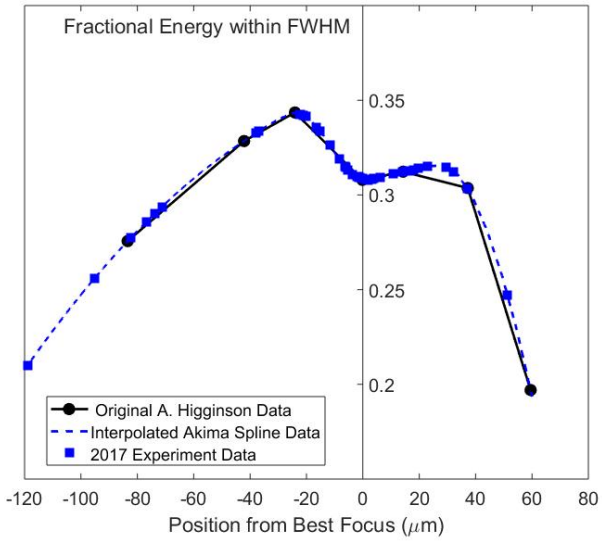

Figure 4.18: Fractional Energy as a function of position from best focus. Original scan (black circles) provided by A. Higginson *et al.* This was then Akima spline interpolated (blue dashed line) and the experiment defocus values determined from Figure 4.16 were found on the spline curve (blue squares).

The Akima spline technique was implemented due to the clear non-linear profile of the A. Higginson curve in Figure 4.18. The same piece-wise, cubic interpolation technique used in the previous section was tested, however this diverged significantly from the original curve. For each shot during the experiment, the position from focus was located on the interpolated curve in Figure 4.18 and the corresponding value of the fractional energy within the FWHM. This was then combined with the energy recorded after the compressor and calorimetry calculations.

As with the 2015 campaign, calorimetry measurements were undertaken for the 2017 experiment. The calorimeter was placed after the plasma mirror and resulted in an average conversion of 34%. Therefore, this value includes the efficiency of the plasma mirror to reflect the beam.

In the 2015 campaign, the defocus issue was not known, therefore it was assumed that the FWHM contained 30% of the energy for each shot. However, this section has detailed the analysis method that determined how the defocus for each shot modifies the energy contained within the FWHM of the beam. This, combined with the calorimetry measurements, allowed a unique energy value to be determined for each shot during the 2017 campaign.

4.3.4.3 Pulse Length Considerations

Auto-correlator data was analysed by the laser team and provided during the experiment. However, the diagnostic did not trigger for a number of shots and could not be resolved during the campaign. Therefore, investigations took place after the campaign to attempt to find a relationship in the pulse length data and resolve the issue through interpolation - as was done for the missing HASO defocus data.

The pulse lengths were compared to the time of day, time after the previous shot, day of the week and shot number of the experiment. Across all of these parameters, the pulse lengths were

variable with no clear relationship being found.

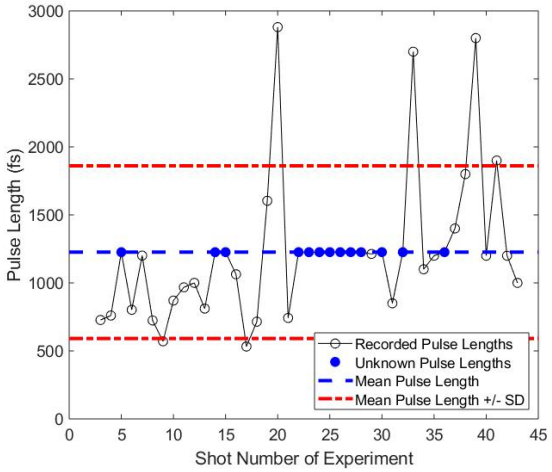

Figure 4.19: Pulse length as a function of shot number of the experiment. Mean ± Standard Deviation pulse length = 1226 ± 635 fs.

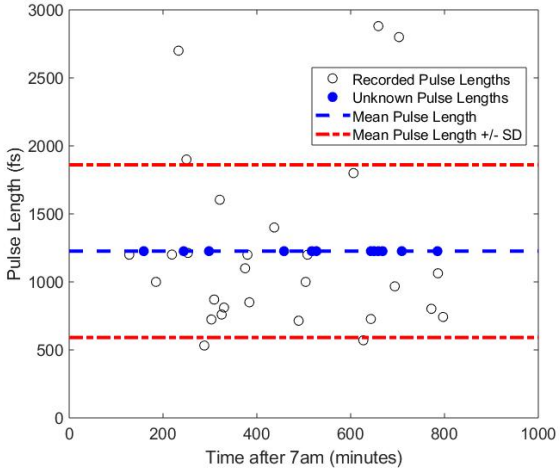

Figure 4.20: Pulse length as a function of time after 7am (approximate time of switch on of system). Mean ± Standard Deviation pulse length = 1226 ± 635 fs.

The mean and standard deviation of the pulse length across the entire campaign was 1226 ± 635 fs. Due to the high variation and lack of clear trend with the investigated parameters, it was decided that interpolation would be unfounded in this instance. Further investigations used the mean pulse length value for the missing shots to calculate an intensity value. However, the standard deviation error held a significant proportion of the value and meant that significant conclusions could not be drawn from the data. Therefore, the shots without the auto-correlator data had to be discarded for the remaining data analysis. This left 68% of the original number of shots undertaken across the campaign.

4.3.4.4 Calculating The Intensity On Target

The laser intensity for each shot is calculated using the size of the FWHM of the laser spot and the energy contained within this area, as well as the temporal length of the pulse. The former two parameters have been considered with the effect of beam defocus.

In the 2015 campaign, section 4.2.3 details how an image of the focal spot at best focus was used to determine the FWHM of the beam, which was then applied to all shots. This was also carried out for the more recent experiment in 2017, however the effect of defocus was also characterised meaning that the beam size was slightly different for each shot depending on how far the beam was from the optimal focal plane.

A further modification for the 2017 experiment was how the energy contained within the FWHM varied with the position from optimal focus. This allowed a specific proportion to be calculated for each shot, instead of the nominal 30% being used for the 2015 campaign.

These parameters have been extensively characterised while taking the effect of defocus into account. This has provided a more rigorous intensity calculation for each shot of the experiment. The average intensity upon the target surface across the whole campaign was determined as $(1.79 \pm 0.89) \times 10^{20}$ Wcm^{-2} (mean $\pm$ standard deviation).

4.3.5 Determining the Laser-Target Interaction Site

One of the requirements established from the 2015 campaign was a method of determining where on the target the laser interaction took place; whether this be on the cone tip structures or the surrounding CH cladding material. Without this knowledge, the environment within which the interaction took place could not be fully understood.

The silicon cones implemented in the latest campaign had tip widths of 40.45 ± 4.78 μm and 29.53 ± 9.58 μm (mean $\pm$ standard deviation) for unclad and clad cones respectively. Although, a number of clad cones implemented in the later stages of the campaign were significantly smaller (e.g. 12.77 μm). The spatial jitter of the Vulcan PW system has also been measured in previous work [77] related to this thesis as 17 ± 14 μm. This suggests that even if the CW alignment laser was positioned perfectly centred on the silicon cone tips, the spatial jitter of the main Vulcan PW laser pulse could drift the beam from the central position onto the CH cladding or side of the unclad cone tips. This would be inevitable for a number of shots, regardless of the precision of the CW alignment technique. Therefore, a method of determining the position of laser incidence upon the target was required on a post-shot basis.

For this purpose, a novel Front Surface Imaging (FSI) diagnostic was implemented. Detailed information on this device is presented in section 3.3 and reference [78], however the results from this diagnostic shall now be discussed and how these were used to determine the success of each shot.

The FSI diagnostic operated in two wavelength modes, the first was an infra-red channel used to aid alignment of the CW beam. The second was a second-harmonic (2ω) channel to infer the position of the main beam from self-emission at the front surface. The latter channel imaged emission predominantly generated via the Relativistic Oscillating Mirror mechanism (section 2.3) which is strongly dependant upon the maximum intensity component of the laser focal region [79].

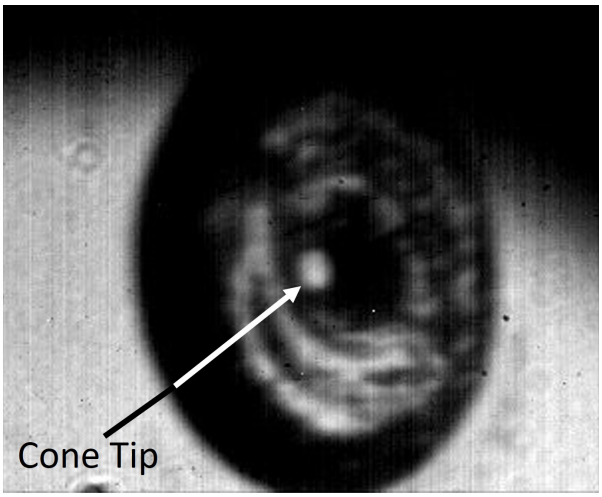

Figure 4.21: IR image of silicon cone front surface. Cone tip visible on image and Vulcan CW alignment laser is also visible during operation aiding in laser alignment.

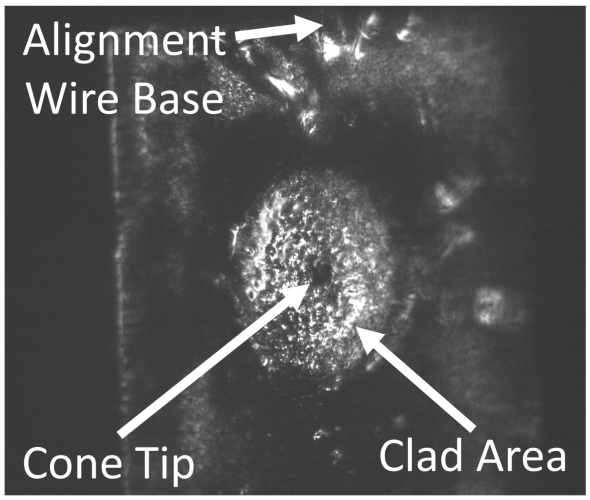

Figure 4.22: Second harmonic reference image of a clad silicon cone target before the shot.

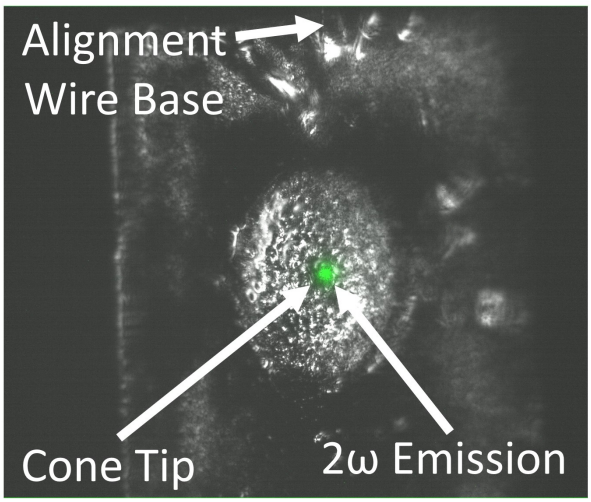

Figure 4.23: Time-integrated second harmonic emission captured during the shot, overlaid with the reference image.

Figure 4.21 shows a silicon cone target in the infra-red channel of the FSI system. This aided laser alignment by using a 1053 nm diode inside of the target chamber to illuminate the surface of the target and provide enough light to capture an image. Due to this arm of the diagnostic operating in the infra-red wavelength regime, the Vulcan CW alignment laser was also visible on the channel, allowing the position of the beam to be monitored during alignment. Whilst the target was positioned at laser focus, a clear change in CW signal was seen as the beam was moved between the cone tip and either the surrounding CH glue or sides of the cone wall. This allowed an estimate of the central position of the cone tip to be determined by finding the edges of where this signal change occurred. The system was extremely useful in aiding the alignment technique throughout the campaign. However, it must be noted that when operating in this mode, the intention was only to aid the procedure; it was clear that the accuracy of determining the exact position of the signal change was not sufficient to be the sole technique for aligning the laser.

Images from the 2ω reference channel are presented in Figures 4.22 and 4.23 where a clad cone target has been imaged before the shot and then the time-integrated self-emission has been overlaid with the reference image. The target is illuminated in the 2ω reference image with a white-light source directed into the target chamber using an optical fibre.

The cone tip is clearly visible in the reference image (Figure 4.22) with the surrounding circular area being the CH cladding. The electron microscope image in Figure 4.13 of an unclad cone target should aid in visualising this target structure. The remaining flat area of the target shown in Figure 4.22 is the foil component of the target, with the side edges clearly visible. The top edge of the target may also be visible to the reader. Connected to this was the 7 μm thick alignment wire which protruded up from the top of the foil. This structure is not visible on the image but it is worth noting the location.

Figure 4.23 shows the same reference image but with the time-integrated 2ω emission overlaid in green. The position of the emission was used to determine the location of the focal spot upon the target surface, taking into consideration the slight angular rotation of the target with

respect to the imaging plane. The shape of the emission is also considered, however this shall be discussed after the following figure. With regards to Figure 4.23, the self-emission is clearly centred upon the tip of the cone structure, therefore this shot would be characterised as being successfully hit.

The success of shots has been characterised into three separate groups so that the subsequent data analysis could be undertaken in the knowledge of how well one would expect any resistive guiding mechanism to perform. The following figures present images for each of these three categories.

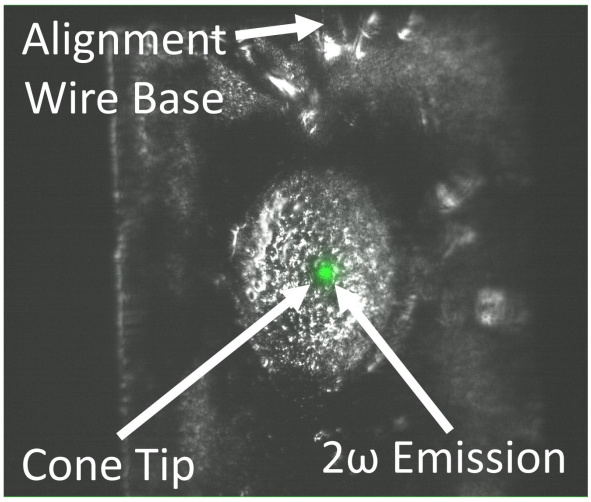

Figure 4.24: Time-integrated second harmonic emission captured during the shot, overlaid with the reference image. Position of emission corresponds to a *hit* on the cone tip.

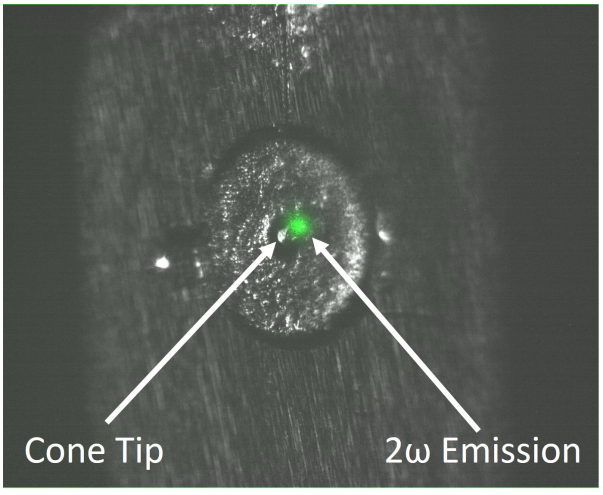

Figure 4.25: Time-integrated second harmonic emission captured during the shot, overlaid with the reference image. Position of emission corresponds to a *missed* shot.

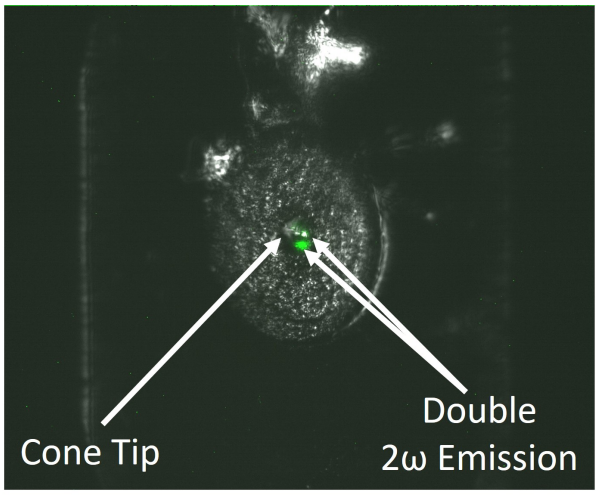

Figure 4.26: Time-integrated second harmonic emission captured during the shot, overlaid with the reference image. Position and double nature of emission corresponds to a *clip* on the cone tip. Emission is split between the cone tip and the wall of the cone/CH cladding.

A *hit* shot is specified as when the laser beam is incident upon the silicon cone tip. Figure 4.24 shows an overlaid image of this situation. It is clear that the emission originates from the same region as the tip of the cone, suggesting that this was the position of the laser interaction.

In direct contrast, Figure 4.25 displays a *missed* shot where the laser pulse completely misses the cone tip and interacts with the surrounding material, whether this be the CH glue for a clad target, or the sloping walls of an unclad cone. This category has been characterised by the emission being centred upon the region outside of the visible cone tip on the reference image.

Finally, a third and intermediate category was determined where the laser pulse *clipped* the cone tip and the surrounding material (CH glue or cone wall). This is visible in Figure 4.26 where the emission is spread across both the cone tip and the area outside of this. However, a notable difference in this example is that the emission is split into two distinct zones instead of being a single, large signal covering the two areas. We attribute this to the three-dimensional nature of the target as seen by the incident laser pulse. We can understand this by considering the following situations.

Consider an unclad cone target where the laser pulse clips the edge of the cone. Emission will originate from this area, but the remaining portion of the beam is incident slightly deeper into the target along the angled wall of the cone. Therefore, from the position of the diagnostic, these two regions are not on the same imaging plane and would therefore be observed as two distinct *spots* of emission.

Next consider a clad target where the laser pulse clips the edge of the cone but also covers the adjacent CH glue cladding. In this situation, the beam interacts with two materials of distinct optical properties. Hence the transmittance and reflectance of the beam across these two areas will differ and be exhibited as two *spots* of emission with contrasting intensities.

In short, not only has the position of the 2ω emission been used to characterise the location of the laser pulse upon the target, but also the shape of the signal has been considered. Smooth,

singular emission regions were attributed to hit and missed targets, while emission from two distinct regions was characterised as the beam clipping the cone tips.

The front surface imaging diagnostic was invaluable in not only aiding the laser alignment procedure, but more importantly allowing the position of the laser pulse upon the target to be found. This was used to determine the success of each shot for the subsequent analysis of the diagnostic data.

4.3.6 Shadowgraphy

A shadowgraphy system was also implemented in the 2017 campaign to image the rear surface plasma expansion from the target. This closely followed the same configuration as that in the earlier campaign (Section 4.2.4) with the optics before - and including - the periscope being specific to the Vulcan system so identical in both campaigns. These optics are collectively termed the *delay system* for ease of reference. The probe diagnostic provided a magnification of $\times 8.3$ and spatial resolution of approximately 4.3 μm. The limiting f/number of the system was approximately f/6.6.

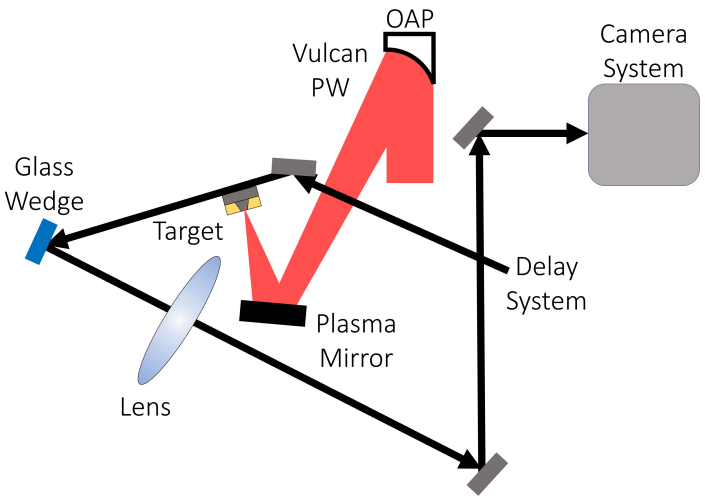

Figure 4.27: Configuration of the shadowgraphy system implemented on the 2017 campaign. Probe beam is picked-off from the main interaction beam and delayed by increasing the path length using timing slides. Beam is then directed across the target and focussed using 7.62 cm diameter lens onto a CCD camera located outside of the chamber. Distances of target→lens = 56 cm and lens→camera = 445 cm.

The probe beam is picked-off from the main interaction beam and then frequency doubled and linearly polarised using a KDP crystal and wave plate respectively [70]. This takes place just after the final turning mirror. Timing slides increased the path length and thus delayed the probe. This was calibrated using a Hamamatsu streak camera which dominated the error in the temporal delay (± 10 ps [70]). For the 2017 campaign, the probe was delayed for either 150 ps or 200 ps after the main beam to observe sufficient plasma expansion to enable analysis. Wavelength filtering to 532 nm, as well as KG5 and ND3 were placed before the camera which used an acquisition time of 100 ms, therefore the expansion observed on the image was time

integrated over this temporal window. The first optic after the target was a glass wedge which reflected approximately 5% of the light to the first lens [112]. This further mitigated against image saturation on the camera CCD.

The system was spatially calibrated by imaging the tip of the 7 μm thick alignment wire in real time. The target was displaced by known amounts and compared to the movement across the CCD. The calibration was calculated as 0.817 μm/pixel.

4.3.6.1 Calculating the Average Rear Surface Expansion Velocity

Figure 4.28 shows the pre-shot reference and post-shot images of a silicon cone target. The main Vulcan PW interaction beam is incident from the right. The location of this interaction can be seen from the self-emission in Figure 4.28b, the centre of which also corresponds to the position of the front surface in Figure 4.28a.

The same MATLAB software as that used in the 2015 campaign (section 4.2.4) has been implemented to unfold the average rear surface expansion velocity and the cut-off density which is imaged as dark regions using the probe.

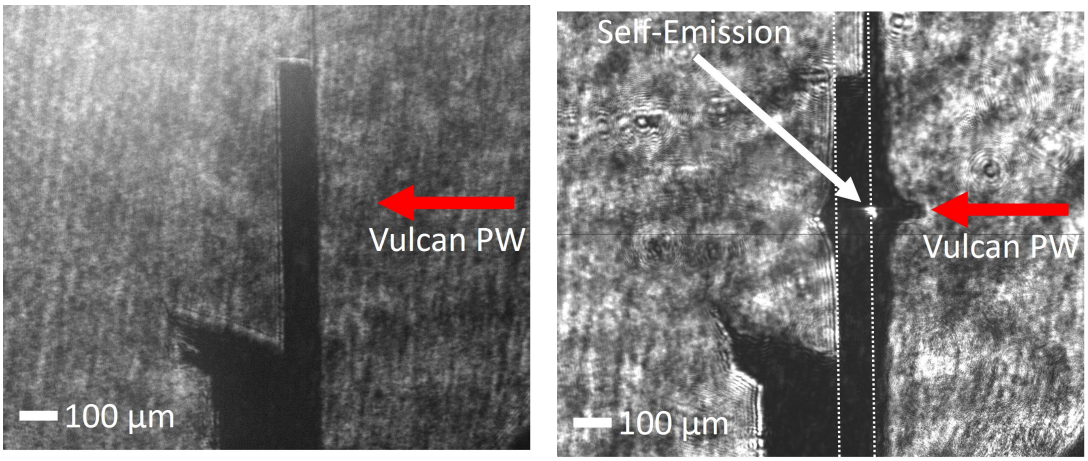

(a) Pre-shot reference image of cone target.

(b) Time-integrated image of cone target.

Figure 4.28: Images from 2017 optical probe diagnostic (a) pre-shot reference of cone target (b) time-integrated (100 ms) image of the same cone target during the shot. White-dashed lines reference unperturbed target surfaces. Probe delayed by 150 ps after main Vulcan beam and incident from the right. 7 μm thick alignment wire visible at the top of the front surface of the target in both images.

The method for calculating the average rear surface expansion velocity follows that detailed in the bulleted list in section 4.2.4.1. Essentially, this involves calculating the distance between the expanded and unperturbed rear surface locations and dividing this by the probe delay. This was undertaken three times so that a mean value and standard deviation could be calculated for each shot.

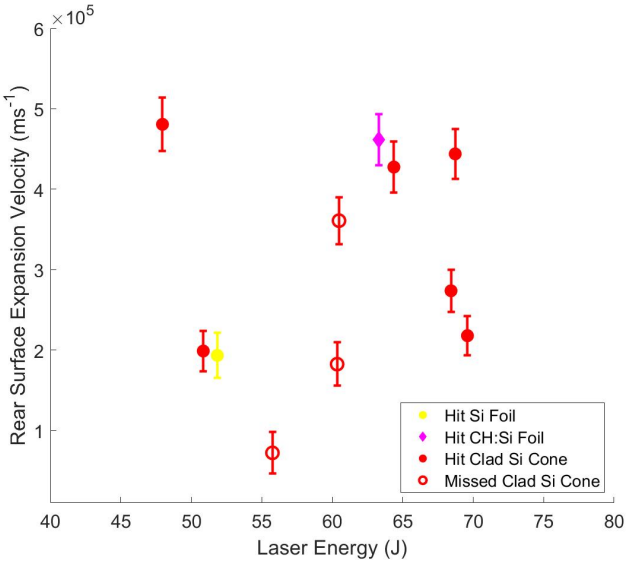

Figure 4.29: Mean rear surface expansion velocity as a function of laser energy for ≈ 100 μm thick silicon targets. Vertical error bars combine the standard deviation between the 3 analysis runs with the system's spatial and temporal delay resolution.

The mean rear surface expansion velocity of approximately 100 μm thick silicon-based targets has been extracted in Figure 4.29. The error bars incorporate the standard deviation in velocity between the three analysis runs with the system's spatial resolution. The streak camera resolution for determining the probe's temporal delay is also incorporated. Across all shots, the spatial resolution of the system was the dominant contributor to the error in expansion velocity.

The *hit* cone targets refer to those where the 2ω emission on the front surface imaging system originated from the cone tip. The silicon and CH:Si control foils were of a large surface area so were inevitably hit by the main Vulcan PW beam. The *missed* clad cone targets are those where the 2ω emission originated from the CH cladding to the side of the silicon cone tip.

The rear surface velocity is variable across the laser energy and target categories presented in Figure 4.29, albeit a clear trend would not be expected across such a narrow laser energy range. The error values are visible but do not significantly change the expansion velocity region in which each shot is located. The results have been further combined with radiation-hydrodynamic simulations to infer the rear surface temperature of each target. These results will be shown in section 4.4, with which a more detailed analysis shall be presented.

4.3.6.2 Determining the Plasma Density

As in the 2015 campaign in section 4.2.4.2, the cut-off density which appears as dark regions on the shadowgram has been determined. To do this, the FWHM of plasma expansion was calculated using the probe images.

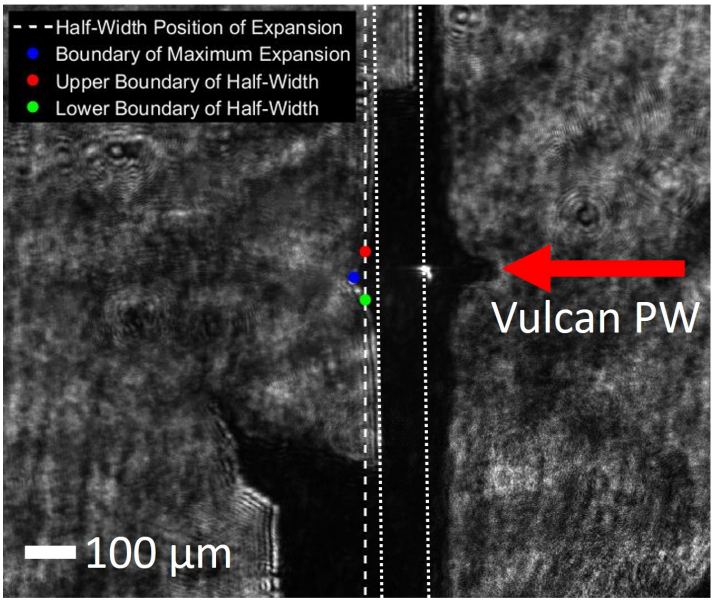

Figure 4.30: On-shot shadowgraphy image used to determine the FWHM of the rear surface plasma expansion. Blue point located at the extreme of the horizontal expansion, vertical dashed-white line positioned at the half-maximum of the expansion (i.e. half-way between the blue point and the unperturbed rear surface). Red and green points located at the top and bottom extremes of the expansion which intersect the white line. FWHM is the difference between the red and green points. White-dotted lines reference unperturbed target surfaces.

The distance between the red (top) and green (bottom) points on Figure 4.30 corresponds to the FWHM of the rear surface expansion. This method was undertaken three times so that a mean and standard deviation could be calculated for each shot. Equation 3.1 was then used to calculate the cut-off density.

For the targets shown in Figure 4.29, the mean cut-off density determined using this method was calculated as (1.59 ± 1.04) $\times 10^{20}$ cm^{-3} (mean $\pm$ standard deviation). The critical density of the plasma without refraction effects being incorporated is 3.95×10^{21} cm^{-3}.

4.4 HYADES Hydrodynamic Simulations

The HYADES code has been used to simulate the rear surface expansion in the same method presented in section 4.2.5 for the 2015 campaign. The rear 30 μm of the bulk target was simulated but with an additional 2 μm of CH tamping applied to the back. The titanium dot was excluded from the simulations due to the small thickness being unlikely to affect the hydrodynamic response of the target.

The target was split into two initial components, the first was 30 μm of Silicon split into 30 zones on the mesh grid. Each zone was 0.84 the thickness of the previous zone. This region was designated with a mass density, atomic number and atomic mass of 2.42 gcm^{-3}, 14 amu and 28.08 amu respectively [99]. A quotidian equation of state (QEOS) was used with a bulk

modulus of 100 GPa [113].

The second component was then the final 2 μm of CH tamping on the rear of the target surface. This was split into 49 zones, each being 0.87 the thickness of the previous zone. This region had a mass density of 1.044 gcm^{-3} [99]. The CH material was generated by weighting the entire 2 μm between 50 : 50 carbon and hydrogen. The carbon had an atomic number and atomic mass of 6 amu and 12.012 amu, while the hydrogen values were 1 amu and 1.008 amu respectively [99]. The region was then described by an Equation of State (EOS) using the inbuilt library from HYADES for Polystyrene.

The choice of using the 0.84 and 0.87 zone thickness multiplication factors for the silicon and CH respectively maintained sufficient spatial resolution at the rear of the target. It also ensured mass-matching between the two materials of different density so that hydrodynamic and energy transport calculations were stable [99]. In Figure 4.31, the silicon and CH mesh walls can be seen as blue and red vertical lines respectively.

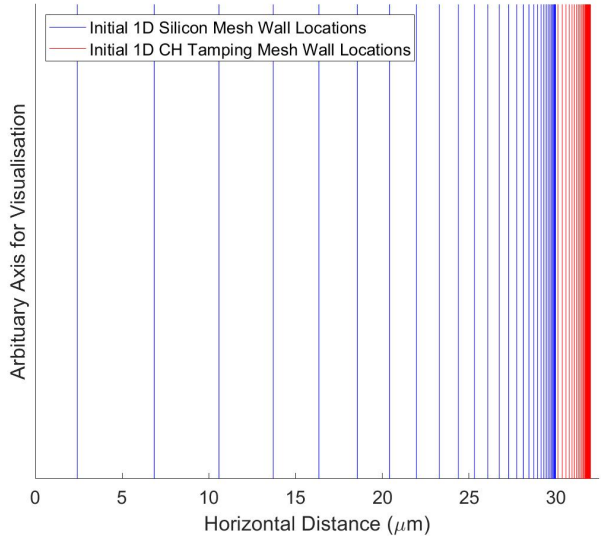

Figure 4.31: HYADES initial cell locations for the 2017 campaign simulation

Both the silicon and CH tamping zones were described by an Average-Atom ionisation model inbuilt into HYADES; chosen due to the target being considered in local thermal equilibrium (LTE) after the relatively long probe delay. A flux limiter was placed on the ions with a multiplier of 0.05. The radiation used the multi-group diffusion model for the wide range of photon mean-free-paths within the dense plasma. This split the radiation into 40 groups with the energies logarithmically interpolated between $1 \times 10^{-6} - 2$ keV.

The simulations were run for a total duration equal to the probe delay for that specific shot; 200 ps for example. This was split into time intervals of 10 ps, for which the required data was saved. The general process presented in the flow-diagram in Figure 4.8 is still applicable to this section. The targets were initially set to a homogeneous temperature and hydrodynamically expanded. At the final time step (i.e. the probe delay), the mesh point with an electron density closest to the probe cut-off density was located along with it's velocity. Subsequent simulations at different temperatures were undertaken until the output velocity matched that determined

using the probe.

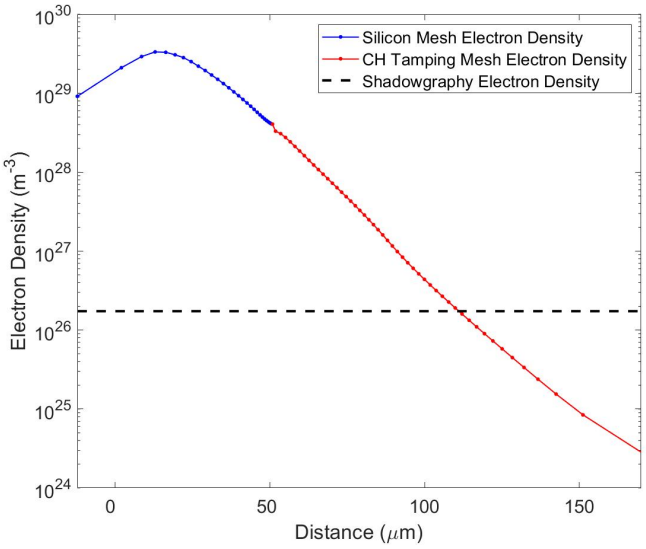

Figure 4.32: HYADES electron density at each mesh wall after 200 ps. Horizontal line represents the cut-off density that was imaged using shadowgraphy.

Figure 4.32 shows the position of each mesh wall as solid, circular data points. Those representing silicon are blue, while those representing the CH tamping are red. The cut-off density from the shadowgram (section 4.3.6.2) is represented by the horizontal, black-dashed line. The mesh point closest to this line was recorded, along with it's velocity. As with the 2015 campaign simulations, this velocity was then plotted as a function of the input temperature for that simulation and interpolated.

The temperature at which the rear surface velocity intersected the interpolation curve was then recorded. Further rounds of simulations were undertaken at increasingly closer temperatures to that determined by the intersection point. This iteratively *zeroed in* on the required temperature until the same expansion velocity was produced as determined using shadowgraphy.

Figure 4.33 shows how the initial simulations were separated by 10 eV, followed by the subsequent simulations at closer temperatures around 148 eV.

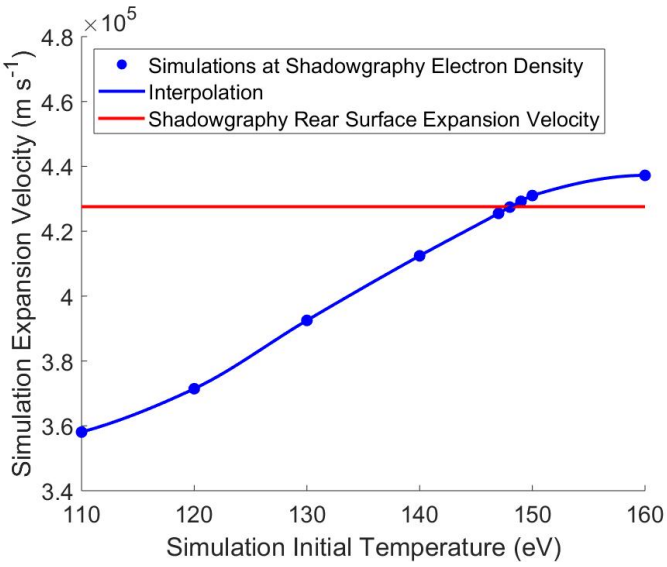

Figure 4.33: Expansion velocity of the mesh position corresponding to the cut-off density after 200 ps. Results for temperature ≤ 140 eV and ≥ 150 eV correspond to the first round of simulation. The remaining results are from the second round of simulations.

The location where the expansion velocity determined by the shadowgraphy (red line) intersects with the simulation interpolation curve (blue) was recorded. The temperature for this position was then used for a final simulation. In all cases, this simulation produced an expansion velocity closest to that determined by the probe. In doing so, the rear surface temperature was inferred as the value that was used for the initial target temperature.

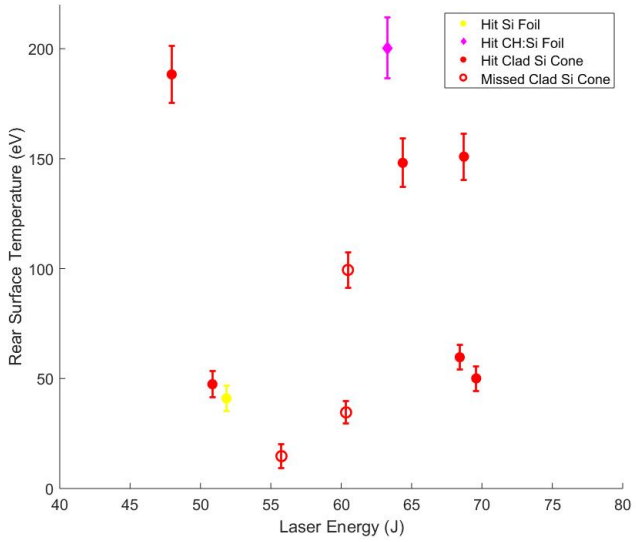

Figure 4.34: Inferred rear surface temperature as a function of laser energy.

The rear surface temperature has been inferred in Figure 4.34 using a combination of shadowgraphy and hydrodynamic simulations. Specifically, the results presented in the figure refer to approximately 100 μm thick targets based on silicon. This corresponds to an areal electron density of 7.2×10^{25} m^{-2} for the hit clad and silicon control foils. This value is calculated by considering a silicon mass density of 2.42×10^{3} kgm^{-3} [99] and a fully ionised plasma due to the high recorded temperatures.

The rear surface temperature is variable across the small laser energy range presented in the results. However, the targets appear to be somewhat split into three temperature regimes. At approximately ≤ 60 eV, three hit clad, two missed clad and the silicon control foil are displayed. At ≥ 150 eV, three hit clad cones and the CH:Si structured foil are present. An intermediate regime is shown where a single, missed clad cone reaches a temperature of approximately 100 eV.

Locating the silicon areal electron density in the work of M. Nakatsutsumi *et al* [16] corresponds to a temperature of approximately < 50 eV in experimental work using laser energies exceeding 214 J. These energies are significantly more than those obtained for the 2017 campaign. This suggests that some of the targets in the cooler subset in Figure 4.34 are still achieving similar rear surface temperatures at less than a quarter of the laser energy than in [16]. Although caution needs to be taken when directly comparing the two methods of calculating the rear surface temperature. The work by Nakatsutsumi *et al* [16] directly measures temporally and spatially resolved optical thermal emission from the rear surface of targets. In contrast, the work presented in this thesis uses shadowgraphy to determine the time-integrated rear surface plasma expansion. Radiation-hydrodynamic simulations are then used to model the rear portion of the target in one-dimension until a similar velocity of expansion is observed. The nature of shadowgraphy means that the images of the expansion are temporally integrated $(150 - 200$ ps) only allowing the average velocity of the expansion during this time to be extract. This does

not allow the peak velocity and therefore maximum temperature to be determined. Nakatsutsumi reports a temporal resolution of 17 ps [16]. Inevitably, the one-dimensional nature of the simulations will not model the real expansion of plasma perfectly. The HYADES simulations also underestimate the cooling of the target, therefore the cut-off density surface will retain energy and travel further for a given input temperature. From this, the average velocity in the simulations will be higher than in reality for the same temperature. Therefore, to achieve the same velocity in the simulations as recorded using the optical probe, a lower temperature will be required. This results in the temperatures in Figure 4.34 being underestimated.

The temperature results are even more prominent in the intermediate and higher subsets of targets in Figure 4.34, with the latter exceeding $\geq$ 150 eV. For these targets, an even clearer enhancement in rear surface heating is seen, and corresponds to the simulations in [16] using a 200 J driver beam. The improvement in heating for the CH:Si control foil may be related to the areal density of this target. This is calculated as 5.3×10^{25} m^{-2} considering silicon and CH mass densities of 2.42×10^3 kgm^{-3} and 1.04×10^3 kgm^{-3} respectively [99] and a fully ionised plasma due to the high recorded temperatures. This areal electron density is less than that of the hit clad cones and silicon foil targets. Nakatsatsumi *et al* show how the temperature in both the experimental and simulation work is improved for lower areal densities, therefore this parameter may contribute to the structured foil performing as well as the highest subset of hit clad cones targets.

The variability in the inferred rear surface temperature was investigated in relation to a variety of other laser and target parameters, such as the laser intensity and cone angle. Despite this, a dependency was not found. The rear surface temperature is primarily driven by the energy of the electrons and how much is transferred to the bulk target through collisions. This is inherently related to the laser energy delivered to the target, or more specifically, the fast electrons. The energy incident upon the target has not only been characterised using calorimetry, but also the effect of defocus has been additionally considered and how this effects the energy contained within the laser FWHM spot.

The developments that were recommended from the 2015 campaign to reduce unknown variability have also been implemented on the later campaign. The front surface imaging system has been used to determine the position of the laser pulse on the cone tips; however, this still does not account for the observed variability as both hit and missed clad cones are within the lower temperature subset in Figure 4.34. The improved surface profile of the silicon targets using the MEMS manufacturing technique meant that any variability due to surface structure has been minimised. Unknown variation in the pulse length has been removed by only using shots where the autocorrelator diagnostic successfully triggered. Finally, the effect of defocus on the laser FWHM and energy contained within this area has been characterised. All of these implementations still do not account for the variation in the temperatures shown in Figure 4.34.

This leads onto a further parameter which we propose plays an important role in the interaction. This is the energy contained outside of the FWHM of the focal spot. An astigmatism in the Vulcan PW beam - even at optimal focus - is caused by the off-axis parabola. Three-dimensional hybrid simulations using ZEPHYROS show an improvement in resistive guiding of fast electrons and enhanced heating at depth for when the laser beam is matched in size to the cone tip [11].

Similar work matches the laser pulse to the cone tip width as standard [12, 13]. This situation was not present in the 2015 or 2017 campaigns if the laser FWHM is considered solely as that of the main peak and the astigmatism is not accounted for. In this case, the laser focal spot (6.1 μm) is smaller than the narrowest silicon cone tip (12.77 μm). However, the astigmatism of the Vulcan spot and the energy contained within regions outside of the main FWHM have been characterised. This has allowed us to determine if the size of the beam is artificially increased by the astigmatism towards that of the silicon cone tips. This shall be presented in the following section using three-dimensional hybrid simulations.

4.5 ZEPHYROS Hybrid Simulations

Three-dimensional, hybrid simulations have been used to investigate the effect of an astigmatic laser beam and how this may affect the fast electron dynamics. The code that has been utilised for this is ZEPHYROS [101], details of which are presented in section 3.9.

The image and corresponding line-out of the laser focal spot for the 2017 campaign (Figure 4.15) shows a significant bright region next to the main spot. This is inherent to the Vulcan system and relates to a slight astigmatism from the OAP focussing. This section sets out to investigate the effect of the energy contained within this region and how the fast electron dynamics are modified. This region shall be termed the *wing* of the beam for reference in this thesis.

A detailed characterisation of the *wing* region was required before initiating these simulations. To determine the intensity on the target, a Gaussian fit was applied to the main peak and the FWHM was calculated as 6.1 μm. The same routine was needed for the bright additional peak in the focal spot. Figure 4.35 presents the line-out of the focal spot along with a Gaussian fit across the *wing* feature.

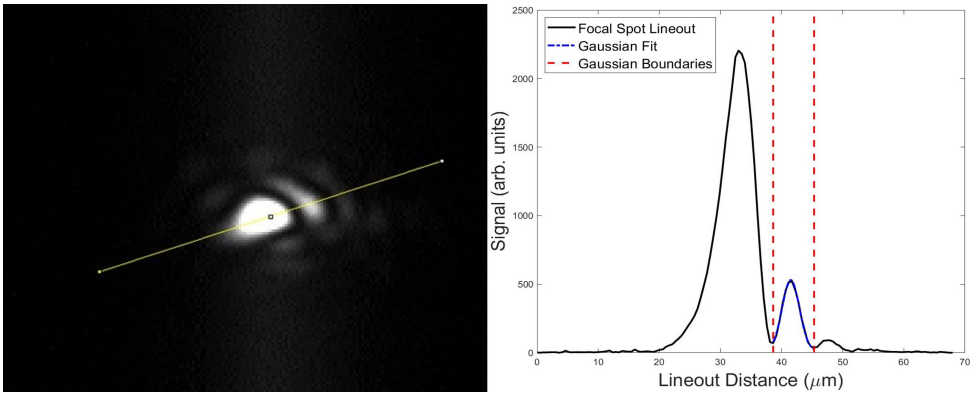

Figure 4.35: Photo of the CW focal spot from the 2017 Vulcan PW campaign and corresponding line-out. Gaussian fit applied to the secondary peak with FWHM = 3.3 μm. Fit boundaries between 38.63 μm and 45.32 μm. Peak value is 24% of the main peak. Separation between the edges of the FWHMs of the main and secondary peak ($\Delta y_{\mathrm{FWHM\ sep}}$) is 2.7 μm.

The FWHM of the main peak was determined earlier as 6.1 μm in section 4.3.4.1. By applying a Gaussian fit to the wing of the astigmatic focal spot, the FWHM of this feature is found to be 3.3 μm. This region contains a peak signal of 24% of the main peak. With the

intensity of the main beam being nominally 1×10^{21} Wcm^{-2}, this corresponds to an intensity within the secondary peak of 2.4×10^{20} Wcm^{-2}. This far exceeds the ionisation threshold of the target and therefore, we suggest that the effective size of the focal spot is increased due to the significant amount of signal within this secondary region.

4.5.1 Simulation Environment

To investigate this effect, foil and conical structures were generated in ZEPHYROS and a novel hybrid laser profile was used to observe the effect on the fast electron population. ZEPHYROS has an inbuilt system for applying a secondary beam travelling from the opposing rear side of the target. This was modified by the code author (A.P.L. Robinson) so that both beams could be directed from the same side of the target. In doing so, the second beam was used to replicate the additional *wing* of the focal spot.

The simulation was set up using a three-dimensional grid of $103 \times 200 \times 200$ cells (x×y×z), with each cell being 1 μm^3 in volume. The laser pulse was directed along the x-axis, whilst the horizontal and vertical planes were y and z respectively. The side boundaries were left open, whilst the front and back were reflective to represent electron refluxing. Recall from section 3.9 that ZEPHYROS doesn't model the laser pulse, but instead generates a fast electron population based upon the laser parameters specified by the user.

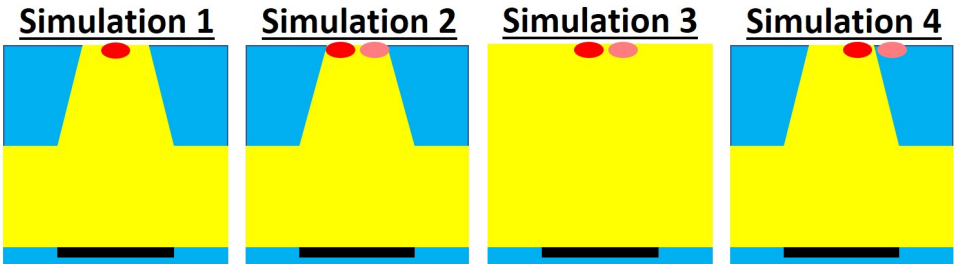

Figure 4.36: Schematic of the four laser-target configurations simulated in ZEPHYROS. Red and pink ovals represent the main and secondary beams respectively. Yellow and blue areas are silicon and CH plastic respectively. Black rectangle is the titanium dot.

The primary factor that the simulations were based upon was the main beam. This was set to an intensity of 1×10^{21} Wcm^{-2} and pulse length of 1 ps in accordance to the nominal Vulcan parameters. The FWHM of the spot was then set to 6.1 μm to replicate the size of the focal spot in the 2017 experiment. For the hybrid laser scheme, an additional spot was then applied that had a peak intensity of 24% of the main beam (2.4×10^{20} Wcm^{-2}) again, in accordance to the experimental focal spot analysis. The pulse length of the secondary beam was also 1 ps.

To keep the energy contained within the second beam consistent with the 24% requirement, the FWHM also was set to 6.1 μm. ZEPHYROS takes the intensity, focal spot size and pulse length and then calculates the energy contained within the spot. Therefore, the size of the spot had to be kept identical to the main beam to ensure that both the peak intensity and energy within the second spot was kept at the 24% ratio. Investigations were undertaken to attempt to match the second spot size to the 3.3 μm determined by the line-out in Figure 4.35, however it became clear that this was artificially increasing the contained energy over the desired 24% level.

Simulation	Target	Laser	Modelling Situation
Simulation 1	Clad Si Cone	Primary Beam	Hit Shot with Primary Beam
Simulation 2	Clad Si Cone	Hybrid Beam	Hit Shot with Hybrid Beam
Simulation 3	Si Foil	Hybrid Beam	Control Hit Shot with Hybrid Beam
Simulation 4	Clad Si Cone	Hybrid Beam	Clipped Shot with Hybrid Beam

Table 4.5: ZEPHYROS simulations used to investigate the effect of energy within the wing of the beam. Main beam is a single beam with intensity = 1×10^{21} Wcm^{-2} to replicate a nominal Vulcan PW spot. Hybrid beam is the same main beam but with a secondary beam to the side with an intensity of 24% of the main beam. Simulation 3 is a control for Simulation 2. Simulation 4 investigates the hybrid beam system but displaced so that the hybrid beam is centred upon the edge of a silicon cone. This replicates a *clipped* shot. Cone tip size matches the total FWHM size of the hybrid beam system.

In accordance with the line-out of the optimised focal spot from the experiment, the distance between the edges of the FWHMs of both beams was kept at 2.7 μm. This shall be denoted as $\Delta y_{\text{FWHM sep}}$ for reference in the remainder of this chapter.

Naturally the laser profile extends beyond the position of the FWHM. This spatial cut-off was determined as the location that the intensity reached 1% of the peak value. This follows the example in the ZEPHYROS manual [101] and corresponds to 7.88 μm from the central position of each laser. Both beams were set to a wavelength of 1.053 μm and described spatially using a Gaussian distribution.

Following the method detailed in section 3.9, the laser parameters are used to generate and inject a fast electron population into the target for each laser pulse. The angular distribution of both these populations was set to Gaussian, with a FWHM divergence of 60° as suggested in [5]. The fast electrons were provided 30% of the laser energy. Previous work using ZEPHYROS [12,13] set the laser spot to the same size as the cone tip, while [11] further showed that in doing so, the fast electron current was less diffuse in the cone; leading to a higher current density and improvement in the resistive magnetic field generation. This was further investigated in [114] where the collimation effect was seen to reduce when the cone tip width was slightly larger than the laser spot (cone $\times 1.25$ larger). For this reason, the cone tip was kept at a constant size across all the simulations so that the width was equivalent to the FWHM of the hybrid laser system, i.e. $\text{width}_{\text{cone tip}} = \text{FWHM}_{\text{laser 1}} + \text{FWHM}_{\text{laser 2}} + \Delta y_{\text{FWHM sep}}$. This meant that the cone tip was 15 μm wide.

The literature [12, 13] indicates that the optimal cone angle was the shallowest of those investigated. This was routinely 5°, therefore the simulations presented in this section used the same value. Therefore, for a 50 μm deep cone, the width of the base was 23 μm. To match the experimental conditions as closely as possible, a 1 μm titanium dot was matched to the base width of the cone and located 100 μm deep into the target. This was then tamped with a further 1 μm of CH plastic; the same material that clad the cone. The titanium dot was kept at 1 μm thickness due to the cell precision of the simulations. Creating a dot of 150 nm to match that in the experimental campaign would have been too small to be resolved.

The target was described as an ideal, hot plasma and set to an initial temperature of 1

eV. Scattering of the fast electrons, electron-ion energy exchange and longitudinal drag of the fast electrons were all applied. The Lorentz force, magnetic diffusion and the Thomas-Fermi ionisation model were used.

4.5.2 Bulk Electron Temperature Results

The simulations were set to run until the end of the laser pulse length (1 ps). At this time, the bulk electron temperature in the middle of the vertical plane was extracted.

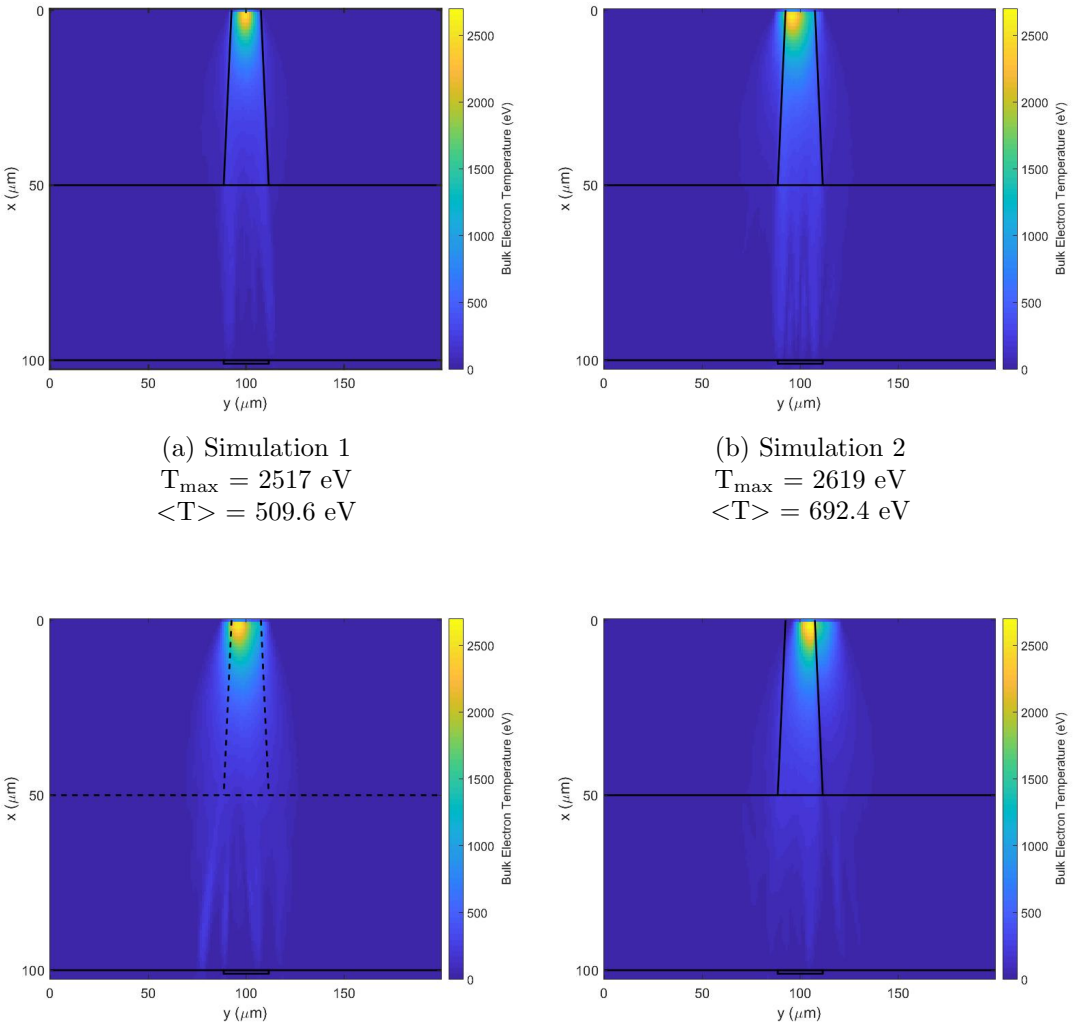

(a) Simulation 1
T_{max} = 2517 eV
<T> = 509.6 eV

(b) Simulation 2
T_{max} = 2619 eV
<T> = 692.4 eV

(c) Simulation 3
T_{max} = 2582 eV
<T> = 634.3 eV

(d) Simulation 4
T_{max} 2692 eV
<T> = 538.0 eV

Figure 4.37: ZEPHYROS simulations of bulk electron temperature. T_{max} is the maximum bulk temperature inside the cone while <T> is the total bulk temperature within this area normalised to the number of cells. (a) Simulation 1: Main beam centred on silicon cone (b) Hybrid beam centred on silicon cone (c) Hybrid beam centred on silicon foil (d) Hybrid beam clipped silicon cone.

Figure 4.37 shows a horizontal slice of the bulk electron temperature after 1 ps. This image

is taken through the centre of the target and the location of the cone and rear surface boundaries are represented by the solid black lines. These reference positions are also shown in the silicon foil target in Simulation 3 for comparison using the dotted lines. Note that a real material interface is not present within this foil target - the lines are solely for visualisation purposes.

For quantitative analysis, the average temperature is calculated by summing the bulk temperature at each cell within the area of the cone at the central plane. This is then normalised to the number of cells within the 2D area. The maximum temperature is the maximum value within the same region. Both these parameters are referring to the cells on the imaged plane (horizontal cross-section at 100 μm height).

Confinement of the electron beam is clearly seen in Simulation 1 for just the primary beam centred upon the silicon cone. One would expect to observe such an effect as this has already been reported in the literature with similar laser conditions [8, 11–13] - although, these matched the laser spot size to the cone tip. The imaged snapshot is taken after 1 ps, which is sufficiently later than the 100s of fs required to generate the resistive magnetic fields. Clearly these fields have become established by this time and aid fast electron collimation. The confinement continues once the electrons leave the conical structure at 50 μm depth, although annular transport is visible. The maximum bulk temperature recorded inside the area of the cone is 2517 eV whilst the averaged heating is to 509.6 eV.

When introducing the secondary beam (Simulation 2), confinement is still visible along with the annular structure once the electrons leave the cone. The maximum and averaged temperatures are increased with respect to the single beam case to 2619 eV and 692.4 eV respectively. At this stage, this can only be attributed to the increased energy being supplied to the system by the additional laser beam. A further point to take from Simulation 2 is the increased heating further outside of the cone compared to Simulation 1. Recall that the fast electrons are injected out into the radial region where the intensity reaches 1% of the peak value; specifically 7.88 μm from the central position of each laser pulse. To fit the additional beam inside the cone, the whole laser system is shifted across the cone so that it is collectively centred on the tip. This means that the electrons injected 7.88 μm from the centre of each laser are now further outside of the cone than they would be if just the main laser was centred on the centre of the tip. Therefore, the existence of heating further outside of the cone when the additional beam is present is likely due to the electrons being injected further out into this region, rather than a reduction in the collimation effect.

The effect of the actual cone structure on the hybrid beam system can then be discussed using the foil in Simulation 3 as a reference. The only difference between this and Simulation 2 is the target structure. The maximum and average temperatures in the foil simulation are 2582 eV and 634.3 eV respectively, both less than when the cone in present in Simulation 2. However, the foil with the hybrid beam appears to perform better than the single beam even when incident on a cone (Simulation 1). This supports the inference that adding a secondary beam will inherently raise the temperature of the system, simply by supplying more energy. This is still the case even when a collimating target structure isn't present. Additionally, not only does the act of injecting the secondary beam enhance the temperature, but the presence of the cone structure further improves the heating throughout the region.

Finally we consider the case of a clipped shot (Simulation 4) where the hybrid system has been translated across the target surface so that the main beam is inside the cone, whilst the secondary beam is onto the CH cladding. The first thing to note is that the average temperature within the cone is reduced to 538.0 eV; this is cooler than when the hybrid laser system is centred on the cone tip or on a foil (Simulation 2 and 3 respectively). If one considers the divergent nature of the fast electrons as they are injected into the target, they are spread radially according to the Gaussian injection function. This means that approximately 50% of the electrons injected from the additional beam are directed away from the cone, so are unlikely to be affected by the confining magnetic fields. If we compare this to Simulation 2 where both FWHMs of the injection points are within the cone, all the electrons injected from these regions are directed inside the cone, albeit some will exit before the resistive magnetic fields have become sufficiently established.

Simulation 4 shows the importance of the position of the laser pulse on the cone tip. Translating the beam across the target so that the *wing* is outside of the cone results in the average temperature being significantly reduced. However, this reduction is not to the extent that is reaches the levels recorded for just the single primary beam in Simulation 1. This suggests that the electrons injected towards the cone from the secondary beam do contribute somewhat to the overall temperature within the cone.

It is appropriate to also discuss the magnetic field generation in the same plane as Figure 4.37. The temperature profiles can then be considered in the context of this.

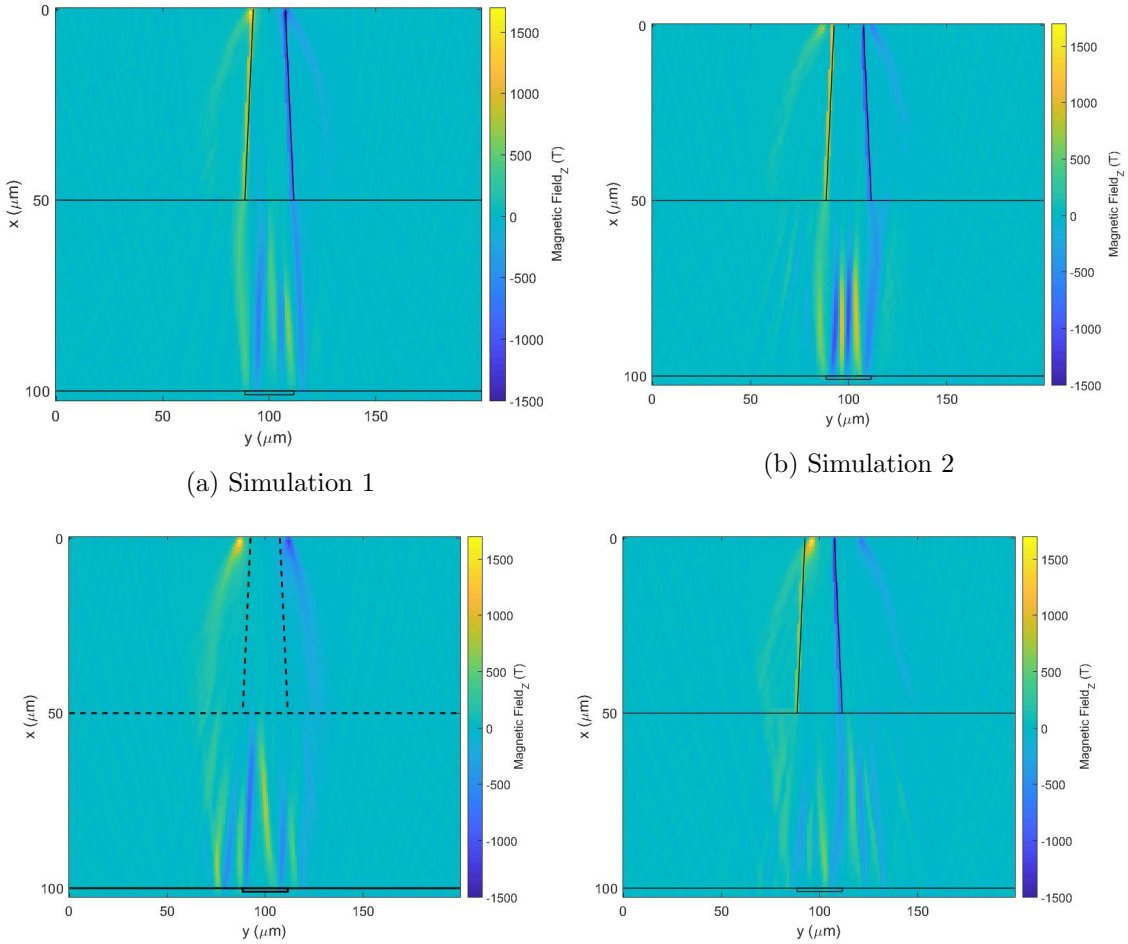

(a) Simulation 1

(b) Simulation 2

(c) Simulation 3

(d) Simulation 4

Figure 4.38: ZEPHYROS simulations of the azimuthal magnetic field in the z-direction. (a) Simulation 1: Main beam centred on silicon cone (b) Hybrid beam centred on silicon cone (c) Hybrid beam centred on silicon foil (d) Hybrid beam clipped silicon cone.

Clear fast electron confinement and subsequent target heating has been shown in Figure 4.37. Figures 4.38a, 4.38b and 4.38d show how azimuthal magnetic fields are successfully generated at the resistive interfaces in the cone targets and provide a clear explanation as to this enhancement in confinement. Figure 4.38c shows the case of the silicon control foil, where azimuthal magnetic fields are visible, but at the edges of the injected hybrid fast electron beam. These fields are also seen in the remaining simulations and show how part of the electron beam diverges into the target and is not confined by the resistive guiding fields. This begins at early times in the simulations before the resistive fields have had sufficient time to become established.

Both Figures 4.38a and 4.38d respectively show when a single beam is smaller than the cone tip, or when the hybrid beam system is displaced across the cone tip, resistive guiding fields are still generated at the cone:cladding interfaces.

In all cases, structures in the magnetic fields for depths of approximately $x \geq 50$ μm suggest

that electron beam filamentation is present. This is further diagnosed by imaging vertical cross-sections at 50 μm and 100 μm depths in the target. These corresponds to the cone base and titanium dot locations and are presented in Figures 4.39 and 4.40. On each image, the cone base width is referenced by a black circle, while the wall is then tracked at the 5° cone angle until 100 μm depth. This is then referenced by the larger red circle.

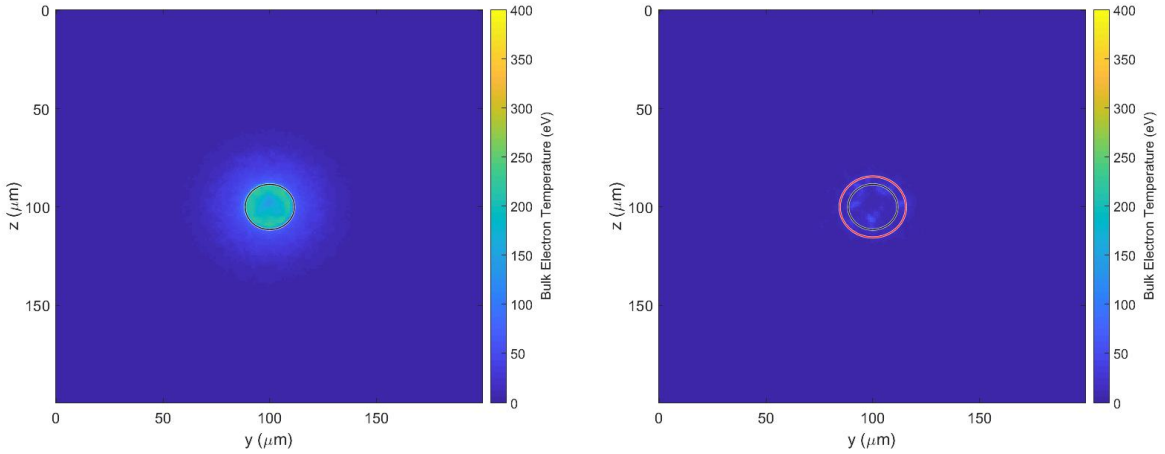

(a) Simulation 1 CS at cone base (50 μm)
T_{max} = 232.5 eV
<T> = 189.2 eV

(b) Simulation 1 CS at Ti dot (100 μm)
T_{max} = 65.0 eV
<T> = 18.1 eV

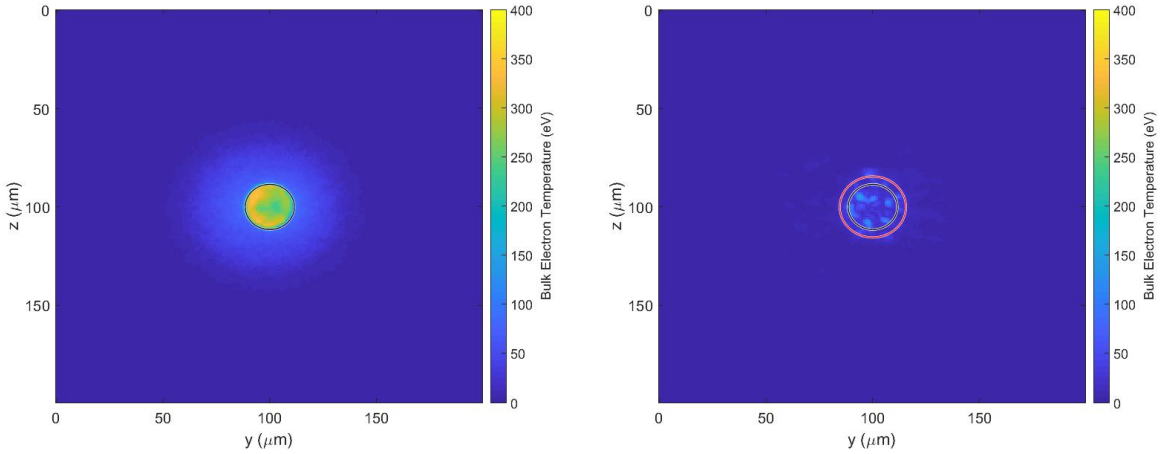

(c) Simulation 2 CS at cone base (50 μm)
T_{max} = 341.7 eV
<T> = 272.3 eV

(d) Simulation 2 CS at Ti dot (100 μm)
T_{max} 152.8 eV
<T> = 44.2 eV

Figure 4.39: Cross-section temperature view of ZEPHYROS Simulations 1&2 at depths of (left) cone base at 50 μm and (right) titanium dot at 100 μm. Inner and outer circles represent the cone base and a projection of the cone walls at 100 μm depth respectively.

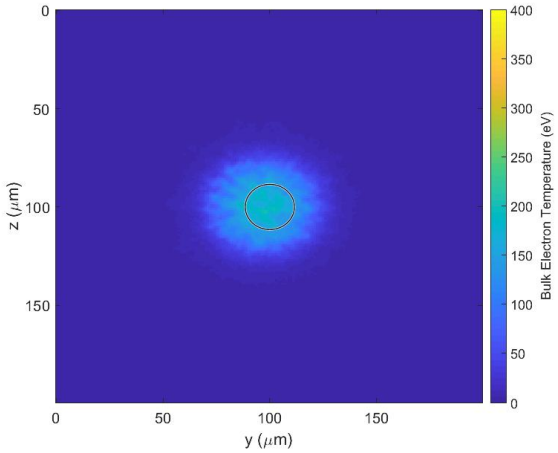

(a) Simulation 3 CS at cone base (50 μm)
T_{max} = 204.1 eV
<T> = 168.1 eV

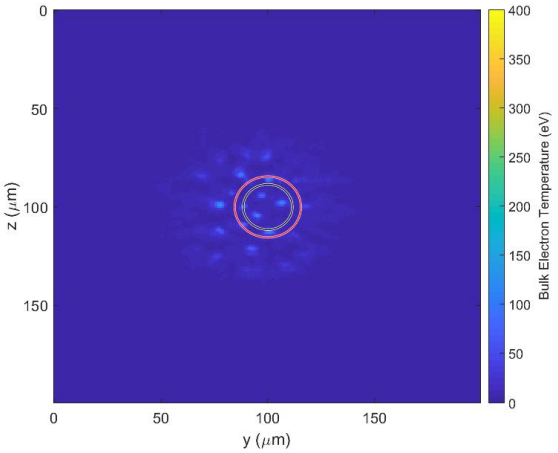

(b) Simulation 3 CS at Ti dot (100 μm)
T_{max} = 129.9 eV
<T> = 16.4 eV

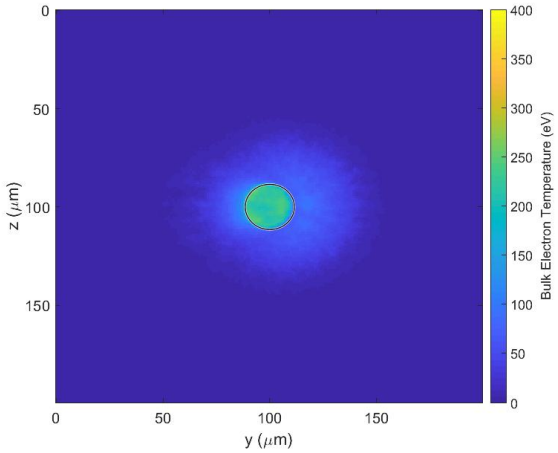

(c) Simulation 4 CS at cone base (50 μm)
T_{max} = 253.3 eV
<T> = 213.8 eV

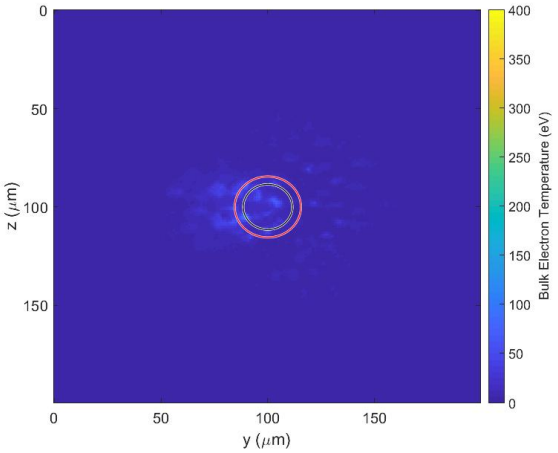

(d) Simulation 4 CS at Ti dot (100 μm)
T_{max} 108.7 eV
<T> = 22.3 eV

Figure 4.40: Cross-section temperature view of ZEPHYROS Simulations 3&4 at depths of (left) cone base at 50 μm and (right) titanium dot at 100 μm. Inner and outer circles represent the cone base and a projection of the cone walls at 100 μm depth respectively. Circles are present on the silicon foil in Simulation 3 for solely visualisation purposes - no cone was present in the simulation.

Figures 4.39 and 4.40 show a cross-section at the end of the cone (50 μm depth) and at the titanium dot (100 μm depth). This allows for comparison between how the fast electron beam is collimated after travelling through the length of the cone and also after it exits the structure and has crossed the 50 μm stand-off distance. Recall from section 2.9 that the fast ignition scheme requires the fast electrons to remain collimated across a stand-off between the cone tip and pre-compressed fuel [53].

The maximum and average temperature values are calculated in the same way as for the top-down view, except that the region of interest is now the black circle corresponding to the size of the cone base at 50 μm. Effectively, the average temperature gives an indication of how well the whole area is heated, whilst the maximum temperature is more likely to be affected by localised heating or filamentation.

For the single main beam centred on a cone tip, Simulation 1 shows that the electron beam remains collimated as far as the end of the cone. This agrees with the top view in Figure 4.37, as does the fact that annular transport is visible in the beam. At the end of the cone, the temperature reaches a maximum of 232.5 eV and an average of 189.2 eV.

Comparing this to when the additional beam is added to the cone, the maximum temperature at 50 μm is increased to 341.7 eV with an improvement in the average temperature to 272.3 eV. Again, we partially attribute this to simply more energy being injected into the system due to the additional beam. However, it is clear that the cone is still having a confining effect. The highest temperatures are kept within the region bound by the base of the cone, whilst some heating is seen around the outside of this area - likely due to electrons escaping from the cone before the magnetic field is generated, as well as those initially injected out into the radial region where 1% of the peak intensity is located. Again, annular structure is visible with the hybrid beam scenario, although the heating is significantly more uniform across the cross-sectional area of the cone base.

The enhanced confinement in Simulation 2 for the hybrid beam system is even more apparent when compared to the silicon control foil (Simulation 3). As expected, when a conical feature is not present, there is no resistivity gradient within the target to aid in the generation of the resistive magnetic fields. The bulk electron temperature is qualitatively more dispersed, with an increased heating outside of the area that represents the cone base (if it were present). With this knowledge of how far the heating would extend radially without the cone, it is clear that the cone structure in Simulation 2 is playing a role in confining the fast electrons. For the foil case, the maximum and average temperatures within the theoretical cone base region are 294.1 eV and 168.1 eV respectively - significantly less than the case for when the cone is present.

The average temperature in the foil simulation is also less than for the case of the single, main beam in Simulation 1. This suggest that even if only a single beam is present, the cone improves the confinement of electrons. Therefore, the temperature is more evenly distributed across the cross-sectional area of the cone base. However, the maximum temperature is slightly improved for the silicon foil with the hybrid beam, this is likely due to not only more energy being injected into the system, but also that the most energetic and least divergent electrons are injected perpendicular to the target surface, so are picked up in the analysis region of interest and contribute to the maximum temperature calculation. Again, this shows that the maximum

temperature parameter is sensitive to specific areas of the simulation and the figure-of-merit used to analyse the results. Therefore, we suggest the average temperature is a more useful measure of cone performance in terms of heating.

Finally, we consider the case of Simulation 4 where the hybrid beam system is displaced to represent a *clipped* scenario. Here we can visually determine that confinement is still achieved within the region of the cone at 50 μm, however heating further out to 140 μm in the y-direction is seen due to the additional beam being shifted across and injecting fast electrons out into this region. The average temperature in the cone base region is 213.8 eV, significantly enhanced and more uniform compared to the foil and single beam incident on the cone (Simulation 3 and 1 respectively). However the average temperature is clearly lower than when the hybrid beam is centred on the cone (Simulation 2). This suggests that even if the secondary *wing* feature of the beam is outside of the cone region, the main beam is still sufficient to generate the collimating fields. Two factors can be attributed to the displaced system heating the cone more uniformly compared to the single beam centred on the cone. Firstly, the main beam is closer to the side of the cone wall, so electrons reach the resistivity boundary sooner and can begin to contribute to generating the magnetic field earlier in time and closer to the front of the target. Secondly, the additional beam is still contributing by generating electrons near the cone wall, some of which are directed into the feature. It is likely that a proportion of these electrons can enter the cone and contribute to further field generation.

At the end of the stand-off distance where the electrons have travelled a further 50 μm from the end of the cone base (100 μm total depth), the general trends continue. The case of the single and hybrid beams on the silicon cones show that the electron beam is still confined within the area of the titanium dot, with the hybrid system improving the heating of bulk electrons. The case of the hybrid beam on a silicon foil shows no effect of collimation, as one would expect. Clearly the cone structure improves the situation, regardless of the type of injected beam.

For the displaced hybrid beam on the silicon cone, the situation is less definable at 100 μm depth. The electron heating due to each beam is clearly distinguishable, whereby the electrons for approximately y = $\leq$ 110 μm are heated to a higher temperature and are in the region corresponding to the higher energy beam. Electrons located at y = $>$ 110 μm are in the region of the additional, lower energy beam.

At the 100 μm depth of the target, filamentation is seen across all of the simulations. However, the filaments appear more tightly bound when the beams are centred upon cone targets, suggesting that the resistive fields aid in bringing the filaments closer together. The annular transport that was recorded at the end of the cone in Simulation 1 is still present at 100 μm in depth, even though the beam is filamented. This radial transport is reduced when the additional wing feature is applied to the beam in Simulation 2, however filamentation is still recorded for this case.

4.6 Preliminary Conclusion

We have performed resistive guiding experiments using conically structured targets for the first time. The Vulcan PW laser system has been used for two campaigns implementing a variety of structured targets. Novel silicon etched targets and a front surface imaging system have been implemented to determine the laser interaction site on the target surface. This has been invaluable in determining the success of shots. Three-dimensional hybrid simulations have also been used to suggest how an astigmatic laser pulse can aid in improving the resistive guiding mechanism by artificially increasing the focal spot to match larger cone tips.

The first campaign in 2015 used conical and foil targets based on aluminium. The analysis of the shadowgraphy diagnostic showed that the average rear surface expansion velocity of the targets was $3.08 \pm 0.21 \times 10^5$ ms^{-1}; subsequently simulating this using HYADES in a one-dimensional geometry inferred the target temperature for each shot. The 100 μm thick aluminium foils reached average bulk temperatures of 88 ± 63 eV, while the clad and unclad cone targets showed enhanced heating to 118 ± 33 eV and 138 ± 41 eV respectively. Variability between the temperature of clad and unclad targets was also reported.

Comparing this to the literature [16], temperatures of 30 eV have been recorded experimentally at a similar areal electron density as the aluminium foils and cones used in the 2015 campaign. However these used driver laser energies of approximately 190 J, significantly more than the $50 - 85$ J in 2015. Simulation results however report temperatures of approximately 150 eV using 200 J laser energy [16]. The results for the clad and unclad cones show that some of these targets achieved a similar rear surface temperate but with less than a quarter of the driver energy.

A clear enhancement in rear surface heating is recorded in the 2015 campaign, however these results are highly variable. This lead to recommendations being implemented on a subsequent experiment in 2017 to mitigate against some of these unknown conditions.

A variety of novel targets were manufactured using MEMS technology [105, 108, 109] to produce highly characterised, smooth-surfaced conical structures. An issue of laser defocus was discovered after the first experiment; this was characterised to determine the effect on the laser FWHM and energy contained within the focal spot. A plasma mirror was introduced to mitigate the effect of pre-plasma at the front surface of the target. Finally, a novel front surface imaging system was developed [77] and deployed to determine the location of the laser-target interaction. This proved invaluable in determining the success of each shot.

Using shadowgraphy, the mean rear surface expansion velocity was recorded as $3.01 \pm 0.85 \times 10^5$ ms^{-1}, similar to the earlier experiment. This was combined with the same HYADES code to hydrodynamically simulate the expansion for each target in one-dimension.

The inferred rear surface temperature appeared to be separated across three subsets of shots. The least heated subset reached temperatures of ≤ 60 eV, with these targets including a silicon control foil and missed and hit clad silicon cones. For the same areal electron density, these temperatures are comparable to those obtained experimentally but at higher laser energies (> 290 J) in [16].

The next possible subset was a single missed clad cone heated to an intermediate temperature of approximately 100 eV. This was then followed by a final set of hit clad cone targets and a

CH:Si structured foil. These reached temperatures between $150 - 200$ eV, showing enhanced heating at approximately a quarter of the laser energy than simulations by Nakatsatsumi *et al* [16]. The reduced areal density of the CH:Si foil may be contributing to the improvement in temperature for this target. Nakatsatsumi *et al* show how the rear surface heating is improved for lower areal density targets.

Clearly, some of the targets showed improved heating, but variability in the data is present. This cannot be accounted for in the target and laser parameters. However, upon investigating the focal spot, a significant proportion (24%) of the signal was contained within a peak outside of the main FWHM. The possible effect of this has been investigated using ZEPHYROS simulations.

ZEPHYROS was implemented in a three-dimensional configuration to replicate four different situations. The average and maximum bulk electron temperature across the cone region was calculated by viewing a horizontal plane and imaging the system from above. Further vertical cross-sections were imaged at the depth of the cone base (50 μm) and titanium dot (100 μm).

The hybrid beam system matched to the cone tip consistently provided the best average heating across the analysis area, regardless of the plane this was imaged in. When the maximum bulk temperature was considered, this system still performed the best in the vertical cross-section planes at 50 μm and 100 μm depths. However, this was out-performed in the top-down analysis plane by the displaced hybrid system on the silicon cone. One suggests that this is due to the maximum temperature being sensitive to filamentation and localised heating in the beam. In the displaced hybrid system, both beams were closest to a single cone boundary and so collectively contributed to generating the magnetic field along this boundary. However, although improved heating is found in this one location, the maximum temperature calculations do not account for the remaining areas of the cone. These do not benefit from both beams being in the vicinity and therefore record a lower average temperature.

In all cases, supplying the additional beam in the hybrid system improved the heating in the cones, regardless of the position on the target. From this, we determined that not only does simply applying the additional beam introduce more energy into the system and improve the heating, but also that a mechanism between the additional beam and the cone structure is taking place. When the hybrid beam was incident upon a foil instead of the cone, the same amount of energy was injected, but all of the measuring parameters were reduced. The only difference between these simulations was the target structure.

These simulations have proved useful in illustrating the possibility that the energy outside of the main FWHM of the laser also plays a significant role in the heating and magnetic field generation. The results indicate that this effectively increases the size of the focal spot towards that of the cone tips; work by [11,114] report that enhancement in the fast electron confinement is found when the laser and cone tip match is size. Our results appear to support this. We also find that the electron collimation is best maintained across the 50 μm stand-off when the hybrid beam is centred on the cone target.

The location of the laser spot is also critical to the extent of maximum heating. If the spot is slightly shifted across the surface of the cone and clips the edge, the maximum temperature can increase above that for when the target is hit centrally. However, this does have a trade off with the uniformity of the heating throughout the cone. This is an important factor to consider

in future experiments; one will need to determine whether the desired situation is to achieve the greatest peak temperature or more controlled and uniform heating. The laser position will have an important role to play in achieving either of these situations.

Chapter 5

Ion-Acceleration as a Diagnostic of Conical Structured Target Performance

5.1 Preamble

This chapter details the use of proton measurements to diagnose the performance of resistive guiding targets in the 2015 and 2017 Vulcan PW campaigns. Measurements using radiochromic film (RCF) indicate improved performance at specific cone angles for the conically structured targets. Geometric and specular reflection arguments are invoked along with three-dimensional hybrid simulations to propose mechanisms underpinning these results.

Proton measurements have been made on numerous occasions at high-intensity laser facilities. P. McKenna *et al* [115] reports the use of nuclear activation stacks to diagnose the proton beam emitted from iron foils at the Vulcan PW facility. A peak laser intensity of 2×10^{20} Wcm^{-2} was achieved and directed at 45° to the 100 μm thick targets. Ion energies up to approximately 42 MeV were recorded.

Radiochromic film has also been utilised within the laser-plasma research community to diagnose proton beams. This diagnostic is most relevant to the work presented in this chapter.

R.A. Snavely *et al* [116] report protons being measured using RCF and attributed to acceleration from the rear target surface. Maximum proton energies up to 58 MeV were achieved using a peak laser intensity of 3×10^{20} Wcm^{-2} and 100 μm thick CH foils.

M. Borghesi *et al* [52] presents a review of proton measurements using a variety of techniques. Scalings of the maximum proton energy are recorded to scale with $E_{max} \propto \left(I_L \lambda_L^2\right)^{0.5}$ for the relatively long pulse durations relevant to this thesis ($0.3 - 1$ ps) [52]. Parameters E_{max}, I_L and λ_L are the maximum proton energy, laser intensity and laser wavelength respectively. It is worth noting that the Vulcan PW laser - which is used in both experiments detailed in this thesis - contributes to this scaling law detailed in [52].

A. Macchi *et al* [50] also provides a detailed review of proton acceleration mechanisms using experimental and theoretical methods. In this work, the maximum proton energy scaling is also shown as $E_{max} \propto \left(I_L \lambda_L^2\right)^{0.5}$ for the relativistic regime. This work invokes the ponderomotive

scaling [117] of the hot electron temperature T_{hot} with the laser intensity. Specifically this is $k_B T_{hot} \propto \left(I_L \lambda_L^2\right)^{0.5}$.

The work of A. Macchi *et al* [50] and others [49,118–120] report the maximum proton energy scaling with the hot electron temperature; which itself scales with the square-root of the laser intensity [49, 50, 117, 120]. Therefore, the maximum proton energy in the relativistic regime is expected to scale with the square-root of the laser intensity.

In this chapter we detail the first proton beam measurements from conically-structured, resistive guiding targets using radiochromic film. The maximum proton energy is used to determine the performance of the targets and the associated effect on the fast electron beam.

5.2 Vulcan Petawatt Campaign 2015

As described in Chapter 4, this campaign implemented aluminium based targets on the Vulcan PW system. The laser pulse was incident at a 13° angle to the target normal, with the protons emitted through the Target Normal Sheath Acceleration (TNSA) mechanism captured using an RCF stack.

The experiment used a half-stack configuration of RCF - 5 cm×2.5 cm (width×height) - which captured the lower half of the proton beam. This allowed other diagnostics line-of-sight to the target from above. The stack was located 5 cm from the target and was composed of Gafchromic HDV2 and EBT3 film. Mylar plastic, aluminium and iron filters were located between each RCF sheet to grade the energy response of the stack.

To calculate this energy response, a MATLAB code created by D. C. Carroll at the Central Laser Facility was implemented. The code uses SRIM stopping data tables to track a single proton through the stack configuration and monitor how the energy is lost to the material. Further details of the code are presented in section 3.5.2. For calculating the stack designs in the 2015 campaign, the code was run with an energy and spatial precision of 0.1 MeV and 0.1 μm respectively. An energy range of $0.1 - 100$ MeV was used to ensure that the maximum energy that the stack would likely capture was included in the response curves. The spatial resolution of the HDV2 and EBT3 films is 5 μm and 25 μm; therefore a smaller resolution was used in the MATLAB code to ensure that the code resolution was not a limiting factor.

5.2.1 RCF Stack Design

The RCF stack design implemented on the 2015 campaign is presented in Figure 5.1.

Layer	Material	Thickness (μm)	Energy (MeV)
1	Aluminium	13	
2	**HDV2**	**109**	**1.1**
3	Mylar	100	
4	**HDV2**	**109**	**4.5**
5	Mylar	500	
6	**HDV2**	**109**	**9.4**
7	Mylar	500	
8	**HDV2**	**109**	**12.7**
9	Mylar	500	
10	**HDV2**	**109**	**15.5**
11	Aluminium	1000	
12	**HDV2**	**109**	**21.4**
13	Aluminium	1000	
14	**EBT3**	**278**	**26.6**
15	Aluminium	1000	
16	**EBT3**	**278**	**31.3**
17	Aluminium	1000	
18	**EBT3**	**278**	**35.4**
19	Iron	920	
20	**EBT3**	**278**	**43.1**
21	Iron	920	
22	**EBT3**	**278**	**50.0**
23	Iron	920	
24	**EBT3**	**278**	**56.2**
25	Iron	920	
32	**BAS-TR**	**427**	
33	Iron	1840	
34	**BAS-TR**	**427**	
35	Iron	2760	
36	**BAS-TR**	**427**	
37	Iron	1000	

Figure 5.1: RCF stack design implemented on the 2015 Vulcan PW campaign. Active HDV2 and EBT3 type RCF in green. Filtering materials of varying thickness in white. Proton energies for each RCF layer calculated using D. C. Carroll's MATLAB code.

A layer of 13 μm thick aluminium foil covered the front of the stack to protect the first layer from target debris and thermal damage. Six layers of Gafchromic HDV2 RCF were located at the front of the stack due to the sheet's $10 - 1000$ Gy dynamic range [85]. As the protons travel deeper into the stack, the cumulative thickness of each layer means that less protons in the spectrum can make it to these depths without completely loosing their energy. Therefore, HDV2 is located at the start of the stack where it can record the higher particle flux, while the more sensitive EBT3 RCF is then located at the deeper layers where the flux is reduced. The dynamic range of EBT3 is $0.2 - 10$ Gy [86].

The inbuilt SRIM data tables for the filter materials and stopping data files for the RCF were used in the MATLAB code to calculate the proton energy that each RCF layer is most responsive to. These are presented as response curves in Figure 5.2.

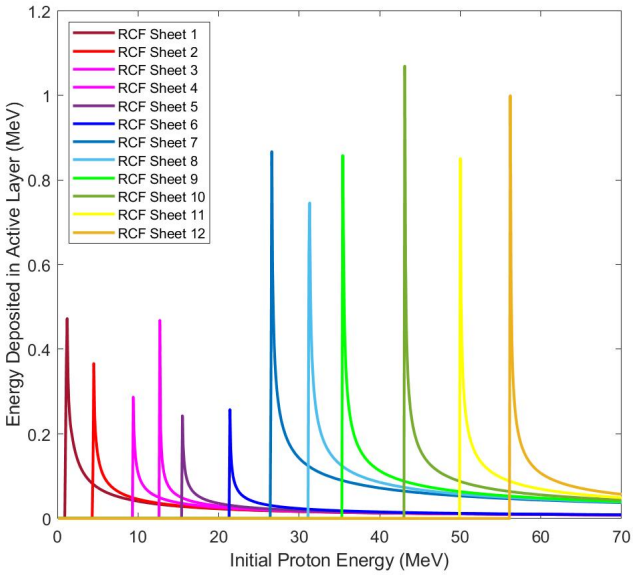

Figure 5.2: RCF response curves for the stack design shown in Figure 5.1. Each peak corresponds to the active layer of an RCF sheet.

Figure 5.2 displays the response curves corresponding to the stack design shown in Figure 5.1. Each peak corresponds to the active layer of the RCF sheet and is centred upon the initial proton energy that the sheet is most responsive to absorbing. For instance, consider the 3$^{\text{rd}}$ peak (in pink) which is centred upon 9.4 MeV. This sheet is the HDV2-type RCF with an active layer of 12 μm thickness (see Figure 3.4 for RCF structure diagram). The code tracks a single proton through the depth of the stack and calculates the energy loss during each 0.1 μm spatial step. It then repeats this for every energy step within the $0.1 - 100$ MeV range in 0.1 MeV increments. The code then locates the full thickness of the 12 μm active layer under consideration and calculates the energies deposited across this thickness. It finally averages these energies to generate the peak shown in Figure 5.2.

As shown in Figure 5.2, the stack covers a large energy range and the active layers are relatively equidistant in energy. If a large gap was present between two sheets, the energy resolution in this area would be reduced. The RCF can only record the protons that are incident upon the active layer not those that are stopped in the filtering material between two RCF sheets. Therefore by reducing the energy separation between RCF sheets, the energy resolution of the stack is increased. The largest energy gap between the RCF sheets is 7.7 MeV between RCF sheets $9 - 10$. The maximum energy is determined as the final sheet with visible colour change due to proton irradiation. The precision of this value is dependant upon the energy separation of the current and subsequent sheet.

RCF is also sensitive to electron and x-ray radiation, although to a lesser extent than the proton irradiation [52,85,86,119]. The electrons and x-rays create a more diffuse, lower intensity colour change than that created by the proton radiation [52]. Therefore, some care needs to be taken in distinguishing between the different populations, however this isn't significantly difficult and can be made simpler by scanning the RCF and viewing the image on a PC. The scanner used

for this was the *Nikon Super Cool Scan 9000 ED Transmission Scanner* located at the Central Laser Facility. The geometry of laser incidence at a 13° angle also meant that the central position of the electron beam directed along the laser axis was shifted by approximately 1.2 cm from the target normal axis along which the protons travel. This displacement is calculated at the 5 cm distance from the target rear surface.

5.2.2 Maximum Proton Energy

The final sheet in the stack that showed visible colour change due to the proton beam was recorded along with the corresponding energy of the response curve (Figure 5.2). In doing so, the maximum proton energy obtained for each shot has been determined and compared to the laser intensity.

Scalings have been applied to each target category in accordance to the suggested $E_{max} \propto \sqrt{I_L \lambda^2}$ in references [50, 52] and those there-in. This follows the ponderomotive scaling of hot electron temperature proposed by Wilks *et al* [117]. These scalings and the Target Normal Sheath Acceleration (TNSA) mechanism that underpins the proton acceleration are detailed in section 2.8. However, it is appropriate to briefly review this in the context of the results under discussion.

The TNSA mechanism was proposed by S. C. Wilks *et al* [121] and revolves around the fast electron population produced at the front surface of the laser-target interaction. These electrons travel relatively unimpeded through the target, where the most energetic escape the rear surface before the target's capacitance is sufficiently built up. The escaped electrons create a charge separation orientated perpendicular to the target plane which can reach teravolts per metre in strength [49, 50, 52, 119]. This is termed the *sheath field* and is sufficient to ionise and accelerate protons and ions from impurities on the rear surface, with the former being most affected due to the increased charge-to-mass ratio.

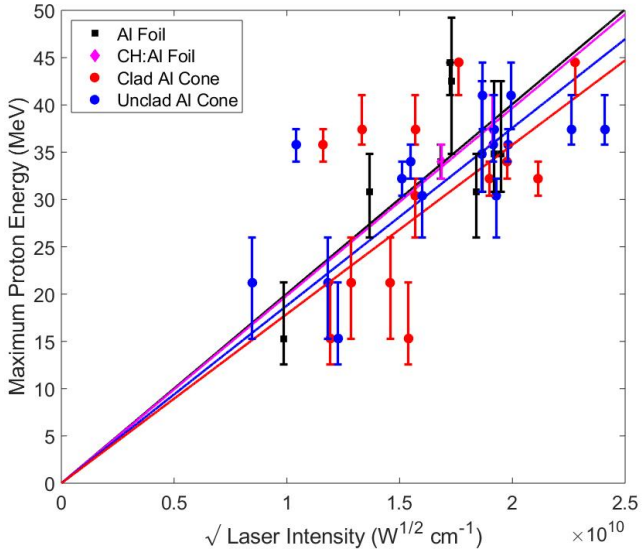

Figure 5.3: Maximum proton energy of 100 μm thick targets. Scaling applied for each target and shown in Table 5.1. Scalings follow the $E_{max} \propto \sqrt{I_L}$ suggested by references in the text.

The maximum proton energy that is achievable through acceleration by the sheath field scales linearly with the hot electron temperature [17,49,50,118–120], which itself scales with the square-root of the incident laser intensity [49, 50, 120]. A detailed review by M. Borghesi *et al* [52] of experimental work using relatively long pulse (300 fs - 1 ps), petawatt-class laser systems, shows how the maximum proton energy follows the expected $\sqrt{I_L\lambda^2}$ scaling. A significant amount of this work was undertaken using the same Vulcan PW system as the work presented in this thesis. For this reason, scalings have been applied to Figure 5.3 that follow this proportionality relationship, with the gradients varying between target categories.

The maximum proton energy is sensitive to the thickness of the target. A. J. Mackinnon *et al* [122] observed protons accelerated to higher energies when the target thickness was reduced. This was attributed to an enhancement in the fast electron density at the rear surface due to the ability of the electrons to reflux in the thinner targets. Although, this is bound by the capacity of the thin targets to maintain structure during the pre-pulse of the laser [52, 119]. For this reason, solely the 100 μm thick targets are presented in Figure 5.3 to remove the dependency on target thickness and aim to isolate the intensity scaling.

Target	**Energy Scaling**
Aluminium Foils	$\mathrm{E_{max}} = (2.00 \pm 0.11) \times 10^{-9}\sqrt{I_\mathrm{L}}$
CH:Al Foils	$\mathrm{E_{max}} = (1.98 \pm 0.31) \times 10^{-9}\sqrt{I_\mathrm{L}}$
Unclad Al Cones	$\mathrm{E_{max}} = (1.88 \pm 0.88) \times 10^{-9}\sqrt{I_\mathrm{L}}$
Clad Al Cones	$\mathrm{E_{max}} = (1.79 \pm 0.16) \times 10^{-9}\sqrt{I_\mathrm{L}}$

Table 5.1: Energy scalings applied to maximum proton energies for 100 μm thick targets in Figure 5.3. Scalings in accordance to references provided in the text. Mean ± Standard Error using OriginPro linear fit software.

Table 5.1 and the corresponding plot in Figure 5.3 shows how the maximum proton energy for each 100 μm thick target category scales with the laser intensity. This follows the $\sqrt{I_L\lambda^2}$ scaling of maximum proton energy (E_{max}) from the literature, however the λ^2 is removed due to all shots being taken using the same 1.053 μm Vulcan PW laser. An increased gradient of E_{max} with $\sqrt{I_L}$ would suggest an improvement in proton acceleration for a given laser intensity. However, when taking into account the standard error of the gradients, a clear improvement in a category of target is not seen. The gradients across all of the categories overlap.

Figure 5.3 shows that the maximum proton energies ranged between $12.7 - 43.1$ MeV and are variable across all four target types. A notable feature is visible where there appears to be a separation between energies of $21.4 - 31.3$ MeV. Initially, one may justify this gap as the energy separation between two consecutive RCF sheets in the stack, however Figure 5.1 shows that an RCF sheet centred on 26.6 MeV is located in-between this range. Nevertheless, the overlapping of the error values suggests that this may not be a significant feature.

If one solely considers the conical structured targets, an interesting feature in the maximum proton energy is found. Figure 5.4 shows how the maximum proton energy varies with the opening half-angle of the cone targets.

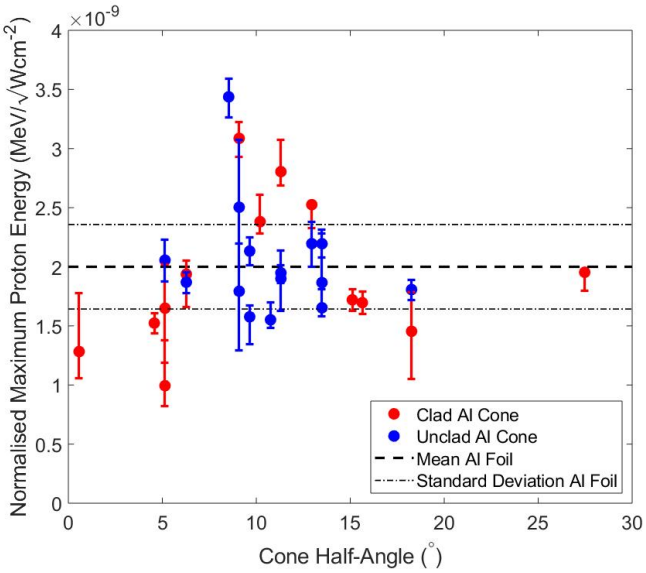

Figure 5.4: Maximum proton energy for conical structured targets. Horizontal, black-dashed lines are the average and standard deviation of the normalised maximum proton energy for 100 μm thick aluminium foils. Values normalised to $\sqrt{I_L}$.

Each normalised value in Figure 5.4 is calculated by dividing the maximum proton energy for the shot by the root laser intensity of that specific shot. The mean and standard deviation lines of the 100 μm thick aluminium foils are calculated by applying the mean and standard deviation calculations to the normalised values.

The majority of cone angles ranged between approximately 5° - 20°, across which a clear deviation between unclad and clad cone performance is not seen. However, while two unclad and four clad cones produce a reduced normalised maximum proton energy compared to the lower standard deviation bound for the aluminium cones, some cones did perform above the higher bound. A further two unclad and four clad cones produced a higher normalised maximum proton energy than the upper standard deviation boundary for the aluminium control foils. These shots are all centred upon $10.2 \pm 1.5°$ (mean±standard deviation), while the six cone targets that perform below the lower standard deviation boundary for the aluminium foils are all outside the $5 - 15°$ range.

The enhancement near the 10° cone angle will be discussed further, along with results from the 2017 campaign in relation to the fast electron population that drives the acceleration. This shall be presented in sections 5.3.2 and 5.5.

5.3 Vulcan Petawatt Campaign 2017

This campaign implemented silicon based targets including the etched clad and unclad cones. A plasma mirror was used and the Vulcan PW beam was incident normal to the target surface. As with the 2015 campaign, a half-stack of RCF was used to capture protons emitted through the TNSA mechanism. This was the same 5 cm×2.5 cm (width×height) stack positioned 5 cm behind the target to capture the lower half of the proton beam.

Gafchromic HDV2 and EBT3 RCF was used to image the proton signal while Mylar and iron filtering graded the energy response of the stack. The same MATLAB code (as in the 2015 campaign) was used to determine the energy response of each layer of RCF in the stack. This code was created by D.C. Carroll at the Central Laser Facility, UK. A respective energy and spatial precision of 0.1 MeV and 0.1 μm were used in the code. Again, the spatial resolution of HDV2 and EBT3 films is 5 μm and 25 μm respectively, therefore using a spatial precision of 0.1 μm in the code ensured that this was not a limiting factor. The energy range covered $0.1-100$ MeV to ensure that the resultant response curves captured the maximum proton energy that was likely to be achieved in the experiment. These parameters are identical to those used in the 2015 campaign analysis.

5.3.1 RCF Stack Design

In the previous campaign (Figure 5.3), two subsets of targets reached slightly different maximum proton energies which were separated by an energy gap of approximately 10 MeV. These subsets were located at approximately $10-20$ MeV and $30-45$ MeV. Although this gap was not caused by an absence of RCF in this range, a slightly different stack design was implemented on the 2017 campaign to increase the energy resolution. This used an increased number of HDV2 and EBT3 RCF as well as replacing aluminium filtering with lower Z Mylar material. This extended the stopping range of the protons to deeper layers of the stack and decreased the energy separation of each RCF sheet.

Layer	Material	Thickness (μm)	Energy (MeV)
1	Aluminium	13	
2	**HDV2**	**109**	**1.2**
3	Mylar	100	
4	**HDV2**	**109**	**4.5**
5	Mylar	200	
6	**HDV2**	**109**	**7.3**
7	Mylar	300	
8	**HDV2**	**109**	**10.0**
9	Mylar	400	
10	**HDV2**	**109**	**12.7**
11	Mylar	500	
12	**HDV2**	**109**	**15.5**
13	Mylar	600	
14	**HDV2**	**109**	**18.3**
15	Mylar	700	
16	**HDV2**	**109**	**21.0**
17	Mylar	800	
18	**HDV2**	**109**	**23.9**
19	Mylar	1200	
20	**HDV2**	**109**	**27.5**
21	Iron	250	
22	**EBT3**	**278**	**30.3**
23	Iron	250	
24	**EBT3**	**278**	**33.2**
25	Iron	750	
26	**EBT3**	**278**	**40.0**
27	Iron	750	
28	**EBT3**	**278**	**46.0**
29	Iron	750	
30	**EBT3**	**278**	**51.5**
31	Iron	1000	
32	**BAS-TR**	**427**	
33	Iron	1000	
34	**BAS-TR**	**427**	
35	Iron	1000	
36	**BAS-TR**	**427**	
37	Iron	1000	

Figure 5.5: RCF stack design implemented on the 2017 Vulcan PW campaign. Active HDV2 and EBT3 type RCF in green. Filtering materials of varying thickness in white. Proton energies for each RCF layer calculated using D. C. Carroll's MATLAB code. Blue BAS-TR image plate in blue used for electron beam investigations which shall be discussed in Chapter 6.

By modifying the stack configuration, the average energy seperation between consecutive RCF sheets was reduced from 5.0 MeV in 2015 to 3.6 MeV for the later campaign. This ensured that the maximum proton energy could be determined to a slightly improved precision. Further reducing the separation would have required even more RCF sheets; increasing the cost and time required to process each stack.

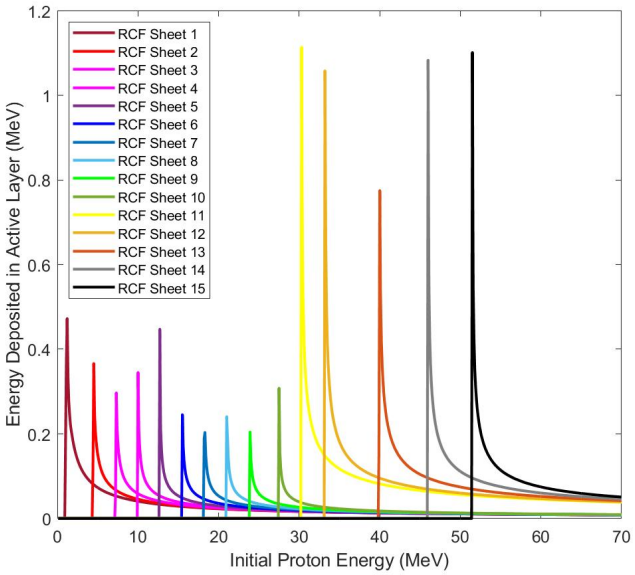

Figure 5.6: RCF response curves for the stack design shown in Figure 5.5. Each peak corresponds to the active layer of an RCF sheet.

The response curves in Figure 5.6 show how the increased number of RCF sheets and use of Mylar filtering reduced the separation between the response peaks.

With the laser pulse incident normal to the target front surface as opposed to the 13° angle in the 2015 campaign, the electrons directed along the laser axis also coincided with the TNSA proton acceleration direction. This meant that the central position of both populations overlapped on the RCF. However, the two populations were easily distinguishable as the electron population was clearly more diffuse across the RCF sheets. This was especially true when viewing the scanned RCF images from the *Nikon Super Cool Scan 9000 ED Transmission Scanner*.

5.3.2 Maximum Proton Energy

The final RCF sheet that displayed a colour change due to the proton beam was recorded and the corresponding response curve energy was used to determine the maximum proton energy for the shot. This is plotted as a function of the square-root of laser intensity, as presented in Figure 5.7.

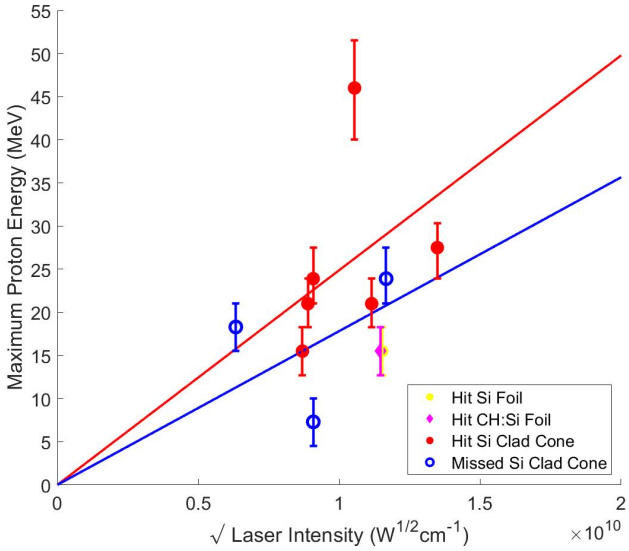

Figure 5.7: Maximum proton energy of 100 μm thick targets. Note the hit Si foil and hit CH:Si foil overlap slightly so may be difficult to resolve. Scaling applied for each target and shown in Table 5.2. Scalings follow the $\propto \sqrt{I_L}$ suggested by references in the text.

Figure 5.7 shows the maximum proton energies for 100 μm thick targets with known pulse lengths (for which the autocorrelator diagnostic recorded data). By solely considering the same thickness of targets, the dependency detailed by A. J. Mackinnon *et al* [122] is removed from the discussion. The wavelength dependency in the $E_{max} \propto \sqrt{I_L \lambda^2}$ scaling [49, 50, 52, 120] is also removed due to all shots being irradiated by the same 1.053 μm Vulcan PW beam.

The location of the laser on the target can now be considered in the 2017 campaign due to the implementation of the front surface imaging diagnostic. This was previously used to categorise the shots as *hit*, *missed* or *clipped* (section 4.3.5). Figure 5.7 compares the hit and missed clad cone targets, as well as a single silicon and CH:Si structured control foil.

The maximum proton energies mainly ranged between $15.5 - 27.5$ MeV, with all but one clad cone performing better than the foil targets. A single hit clad cone shows a significant improvement in performance to 46 MeV while a missed clad cone is shown at 7.3 MeV. The separation between these two targets and the main bulk of the shots is not due to large energy gaps between the RCF sheets; multiple sheets are located within these areas of the stack.

A scaling proportional to $\sqrt{I_L}$ has been applied to the missed and hit clad cone targets, while the Si and CH:Si control foils are the only targets within their categories so a clear trend cannot be drawn.

Target	Energy Scaling
Si Foil	Single Target - No Scaling
CH:Si Foil	Single Target - No Scaling
Hit Clad Si Cones	$E_{max} = (2.49 \pm 0.40) \times 10^{-9}\sqrt{I_L}$
Missed Clad Si Cones	$E_{max} = (1.78 \pm 0.52) \times 10^{-9}\sqrt{I_L}$

Table 5.2: Energy scalings applied to maximum proton energies for 100 μm thick targets in Figure 5.7. Scalings in accordance to references given in the text. Mean ± Standard Error using OriginPro linear fit software.

When comparing the scalings applied to the clad silicon cones, it initially appears that if the laser pulse is successfully located on the cone tip (*hit*), then the performance in terms of maximum proton energy is slightly improved than if the laser is instead incident upon the CH cladding (*missed).* However, the standard error values of the two scalings cause these to both overlap, at which point the improvement cannot be determined.

This again, leads one to consider the maximum proton energy in terms of the target structures. As with the 2015 campaign, the normalised values display an interesting effect when compared to the opening half-angles of the cones.

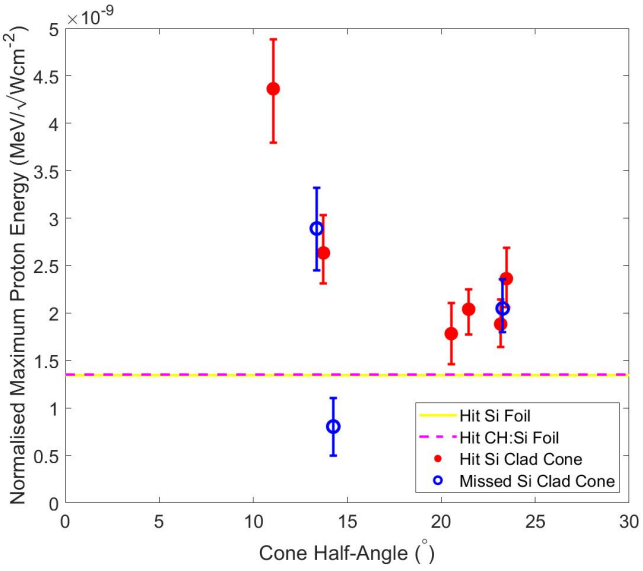

Figure 5.8: Maximum proton energy for conical structured targets. Horizontal, dashed lines are the normalised maximum proton energies for the silicon and CH:Si foils. Values normalised to $\sqrt{I_L}$.

The maximum proton energy for each target has been normalised to the square-root of the laser intensity for that shot, then considered in relationship to the opening half-angle of the cone. For the hit silicon and CH:Si foils where the cone structure does not exist, horizontal lines are presented showing the normalised maximum proton energy for each of these targets. Note that due to the similar intensities and the final RCF sheet with proton signal being the same for both shots, these two lines overlap. The CH:Si target shows a slightly - albeit negligible -

improvement to the homogeneous silicon foil by 7.05×10^{-12} MeV/W$^{0.5}$cm^{-1}.

All clad cone targets, excluding a single missed clad cone at 14.3°, showed an improvement in the maximum proton energy after $\sqrt{I_L}$ normalisation. The single shot that opposes this trend is the same target that produced the lowest maximum proton energy in Figure 5.7.

An interesting trend appears again in the 2017 campaign data where the cone targets with an opening half-angle of approximately 10° produce a significant increase in the normalised maximum proton energy. The lack of data, especially below 10°, makes this artefact somewhat less distinct compared to the 2015 data in Figure 5.4.

5.4 Specular Reflection of Fast Electrons

In order to gain a deeper understanding of this behaviour, we must revisit the physics of the specular reflection model of resistive guiding. This considers the resistively generated magnetic fields as rigid, reflecting walls that follow the cone:cladding interface [11–13]. Electrons are reflected at the position of the magnetic fields so that they are contained within the cone and reduce in divergence after each reflection. To a first approximation, the magnetic fields act as rigid reflectors; however, in reality, electrons will penetrate a depth of the Larmour radius into the field [11].

5.4.1 Reflection Angle

A. P. L. Robinson *et al* [12,13] show that through geometrical arguments, an electron with initial divergence θ_e impinging on a cone wall of angle α_c is specularly reflected with an angle θ_{e1}.

$$\theta_{e1} = 2\alpha_c - \theta_e \tag{5.1}$$

Figure 5.9 shows an example situation of an injected electron reflecting off the walls of a conically structured target. This target structure is simply for demonstration purposes and is based upon those implemented in the 2015 and 2017 Vulcan PW campaigns for consistency.

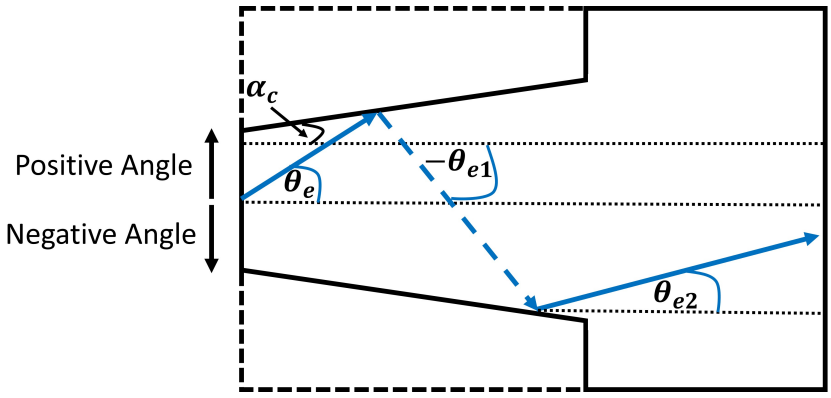

Figure 5.9: Schematic of specular reflection. Electron injected at the centre of cone tip with initial angle θ_e. Cone angle α_c. Electron specularly reflected off first wall with angle θ_{e1} and θ_{e2} for second reflection. Positive angles (solid lines) directed upwards, negative angles (dashed line) directed downwards.

Cones of angle $\alpha_c = 5°, 10°, 15°$ and $20°$ have been considered with initial electron angles in the range of $\theta_e = 10° - 70°$ in $10°$ increments. The angle that the electron then travels after a single bounce from a cone wall has been calculated using Equation 5.1 and is presented in Figure 5.10. The dashed vertical line is used for reference of a $30°$ half-angle divergence that is expected for the nominal Vulcan PW laser intensity of 10^{21} Wcm^{-2} [5]. The point of intersection of this line with the diagonal lines shows the angle at which an electron will bounce from the cone wall after a single bounce. Each diagonal line represents one of the $5°$, $10°$, $15°$ or $20°$ cones under consideration. Solid diagonal lines show when the electron bounces towards the opposing cone wall.

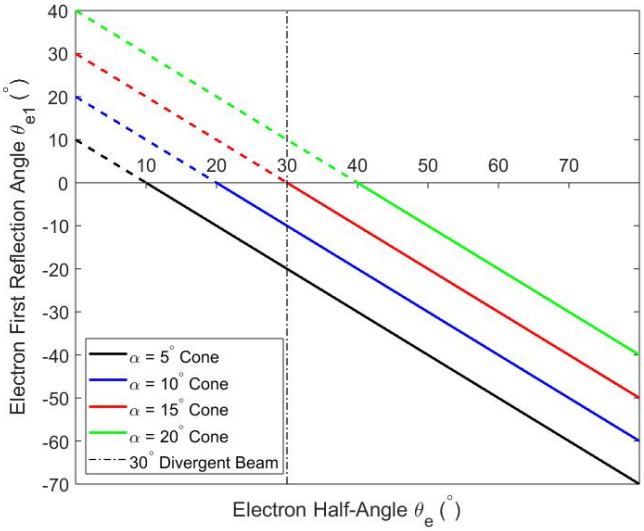

Figure 5.10: Angle an electron travels θ_{e1} after specularly reflecting with a cone wall of angle α_c. Electron is initially travelling with angle θ_e. Solid lines show when the electron is reflected in the opposing sign direction (i.e. towards the opposite cone wall). Dashed diagonal lines show when the electron bounces towards the same cone wall. Vertical black line references a $30°$ half-divergence electron expected for the nominal Vulcan PW laser intensity [5].

First, consider the $30°$ input angle case represented by the vertical dashed line. If one tracks this line vertically to where it intersects the diagonal lines, we see the angle that the electron will bounce off the first cone wall. For instance, in the case of the $20°$ cone represented by the green diagonal line, the vertical line intersects this at $\theta_{e1} = 10°$. This angle is positive and therefore suggests that the electron still travels towards the same cone wall, but at a shallower angle.

The point of intersection between the vertical dashed line and the $15°$ diagonal line shows that the electron bounces off the first cone wall, leaving with an angle of $\theta_{e1} = 0°$. In this case, the angular divergence has been reduced such that the electron is directed along the target normal.

Considering the case of the $10°$ cone represented by the blue diagonal line, the intersection location is at $\theta_{e1} = -10°$. This means that the electron will bounce off the first cone wall and leave with an angle of $10°$, but now be directed towards the opposing cone wall. For instance, if the electron was initially directed towards the top cone wall in Figure 5.9 with an angle of $30°$,

it will bounce towards the lower wall at 10° in magnitude. In this case, the new propagation angle of the electron is same as that of the cone wall ($\theta_{e1} = \alpha_c = 10°$). The electron now travels parallel to the opposing cone wall and cannot reach it to undergo a second bounce.

Finally, in the case of the 5° cone, the electron leaves with an angle of $\theta_{e1} = -20°$. Again, the negative value means the electron is directed towards the opposing cone wall, however in this case at a sharper angle than the cone. Therefore, considering an infinity long cone, the electron is able to reach the opposing cone wall and undergo a second bounce; something which the other cones could not achieve.

The interaction of this second bounce can be considered using Equation 5.1. The electron is now directed with a new angle of −20° towards the cone wall of angle −5°; from which it will deflect, leaving with a final angle of 10°. Therefore, after two bounces, the 5° cone matches the performance of the 10° target, both reducing the initial 30° half-angle of the electron to 10° in magnitude.

Figure 5.11 shows a visual representation of the electron propagation in each of the four α_c cases. The angles after the first and second bounce (when possible) have been extracted and presented in Table 5.3.

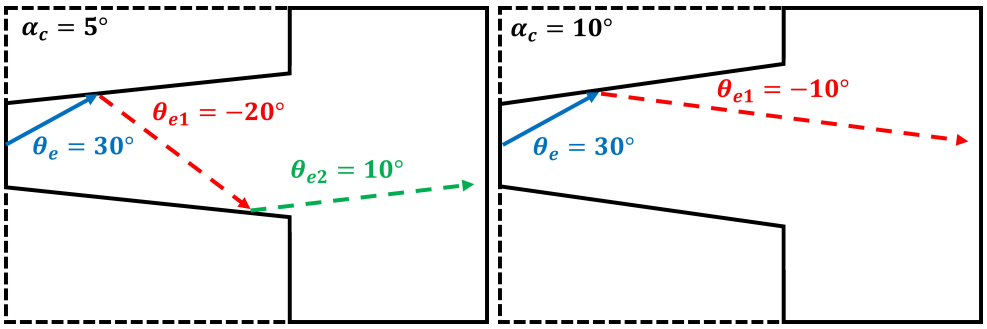

(a) Cone angle $\alpha_c = 5°$. After two bounces, electron half-angle reduced to $\theta_{e2} = 10°$.

(b) Cone angle $\alpha_c = 10°$. After one bounce, electron half-angle reduced to $\theta_{e1} = -10°$.

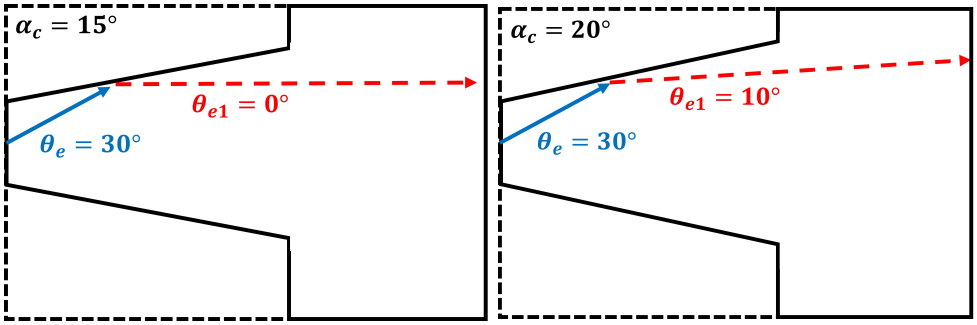

(c) Cone angle $\alpha_c = 15°$. After one bounce, electron half-angle reduced to $\theta_{e1} = 0°$.

(d) Cone angle $\alpha_c = 20°$. After one bounce, electron half-angle reduced to $\theta_{e1} = 10°$.

Figure 5.11: Schematic showing electron propagation through cones of varying opening half-angles. Electron injected with divergence half-angle of $\theta_e = 30°$. Cone opening half-angles α_c of (a) 5° (b) 10° (c) 15° (d) 20°. Electrons in cones of $\theta_c \geq 10°$ can only undergo a single bounce as the angle θ_{e1} after the reflection forbids the electron reaching the opposite cone wall.

Cone Angle α_c (°)	**1st Bounce Angle θ_{e1} (°)**	**2nd Bounce Angle θ_{e2} (°)**
5	-20	10
10	-10	Doesn't hit wall
15	0	Doesn't hit wall
20	10	Doesn't hit wall

Table 5.3: Specular reflection of an electron with divergence half-angle $\theta_e = 30°$. Reflection angles calculated using Equation 5.1. Positive angles denote a reflection towards the same cone wall as initial directed. Negative angles denote reflections towards the opposing wall.

Figure 5.11 and Table 5.3 show the propagation and corresponding angles that an initial 30° electron travels within the four cones. It is clear that only the 5° cone can cause the electron to undergo two bounces, after which the angular divergence is reduced to 10°. The 10° and 20° cones also reduce the electron angle to 10° in magnitude, however they achieve this after a single bounce. The 15° cone reduces the electron angle to 0° after one bounce, this is the best performance when considering a single reflection.

Therefore, after a single bounce, the most effective cone is the 15° case, jointly followed by the 20° and 10° cones. The 5° cone performs the least effective after a single bounce, however this is the only cone that directs the bounced electron towards the opposite cone wall to undergo a second bounce. After which, the electron then leaves at 10° and matches the performance of the 10° and 20° cones.

In an infinitely long, theoretical cone of 5° opening angle, the electron will always be able to reach the opposing cone wall and undergo the second bounce. As such, the performance will match the 10° and 20° cones. However, this leads one to consider the realistic structured targets implemented on the 2015 and 2017 experimental campaigns which consisted of 50 μm long cones. This finite length adds a constraint to this model, where the electron must reach the opposing cone wall within 50 μm, otherwise it leaves the cone and a second reflection is forbidden.

MATLAB code has been developed to track a single electron of 30° half-angle divergence as it propagates through the 50 μm depth of a 5° cone. The maximum tip width that allows a secondary bounce to take place has been calculated. If the cone tip exceeds this value, the electron has to travel too far along the depth of the cone until it interacts with the first wall. At this location, there isn't enough of the 50 μm cone depth remaining for the electron to then reflect and reach the opposite cone wall to undergo a second reflection.

The investigated tip width has been iterated between $1-20$ μm in 0.2 μm increments. These limits were chosen as a preliminary investigation to determine if they contained the cut-off width forbidding a secondary reflection.

The position of the first and second bounces have been calculated using trigonometry and Equation 5.1.

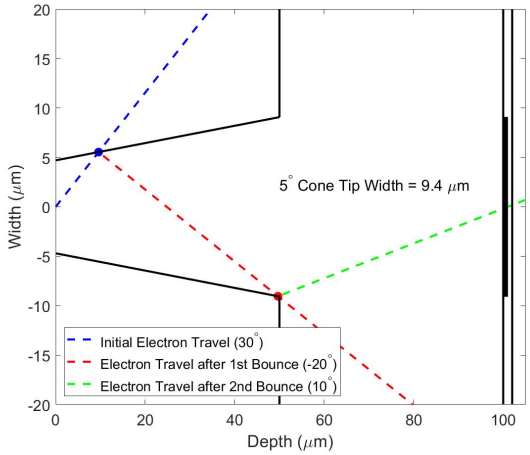

Figure 5.12: Tracking of a $\theta_e = 30°$ (half-angle) divergent electron along the 50 μm cone depth. Cone angle $\alpha_c = 5°$. Blue $(9.6, 5.5)$ μm and red $(49.7, -9.0)$ μm points represent the position of the first and second bounces. Electron injected at the cone centre and reflects off the first wall with an angle of $\theta_{e1} = -20°$. A further reflection is then allowed with an angle of $\theta_{e2} = 10°$.

Figure 5.12 shows that for a 5° cone with a 9.4 μm wide tip, the electron is able to undertake a second bounce within the 50 μm depth. After this, the electron travels with a 10° angle (green-line) such that the divergence has been reduced to the same level as for a single bounce in a 10° and 20° cones (see Table 5.3).

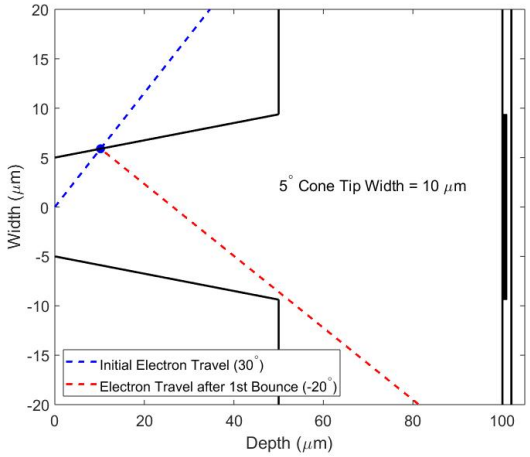

Figure 5.13: Tracking of a $\theta_e = 30°$ (half-angle) divergent electron along the 50 μm cone depth. Cone angle $\alpha_c = 5°$. Blue point $(10.2, 5.9)$ μm represents the position of the first bounce. Electron injected at the cone centre and specularly reflects off the first wall with an angle of $\theta_{e1} = -20°$. The cone is too wide for the electron to reach the lower cone wall to undergo a secondary bounce within the 50 μm depth.

When the cone tip width exceeds the 9.4 μm constraint, the electron undergoes the first bounce but has to travel too far along the length of the cone to reach this point. This then means that there isn't enough of the 50 μm depth remaining for the electron to reach the opposing cone wall. As shown in Figure 5.13, the electron travels further than the 50 μm depth and doesn't undergo a second bounce. In this case, only a single reflection is possible which reduces the propagation angle to $-20°$. This is 10° more divergent (in magnitude) than the cases of a single bounce in both the 10° and 20° cones (see Table 5.3).

In addition to the angle of the cone, it has been shown that the width of the tip is an important factor in determining the performance of the cones in reducing the electron divergence through specular reflection. This leads one to re-consider the structure of aluminium and silicon cones on the 2015 and 2017 experimental campaigns. In sections 4.2.1 and 4.3.1, the tip widths of the cones were evaluated. Table 5.4 now shows a compilation of these values for ease of reference.

Campaign	**Target**	**<Tip Width> ± σ**	**<Total Tip Width>**
2015	Unclad Al Cone	33.7 ± 13.5	
2015	Clad Al Cone	37.3 ± 11.8	
			35.2
2017	Unclad Si Cone	40.45 ± 4.78	
2017	Clad Si Cone	29.53 ± 9.58	

Table 5.4: Mean tip widths of the aluminium and silicon cones used on the 2015 and 2017 Vulcan PW campaigns. Symbols < > and σ denote the mean and standard deviation of values respectively. <Total Tip Width> calculated by averaging the mean tip widths for all the cone targets.

As presented in Table 5.4, the tip widths of all the conical structured targets on both campaigns were significantly larger than the 9.4 μm boundary determined in Figure 5.12. Therefore, in all the experiment cones, an electron travelling from the centre of the tip with a 30° divergence half-angle would only be able to undergo a single specular reflection; thereby reducing the divergence to 20° in magnitude (considering a 5° cone).

These specular reflection and trigonometric arguments suggest that the cones used on the experiment are too wide to allow an electron in the 5° cone to undergo two bounces. Therefore, this cone cannot match the performance of the sharper angled cones that have been considered. This provides a possible explanation for the 10° cone performing better than the 5° cone in Figures 5.4 and 5.8. However, this does not account for the visibly improved performance (in maximum proton energy) of the 10° cone compared to the sharper angled cones ($\alpha_c = 15°$ and 20°). This shall now be discussed in the following section.

5.4.2 Ability to undergo Specular Reflection

If one considers Equation 5.1, the angle that an electron travels after a single bounce θ_{e1} is related to it's initial propagation angle θ_e and the angle of the cone α_c.

If specular reflection takes place so that a further bounce is possible, the reflection angle must be of opposing sign to the original injection angle. This means that the electron is directed towards the opposite cone wall to bounce a second time.

$$\theta_{e1} = 2\alpha_c - \theta_e < 0 \tag{5.2}$$

Therefore, to satisfy this condition, only electrons with initial angle θ_e greater than twice the cone angle α_c will be specularly reflected off the cone wall.

$$\theta_e > 2\alpha_c \tag{5.3}$$

Therefore, as the cone angle α_c is increased, only the most divergent electrons can satisfy this condition and be specularly reflected. This puts an upper angular constraint on the cones performance.

In addition to this, one may also consider the distance which an electron must travel until it reaches the cone wall. In Table 5.4, the average tip width across both experiments was approximately 35 μm. Again, using trigonometric arguments, the distance that the electron travels to the position of the first specular reflection can be calculated. This has been undertaken for an initial electron half-angle of $\theta_e = 30°$ and for cone angles $\alpha_c = 5°$,10°,15° and 20°. The tip width has been varied between $10 - 40$ μm for the results presented in Figure 5.14.

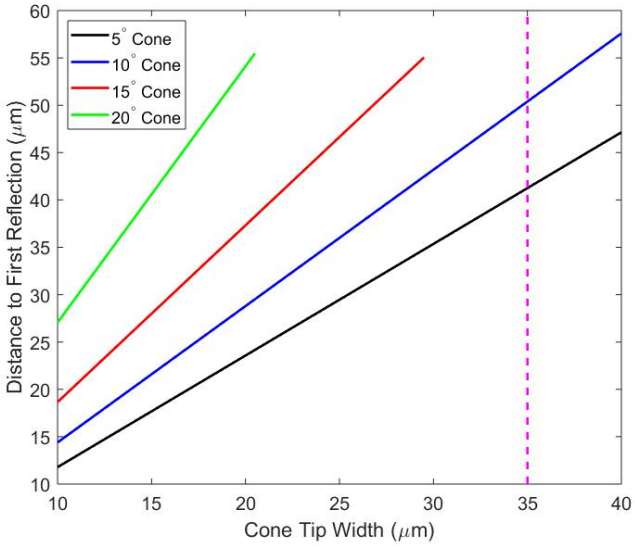

Figure 5.14: Distance a 30° divergent (half-angle) electron travels until reaching the 1st cone wall. Purple line is a marker for the approximate average of the tip widths across both experiments. Electron in the 15° and 20° cones cannot reach the cone wall in the 50 μm depth.

For the 5° and 10° cones with 35 μm tip widths, the electron has to travel significant distances of approximately 41.3 μm and 50.4 μm respectively before reaching the cone wall to undergo the first bounce. However in the 15° and 20° cones with tip widths of 35 μm, the electron has already travelled further than the 50 μm cone depth and exited the cone. Therefore the electron is forbidden from undergoing even a single bounce. This can be seen by the green and red lines in Figure 5.14 not reaching the 35 μm tip width reference line. So for relatively large cone widths ($\geq$ 30 μm and $\geq$ 20 μm for the 15° and 20° cones respectively), the electron cannot reach the first cone wall and experience further angular reduction through specular reflection. This is in addition to the previous reasoning whereby, even if the electron could reach the wall, a smaller proportion of the population can satisfy the criterion in Equation 5.3.

5.5 Hybrid Simulations of the Fast Electron Density

5.5.1 Plasma Expansion Model

An increase in the normalised maximum proton energy for conical targets with an opening half-angle of approximately 10° has been recorded in both the 2015 and 2017 campaigns. This suggests that an underlying effect of the target geometry may be a contributing factor to the performance of conically structured targets. Geometrical considerations have been discussed as to why this performance may be improved for the 10° cone. This shall be further investigated in the following sections by relating the proton acceleration to the fast electron population and presenting hybrid simulation results. We begin this work by considering how an improvement in fast electron confinement would affect the acceleration of protons to higher energies.

First, consider the P. Mora [17] model of one-dimensional plasma expansion into vacuum.

The maximum energy of the proton spectrum accelerated by the sheath field is given by Equation 5.4:-

$$E_{max} = 2E_0 \left[\ln\left(2\tau\right)\right]^2 \tag{5.4}$$

where $E_0 = Zk_BT_e$ and $\tau = \omega_{pi}t/\sqrt{2\exp\left(1\right)}$

However, the dependency of τ on the ion plasma frequency ω_{pi} can also be considered assuming quasi-neutrality:-

$$\omega_{pi} = \sqrt{\frac{n_{e0}Z^2e^2}{m_i\epsilon_0}} \tag{5.5}$$

Substituting the parameters of E_0, τ and ω_{pi} into Equation 5.4 gives:-

$$E_{max} = 2Zk_BT_e \left[\ln\sqrt{\frac{2Z^2e^2n_{e0}t}{m_i\epsilon_0}} - \frac{1}{2}\right]^2 \tag{5.6}$$

Considering the main variables:

$$E_{max} \propto k_BT_e \left[\ln\left(\sqrt{n_{e0}}\right)\right]^2 \tag{5.7}$$

Solely considering the dependency on the electron density, which may be in the relativistic regime [17] such that $n_{e0} = n_f$.

$$E_{max} \propto \left[\ln\left(\sqrt{n_f}\right)\right]^2 \tag{5.8}$$

where n_f is the fast electron density. Using the logarithmic identity $\ln(\mathrm{a}^\mathrm{b}) = \mathrm{b}\ln(\mathrm{a})$, this becomes:

$$E_{max} \propto \left[\frac{1}{2}\ln\left(n_f\right)\right]^2 \tag{5.9}$$

Removing the factor of $\frac{1}{2}$ to consider only the proportionality, we obtain the final dependency of the maximum proton energy (E_{max}) on the fast electron density (n_f):

$$E_{max} \propto \left[\ln\left(n_f\right)\right]^2 \tag{5.10}$$

This suggests that an increase in the fast electron density at the rear surface will result in an improved performance of accelerating protons to higher energies. Hybrid simulations shall now be presented in which varying cone angles are investigated along with their effect on the fast electron density.

5.5.2 Simulation Environment

Three-dimensional hybrid simulations have been implemented using ZEPHYROS to investigate how the fast electron density varies using different conical structures. A review of the code is presented in section 3.9.

Identical simulation parameters were used as for Simulation 1 in section 4.5, however additional cones were implemented with opening angles of 10°, 15° and 20°. The results for the 5° cone in section 4.5 are used in this work. For completeness and ease of reference, the main simulation parameters shall be reiterated here.

The simulation grid was generated in the x×y×z dimensions with $103 \times 200 \times 200$ cells. Each cell was 1 μm^3 in volume. The laser pulse was directed along the x dimension where the front and rear boundaries were reflective to allow electron refluxing. The side boundaries were open. A clad silicon cone was investigated following the general target geometries used on the 2017 campaign. This was a 50 μm long cone clad in CH plastic, followed by a further 50 μm of silicon foil. A 1 μm thick titanium dot was located at the rear surface, which was tamped by a further 1 μm of CH. The tip widths of the cones were set to 15 μm for consistency with the simulations used for investigating the additional laser beam system in the previous chapter.

In accordance with the previous specular reflection arguments where the electron is injected in the middle of the cone tip, a single laser beam was centred on the silicon cone. Nominal Vulcan intensity and pulse length parameters were used, specifically 1×10^{21} Wcm^{-2} and 1 ps. The spatial FWHM of the beam was set to 6.1 μm to replicate the size of the focal spot in the 2017 experiment. Recall that ZEPHYROS doesn't explicitly model the laser pulse but instead creates a fast electron distribution from the designated laser parameters. For this, 30% energy conversion to fast electrons was selected and a Gaussian angular distribution of 60° FWHM as suggested by [5]. This is consistent with the 30° half-angle used in the previous specular reflection work in section 5.4.

5.5.3 Fast Electron Number Density

The simulations were run for 1 ps and analysed at this time. This corresponds to the end of the laser pulse length. For analysis purposes, a cross-section of the target was imaged at 100 μm where the titanium dot was located. This is in the same way to the work presented earlier in section 4.5.2. At this plane, the average fast electron density was calculated within a circular region corresponding to the size of the cone base. This was calculated for simulations of 5°, 10°, 15° and 20° silicon cones. The remaining target, laser and simulation conditions were kept identical across the simulations. The only varying parameter was the cone angle, which then naturally changed the base width and analysis area between simulations. To minimise this effect, the average fast electron density was calculated instead of the maximum value, which is more sensitive to filamentation and size of the analysis area.

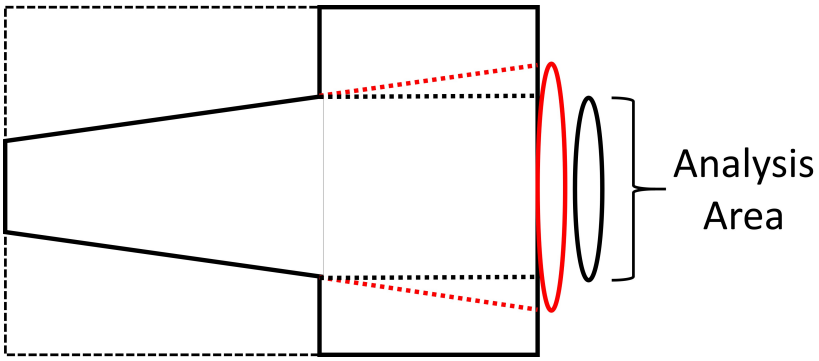

Figure 5.15: Example of a conically structured target and the tracking of the cone wall. Inner black circle is the width of the cone base and all quantitative analysis in ZEPHYROS is within this area. Larger red circle projects the cone wall onto 100 μm depth.

A larger circle was applied to the images to reference the area that the cone would subtend if it was 100 μm long. All quantitative analysis was within the smaller circular area; the larger circle is for visual reference for tracking the cone if it was 100 μm long.

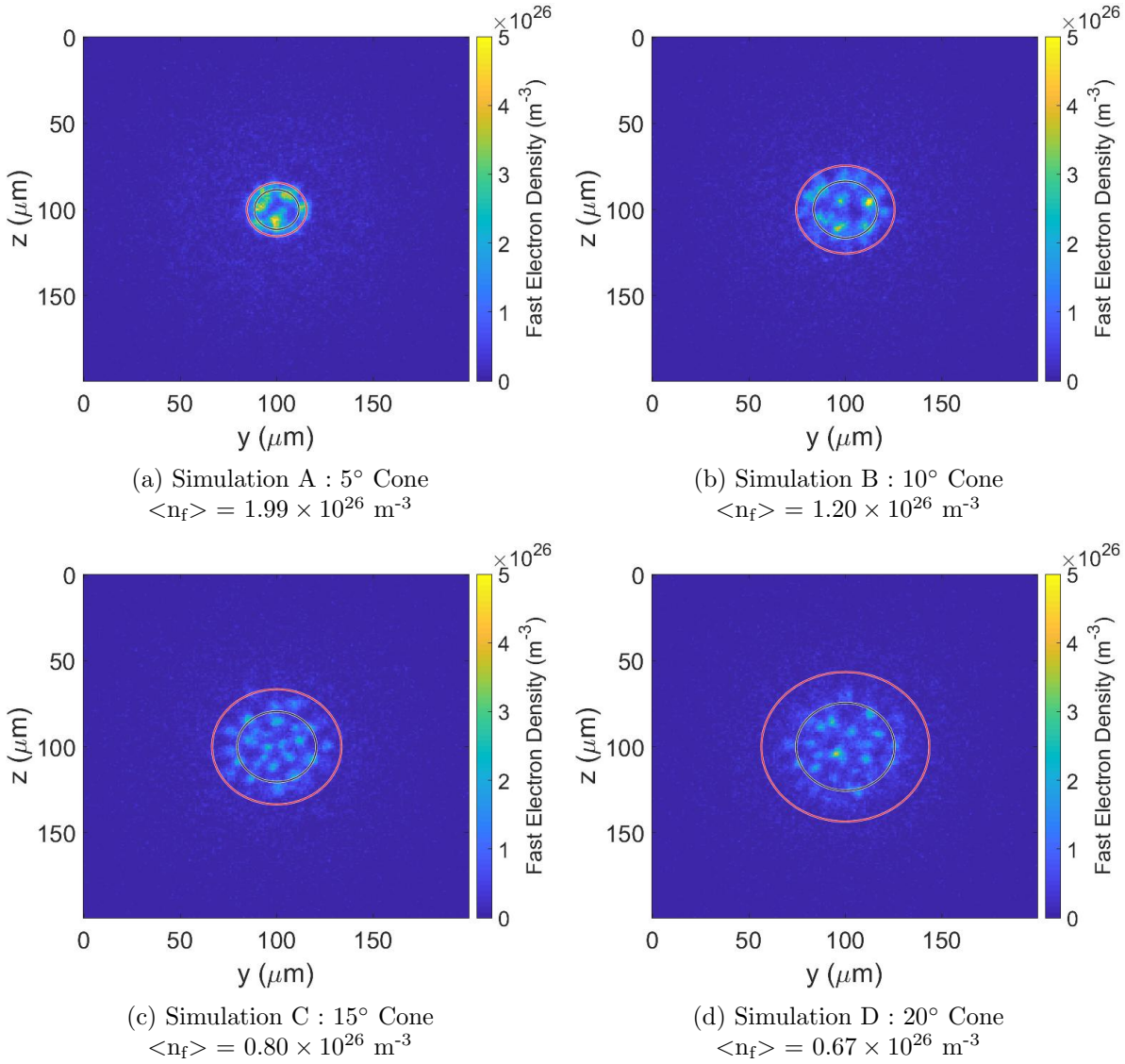

(a) Simulation A : 5° Cone
$<n_f> = 1.99 \times 10^{26}$ m^{-3}

(b) Simulation B : 10° Cone
$<n_f> = 1.20 \times 10^{26}$ m^{-3}

(c) Simulation C : 15° Cone
$<n_f> = 0.80 \times 10^{26}$ m^{-3}

(d) Simulation D : 20° Cone
$<n_f> = 0.67 \times 10^{26}$ m^{-3}

Figure 5.16: ZEPHYROS simulations of fast electron density. $<n_f>$ is the mean fast electron density within the inner black circular area representing the cone base cross-section. Outer red circle represents a projection of the cone base if the cone was 100 μm long. Cross-sectional view at 100 μm deep. (a) Simulation A: Single beam centred on 5° silicon cone (b) Simulation B: Single beam centred on 10° silicon cone (c) Simulation C: Single beam centred on 15° silicon cone (d) Simulation D: Single beam centred on 20° silicon cone.

The cross-section of the fast electron number density at 100 μm depth is presented in Figure 5.16. All values are calculated within the inner black circles which represent the size of the cone base. The outer red circles represent a projection of the cone walls if the cones were 100 μm long instead of 50 μm. Figure 5.15 shows a schematic to aid visualisation of these zones. Simulations A through D are for cone half-angles (α_c) increasing in 5° increments. The corresponding averaged values are displayed below each figure. These are calculated through addition of the fast electron density at each cell within the circular area and normalising this to the number of cells.

Filamentation is clear in all simulations, with an increasing number of filaments as the simulations increase in cone angle between Figure 5.16a to 5.16d. In all cases, the filaments appear to be mainly confined within the larger circles that track the cone wall to 100 μm depth. This suggests that the electrons track the magnetic field along the cone wall and are confined within this area.

The average fast electron density within the inner (black) circular regions has been extracted for each simulation and plotted against the cone angle. This is presented in Figure 5.17.

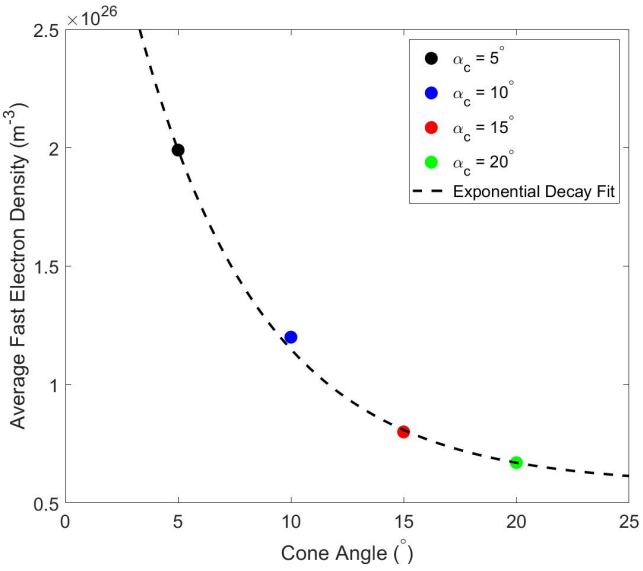

Figure 5.17: $< n_f >$ for each cone angle simulated using ZEPHYROS in Figure 5.16. Exponential decay fit using OriginPro *ExpDecay1* fitting software. Calculated fit presented in Equation 5.11.

$$< n_f >= 0.576 \times 10^{26} + 1.414 \times 10^{26} \exp\left(\frac{-(\alpha_c - 5)}{5.542}\right) \tag{5.11}$$

Figure 5.17 presents the average fast electron densities for each cone presented in Figure 5.16. The Gaussian fit shown in Equation 5.11 has been applied showing the exponential decay of $< n_f >$ with increasing cone angle α_c. $< n_f >$ and α_c in units of m^{-3} and degrees respectively.

As the cone angle is increased between 5° and 20°, the fast electron density at 100 μm is reduced by over 50% between 1.99×10^{26} m^{-3} to 0.80×10^{26} m^{-3}.

Recall the experimental results from both campaigns where the maximum proton energy was enhanced for cone angles of approximately 10°. The evaluation of the P. Mora model in section

5.5.1 showed that the maximum proton energy has a component that scales positively with the fast electron density. Specifically, $E_{max} \propto [\ln(n_f)]^2$ as shown in Equation 5.10. Therefore, an increased fast electron density should result in an increased maximum proton energy.

First consider the ZEPHYROS results for cone angles of $\alpha_c \geq 10°$. The exponential decay of the fast electron number density shows that as the cone angle is increased, the average number of fast electrons with the analysis area at the rear surface decreases. The P. Mora model scaling of $E_{max} \propto [\ln(n_f)]^2$ suggests that this decrease in n_f would cause the maximum proton energy to also decrease for sharper cone angles. This is reported in the experimental results in both the 2015 and 2017 campaigns in Figures 5.4 and 5.8 respectively. This further supports the suggestion that as the cone angle is increased, a smaller proportion of the fast electron population can satisfy the condition of specular reflection ($\theta_e \geq 2\alpha_c$). Only the most divergent electrons (large θ_e) can satisfy this condition. Therefore, in the case of the $\alpha_c = 10°$, 15° and 20° cones, more of the electron population can satisfy this condition in the 10° cone and specularly reflect. In this case, the electron collimation effect is enhanced and the number density at the rear surface increased. This enhances the charge density and sheath field at the rear surface, resulting in the protons being accelerated to greater energies.

Now considering the case of $\alpha_c < 10°$ - i.e. the 5° cone in the simulations - the fast electron density is at a maximum. This would suggest that the highest maximum proton energy would be found at this cone angle, however this is not reported in the 2015 experimental results (Figure 5.4). Instead, the 5° cones result in a reduced maximum proton energy compared to the 10° cones. However, the uncertainty and limitations in the 2015 measurements may be a contributing factor to this. The defocus in the Vulcan PW beam, which was present but unknown at the time of the experiment means that the laser conditions are not quantifiable. The lack of a plasma mirror would inevitably mean a low density plasma would be present at the front surface due to the low intensity pre-pulse of the laser. This will change the electron generation mechanism, to which the highest energy electrons are most sensitive. Finally, the lack of ability to determine the laser position upon the cone targets means that it cannot be determined if the laser pulse hit the cone tips or the surrounding cladding or cone wall in the case of the unclad cones. These uncertainties in the experimental conditions may offer some explanation as to why the expected improvement in performance of the 5° cone are not seen in the experimental measurements.

A lack of shots at cone angles of $\alpha_c < 10°$ in the 2017 campaign (Figure 5.8) also means that the performance of 5° cones cannot be investigated in this experiment. The ability to determine the laser interaction site using the front surface imaging (FSI) system in addition to the autocorrelator not triggering for a number of shots means that the amount of usable shots for Figure 5.8 is reduced. However, it must be stated that the uncertainty in the presented shots from this experiment is improved due to the implementation of the FSI, plasma mirror, highly characterised silicon etched targets and the analysis of the defocus of the Vulcan PW beam. In this experiment, the laser-target conditions are less uncertain.

5.6 Preliminary Conclusion

Radiochromic film (RCF) half-stacks have been implemented on both the 2015 and 2017 Vulcan PW campaigns. In both cases, the half-stacks were located 5 cm from the target rear surface to collect the lower half of the proton beam emitted normal to the target. Response curve analysis for each stack design resulted in the maximum proton energy being determined for each shot. These results have been compared to the laser intensity and cone angle parameters.

In both campaigns, the maximum proton energy is seen to approximately scale with the square-root of the laser intensity ($E_{max} \propto \sqrt{(I_L)}$). This trend follows that presented by M. Borghesi *et al* [52]. On close inspection, the maximum proton energy achievable through acceleration by the rear surface sheath field scales with the hot electron temperature [17,49,50,118–120]; which itself scales with the square-root of the laser intensity [49, 50, 120].

Considering the conical targets on both campaigns, a clear increase in the maximum proton energy is found for targets with an opening cone angle of approximately $\alpha_c = 10°$. These results are presented in Figures 5.4 and 5.8. Geometric arguments and the P. Mora model [17] have been invoked to provide a possible explanation behind this enhancement in proton cut-off energy. Three-dimensional hybrid simulations using ZEPHYROS have also been implemented and support this work for cones angles $\geq 10°$.

Considering the geometric arguments, specular reflection of an electron from a cone wall of angle α_c causes an incident electron with angle θ_e to be reflected with an angle $\theta_{e1} = 2\alpha_c - \theta_e$. This has been considered in section 5.4.1 with cone angles of $\alpha_c = 5°, 10°, 15°, 20°$. For an electron with a divergence half-angle of $\theta_e = 30°$ undertaking a single reflection on a cone wall, the 15° cone fully collimates the electron to $\theta_{e1} = 0°$. This performance is then jointly followed by the 10° and 20° cones reducing the angle to 10° in magnitude. The 5° cone has the least effect and reduces the electron angle to 20° in magnitude. However, the latter cone can match the performance of the 10° and 20° cones if a second bounce is considered with the opposite cone wall. If this takes place, the angle of the reflected electron is further reduced to 10° in magnitude. A breakdown of these results has been presented in Table 5.3.

The effectiveness of each cone at specularly reflecting an electron has therefore been determined, however this then leads one to consider if the reflections are actually possible using the targets implemented on the experimental campaigns. Section 5.4.1 presents results using MATLAB code that track a single 30° electron through the depth of a 50 μm cone. The cone tip width has been varied to determine at what size the electron is unable to undergo two reflections. At this tip width, the electron has to travel too far along the depth of the cone before reaching the first cone wall, this then means that there is not enough of the 50 μm cone depth left for the electron to reach the opposite wall for a second reflection. For a 5° cone, this cut-off width was determined as 9.4 μm. Therefore, when considering specular reflection, any 5° cone with a larger tip width will only be able to reduce the electron angle to 20° in magnitude. At which stage the remaining cone angles show a better performance after a single reflection.

Considering the cones implemented on both campaigns, the average tip width was approximately 35 μm; significantly larger than the 9.4 μm cut-off width. Therefore, it is unlikely that a secondary bounce would be possible in the experiment cones, so the 5° cone would not aid in significantly reducing the electron divergence. This leaves the 10°, 15° and 20° cones to be

considered.

Again, regarding specular reflection, only electrons with initial angle $\theta_e > 2\alpha_c$ will undergo reflection. For the largest two cone angles, only the most divergent electrons will meet this requirement and have their angle reduced after interacting with the cone wall [12]. Therefore, a smaller proportion of the injected electron population will meet this requirement.

Considering the size of the cone tips and an electron injected with $\theta_e = 30°$, Figure 5.14 shows that if the tip width is greater than approximately 30 μm and 20 μm for the 15° and 20° cones respectively, the electron will not reach the cone wall before it has travelled along the 50 μm depth and exited the cone. Therefore in this case, specular reflection of the electron would not be possible. Again with the average tip width implemented on the campaigns being approximately 35 μm, a large proportion of the cones will be too wide for specular reflection to even take place.

Therefore, two possible factors have been proposed as to why the experimental results show cones with angle greater than approximately 10° produce a reduction in maximum proton energy. With these cones, less of the electron population are able to satisfy the requirement for specular reflection of $\theta_e > 2\alpha_c$, as well as the majority of the experimental cones being too wide to allow a $\theta_e = 30°$ (half-angle) divergent electron to even reach the cone wall in the required 50 μm depth. A mechanism behind the lower angle boundary of the cones has also been suggested whereby the 5° cone will only match the performance of the higher angled cones - specifically the 10° and 20° - if two electron bounces are possible. The cones implemented on the experiments are too wide to allow this. Therefore, the 5° cone cannot match the performance of the sharper cone angles.

Hybrid simulations have been implemented to further investigate the suggested contributing factors to the improvement in proton cut-off energy for cones with $\alpha_c \sim 10°$ angles. The P. Mora model [17] of plasma expansion has been considered in terms of the fast electron density, and in doing so, Equation 5.10 shows that the maximum proton energy E_{max} has a component depending on the fast electron density n_f in the form of $[\ln(n_f)]^2$. An improvement in confinement within the cone targets would suggest an increase in the fast electron density at the rear surface, leading to an enhancement in proton acceleration.

With this in mind, ZEPHYROS was used to simulate a single laser beam incident on clad silicon cone targets with angles ranging from $\alpha_c = 5°$ to 20° in 5° increments. The average fast electron density was calculated within a circular area equivalent to the base of the cone at a cross-sectional depth of 100 μm. Figures 5.16 and 5.17 show that as the cone angle is increased, the average fast electron density at the 100 μm depth decreases exponentially. This follows the exponential decay fit presented in Equation 5.11.

The hybrid simulation results support the proposal of reduced specular reflection in the 15° and 20° cones (compared to 10°), resulting in the divergence of the fast electron beam being mitigated less effectively. This then results in a more diffuse fast electron beam at the 100 μm analysis depth. However, consideration of the 5° cone being too wide for a second reflection does not appear to be emulated in the ZEPHYROS results. The specular reflection arguments imply that the electron cannot undergo a second reflection in such a wide cone, and thus the angle of propagation is not reduced to that achieved in a single bounce in the 10° cone. One

would expected this to be emulated in the ZEPHYROS simulations by presenting a reduced fast electron density for the 5° cone, however this is not the case. Further investigation of this result is required. The first proposal is to increase the size of the cone tip such that the system is moved further away from the maximum 9.4 μm width determined at which a secondary reflection is possible.

The disparity between the hybrid simulation results and the specular reflection arguments leads one to examine the effectiveness of considering the cone walls as rigid, specular reflectors [11–13]. Instead of the electrons reflecting at the exact position of the cone wall, they will in fact travel a distance equivalent to the Larmor radius into the magnetic field before being reflected. This will slightly modify the location of the reflection.

Regarding the specular reflection of a single electron presented in section 5.4. Two main assumptions are made: (1) the electron is injected with a divergence half-angle of $\theta_e = 30°$ and (2) the electron is injected at the centre of the cone tip. Regarding the first assumption, in reality the electrons are injected with a range of angles, meaning some will exceed the required $\theta_e > 2\alpha_c$ for specular reflection while others will be significantly less than this. For the ZEPHYROS simulations, a Gaussian angular distribution with FWHM of 30° was injected, however the specular reflection work does not account for such a profile. The second assumption considers the location of electron injection. In reality, the electrons will be injected across an area similar to the spot width of the laser pulse, and directed with a range of angles. This is accounted for in the ZEPHYROS simulations where the maximum radius of injection is when the laser intensity reaches 1% of the peak value (approximately 7.88 μm radially). The specular reflection analysis presented in section 5.4 injects a single electron at only the centre of the cone. With some electrons actually being injected a radial distance from this location, they will be closer to the cone walls. Therefore, the possibility of these electrons undertaking multiple bounces is more likely, as they don't have to travel as far along the depth of the cone before reaching the wall; this then leaves more of the cone depth for the electron to reach the opposing cone wall. As such, the 9.4 μm maximum tip width that allows a second reflection in the 5° cone will actually be larger.

Finally, we consider the applicability of the P. Mora model [17] which uses a Boltzmann distribution of fully thermalised electrons. In the TNSA model of ion acceleration, there are at least two components of the electron distribution: (1) the cold background electrons and (2) the high-energy, highly-directional hot electrons that are accelerated by the laser pulse. The latter component travel through the target effectively collisionlessly and can only thermalise if they get chance to reflux multiple times within the target. Therefore, implementing a Boltzmann distribution will not account for both these populations, leading us to consider perhaps a more realistic model of the electron distribution. The work by H. Schmitz [120] considers the cold electrons using the Boltzmann distribution while the hot component is accounted for with a kinetic description. This work reports how the sheath field strength and subsequent acceleration of ions is determined by the longitudinal component of the hot electron temperature [120]. Therefore, if we consider the case of a reduction in the angular divergence of electrons due to successful resistive guiding in a conical target, one would expect an improvement in the longitudinal directionality of the fast electron temperature through the target. Hence, with the

H. Schmitz model [120] in mind, this would result in an enhancement in the sheath field at the rear surface and acceleration of ions to higher energies. Either way, both the P. Mora [17] and H. Schmitz [120] models both suggest that an improvement in either the fast electron density or longitudinal hot electron temperature results in an enhancement in the sheath field and subsequent ion acceleration. If resistive guiding is successfully taking place, we expect both these electron parameters to be increased, suggesting validity in the application of these models in the analysis presented in this chapter.

Through the use of radiochromic film, the maximum proton energy has been diagnosed experimentally for the first time in relation to conically structured targets implemented for resistive guiding. The results from two experimental campaigns suggest that proton acceleration via TNSA may be somewhat sensitive to the cone geometry. An enhancement in the maximum proton energy for approximately 10° cones on both campaigns has been recorded. Mechanisms behind these results have been proposed using specular reflection considerations and hybrid simulations.

Chapter 6

Filamentation of Fast Electrons in Conical Structured Targets

6.1 Preamble

A combination of image plate (IP) and Coherent Transition Radiation (CTR) diagnostics have been used to investigate the fast electron beam that leaves the rear surface of the target. This population forms part of the high-energy tail of the fast electron distribution that escapes the target before the confining sheath field has sufficiently developed.

The fast electrons in this high-energy tail of the electron distribution have transit times through the 100 μm targets of approximately 330 fs (assuming a speed of $0.996c$ for a 5.4 MeV electron). This means that they reach the rear surface and escape before the resistively generated magnetic fields have become fully established at the cone:cladding material interface. These fields take on the order of hundreds of femtoseconds to picoseconds to develop [8, 10, 13] and therefore do not significantly affect the escaped electrons. Although one of the main focuses of this thesis is understanding the resistive guiding technique in an experimental setting, it is valuable to measure the escaped electrons to gain a complete picture of the entire fast electron distribution and the general laser-target interaction. For this reason, the IP and CTR diagnostics were implemented on the 2017 campaign.

This chapter is broken down into two main components. The first presents results from the IP diagnostic including the maximum and total signals generated by the electron beam. The angular spread that the signal subtends across the IP is calculated and provides evidence of electron beam filamentation. Electron energies exceeding ≥ 5.4 MeV are routinely recorded.

We show that the IP diagnostic is incapable of capturing the entire filamentation of the electron beam, therefore the analysis progresses to the CTR diagnostic. The recorded images of the electron beam from the IP and CTR diagnostics are compared and confirm the break-up of the beam. Results of the size and total CTR signal shall be discussed and show consistencies with the literature [18]. Further evidence of electron beam filamentation will be presented and compared with three-dimensional hybrid simulations using ZEPHYROS [101]. These simulations show comparable filamentation and suggest that the break-up of the electron beam does not significantly disrupt the resistive guiding technique.

6.2 Electron Beam Analysis using Image Plate Film

FUJIFULM image plate (IP) is a radiation detection medium that can be used to record the electron beam emitted during laser-solid interactions. The BAS-TR form of IP has been implemented on the 2017 campaign. Upon exposure to ionising radiation, a proportion of energy is deposited into the active layer of the IP, causing Eu^{2+} dopant atoms within the medium to become excited to a metastable Eu^{3+} state. This then decays during the scanning process using a laser, resulting in the emission of photons in the process of Photo-Stimulated Luminescence (PSL). This is captured and used to visualise the profile of the electron beam incident upon the image plate. Further details of the diagnostic and image processing techniques have been presented in section 3.6.

If the electron beam signal on the IP is sufficient to saturate the image after scanning, the film is subsequently scanned multiple times until an unsaturated image is obtained. This process was introduced in section 3.6.1.

An example image of scanned IP from the 2017 campaign is presented in Figure 6.1. The IP has been scanned twice in order to unsaturate the image. The same IP will be followed through the analysis process throughout this chapter.

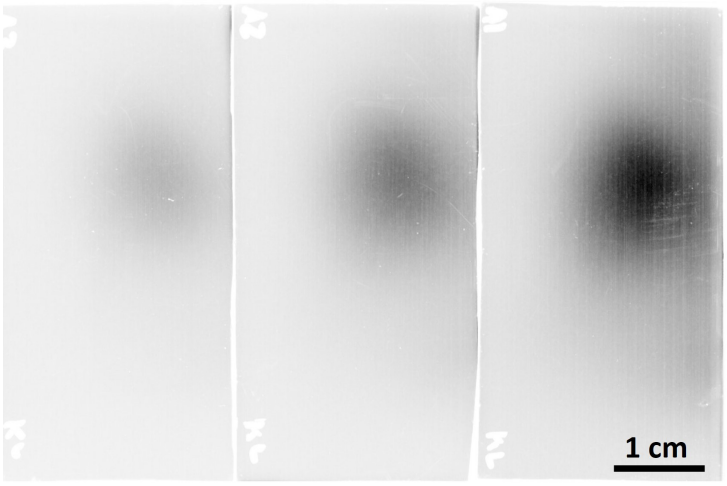

Figure 6.1: Unsaturated image of an IP after being scanned twice. IPs from right to left of the image are located progressively further into the stack. Note the ink marks on the left corners of each IP used for reference during the experiment.

The three IPs in the stack are presented in Figure 6.1, with the front most plate at the right side of the image. Each IP is 5×2.5 cm in size. The dark areas correspond to high electron signal which reduces as one moves progressively deeper into the stack due to increased filtering. When implemented on the experiment, the length of the IP (vertical direction in Figure 6.1) is placed horizontally, therefore in reality the scan is rotated by 90°.

The minimum electron energies capable of travelling through the RCF stack and reaching the first IP has been estimated using the NIST ESTAR tables [123]. The RCF and IP stack design implemented on the experiment has been used to determine the thickness of each material component before the first IP. For this, the HDV2 and EBT3 structures were used to calculate the thickness of each RCF sheet. These are previously presented in Figure 3.4 from which the

active layer has been assumed to consist completely of Mylar as a first approximation. The exact chemical formulae of these layers are not presented in the literature [85, 86].

The total thickness of the stack located before the first IP was then determined as 1.0043 cm along with the relative thickness of each separate material. The average density of the stack was then calculated using the relative thickness' of each material and their mass densities. This was calculated as 3.1598 gcm^{-3}.

The desired CSDA (*Continuous Slowing Down Approximate*) range value for the specific stack up to the first image plate was calculated by multiplying the stack thickness and average density up to that position. This was found to be 3.1734 gcm^{-2} and represented by the horizontal blue line in Figure 6.2. This is an estimate of how far the electron can travel until loosing all of its initial energy to the material.

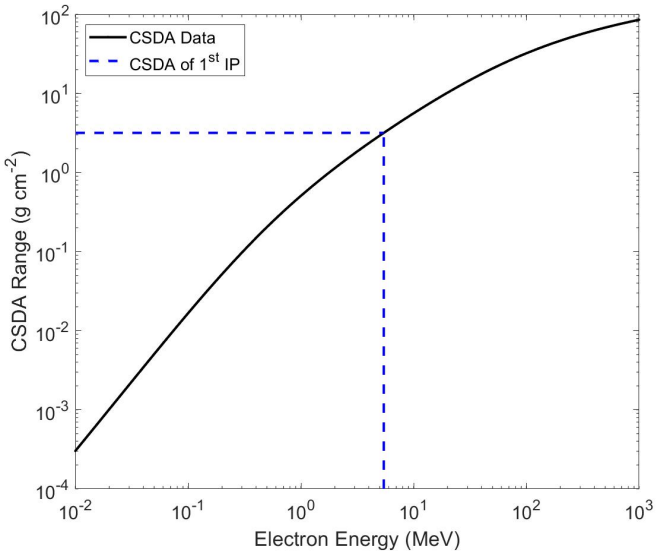

Figure 6.2: CSDA range for the 2017 RCF and IP stack up to the depth of the first IP. The required CSDA value is represented by the horizontal blue line. The minimum electron energy capable of reaching this depth is signified by the vertical blue line at approximately 5.4 MeV.

The CSDA range for the specific RCF and IP stack is presented in Figure 6.2. This shows the stopping range for a specific input electron energy. The horizontal blue line represents the CSDA value for the first IP in the stack while the vertical blue line is an estimate of the minimum electron energy capable of reaching this depth. This is found to be approximately 5.4 MeV.

The scanned images were converted from grayscale to colour-maps in MATLAB. This allowed the profile of the signal to be more visible and for a legend to be applied. Figure 6.3 displays the color-map of the example IP after being scanned twice.

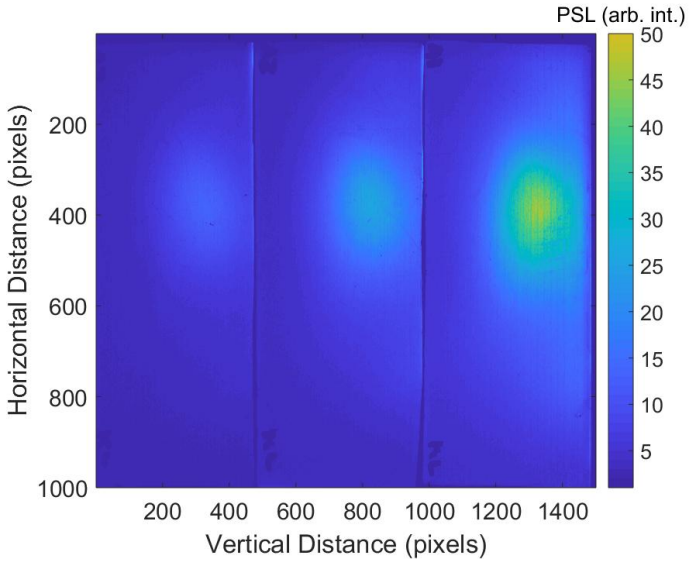

Figure 6.3: Colour-map image of the example IP in Figure 6.1 after being scanned twice. IPs from right to left are progressively deeper into the stack.

The colour-map in Figure 6.3 displays the same 3 IPs as in Figure 6.1 after being scanned twice to unsaturate the image. For each shot, the PSL from the first scan is retrieved by extrapolating the values after the IP has been scanned multiple times. This is closely based on the work by D. Rusby [28]. The method is presented in detail in section 3.6.1 where Equation 3.2 described how the PSL decays as the IP is scanned n number of times. For ease of reference, this equation is presented below. The parameters a and b have been substituted between the equations.

$$PSL_n = 0.998n^{-1.771} \times PSL_1 \tag{6.1}$$

rearranging this, the PSL for the first scan (PSL_1) can be determined from:-

$$PSL_1 = PSL_n \frac{n^{1.771}}{0.998} \tag{6.2}$$

rearranging PSL_1 is the retrieved PSL after one scan and PSL_n is the signal after being scanned n times. A root-mean-squared (RMS) error on the fit was determined as 0.0129 and shall be used in further error analysis in the chapter.

The PSL value at each pixel in Figure 6.3 is then converted to the PSL value from the first scan using Equation 6.2. This results in the following colour-map where the signal at each pixel has increased.

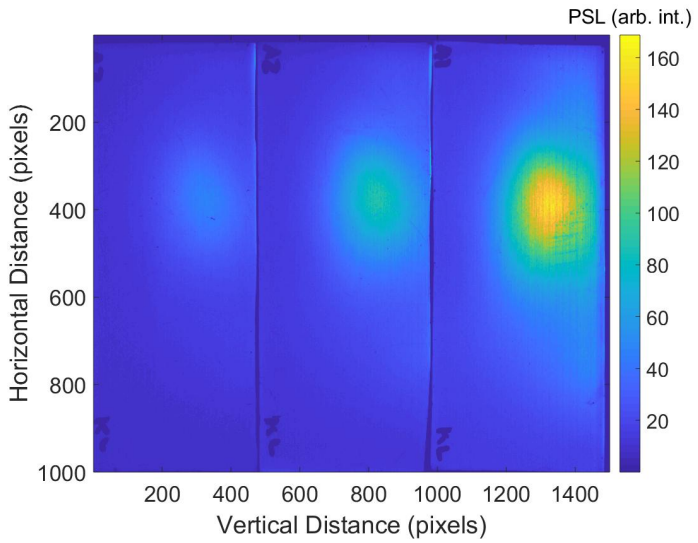

Figure 6.4: Colour-map image of the example IP after the first scan has been reconstructed. IPs from right to left are progressively deeper into the stack.

Figure 6.4 shows the colour-map of the three IPs but after the first scan has been reconstructed. This is evident by comparing the colour-map intensities between the two plots. The electron beam profile is identical between Figures 6.3 and 6.4 but the signal at each pixel has increased in accordance to Equation 6.2. For example, the PSL in the centre of the beam on the first (far-right) IP before reconstruction (Figure 6.3) is approximately 50 arb. int.. This significantly increases to approximately 160 arb. int. after the first scan has been reconstructed (Figure 6.4). By retrieving the first scan, comparison between shots can be made.

6.2.1 Analysis along the IP length

Lineouts along the length of the first IP were recorded for the reconstructed first scan images for each shot. This is along the vertical direction in Figure 6.4. To undertake this analysis, MATLAB code was generated to load the desired scan image and present it in the form of a colour-map. The first IP in the stack was then analysed; this is the right-most plate in Figure 6.5.

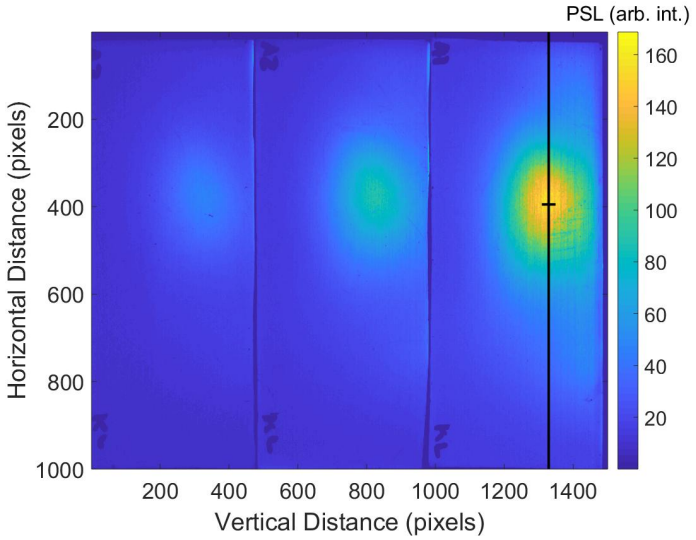

Figure 6.5: First scan reconstruction of scanned IP. Lineout along the length of the first IP in the stack. This is along the vertical direction in the figure. Lineout positioned visually upon the beam centre.

Figure 6.5 shows the reconstructed first scan image of the example IP stack. The line-out position is indicated by the long, vertical black line. The PSL at each pixel down this line was then plotted as a function of the pixel number. This is presented in Figure 6.6.

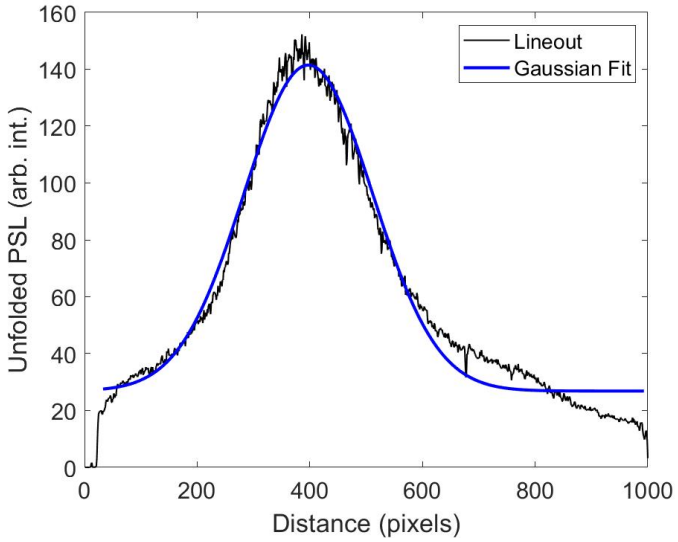

Figure 6.6: Lineout along the length of the first scan reconstruction of the first IP in the stack. Gaussian fit applied to the line-out.

A Gaussian fit has been applied to the line-out shown in Figure 6.6 along the length of the IP. The fit is used to determine the FWHM and peak signal. For the example IP under discussion, this results in a maximum PSL of 141.45 arb. int. and a FWHM of 268.60 pixels.

The MATLAB code was implemented for each shot throughout the experiment so that the maximum PSL and FWHM of the line-out along the length of the IP was determined.

A further step was then undertaken to convert the FWHM of the line-out into an angular divergence. For this, the FWHM was converted from pixels to centimetres using the known 5 cm length of the IP and the 1000 pixels that this corresponds to on the scanned image. A pixel-to-centimetre spatial calibration of 0.005 cm/pixel was calculated. The known distance between the target and first IP in the stack were then used to determine the angle that each pixel subtends from the target.

The angular calibration along the length (horizontal direction) of the IP was determined as $\theta_{Horizontal} = 0.046$ degrees/pixel. Using this value, the FWHM of the Gaussian in Figure 6.6 was converted to 12.37°. This method of converting the Gaussian FWHM to an angular range has been applied to all of the first IPs under analysis.

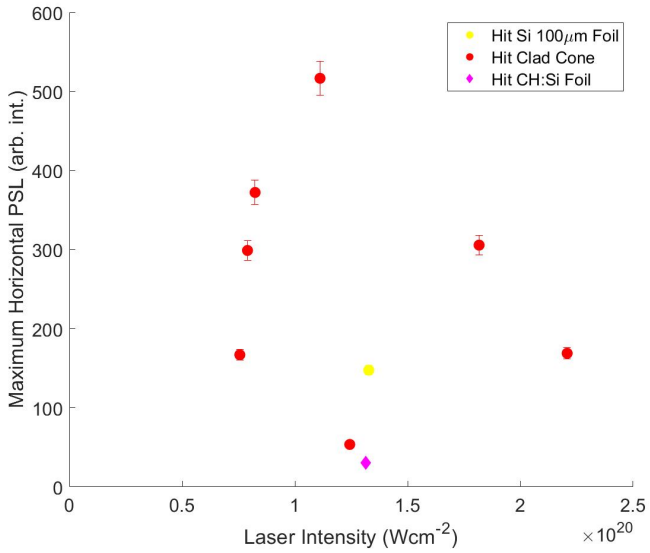

Figure 6.7: Maximum PSL of the line-out across the length of the IP. Plotted against the laser intensity. Silicon foil and clad cones 100 μm thick, CH:Si control foil 92.7 μm thick. All targets determined as *hit* using the front surface imaging diagnostic and have a known pulse length from when the auto-correlator successfully triggered. Error of 4.1% in the maximum PSL for all shots.

Figure 6.7 presents the maximum PSL signal from the line-out across the length of the IP. This is plotted against the incident laser intensity for 100 μm thick targets that have been determined as *hit* using the front surface imaging diagnostic. Only shots where the autocorrelator triggered so the pulse length is known have been included in this figure. The error in the maximum PSL was determined as approximately 4.1% with the dominant contributor being the ability to position the line-out at the centre of the beam.

All the clad silicon cone targets - bar one shot - generate a higher peak PSL signal compared to the planar silicon and structured CH:Si foils. An increased PSL signal may indicate two things (1) fast electrons of higher energy (2) an increased number of fast electrons. Tackling the former point, higher energy electrons are capable of exciting multiple Eu^{2+} atoms to the metastable Eu^{3+} state as they travel through the image plate. Therefore when these decay, there is an increased number of radiating atoms contributing to the PSL signal. The second point

suggests an increased number of fast electrons. In this case, simply more electrons are capable of exciting more Eu^{2+} atoms. Again when these decay, there are more contributing atoms that radiate. The two mechanisms essentially result in a higher number of radiating Europium atoms within the active layer of the IP, thereby increasing the measured PSL.

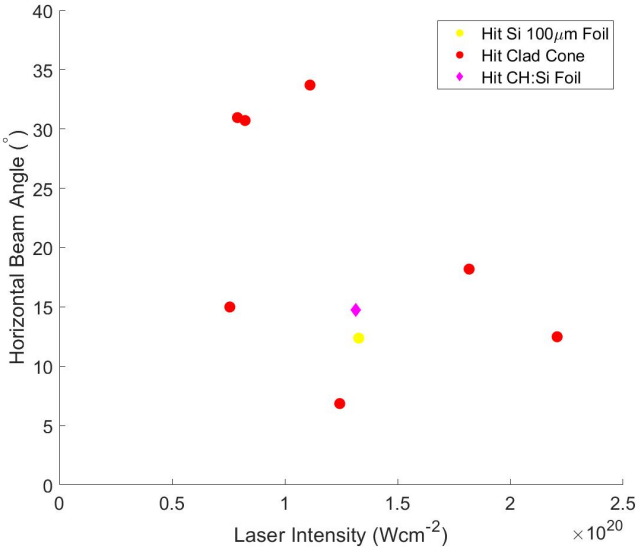

Figure 6.8: Full angle subtended by the electron beam across the length of the first IP in the stack. Plotted against the laser intensity. Silicon foil and clad cones 100 μm thick, CH:Si control foil 92.7 μm thick. All targets determined as *hit* using the front surface imaging diagnostic and have a known pulse length from when the auto-correlator successfully triggered. Error of 0.6% in the beam angle.

Figure 6.8 considers the full-angle that the electron beam subtends across the length of the IP. Error in the beam angle of 0.6% due to the resolution of the IP and the ability to position the line-out at the centre of the beam. This error is presented in Figure 6.8 but is too small to be resolved. Two subgroups of targets are shown that achieve relatively different divergence angles across the horizontal direction. Four shots onto clad cones generate a similar signal divergence to the silicon and CH:Si control foils. These control foils produce a signal divergence of 12.4° and 14.7° respectively at comparable laser intensities. The four clad cones achieving a similar divergence span from 6.9°-18.2° across the full range of laser intensities presented in the figure ($0.76 \times 10^{20} - 2.21 \times 10^{20}$ Wcm^{-2}).

A separate subset of clad cone targets generate a significantly more divergent signal on the IP. These range in angle from $30.7° - 33.7°$ across laser intensities of $0.79 \times 10^{20} - 1.11 \times 10^{20}$ Wcm^{-2}. These three clad cone targets also generated a peak PSL signal (Figure 6.7) that exceeded that of the silicon and CH:Si control foils; suggesting that the most diffuse signals also generate the brightest peak PSL across the length of the image plate.

6.2.2 Integrated Signal Analysis

The total signal captured across the first IP in the stack has also been determined for all shots during the 2017 campaign. To do this, MATLAB code was developed that loaded the colour-map image of the reconstructed first scan of the IP. A rectangular *Region of Interest* (ROI) was then created and moved by the user to cover the electron beam signal on the first IP in the stack. The position of the ROI for the example IP is presented in Figure 6.9.

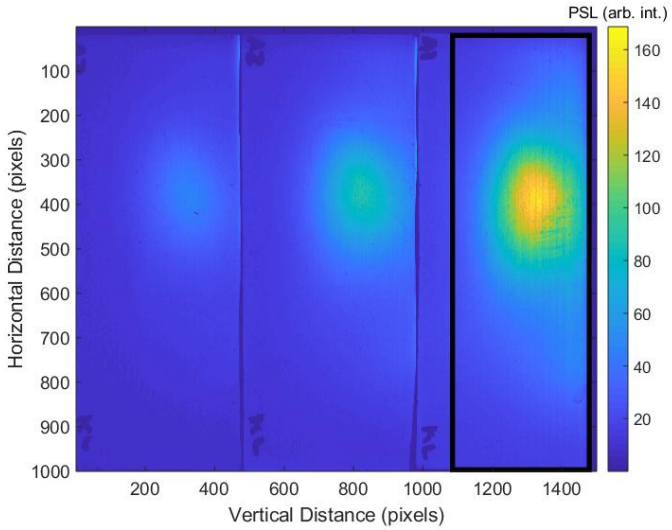

Figure 6.9: Reconstructed first scan colour-map with ROI positioned over the first IP in the stack. ROI size of 393×977 pixels. Total PSL calculated by summing the PSL at each pixel within the ROI represented by the black rectangle.

The region of interest was kept a constant size of 393×977 pixels between shots for consistency. This was slightly smaller than the IP size to ensure that the pen markings in the left corners were not included. Once the ROI was positioned over the desired area by the user, the total PSL was calculated by summing the PSL at each pixel within the ROI area. This was then recorded in an external data file along with the ROI corner positions.

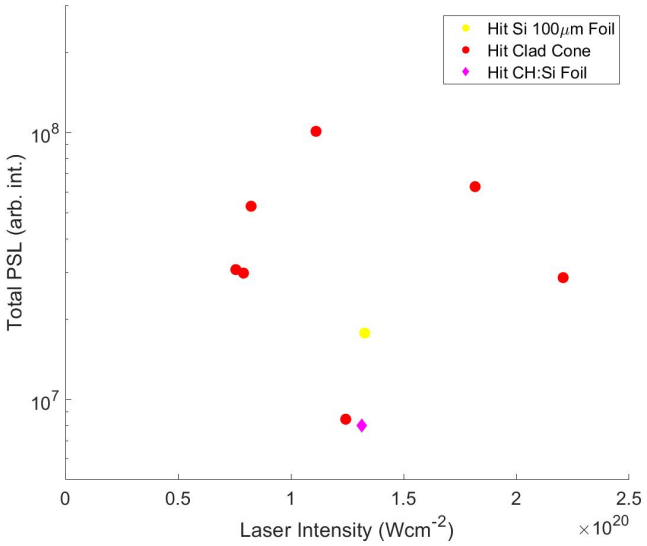

Figure 6.10: Logarithmic plot of total PSL within the rectangular ROI for *hit* shots. ROI kept a constant size of 393 × 977 pixels between shots for consistency. Total PSL calculated by summing the PSL at each pixel. Final values plotted against laser intensity. Total PSL error of 0.3%. Error bars are present on the figure but significantly narrow to be visible on the logarithmic scale.

Figure 6.10 presents the total PSL across the first IP in the stack as a function of laser intensity. An error in the total PSL of 0.3% is dominated by the positioning of the ROI by the user. These errors are present on the figure but are too narrow to be resolved on the logarithmic scale. A similar trend in total PSL is visible when compared to the maximum PSL from the line-out across the length of the IP (Figure 6.7). The same clad cone at a laser intensity of 1.2×10^{20} Wcm^{-2} and CH:Si control foil that generated the weakest peak signal in Figure 6.7 also generate the weakest integrated signal. In both these cases, the total PSL is below 9×10^6 arb. int. and the maximum PSL below 55 arb. int.. The same clad cone target that generated the brightest peak signal in Figure 6.7 also generates the greatest integrated signal. This is located at a laser intensity of 1.1×10^{20} Wcm^{-2} and generates a total PSL of 1.0×10^8 arb. int. within the ROI on the first IP. This is over an order of magnitude in total PSL more than the lowest clad cone target. As with the maximum PSL in the horizontal line-out direction, all of the clad cone targets - bar the single shot at 1.2×10^{20} Wcm^{-2} - generate a total PSL that exceeds that of the single silicon control foil. The total PSL for this control foil is recorded as 1.8×10^7 arb. int.. The similar trends across the maximum and total PSL results suggest that these parameters are somewhat inherently linked. However, clear variability is apparent across all targets which does not appear to be related to the laser intensity. The maximum PSL of the clad cone shots ranges over 500 arb. int., while the beam angle is spread over a 30° range. The total PSL for these targets is also variable, ranging by over an order of magnitude. This leads us to consider the IP stack configuration implemented on the 2017 campaign and if this is sufficient to capture enough information of the beam.

6.2.3 Angular Distribution of the Electron Beam

Variability in the maximum, total and angular divergence of the PSL has been presented in the previous sections. These results do not appear to be linked to the laser intensity. The nature of the half-stack of image plate means that only a portion of the electron beam can be measured. This is sufficient if the electron beam from each target is perfectly symmetrical and centred upon the top of the IP. In this case, precisely half of the beam is collected for each shot, from which the full beam profile can be inferred using symmetry. However, in reality the electron beam will not be perfectly symmetric. The presence of multiple electron signals on some IPs also suggests that a further mechanism is taking place that may attribute to the variability. To investigate this, a method of presenting the signal upon the IP in an angular plot is shown. This suggests the presence of electron beam filamentation which the IP cannot fully diagnose alone.

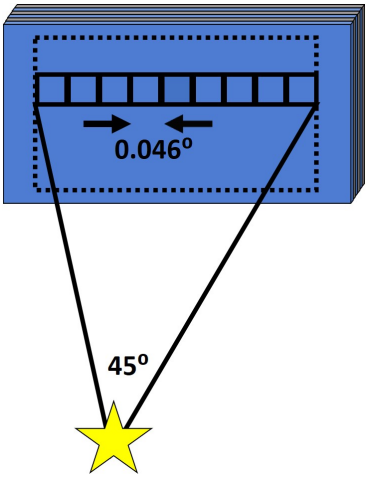

Figure 6.11: Angular range that the IP records. Single pixel represented by black squares. Each pixel subtends an angle of 0.046° in the horizontal direction. The complete 977 pixel long ROI subtends an angle of 45° and is represented by black-dashed rectangle. TCC and total IP represented by yellow star and blue rectangle respectively.

The MATLAB code developed for the total PSL analysis in section 6.2.2 was modified such that the user positioned the 393×977 pixels ROI on the first image plate. The maximum PSL down each column was then found within the ROI. The location of each pixel column across the IP was converted to an angle using trigonometry. This corresponded to each pixel subtending an angle of 0.046°. Therefore, the whole ROI recorded a full angle of 45° in the horizontal plane. The maximum PSL at each position was plotted against the angle that position represents. This resulted in a polar plot of the calculated signal.

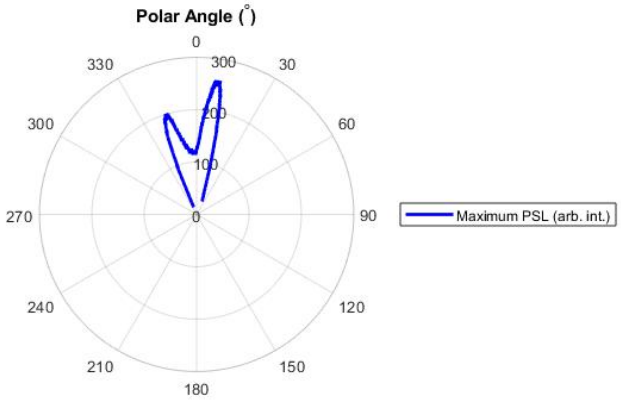

(a) Polar plot of maximum PSL for a filamented electron beam recorded on the first IP in the stack.

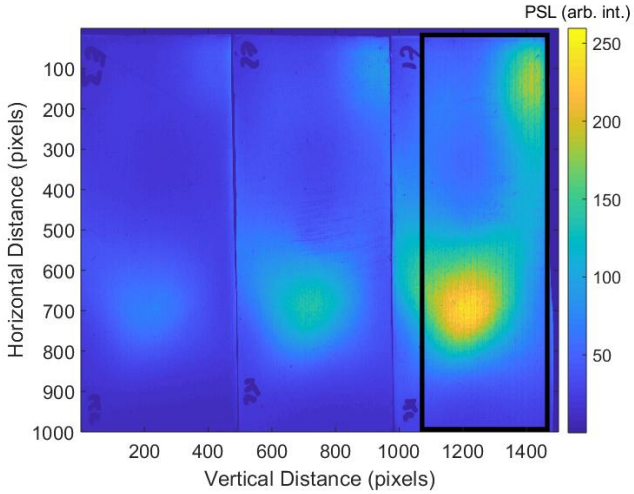

(b) Corresponding colour-map of IP with the ROI presented as black rectangle. Maximum PSL found down each pixel column down the vertical direction of the IP (horizontal direction on the image).

Figure 6.12: Angular polar plot of the first IP in the stack. Image shows a filamented electron beam. (a) angular plot (b) corresponding colour-map and ROI. Full ROI of length 977 pixels records an angle of 45°.

Figure 6.12 presents a polar plot and corresponding analysis area for the first IP in the stack. Two signals are clearly visible on the IP and are reproduced in the polar plot. The most intense beam generates a maximum PSL of approximately 250 arb. int. at an angle of approximately 10° from the centre of the IP (laser axis). The second beam located at the top right of Figure 6.12b generates a lower maximum PSL of approximately 200 arb. int.. This beam is located at approximately 340° on the polar plot, corresponding to 20° from the laser axis.

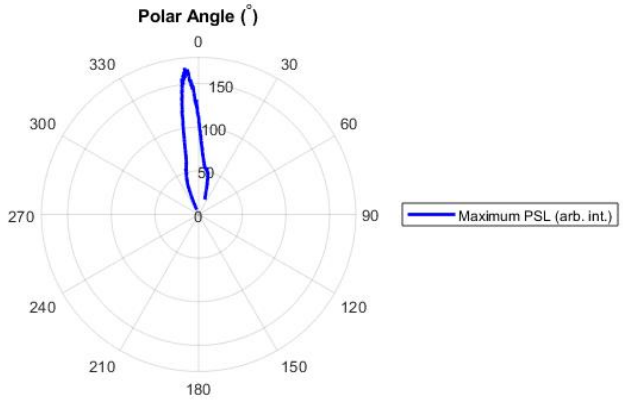

(a) Polar plot of maximum PSL for a singular structured electron beam recorded on the first IP in the stack.

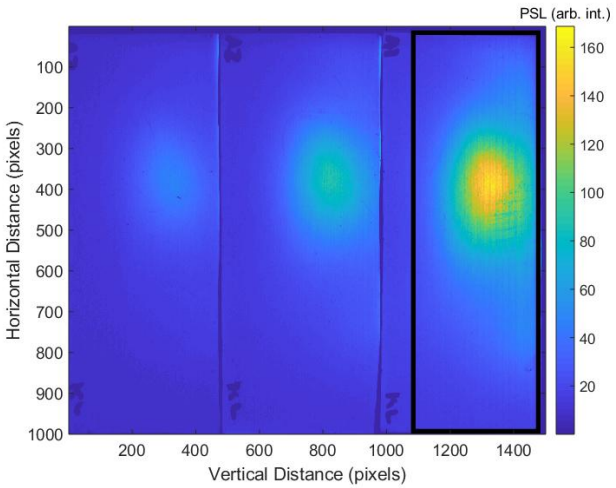

(b) Corresponding colour-map of IP with the ROI presented as black rectangle. Maximum PSL found down each pixel column in the vertical direction of the IP (horizontal direction on the image).

Figure 6.13: Angular polar plot of the first IP in the stack. Image shows a single structure captured on the IP. (a) angular plot (b) corresponding colour-map and ROI. Full ROI of length 977 pixels records an angle of 45°.

Figure 6.13 presents a second polar plot and the corresponding ROI on the first IP in a different stack. In this case, only a single structure is visible on the IP and polar plot. A maximum signal of approximately 160 arb. int. is found at the centre of the beam which is located at approximately 5° from the laser axis.

Both of the polar plots show how some of the IPs captured a single beam during the experiment, whilst others showed multiple signals on the same plate. The presence of two electron beam signals on the image plate would suggest two distinct populations of electrons. One would attribute these to be generated from the resonance absorption and $\mathbf{J} \times \mathbf{B}$ heating mechanisms which accelerate the electrons along the target normal and laser k vector axes respectively. However, in the 2017 campaign from which the IP scans are obtained, a plasma mirror was

used to direct the Vulcan PW laser pulse along the target normal axis. Therefore, the electrons generated from these two distinct mechanisms are directed along the same axis and should be captured at the same location upon the image plate. A caveat to this would be if the target was rotated with respect to the laser axis. However, diligence was taken at multiple stages of the alignment process to ensure that the target was positioned in the mount without rotation. These included positioning the target in the mount using a three-axis alignment jig and monitoring any subsequent rotation within the target chamber using the real-time transverse probe and OTR images. These methods ensured that rotation of the target was minimised so that the laser and target-normal axes overlaid. Therefore, multiple signals upon the IP are unlikely attributed to two distinct electron populations. This leads one to consider the most likely cause being filamentation of the electron beam, with each signal captured by the IP being from a distinct filament.

As previously determined, the length of the ROI covers an angular range of 45°. Considering the expected electron divergence of approximately 60° for nominal Vulcan PW laser conditions [5] means that the most divergent fast electrons will not be captured by the IP. At the 6.30 cm distance between the IP and target, an electron travelling at a 30° half-angle divergence will extend 3.64 cm radially from the target normal axis. This is over 1 cm outside of the IP collection region either side of the IP and suggests that if the electron beam is filamented, the IP may not capture the most divergent filaments. In addition to this, the implementation of a half-stack of IP means that it is only possible to capture the lower half of the electron beam. Any structures or information in the upper half of the beam cannot be sampled.

Therefore, other diagnostics were considered which would be able to diagnose the extent of the proposed filamentation. This was the Coherent Transition Radiation diagnostic which had a larger field of view of the full rear surface of the target.

6.3 Coherent Transition Radiation Investigations

Optical Transition Radiation (OTR) has been collected from the rear side of the target throughout the 2017 campaign. The radiation is emitted by rear surface atoms as electrons escape into vacuum. Analysis of the coherent variation of the radiation - Coherent Transition Radiation (CTR) - will be presented in this section.

The diagnostic layout implemented to capture and image the CTR is presented in Figure 3.11 in section 3.7.3. Images at the CTR wavelength ($2\omega = 532$ nm) were captured for each shot and processed according to the following section. This resulted in a final image from which the signal intensity and radial size have been extracted. The system had a spatial resolution - limited by the optical setup - of 3 μm.

However, the first step was to compare the raw images of the CTR with the processed IP scans to determine if the proposed filamentation was present. The CTR diagnostic imaged the full width (approximately 1 cm) of the target so had the ability to capture all of the electron beam filaments - if present. An example image is presented in Figure 6.14 which compares the IP scan and raw CTR image for the same shot.

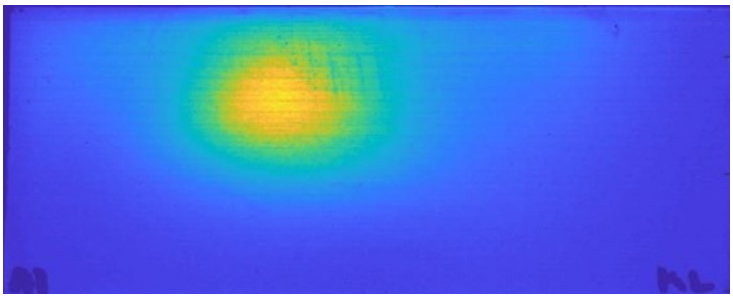

(a) Reconstructed first scan for the first IP.

(b) Raw CTR image for the same shot. CTR filaments have been magnified to the top right corner of the image.

Figure 6.14: Comparison of (a) 1st IP in the stack (b) Raw CTR image for the same shot. Note the single area of signal on the IP but filamentation in the CTR emission. Images not to scale.

The IP scan presented in Figure 6.14a clearly shows a single area of signal. However, the CTR image in Figure 6.14b shows three distinct features corresponding to filamentation of the electron beam that escapes the rear surface of the target. This suggests that the IP has only captured a single filament. Such a disparity between the two diagnostics was found in approximately 67% of the shots analysed in this chapter.

The disparity between the two images supports the proposal that the image plate diagnostic is incapable of capturing the complete picture of electron beam filamentation. Therefore, the analysis of the CTR diagnostic progressed to determine the extent of filamentation as well as making comparisons of the size and total amount of signal to the literature.

6.3.1 CTR Image Processing

For each shot, a raw image was obtained in the second harmonic wavelength. This was initially in grey-scale but has been colour adjusted to green for ease of viewing. An example raw image obtained from the 2017 campaign is presented in Figure 6.15. This image is 2560 × 2160 pixels (width × height) in size.

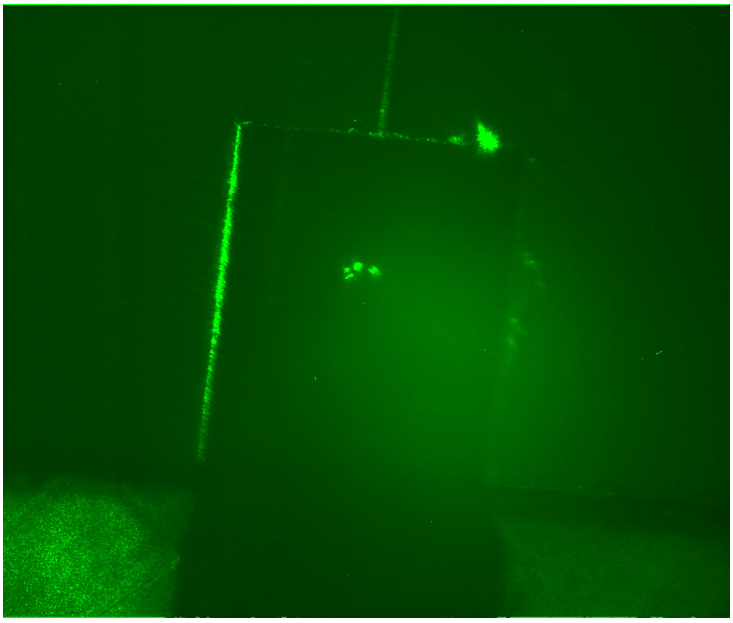

Figure 6.15: Unprocessed CTR image of the rear surface of a clad cone target. Note the 7 μm thick alignment wire at the top of the target and the filamentation of the emitted radiation.

The CTR signal is clearly visible in the centre of the target in Figure 6.15 and appears filamented. The 7 μm thick, carbon fibre alignment wire is visible on the top edge of the target. Background emission is present across the whole image, with a significant amount being located towards the centre right of the figure. This is mainly caused by background light from sources within the target area being collected by the camera CCD.

A notable feature of the raw CTR image in Figure 6.15 is the emission from the target edges and alignment wire. A significant amount of this radiation is emitted along the left edge of the target and near the top-right corner. One likely cause of this emission is surface transport of electrons which reach the target edges and radiate. Penetration of OTR signal with target depth is significantly less than CTR [18], and thus the signal strength is reduced at depth compared to CTR emission. This suggests that it is unlikely that the edge emission is OTR captured at the 2ω wavelength. If this was the case, the reduced penetration of OTR would cause the edge emission to be less intense that the central CTR emission, however this is not recorded in Figure 6.15.

The first step in processing the raw image was to subtract the background signal caused by stray light within the target area and undesired emission in the 2ω region. A square *region of interest* (ROI) of 75 × 75 pixels was positioned either side of the emission and the mean signal calculated. The squares were positioned as close to the CTR radiation as possible but not to such an extent that they included this signal. The ROI were positioned on symmetric sides of

the emission to capture any profile in the background signal, if present. The mean signal in each ROI was then averaged to produce a final background signal value. This was then subtracted from each pixel across the entire image. Figure 6.16 shows the background subtracted image for the same shot as previously presented in Figure 6.15.

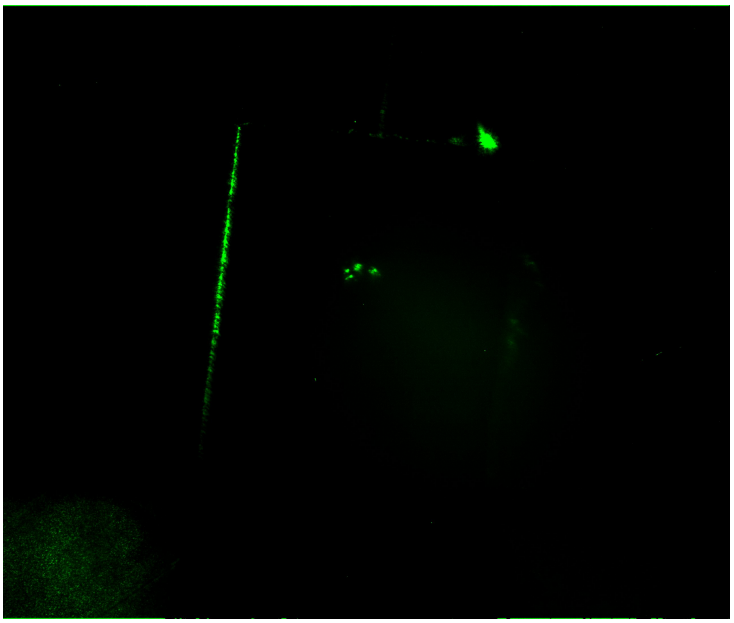

Figure 6.16: Background subtracted CTR image. Background signal determined by square ROI either side of the CTR emission region. Raw image presented in Figure 6.15.

The level of background signal has been significantly reduced in the background subtracted image in Figure 6.16. The stray light towards the centre right of the raw image (Figure 6.15) is no longer visible. The main features of the image that are distinguishable are now the desired CTR emission in the centre of the target and the emission along the target edges. The latter is not required for analysis, but is well separated from the emission region and can be easily avoided during the analysis process.

6.3.2 CTR Signal Strength

ImageJ software has been used to determine the signal strength of CTR emission within a region-of-interest (ROI). The first step to achieving this was to determine a suitable ROI size. If too small, the ROI would not capture the entire emission. However, if too large, undesired low-level light far from the emission may be captured. As shown in Figure 6.16, background subtraction was not capable of completely removing signal far from the CTR emission filaments; such as that along the target edges.

To determine the analysis ROI size, a line-out was taken across the background subtracted image in the direction that the emission was widest. This was carried out for all shots during the 2017 campaign.

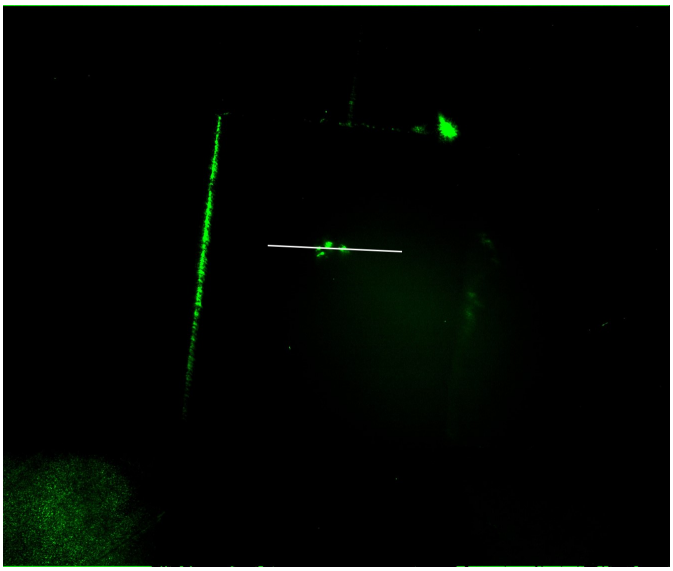

(a) Background subtracted CTR image with line-out to determine the analysis ROI size. Line-out across the direction that the CTR emission was widest.

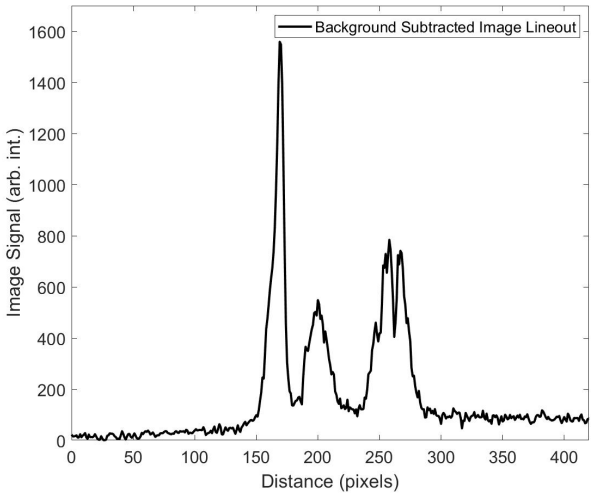

(b) Lineout data across the background subtracted CTR image.

Figure 6.17: Line-out to determine the analysis ROI size. (a) Background subtracted CTR image with line-out location (b) corresponding line-out data.

The line-out presented in Figure 6.17b shows three peaks corresponding to the CTR filaments that the line-out covers in Figure 6.17a. This emission region ranges from approximately $140 - 300$ pixels along the line-out, suggesting a size of 160 pixels in total. Therefore, the analysis ROI was set to 200 pixels in diameter; this was large enough to cover all of the emission in this image as well as that from the other shots.

The analysis then progressed to using a circular ROI of 200 pixels in diameter to cover the CTR emission. This was centred over the emission region by eye, ensuring that all visible filaments were captured within the circle.

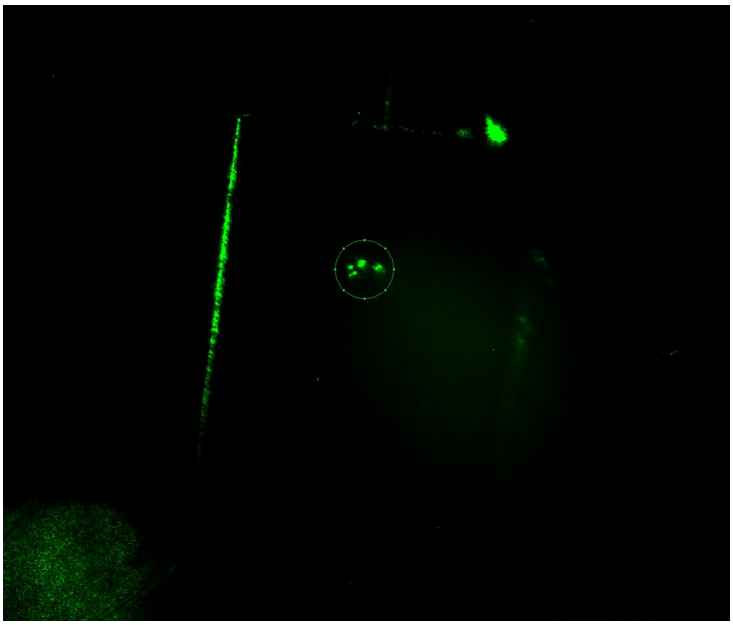

Figure 6.18: Background subtracted CTR image with analysis ROI centred over the emission region by eye. Circular ROI of 200 pixel diameter. ImageJ *Raw Integrated Density* function was used to sum the signal contained within the ROI.

The *Raw Integrated Density* function in ImageJ was then used to sum the signal value at each pixel within the analysis ROI. This was undertaken for all shots during the experiment. The Raw Integrated Density value for Figure 6.18 was calculated as 2.02×10^6 arbitrary intensity (arb. int.) units. The size of the region of interest was kept consistent between shots, therefore the number of pixels contained within the summation was also constant.

Neutral Density (ND) filtering was located before the CCD camera to reduce the emission and background signal below the saturation levels of the camera. However, the amount of filtering varied between shots and therefore required accounting for so that the Raw Integrated Density values could be compared. KG5 Schott glass was used for all shots, so this was not accounted for as any signal reduction would be consistent between shots.

$$\text{Signal}_{\text{Before ND}} = \text{Signal}_{\text{After ND}} \times 10^{\text{ND}} \tag{6.3}$$

ND is the Neutral Density filter level. This ranged between shots with values of 2.0, 2.5 and 3.0.

For each shot, the ND filtering was accounted for by calculating the signal strength before the filter using Equation 6.3. This meant that the Raw Integrated Density could be compared between each shot. Now that the ND filtering has been incorporated, the values shall be referred to as the *Total Signal Strength* to be distinguishable from the Raw Integrated Density. These results are presented in Figure 6.19 and 6.20.

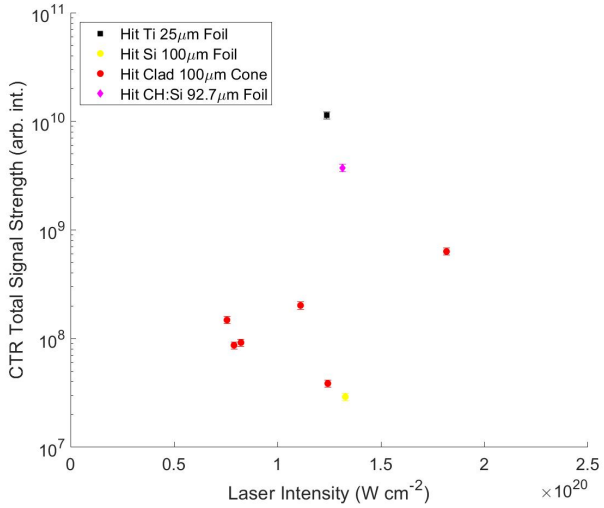

Figure 6.19: Total CTR signal within the circular ROI. Neutral density filtering and background subtraction has been accounted for. Plotted against the laser intensity. The presented shots are those that are determined as *hit* using the front surface imaging system and for when the autocorrelator diagnostic successfully triggered (so the pulse length is known). Error in CTR total signal is 7.65%, dominated by the background subtraction.

Figure 6.19 presents the total CTR signal within the circular ROI plotted against the laser intensity. An error of 7.65% in the total signal is dominated by the background subtraction using two square ROIs. An overall correlation between the total CTR signal and laser intensity is not evident from the figure, however a clear separation between the types of target is shown.

The clad silicon cone targets span the full range of laser intensities and over an order of magnitude in total CTR signal. These range between $3.86\times10^{7}-6.34\times10^{8}$ arb. int. Considering the target structure, these have all been determined as *hit* using the front surface imaging system, i.e. the laser was incident upon the silicon cone tip. Therefore, in a simple consideration of the material structure, the target is essentially 100 μm of silicon followed by the titanium dot and CH tamping on the rear surface. The same structure is found in the silicon control foil (yellow data point in Figure 6.19). This control foil generates the lowest CTR signal of 2.91×10^{7} arb int., which is similar to the clad cone at a comparable laser intensity.

The two remaining control foils are recorded at significantly higher CTR signals for a similar laser intensity. The titanium foil (25 μm thick) generated the highest total CTR signal of 1.13×10^{10} arb. int. while the CH:Si structured foil generated 3.74×10^{9} arb. int.. These are both at comparable laser intensities. Both the titanium and CH:Si structured control foils are of a different target structure than the hit clad cone and silicon foils. Notably the titanium foil is of a higher material density and thinner at 25 μm. The CH:Si foil is of a similar thickness as the silicon foil and clad cones, however the material is 42.7 μm of CH followed by the 50 μm of silicon. The hit clad cones and silicon foil however are 100 μm of silicon material. At similar laser intensities, the CH:Si structured foil and thinner titanium foil generate a higher integrated CTR signal compared to the planar foil or clad cones. Figure 6.20 and 6.21 investigate the role of target structure by comparing the total CTR signal with the thickness and electron areal density of each target.

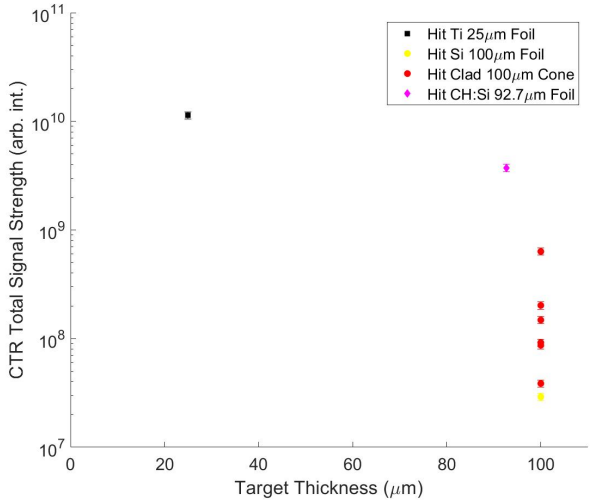

Figure 6.20: Total CTR signal within the circular ROI plotted against the target thickness. The presented shots are those that are determined as *hit* using the front surface imaging system and for when the autocorrelator diagnostic successfully triggered (so the pulse length is known). Error in CTR total signal is 7.65%, dominated by the background subtraction.

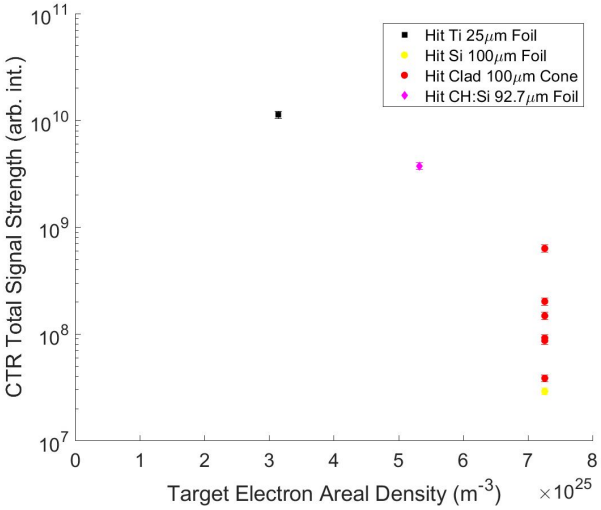

Figure 6.21: Total CTR signal within the circular ROI plotted against the target electron areal density. The presented shots are those that are determined as *hit* using the front surface imaging system and for when the autocorrelator diagnostic successfully triggered (so the pulse length is known). Error in CTR total signal is 7.65%, dominated by the background subtraction.

A general trend is presented in Figures 6.20 and 6.21 where the total CTR signal reduces as the target thickness and areal density is increased. The greatest CTR signal is produced from the thinnest of targets with the lowest areal density. This is the 25 μm thick titanium foil which generated an integrated CTR signal of 1.13×10^{10} arb. int.; this is approximately 18 times the signal of the brightest clad cone but at a quarter of the target thickness.

The thicker 92.7 μm CH:Si control foil generated a reduced signal compared to the titanium foil, albeit this was still within the 10^9 arb. int. regime. The thickest (100 μm) and greatest areal density targets - the clad cone and silicon foil - produced the lowest total signal. The areal density of these targets is calculated as purely 100 μm of silicon material; this has been applied to the clad cones as these have been categorised as *hit* using the FSI diagnostic. As such, the beam is determined as being incident on the silicon cone tip, which can be assumed to a first approximation as 100μm of silicon (50 μm cone + 50 μm stand-off distance). Between the 100 μm targets, the results are clearly variable so caution is required when drawing specific quantitative information from these results.

J. J. Santos *et al* [18] presents similar work measuring CTR emission as a function of target thickness. The second harmonic emission was investigated from the rear side of aluminium foil targets irradiated by the *salle jaune* Ti:sapphire laser (0.7J, 40fs, 6×10^{19} Wcm^{-2}) at normal incidence. The *integrated energy per spectral increment* was investigated as a function of the target thickness. Scalings of this parameter with target thickness are not presented, however models are applied with varying electron temperatures which closely follow the experimental results. Direct quantitative comparison cannot be made between this work and the results presented in this thesis due to the different descriptions of the signal strength. This thesis investigates the total CTR signal while J.J. Santos *et al* presents the total emission, but with energy and spectral resolution. However, general comparisons can be made to determine if there are consistencies between how the CTR signal - regardless of definition - changes with target thickness.

J. J. Santos *et al* records the integrated energy of the second harmonic OTR radiation decreasing over two orders of magnitude as the aluminium foil thickness is increased from 10 μm to 50 μm. As the target thickness continues to increase to 200 μm, the signal strength remains relatively constant for the second harmonic case. A similar trend is presented in Figure 6.20 where the 25 μm thick titanium foil generated the greatest integrated CTR signal which then decreased as the target thickness was increased to 100 μm.

6.3.3 CTR Emission Size

The radial size of the CTR emission has also been extracted for each background subtracted image. The filamentation of the CTR emission initially posed a difficulty in extracting this parameter and determining the central location of the filamented emission. However, a method using the weighted-average location of the filaments has been implemented to overcome this issue. This was developed by William Trickey (The University of York) [105] to extract the central locations, which have then been used in the subsequent analysis by the author.

The central location of a filamented CTR signal was determined using the weighted-average location $\bar{x}$ in Equation 6.4.

$$\bar{x} = \frac{\sum_{i=1}^{N} x_i w_i}{\sum_{i=1}^{N} w_i} \tag{6.4}$$

x_i and w_i are the location and number of signal counts in the filament peak i. $\bar{x}$ is the weighted-average location of a total number N filaments in the CTR emission.

To determine the radial size of the emission, a circular ROI was centred upon the weighted-averaged location of the filaments. If the CTR emission was unfilamented, the ROI was centred upon the location of the maximum signal. The ROI was kept a constant radius of 200 pixels between shots, and the ImageJ *Radial Profile* tool was used to extract a radial line-out. This tool sums the value at each pixel within a concentric ring, and then normalises this total to the number of pixels within the ring. This results in a radial line-out where the normalised integrated signal is plotted against the radial position. The radial line-out for the example shot presented in the previous sections (Figure 6.16) is displayed in Figure 6.22.

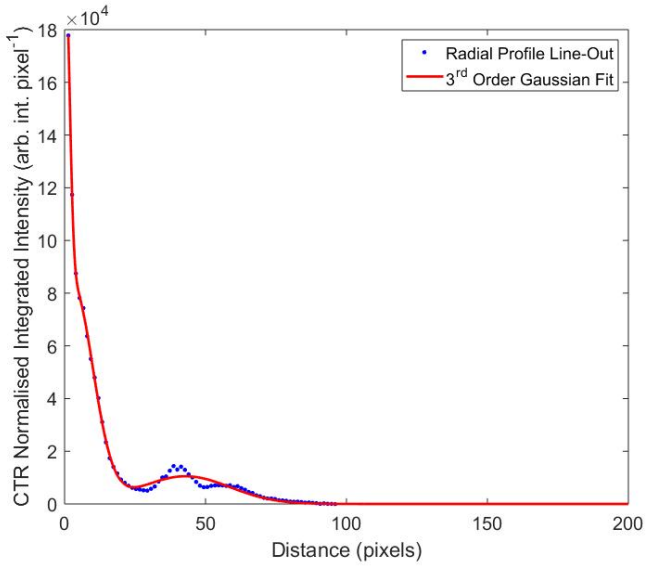

Figure 6.22: Radial line-out using ImageJ *Radial Profile* tool centred upon the weighted-averaged location of the CTR filaments. Blue data is the normalised total signal in each concentric ring. Red line is a 3rd order Gaussian fit applied to the line-out for further analysis.

The radial line-out in Figure 6.22 is presented as blue circles. Each data point corresponds to the total signal within a single concentric ring, normalised to the number of pixels within the ring. A 3rd order Gaussian fit has then been applied to generate a curve that can be later used to calculate the FWHM. Essentially, this allowed the general radial line-out shape to be interpolated with a larger number of data points. Lower-order Gaussian fits were tested, however these diverged from the radial data if small structures were present in the line-outs. High-order Gaussian curves were also tested but these provided insignificant improvement in the fitting.

A linearly spaced array of numbers was then generated and substituted into the 3rd order Gaussian equation to create the curve fit but at a higher precision. By increasing the number of data points in the Gaussian curve, the location of the half-maximum signal could be found to a higher precision.

The distance axis was converted from pixels to microns and the curve replotted. This conversion was calculated in similar methods to the spatial calibration of the optical probe in Chapter 4, where the tip of a 7 μm thick alignment wire was imaged on the CTR diagnostic channel. The target was then moved in the horizontal and vertical directions by known distances, and the displacement across the CCD was recorded. By comparing the known target movement to the displacement across the CTR image in these directions, an average spatial calibration factor was calculated. This was determined as 0.666 μm/pixel.

Each pixel location (horizontal-axis in Figure 6.22) was multiplied by the spatial calibration factor and the 3rd order Gaussian curve was re-plotted using the linear spaced array. This is presented in Figure 6.23.

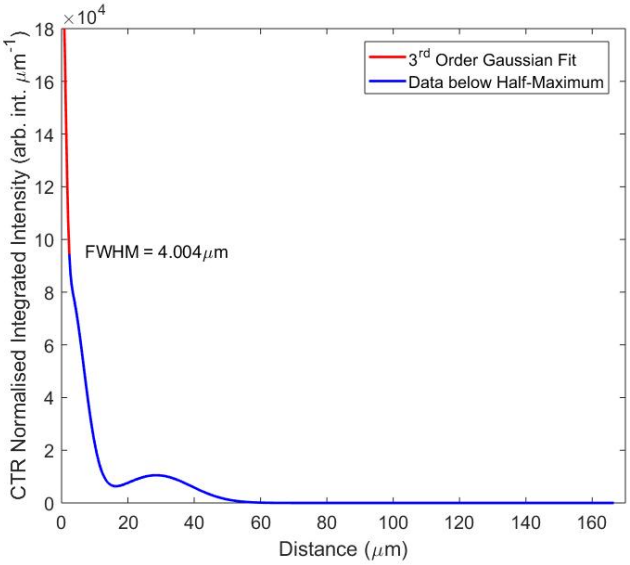

Figure 6.23: 3rd order Gaussian fit applied to the radial line-out. Red and blue lines signify data above and below the half-maximum position respectively. Distance between the half-maximum and zero distance is the HWHM of the CTR emission.

The 3rd order Gaussian curve is presented in Figure 6.23 where the horizontal axis has been converted to microns using the spatial calibration factor. The peak Normalised Integrated Intensity is 1.997×10^5 arb. int./ μm which is located near the centre of the ROI (Distance = 0.333 μm). The half-maximum value is calculated and the nearest data point to this value is located. For the example under discussion, the half-maximum value is 9.98×10^4 arb. int./ μm. The nearest data point to this value was found to be 9.44×10^4 arb. int./ μm located at 2.336 μm from the centre of the ROI. The discrepancy between the actual half-maximum and nearest data point to this value corresponds to a spatial difference of approximately 0.3 μm.

The difference between the location of the nearest data point (2.336 μm) to the location of the maximum signal (0.334 μm) is then calculated and doubled to provide the full-width

half-maximum (FWHM) size of the emission. Therefore, for the example under discussion, this is 4 ± 3 μm. Here the error is dominated by the resolution of the CTR diagnostic.

The process of determining the FWHM of the radial line-out is repeated for the remaining shots. In some cases, the beam was significantly filamented such that the radial line-out was centred upon a region that had multiple filaments either side. This resulted in the radial profile showing both sides of the Gaussian profile, i.e. the maximum signal was located further away from the central location. In this case, the FWHM was calculated by finding the nearest data points to the half-maximum signal either side of the peak. The difference in these locations was then used as the FWHM.

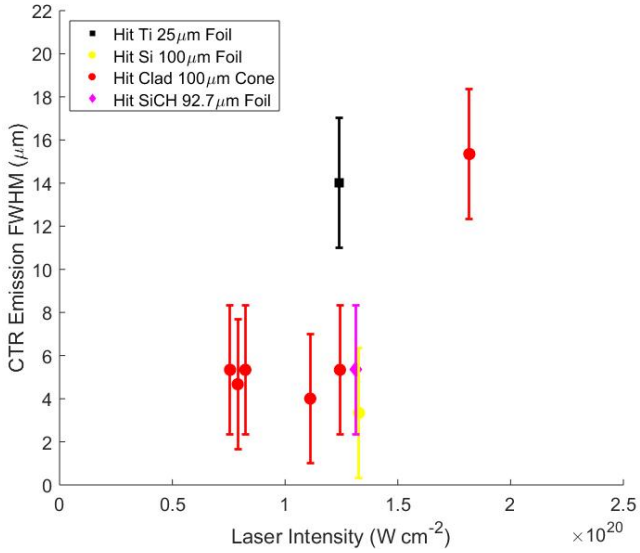

Figure 6.24: CTR emission FWHM as a function of laser intensity. Only shots with a known pulse length (successfully triggered auto-correlator) and determined as *hit* using the front surface imaging diagnostic. Error in CTR Emission Size of 3 μm.

The radial size of the CTR emission is plotted against the laser intensity in Figure 6.24. The majority of targets generate a CTR emission smaller than 5 ± 3 μm, while a further subset of two targets are located above 14 ± 3 μm. The larger emission is generated from the 25 μm titanium foil and a single clad cone which is at the highest laser intensity. The size of the emission from these targets are within error of one another.

The smallest emission is from targets consisting of the silicon 100 μm foil, CH:Si foil and the remaining clad cones. Again, the emission sizes are all within error of one another. These targets span an intensity range of $0.7 - 1.3 \times 10^{20}$ Wcm^{-2}, while the larger emission from the titanium foil is also located within this range. This suggests a possible target thickness or material affect causing the increased emission size in the thinner, titanium foil.

J.S. Green *et al* [5] reviews the fast electron beam divergence as a function of laser intensity. This paper compares electron divergence measurements using a variety of diagnostic techniques including x-ray Kα, optical transition radiation and shadowgraphy (references within [5]). The work reports the electron divergence angle (full-angle) increasing from approximately 20° to 60° as the laser intensity is increased across the order of $10^{18} - 10^{21}$ Wcm^{-2}. However, one would not

expect this to be visible across the relatively narrow laser intensity range shown in Figure 6.24. Across this intensity range in [5], the electron divergence is represented by a single data-point.

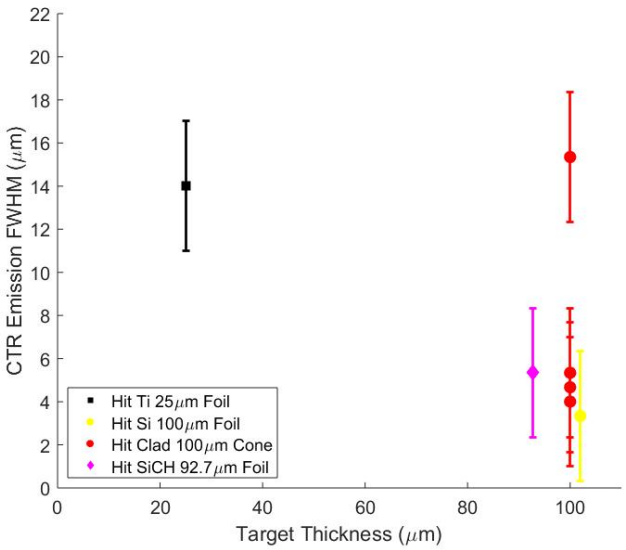

Figure 6.25: CTR emission FWHM as a function of target thickness. 100 μm silicon foil displaced slightly in target thickness to be resolved from the clad cones. Only shots with a known pulse length (successfully triggered auto-correlator) and determined as *hit* using the front surface imaging diagnostic. Error in CTR Emission Size of 3 μm.

Figure 6.25 presents the CTR emission size against the target thickness. The two largest emission regions from the 25 μm titanium foil and single clad cone are visible, while the smaller emission is generated from the thicker targets ($\geq$ 92.7 μm).

Comparison of the emission size from the CTR with other diagnostics implemented on the experiment shall not be presented in this thesis. As shown in J.S Green *et al* [5] and K.L. Lancaster *et al* [6], the measured signal size at the rear surface of the target is sensitive to the diagnostic. In addition to this, the CTR emission is dependant upon the most energetic fast electrons that cross the rear surface and escape the target. This portion of the distribution is not significantly divergent, therefore one would not expect to see a significant change in the signal size.

However, J.J. Santos *et al* [18] presents emission size results from aluminium foil targets using comparable OTR and CTR diagnostics to those used in this thesis. Therefore, comparisons to this work shall be presented. In [18], the second harmonic radiation is reported to grow steadily in size as the target thickness is increased from 10 μm to 50 μm. Over this range, the FWHM of the emission size grows from approximately 20 μm to 90 μm, following a 30° divergence. As the target thickness further increases to 100 μm, the emission FWHM reduces back to slightly above the initial size for the thinnest of targets. At 100 μm, the FWHM is approximately 30 μm. The rapid increase in the emission size for the targets ranging up to 50 μm thickness is attributed to the broad thermal component contributing to the signal in addition to the CTR. Above the 50 μm thickness, the thermal emission is less capable of penetrating to the rear surface and the

narrower CTR becomes dominates. Hence, the signal size reduces to follow approximately 5° divergence.

A similar trend is seen in Figure 6.25 where the 25 μm thick titanium foil generates one of the largest emissions of 14 ± 3 μm. Assuming the electrons contributing to this emission originate from the centre of the laser spot (as in [18]), this corresponds to a full beam divergence of approximately 30°. The majority of the remaining targets of thickness ≥ 50 μm then generate emission smaller than 5 ± 3 μm; corresponding to a full divergence of less than 3°. Therefore, a significant difference in the divergence angle is present between the thin 25 μm titanium target and the majority of the thicker targets. This follows the same general trend as in J.J. Santos *et al* [18].

As suggested by J.J. Santos *et al*, thermal emission captured at the 2ω wavelength may be contributing to the broad signal recorded for the 25 μm titanium foil. The thermal radiation is associated with the more divergent, bulk component of the electron distribution so will act to widen the captured signal. For targets thicker than ≥ 50 μm, J.J. Santos *et al* records the CTR contribution to significantly dominate any thermal contribution, hence the signal size is reduced. This is also seen in Figure 6.25 where the majority of clad cone, silicon foil and CH:Si control all generate a smaller emission than the thinner titanium foil. However, a single clad cone target deviates from this trend and generates a signal of similar size to the titanium foil. This target also generated the brightest signal of all the clad cones. The increased emission size for this target may be attributed to the scaling of electron divergence with intensity presented by J.S. Green *et al* [5]. This target is at the highest laser intensity of all the clad cones, therefore the scaling would suggest a more divergent electron beam for this shot. However, one would not expect a clear change in divergence across the relatively narrow range of laser intensities presented in Figure 6.25. In addition to this, the results are clearly variable and caution needs to be taken in drawing conclusions of the electron beam divergence for specific shots.

6.3.4 CTR Filamentation and Hybrid Simulations

A large proportion of the CTR images suggested that the emission was filamented. This is evident in the example used in this thesis in Figure 6.16. CTR is emitted from oscillating ions at the target rear surface as the fast electrons cross the rear target-vacuum interface. Section 3.7 in Chapter 3 provides details of this mechanism. Therefore, it follows that the location of CTR emission corresponds to the location on the target rear surface that the electrons cross into the vacuum. Filamented CTR emission suggests that the electron beam that drives the atomic oscillations and subsequent radiation emission is also filamented.

To diagnose the extent of the filamentation, the separation between the emission regions has been characterised for each shot and compared to three-dimensional hybrid simulations using ZEPHYROS [101].

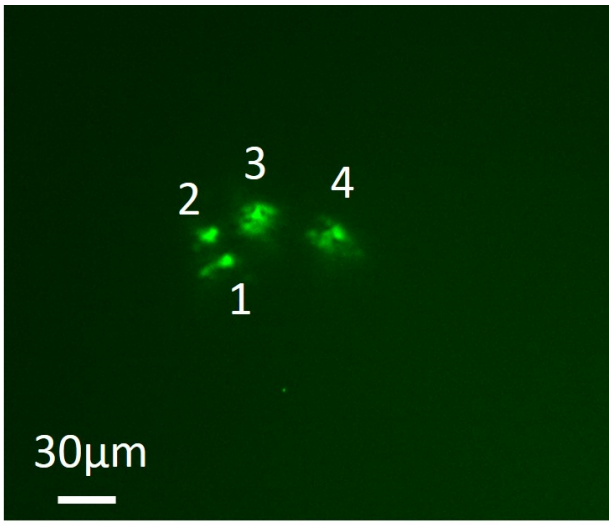

(a) Magnified image of CTR filamentation for a clad cone target. This is the same target used as the example in the previous CTR sections (e.g. Figure 6.16). Filaments numbered for reference in the text.

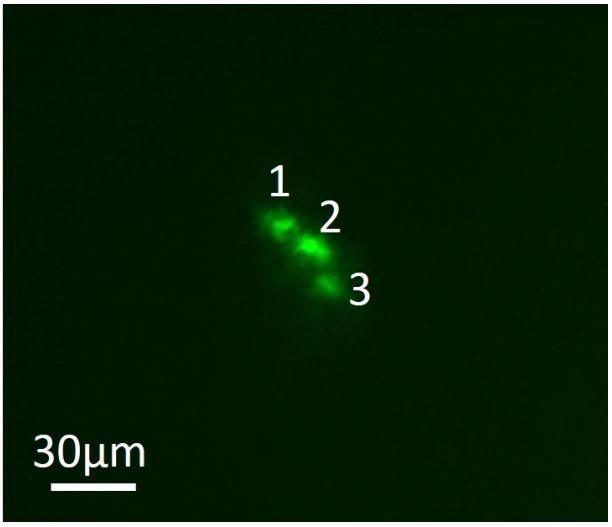

(b) Magnified image of CTR filamentation for a clad cone target. Filaments numbered for reference in the text.

Figure 6.26: Magnified images of background subtracted CTR emission. Main filaments numbered for reference in the text.

Figure 6.26 presents two examples of background subtracted CTR images where the emission is filamented. The centre of each filament has been located and the separation calculated between each position. The spatial calibration factor has then been used to convert these distances from units of pixels to microns. Tables 6.1 and 6.2 present the separation of the filaments in these two examples.

Filament Comparison	**Separation (μm)**
$1-2$	13 ± 4
$1-3$	29 ± 4
$1-4$	59 ± 4
$2-3$	29 ± 4
$2-4$	64 ± 4
$3-4$	38 ± 4

Table 6.1: Filament separations for the example CTR image presented in Figure 6.26a. Error of 4 μm calculated in quadrature (3 μm error from each filament location).

Filament Comparison	**Separation (μm)**
$1-2$	13 ± 4
$1-3$	29 ± 4
$2-3$	17 ± 4

Table 6.2: Filament separations for the example CTR image presented in Figure 6.26b. Error of 4 μm calculated in quadrature (3 μm error from each filament location).

The separation between two filaments is calculated by locating the centre of each and the corresponding distance. The location of each filament centre is limited by the 3 μm resolution of the system. Therefore, the error of ± 4 μm in the filament separation is determined in quadrature from the 3 μm error in each filament location.

As presented in Tables 6.1 and 6.2, the closest filaments were $1-2$ in Figure 6.26a which were separated by 13 ± 4 μm. Notably, this is the smallest separation recorded across all of the filamented CTR shots that have been analysed in this method. A similar separation is also recorded between filaments $1-2$ in Figure 6.26b. The largest separation is between filaments $2-4$ in Figure 6.26a, corresponding to 64 ± 4 μm. This is the largest separation of the filamented CTR shots analysed in this method.

Therefore, across all of the filamented CTR images analysed, the filaments ranged in separation between 13 ± 4 μm and 64 ± 4 μm. The mean $\pm$ standard deviation of these separations was calculated as 30 ± 13 μm.

The size of the filaments has also been determined to gain a general understanding of the extent to which the fast electron beam breaks up. To do this, the visually smallest and largest filaments were found and then a line-out was taken across the structures. A Gaussian fit was then applied from which the FWHM was calculated. These fits are presented in Figure 6.27.

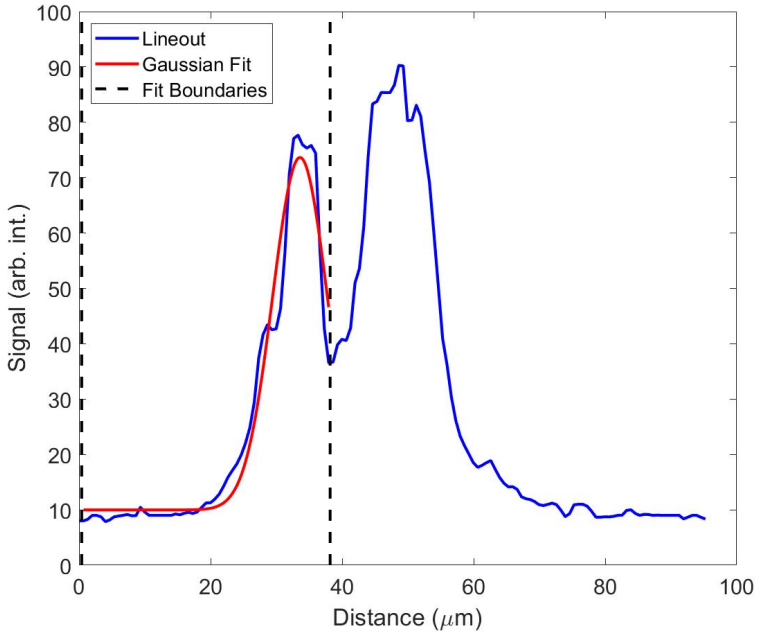

(a) Line-out and Gaussian fit across the visually smallest filament on the CTR images under analysis from the 2017 experiment. FWHM = 10 ± 4 μm.

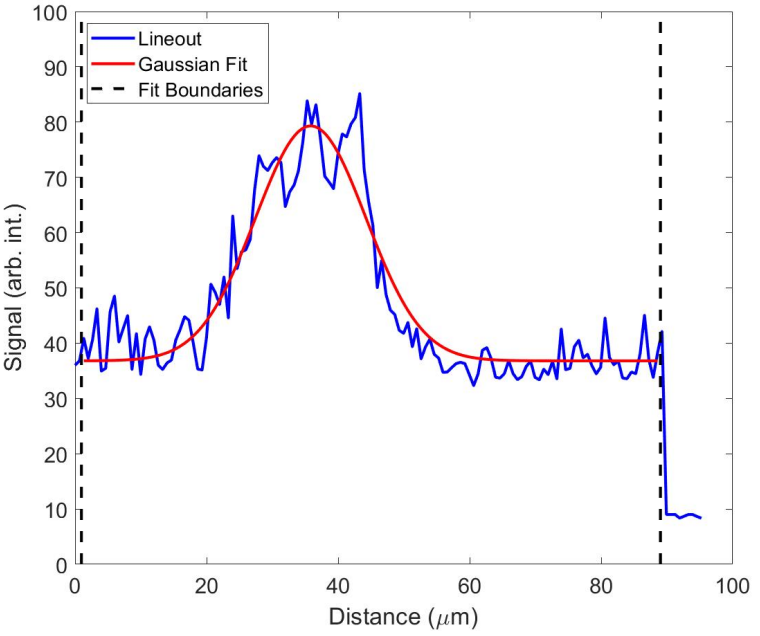

(b) Line-out and Gaussian fit across the visually largest filament on the CTR images under analysis from the 2017 experiment. FWHM = 20 ± 4 μm.

Figure 6.27: Lineouts across the CTR filaments and Gaussian fits applied to determine the size. (a) Smallest filament (b) Largest filament determined visually on each image across the experiment.

The smallest and largest filaments seen on the CTR images under analysis have been determined as 10 ± 4 μm and 20 ± 4 μm in FWHM size respectively. All other filaments in the remaining CTR images are within this relatively small range of sizes.

Three dimensional hybrid simulations were used to determine if the filamentation recorded on the CTR images would still take place even if the fast electron beam was guided by the resistive magnetic fields in the cone targets. In order to investigate this, the simulation of the double laser beam system incident upon a clad silicon cone were used. This is Simulation 2 in section 4.5.1 in Chapter 4, however the cross-section of the fast electron density has been extracted at a depth of 100 μm to characterise the filamentation.

It is beneficial to briefly recap the environment of this simulation. A further simulation will also be discussed which used identical parameters, however the cone opening half-angle was 10° rather than the original 5°. The simulation x×y×z grid was 103×200×200 cells in size, with each cell being 1 μm^3 in volume. The laser system was directed along the x-axis in the centre of the yz plane. The side boundaries were open, while the front and rear (x= 0 μm and x= 103 μm) were reflective to replicate electron refluxing. A double laser system was implemented to simulate an astigmatic laser profile with a secondary peak holding 24% of the main peak intensity. This profile was seen in the line-out of the optimised focal spot in the 2017 campaign (Figure 4.35). Each of the beams used in the simulations were 6.1 μm in FWHM size and 1 ps in duration. The main and secondary beams held peak intensities of 1×10^{21} Wcm^{-2} and 2.4×10^{20} Wcm^{-2} respectively. The main beam intensity was chosen as the nominal Vulcan peak value, while the secondary beam then held 24% of this value in accordance to the experiment focal spot line-out. The edges of the FWHMs were separated by 2.7 μm, also in accordance with the line-out. Recall how ZEPHYROS does not explicitly simulate the laser pulse, but instead injects a fast electron population based on the laser parameters. These populations were set to hold a Gaussian divergence with FWHM of 60° in accordance to J. S. Green *et al* [5].

The beams were directed onto the tip of a silicon cone of 15 μm width. The structure then expanded across a 50 μm depth with an opening half-angle of either 5° or 10°, depending on the simulation. A further 50 μm of silicon then followed from the cone base, as well as a 1 μm thick titanium dot. The whole system was then tamped in 1 μm of CH at the rear surface. The cone was also clad in this material. A silicon control foil was also simulated as 100 μm of silicon followed by the same titanium dot and tamping.

At 1 ps, the fast electron density was extracted and imaged at 100 μm depth. These images present a cross-sectional view of the yz plane so that the electron beam profile can be visualised to observe any filamentation, if present. These are displayed in Figures 6.28 - 6.30.

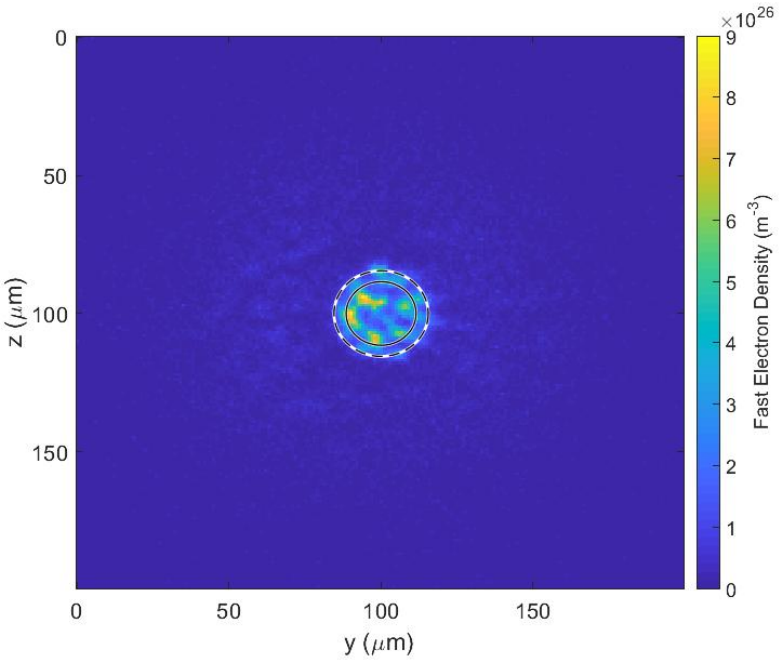

Figure 6.28: ZEPHYROS simulation of a 5° silicon cone. Fast electron density imaged at 100 μm depth. Cone base size denoted by the inner circle. Larger circle is a projection of the cone wall.

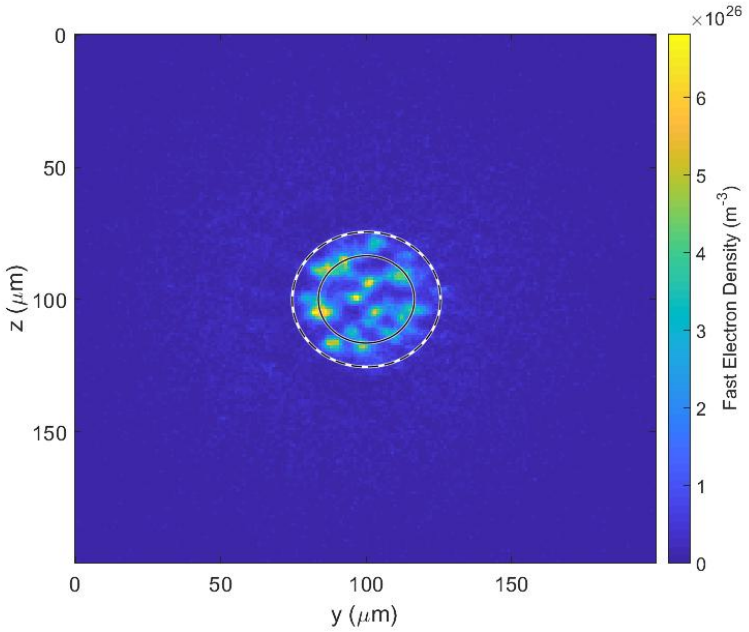

Figure 6.29: ZEPHYROS simulation of a 10° silicon cone. Fast electron density imaged at 100 μm depth. Cone base size denoted by the inner circle. Larger circle is a projection of the cone wall.

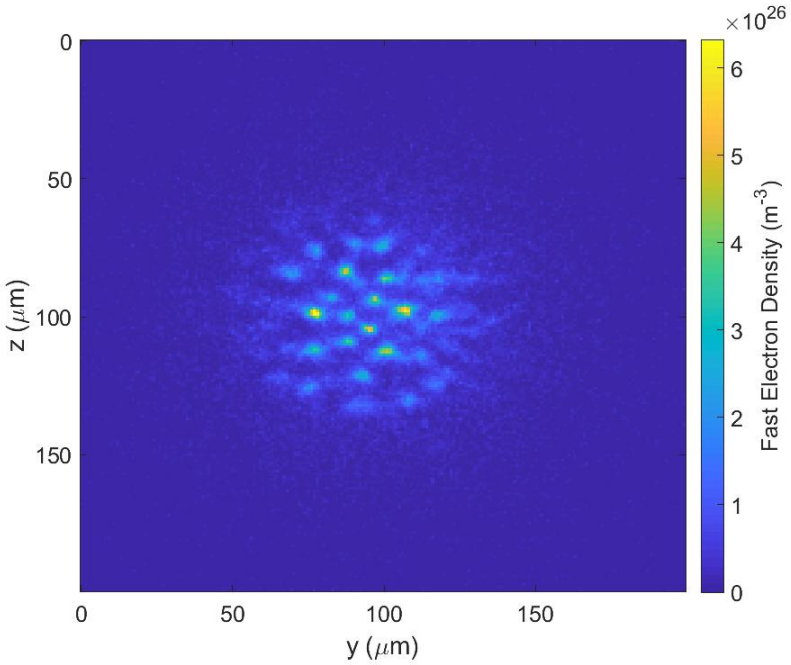

Figure 6.30: ZEPHYROS simulation of a 100 μm silicon foil. Fast electron density imaged at 100 μm depth.

MATLAB was used to load the saved 3D array of data from ZEPHYROS at 1ps. The plane corresponding to 100 μm depth was located and visualised to obtain an image like those shown in Figures 6.28 - 6.30. The inbuilt cursors were then used to find the pixel coordinates either side of each filament. The differences between locations were calculated in quadrature to give the size of each filament. These are presented in Table 6.3 where the mean $\pm$ standard deviation of the calculated sizes for each figure is displayed.

Figure	**Simulation Target**	**<Filament Size> $\pm$ SD (μm)**
Figure 6.28	5° silicon cone	6 ± 2
Figure 6.29	10° silicon cone	7 ± 2
Figure 6.30	100 μm silicon foil	7 ± 1

Table 6.3: Mean $\pm$ standard deviation of filament sizes for the ZEPHYROS simulations presented in Figures 6.28 - 6.30.

Table 6.3 shows how the average sizes of filaments across all three targets are similar at approximately 7 μm. Naturally taking into account the standard deviation increases the range between $4-9$ μm. These are of comparable size and within error of the filaments observed in the CTR analysis which ranged from approximately 10 ± 4 μm to 20 ± 4 μm in FWHM size. There are clear differences in the conditions simulated in ZEPHYROS and those found throughout the experiment, however this gives a general understanding of the filaments and shows that those observed in the CTR diagnostic are comparable in size to hybrid simulations. The ZEPHYROS simulations clearly showed a degree of fast electron confinement by the resistively generated magnetic fields around the cone:cladding interface. This suggest that the confining magnetic field cannot sufficiently mitigate against the break-up of the fast electron beam. However, it is

clear that electron filamentation does not significantly disrupt the resistive guiding mechanism.

Considering the separation of the fast electron filaments in the ZEPHYROS simulations, Figures 6.28 and 6.29 shows that the majority of fast electrons are relatively well confined within the projection of the cone walls. However, the simulations do exhibit filamentation. In the 5° cone case, the centre of the electron filaments are separated across a range of approximately $7-23$ μm. The 10° cone presents filaments more widely separated by approximately $6-40$ μm. Is it apparent that the lack of resistive guiding in the silicon foil in Figure 6.30 results in the filaments extending further out in the radial direction. This increases the range over which the filaments are separated to approximately $8-58$ μm.

Comparing this to the CTR filaments found to range between approximately 13 ± 4 μm and 64 ± 4 μm, similar distances as found within the hybrid simulations. As with the filaments sizes, differences between the CTR and hybrid simulations are to be expected due to differing laser pulse, cone angle, cone tip size etc. However, the general size and separation of the filaments in the hybrid simulations support the results found using the CTR diagnostic. The simulations of the 5° and 10° cones in Figures 6.28 and 6.29 show how resistive guiding takes place, alongside filamentation. This suggests that the break-up of the electron beam does not significantly inhibit the guiding mechanism. Similar sized filaments are also recorded in the silicon foil target simulation in Figure 6.30, however the lack of resistive guiding shows how the filaments are no longer contained within the cone area.

6.4 Preliminary Conclusion

The high-energy fast electron population that escapes the rear surface of the target has been investigated in this chapter for the 2017 Vulcan PW campaign. Image plate has been used to probe the lower half of the electron beam and propose the existence of filamentation that would not be fully captured by the diagnostic. This led to the analysis of the Coherent Transition Radiation (CTR) which clearly showed electron beam break-up in a large number of targets and supported the proposal of filamentation. Three-dimensional hybrid simulations have been implemented to characterise the filamentation that would be expected from the targets implemented on the 2017 Vulcan PW campaign and compared to the experimental CTR results. These generated similar electron filaments in terms of size and separation as those recorded in the CTR images. In the hybrid simulations, fast electron confinement was recorded in the presence of filamentation; suggesting that the break-up of the electron beam does not significantly inhibit the resistive guiding mechanism within the conical structured targets.

The first scan of the image plates (IP) has been retrieved to allow for comparison between shots. Line-outs and Gaussian fits have been applied along the length of the image plate to determine the maximum PSL and divergence of the signal. The total PSL upon the first plate has also been determined using a rectangular region of interest. Results have been presented for 100 μm thick targets determined as *hit* using the front surface imaging diagnostic. The NIST ESTAR tables [123] have been used to estimate the minimum electron energy capable of reaching the depth of the first IP in the stack. This was determined to be approximately 5.4 MeV.

The line-outs across the length of the image plates show the CH:Si control foil and a single

clad cone performing the lowest in terms of peak PSL. Three clad cones consistently generated a brighter peak PSL than the silicon control foil. These targets also generated the most divergent signal upon the image plates. A significant relationship between the peak PSL, signal divergence and laser intensity was not recorded, and clear variability was present between the targets.

In terms of total PSL upon the first IP, the majority of clad cone targets produced a greater total signal compared to the silicon foil and CH:Si structured control targets. Again, this does not appear to be related to the laser intensity. The same clad cone that generated the weakest peak signal in the line-outs also produced the lowest total PSL.

Angular plots of the image plates have been presented in section 6.2.3. These indicate that multiple areas of signal are present at different locations upon the IP for some shots. In the 2017 campaign, a plasma mirror was used so that the Vulcan PW beam was directed along the target normal axis. Therefore, the two electron populations directed along the laser k vector and target normal directions should propagate along the same axis. These electrons are accelerated through the resonance absorption (target normal direction) and $\mathbf{J}\times\mathbf{B}$ (laser k vector direction) mechanisms respectively. The presence of two electron signals on the IP scans cannot be attributed to the two electron populations, as these should both propagate along the same axis and reach the IP at the same location.

A possible further explanation could be that the target was rotated slightly so that the target normal and laser axes were spatially separated at the rear surface. However, throughout the experiment it was ensured that the RCF and IP stack remained central to the target and parallel to the rear surface. An alignment jig was used to maintain the correct target position in the holder, and the alignment method ensured that the target was perpendicular to the laser axis. This guaranteed that any possible rotation in the target was minimised. If slight rotation was present, the location of the proton signal (normal to the target) upon the RCF would be spatially separated from the location of the electron signal (laser axis) on the IP. However, this was not seen and suggests that the target and IP stack were aligned without rotation.

This leaves the most likely cause of the multiple electron signals on the IP as being generated through filamentation; with each signal originating from distinct filaments. However, this does not mean that the electron beam is not filamented when only a single area of signal is recorded on the IP. It has been shown that the IP captures a full angular range of approximately 45° from the target rear surface. However, a half-stack was implemented meaning that only the lower half of the electron beam is captured. If filamentation is taking place, some will be present above the half-stack and not be captured. Therefore, the analysis progressed to the Coherent Transition Radiation (CTR) to further investigate the filamentation of the fast electron beam. This diagnostic imaged the complete rear surface of the target so was capable of capturing the emission from all of the electron beam filaments.

The analysis began with a visual comparison of the reconstructed first scans of the IP and the raw CTR images. In approximately 67% of the shots under analysis, the CTR images displayed filamentation while the IP scans only showed a single area of signal. An example of this situation is presented in Figure 6.14. This confirmed the proposal that the electron beam was exhibiting filamentation which was insufficiently captured on the image plate diagnostic. This knowledge - coupled with the variability in the results - suggests that substantial conclusions cannot be

drawn from solely the image plate results.

The CTR analysis then progressed with subtraction of the background signal for images obtained from *hit* targets with a known pulse length. Neutral Density filtering was also accounted for. The total signal within a constant ROI and the FWHM of the emission has also been determined.

A clear separation between the total CTR emission has been recorded for the different targets. The total emission from the clad cones ranged from $3.86 \times 10^7 - 6.34 \times 10^8$ arb. int. and was brighter than the 2.91×10^7 arb. int. obtained from the silicon control foil. The 25 μm thick titanium foil and CH:Si structured control target generated significantly brighter CTR emission compared to the clad cones. These were both within the 10^9 arb. int. regime.

The CTR signal shows an effect related to the target thickness and electron areal density. The thinnest and lowest areal density target (25 μm titanium foil) generated the brightest CTR signal, progressively decreasing in strength as the target thickness or areal density was increased. The thin titanium foil generated a signal approximately 18 times greater than the brightest clad cone, at a quarter of the target thickness. J. J. Santos *et al* [18] reports how the CTR emission at the second-harmonic wavelength decreased as the target thickness increased between 10 μm to 50 μm. The emission strength then remained relatively constant as the thickness further increased. Although using a different definition of the signal strength, the results presented in this thesis are consistent with the general trend detailed by J.J. Santos *et al*.

The CTR emission size has also been extracted and shows two subsets of targets. The 25 μm titanium foil and a single clad cone at the highest laser intensity generated a CTR signal exceeding 14 ± 3 μm in size. The silicon foil, structured CH:Si control and remaining clad cones generated a smaller signal of less than 5 ± 3 μm. These results appear unrelated to the laser intensity. J.S. Green *et al* [5] reports how the fast electron beam becomes increasingly divergent with laser intensity. However, one would not expect to see this across the relatively narrow laser intensity range of $0.7 - 1.8 \times 10^{20}$ Wcm^{-2} in the 2017 Vulcan PW experiment.

Comparing the emission size to the target thickness shows that the emission generally becomes smaller with increasing thickness. The largest emission is generated from the thinnest 25 μm titanium foil and a single 100 μm thick clad cone. The remaining CH:Si (92.7 μm), silicon foil (100 μm) and clad cones (100 μm) all generate significantly smaller emission. J.J. Santos *et al* [18] reports the second-harmonic OTR growing steadily at approximately 30° until a target thickness of 50 μm; after which the signal reduces in size to slightly above the initial value. For targets thicker than ≥ 50 μm, the reported emission size scaled with 5°. The increasing emission size until 50 μm thickness is attributed to the more diffuse thermal emission contributing to the signal. The emission is broadband but the component at 2ω will contribute to the CTR emission captured at this wavelength. For targets exceeding 50 μm in thickness, the thermal emission is significantly reduced at the rear surface and dominated by that generated through the CTR mechanism.

A similar mechanism may be attributing to the CTR emission size results presented in this thesis. The emission generated from the 25 μm thick titanium foil may be effectively widened by the more diffuse thermal emission that is capable of penetrating the relatively small depth to the rear surface. This component of the emission is less capable of reaching the rear surface of

the thicker CH:Si, silicon foil and clad cone targets, hence the significant reduction in the CTR emission size. However, this does not account for the single clad cone target that generates the widest emission of all the targets. A possible cause of this is that this shot was at the maximum laser intensity and hence the fast electron beam may be exhibiting the increased divergence as expected by [5]. However, the strength of this effect would not be considered significant over the small laser intensity range seen in the 2017 experiment.

The filamentation of the CTR has also been investigated and compared to three-dimensional hybrid simulations using ZEPHYROS [101]. The separation between the CTR filaments ranged between 13 ± 4 μm and 64 ± 4 μm across the shots analysed in this thesis. The size of the filaments have also been calculated by implementing Gaussian fits and determining the FWHM. These ranged between 10 ± 4 μm and 20 ± 4 μm.

ZEPHYROS simulations have been conducted using 5° and 10° clad silicon cones, as well as a silicon control foil to determine if the CTR filamentation observed during the experiment would still occur if resistive guiding was taking place. In the simulations using conical targets, the fast electrons were confined within the circular region that the cone walls projected onto the rear surface. The majority of the filamentary structures were generally 7 μm in size, with standard deviations of approximately 2 μm. This is similar to those observed in the CTR images. The separation of the filaments in the hybrid simulations is recorded as approximately 7 μm - 23 μm in the 5° cone case and 6 μm - 40 μm for the 10° cone. The silicon foil target which - as expected - does not exhibit resistive guiding, results in a larger spread of filaments across approximately 8 μm - 58 μm. Again, these are relatively comparable to the CTR results considering the differences in the laser conditions and cone structure between the hybrid simulations and the experiment. The spatial resolution of the CTR diagnostic implemented on the 2017 Vulcan PW campaign was approximately 3 μm. This suggests that the filamentation in ZEPHYROS - which is both larger and more separated than this precision - would be resolved on the CTR images. The presence of both filamentation and resistive guiding in the ZEPHYROS simulations suggests that the observation of electron beam filaments in the CTR and IP analysis does not imply the lack of resistive guiding within the conical structured targets implemented on the 2017 campaign.

This chapter has detailed electron beam measurements using image plate and CTR diagnostics. Significant variability in the results is somewhat attributed to the filamentation of the electron beam and the inability of the IP to diagnose this. CTR measurements are consistent with trends presented in the literature [18] and show clear break-up of the electron beam in 67% of shots which cannot be determined using the IP diagnostic. Hybrid simulations also present electron filamentation on the same scale as observed in the CTR results. These simulations show that the presence of filamentation does not significantly inhibit the resistive guiding mechanism of collimating the fast electrons in conically structured targets.

Chapter 7

Conclusions

The divergent nature of fast electrons generated in high-intensity laser-solid interactions is a major obstacle to fast ignition. Previous simulation work - using the LEDA and ZEPHYROS codes - has shown how the implementation of a resistive gradient in the target can establish magnetic fields that act to reduce this divergence [8, 11–13]. This is termed *Resistive Guiding* and has been the main focus of this thesis.

The work presented in this thesis details the first experimental work implementing conically structured targets to investigate the resistive guiding technique. This distinguishes itself from the previous experimental work [9, 10] by progressing to cone structured targets and implementing novel target fabrication and imaging diagnostics. This thesis is the result of two experimental campaigns at the Vulcan PW laser facility, with the first in 2015 generating a significant amount of data and recommendations for the subsequent campaign in 2017. These were then implemented through a variety of methods and allowed characterisation of the laser-target interaction to be improved. This work has advanced the knowledge of what is required for implementing resistive guiding experiments and has allowed us to better understand how to perform future campaigns.

7.0.1 Target Heating

Chapter 4 has reported on a combination of shadowgraphy probing and HYADES simulations to infer the rear surface temperature of targets in the 2015 and 2017 campaigns. The laser focal spot and it's location upon the cone tip has proved to be an important feature that can modify the fast electron confinement and heating of the target.

Across both the 2015 and 2017 Vulcan PW campaigns, the majority of cone targets reached greater rear surface temperatures than the control foils. In the first experiment, temperatures of 60 eV - 200 eV were recorded for the clad and unclad aluminium cones, while control foils generally peaked at a lower temperature of 90 eV. In the 2017 campaign, heating was split into three subsets of temperature; specifically ≤ 60 eV, approximately 100 eV and 150 eV - 200 eV. Within this range, the missed clad silicon cones and homogeneous control foils were all found in the lower temperature regimes. A significant number of hit clad cones reached the highest temperature regime of 150 eV - 200 eV. Simulations in the literature have previously shown that matching the laser spot width to the cone tip enhances the resistive guiding mechanism.

We therefore investigated the astigmatism in the laser focal spot in the 2017 campaign and the possible result of this effectively increasing the size of the laser pulse towards that of the cones. In doing so, this was considered as a possible cause of the enhanced heating in the subset of hit clad cones.

The optimised focal spot in the later campaign held significant energy outside of the FWHM. The effect of this was investigated using ZEPHYROS simulations which showed how this feature can effectively increase the size of the beam. In this case, the beam tended towards the size of the cone tip and enhanced the fast electron confinement. This resulted in a significant improvement in volume-averaged heating inside the target. The effect of the focal spot is clearly important and is suggested as a mechanism behind the different temperature regimes observed in the 2017 campaign, where the focal spot is effectively increased in size towards the widths of the experiment cones.

The inferred rear surface temperature results in both campaigns showed an improvement in heating compared to the established literature. M. Nakatsatsumi *et al* [16] shows how the temperature is dependant upon the areal density of the target, with a temperature of < 30 eV recorded at the aluminium and silicon areal densities using laser energies exceeding 214 J. In all cases, the temperatures inferred during the Vulcan PW campaigns improved on this value with significantly lower laser energies of $50 - 85$ J.

7.0.2 Proton Acceleration and Specular Reflection

Chapter 5 detailed the use of RCF to capture the proton beam emitted through the TNSA mechanism during both Vulcan PW campaigns. The maximum energies of the proton spectra has been determined and an enhancement recorded for cone angles of approximately 10°.

The maximum proton energies in the 2015 and 2017 campaigns generally ranged between $15 - 45$ MeV and $7 - 28$ MeV respectively. A single clad cone was located at 46 MeV in the 2017 campaign, however this clearly deviated from the other shots. These results scale with $E_{max} \propto \left(I_L \lambda_L^2\right)^{0.5}$ as suggested in the literature [50, 52]. This scaling accounts for the improvement in overall proton energies reported in 2015 compared to the 2017 campaign. In the later experiment, a plasma mirror was implemented and therefore reduced the energy (and intensity) incident upon the targets.

Considering the normalised (to $\sqrt{I_L}$) maximum proton energy against the half-angles of the conical targets shows that an enhancement is found for approximately 10° cones. This is reported in both campaigns where these cones not only perform better than the control foils, but also the remaining conical targets of different angles. The P. Mora model [17] was invoked to show how the maximum proton energy holds a dependency upon the fast electron density at the rear surface. An improvement in electron confinement should increase the fast electron density at this location and result in enhanced acceleration of protons to higher energies. Complimentary to this, the work by H. Schmitz model [120] shows how the sheath field and acceleration of protons is dependant upon the longitudinal component of the hot electron temperature. This should increase when resistive guiding of the electrons takes place, suggesting that an improvement in the mechanism will result in acceleration of ions to higher energies. This effect has been considered using specular reflection and ZEPHYROS simulations to understand how the

confinement varies for different cone angles.

Specular reflection of a single electron (of 30° half-divergence) has been investigated in cones of 5°, 10°, 15° and 20° angles. This work suggests that the 15° cone is most effective at collimating the electrons, jointly followed by the 10° and 20° cones. The 5° cone can match the performance of the latter two cones, but only if the electron can undergo two reflections. It has been shown that two reflections are only possible in cone tips smaller than 9.4 μm, which rules out all those implemented on both campaigns. This provides an explanation of the improved performance of 10° cones compared to the 5° cones. It has also been shown that as one moves to larger cone angles, less of the electron population have the ability to have their divergence reduced through specular reflection. As such, an upper angle limit is placed on the cones and provides a justification to the enhancement in the 10° cones compared to higher angles.

This work treats the cone walls as perfectly reflecting magnetic mirrors, this has also been the case in [12,13]. Reference [11] shows how the electrons will actually penetrate a Larmour radius into the magnetic fields and thus the reflection location will be slightly modified. However, this effect will be negligible compared to the assumptions we have made about the electron beam, i.e. a perfectly 30° half-angle divergent electron injected at the centre of the cone. Naturally an angular distribution of electrons will be injected into the target, not just those at 30°. The central tip location is chosen due to this being the location of maximum laser intensity for a perfectly hit shot. C. Brenner *et al* [124] shows how the fast electrons are injected over a radius equivalent to the laser spot, and therefore if the beam is perfectly centred upon the cone tip, the single electron will most likely be injected at the location of maximum intensity - the centre of the cone. These all assume that the laser pulse is perfectly centred upon the cone tip; however in reality, the front surface imaging results have shown that the spatial jitter of the laser routinely moves this location across the cone. Therefore, one needs to take caution in applying these results directly to the experimental data; instead the intention is to consider the idealised case to obtain a general understanding of electron reflection through the cone.

ZEPHYROS simulations have shown how the fast electron density at the rear surface decays exponentially with increasing cone angle. This supports the proposal that the 10° cone performs better than the higher angled cones in terms of electron confinement, however the same cannot be said for the lower angles cones. The specular reflection arguments suggest that in a cone with tip larger than 9.4 μm - as implemented on the experiments and ZEPHYROS simulations - the 10° cone enhances electron confinement compared to the 5° cone and would therefore improve the fast electron density at the rear surface. This is not found in the simulations and suggests that a further mechanism is at play. A possible resolution to this is that in both campaigns there are shots corresponding to $\geq 10°$ cones; therefore this regime is relatively well characterised. However, only the earlier campaign has shots for $< 10°$. This campaign held more uncertainty in the laser focussing conditions, such as the unquantifiable defocus and proportion of energy contained within the laser spot, as well as the likelihood of a low density front surface scale length due to no plasma mirror being implemented. The lack of the front surface imaging system at this time also means that we cannot be certain of whether the cones in the 2015 results were successfully hit or not. This leads us to suggest that this region is less well defined and needs further investigation to see if the results of the 2015 campaign are replicated. The specular

reflection formulation assumes a perfect laser-cone interaction and perfectly rigid, specularly reflecting walls. Clearly, this idealised environment is not found in an experimental setting; for instance, the cones in 2017 have been shown to present curved walls on the electron microscope images.

7.0.3 Fast Electron Filamentation

Chapter 6 has presented investigations into the high-energy tail of the electron distribution in the 2017 campaign using a combination of image plate (IP) and optical transition radiation (OTR) diagnostics. These electrons have sufficient energy to travel through the target and escape before the resistively generated magnetic fields have become fully established. Therefore, these electrons will not be heavily affected by the resistive guiding fields, however, it is important to investigate the full electron spectrum to gain a broad understanding of the laser-target interaction [28].

NIST ESTAR [123] tables have shown that electrons with energy exceeding 5.4 MeV will be able to reach the first IP in stack. This is typical of such laser-target interactions, with similar energies reported in previous work using a comparable laser system [28]. The calculation assumes the active layers of RCF to consist completely of Mylar plastic since the exact composition is not presented in the literature [85, 86]. The thickness of the active layers is ≤ 28 μm compared to a total stack thickness of approximately 2.5 cm, therefore any deviation from Mylar is unlikely to significantly affect the calculated areal density of the stack and subsequent 5.4 MeV result.

In terms of maximum and total PSL, the majority of clad cones perform better than the control foils. Three of the hit clad cones that generate the greatest maximum PSL also present the most diffuse signal (larger FWHM). An increased PSL would suggest that either more electrons are leaving the target or that the electrons are more energetic. Either of these mechanisms would result in more Eu^{2+} atoms becoming excited in the IP and radiating to contribute to an increased PSL level. A further mechanism could be that electrons that would initially travel along the edges of the beam are instead being brought into the FWHM and contributing to the increased signal. However, the three brightest PSL shots also present the largest signal, so it is unlikely that this mechanism is taking place.

The angular distribution of the electron signal upon the IP suggested filamentation was taking place. This was confirmed in the CTR images and showed how the IP would only capture $< 45°$ divergence of electrons. Considering the nominal Vulcan PW intensity of 10^{21} Wcm^{-2}, this is less than the expected $60°$ divergence of the fast electron beam [5].

The total CTR signal within a circular region-of-interest is shown to scale well with the established literature. J.J. Santos *et al* [18] reports how the 2ω emission decreases rapidly up to target thickness's of 50 μm, and then begins to plateau for even thicker targets. A general decrease in signal is also found as one moves towards thicker targets in the 2017 results. The 25 μm titanium foil generated a signal $\times 18$ brighter than the most intense signal from the 100 μm clad cones targets. Considering solely the 100 μm targets, the clad cones consistently generated a brighter signal than the silicon control foil, however the cones themselves were variable in signal strength. Filamentation is clear on the CTR images and is a likely source of this variability. We attribute the decreasing signal strength with target thickness to the same mechanism described by [18]. The increased signal for thinner targets is attributed to contributions from the thermal

emission captured at the 2ω wavelength. This is generated from resistive heating of the target due to the more divergent, bulk electrons. As the target thickness is increased, the penetration of these particles is reduced and the CTR emission becomes dominant [18].

The size of the CTR emission also shows a similar trend to J.J. Santos *et al* [18] where the 2ω signal grows steadily in size until a target thickness of 50 μm, after which the signal returns to slightly above it's original size. In the 2017 results, the thinnest target of 25 μm titanium generated one of the largest signals along with a single clad cone. However, the remaining targets of thickness ≥ 92.7 μm generated a signal that was approximately 1/3 the size of the titanium foil emission. The larger emission for the titanium foil is again, attributed to the broad, thermal emission contributing to the signal in thinner targets [18].

Comparable filamentation is terms of size and separation was also recorded in 3D ZEPHYROS simulations using the double spot laser arrangement (*hybrid beam*) implemented in Chapter 4. This work investigated 5° and 10° clad silicon cones and showed that the fast electrons were clearly confined throughout the 100 μm depth of the targets. Filamentation was observed in both cases, ranging between $8 - 14$ μm in size. Those analysed from the CTR presented similar results of 10 ± 4 μm and 20 ± 4 μm.

The separation of the filaments in the ZEPHYROS simulations also correspond well to those observed on the CTR images. The simulations show filaments separated by $6 - 40$ μm with the largest distances being in the 10° cone. In contrast, the CTR filaments range between $(13 - 64) \pm 4$ μm. Again, of a similar order to the simulations.

Naturally, the simulations make assumptions of an idealised case, therefore, reasonable caution needs to be taken in directly applying the quantitative results to experimental data. However, one of the most poignant results is that although filamentation is observed in the simulations (and experimental data), this does not appear to significantly inhibit the resistive guiding of the fast electrons.

7.0.4 Future Prospects

It is clear that the resistive guiding mechanism is highly sensitive to the alignment of the laser pulse upon the conical surfaces. Variability in target heating has been presented in Chapter 4, with three subsets of targets reaching different temperatures. Hybrid simulations have shown how the location of the laser pulse upon the target surface can significantly modify the confinement of electrons. With this in mind, the implementation of the front surface imaging diagnostic has been invaluable in the 2017 campaign to aid alignment and determine the location of the main laser pulse upon the target surface on a shot-to-shot basis. This has reduced the effect of any possible variation due to laser-target positioning by allowing the data to be categorised into *hit*, *missed* or *clipped* shots. This system has proved invaluable and would likely benefit future campaigns - not only investigating resistive guiding - but those requiring the laser pulse to be accurately delivered to small scale structures on the order of the laser jitter.

The effect of defocus upon the laser has also been characterised in accordance with the method of A. Higginson *et al* [29]. This has systematically shown how the intensity, energy and size of the beam can be modified by a defocus error throughout a campaign. Not only is the energy and intensity important to the resistive guiding technique, but ZEPHYROS simulations

have shown how matching the size of the laser to the cone tips improves fast electron confinement. Therefore, understanding these laser parameters is extremely important when investigating the resistive guiding technique.

Target heating and ZEPHYROS simulations in Chapter 4 have shown the significant effect of an astigmatic laser, i.e. with considerable energy in the wings, upon the confinement of electrons. The Vulcan PW beam has long been known to hold slight astigmatism, but these results show how significant this is for resistive guiding experiments. We suggest that future campaigns will need to take the astigmatism into account when investigating resistive guiding, as well as it being useful to implement spectroscopy measurements to validate the inferred temperature results presented in this thesis. The beam could also be systematically defocused so that the spot tends towards the size of the cone tip, with experimental investigations being undertaken to determine the effect of this on the guiding of fast electrons.

A significant peak in maximum proton energy has been reported in Chapter 5, and is repeated in both the 2015 and 2017 campaigns. Specular reflection arguments, combined with the Mora model [17] and ZEPHYROS simulations provide reasoning behind the enhancement in 10° cones compared to larger angles. However, the enhancement at 10° compared to lower angled cones is not fully resolved. The specular reflection consideration suggests that the lower angled cone (5°) would only match the performance of the 10° cone if a secondary reflection of an electron is possible. It has been shown that this would not be expected in cones with tip widths greater than 9.4 μm. However, the ZEPHYROS simulations do not appear to support this, and instead, show an enhancement in fast electron density in the smallest angled cones. Further investigations to resolve this disparity could implement a greater number of cones to not only improve statistics, but also provide more data below the 10° cone regime. In the 2017 experiment, the autocorrelator did not trigger for shots with cone angles $\approx 5°$, so conclusions could not be drawn from these shots. Spectral analysis of the proton beam would also be advantageous. The number of protons scales with the number of electrons at the rear surface, and as such, integration of the proton spectra may provide some indication of the fast electron density - and therefore confinement - at this location.

Finally, Chapter 6 has shown that implementation of image plate in a half-stack configuration is insufficient to fully characterise the electron beam. Therefore, it is suggested that other diagnostics, such as CTR, are used in tandem. IP electron energies and CTR trends compare well with the established literature [18,28], however filamentation of the electron beam is clearly causing variability in the results. Encouragingly for resistive guiding, simulations generated similar filamentation and show how the presence of electron beam break-up does not significantly impair the resistive guiding mechanism.

In order for fast ignition to become a viable scheme of ICF, the divergence of fast electrons needs to be reduced and controlled. Resistive guiding is a promising method of achieving this, however this thesis shows that implementing the technique on an experimental setting is extremely challenging and highly sensitive to the interaction conditions. Future investigations will require the laser system to be relatively long pulse - such as Vulcan PW - so that the magnetic fields have sufficient time to become established. However, this thesis has shown that the laser-target interaction will need to be highly characterised and monitored so that clear conclusions

can be drawn from the data.

There is a broad space within which future campaigns could be investigated. The implementation of spectroscopy would be a useful addition to experiments to validate the inferred temperature results presented in this thesis. Probing of the resistive fields is also an attractive prospect, allowing the evolution of the fields to be investigated. A possible approach to this would be to use proton probing [125]. A novel target design could be implemented which acts to minimise the effect of laser jitter and decouple this from the resistive guiding mechanism. Such a target may consist of a number of alternating layers of high and low Z material. In doing so, the resistive guiding effect should work irrespective of the laser position; even if the interaction is on a low Z area, the fast electrons will be guided along the two adjacent high Z layers. We would not expect the guiding effect to be as pronounced as for conical structures, however these targets would allow a more consistent evaluation of the important physics underpinning resistive guiding to be built up experimentally.

Bibliography

[1] T. F. Stocker, D. Qin, G.-K. Plattner, M. M. Tignor, S. K. Allen, J. Boschung, A. Nauels, Y. Xia, V. Bex, and P. M. Midgley, "Climate change 2013: the physical science basis. contribution of working group i to the fifth assessment report of ipcc the intergovernmental panel on climate change," 2014.

[2] T. Masson-Delmotte, P. Zhai, H. Pörtner, D. Roberts, J. Skea, P. Shukla, A. Pirani, W. Moufouma-Okia, C. Péan, R. Pidcock, *et al.*, "Ipcc, 2018: Summary for policymakers. in: Global warming of 1.5 c. an ipcc special report on the impacts of global warming of 1.5 c above pre-industrial levels and related global greenhouse gas emission pathways, in the context of strengthening the global," *Geneva, Switzerland*, 2018.

[3] M. Tabak, J. Hammer, M. E. Glinsky, W. L. Kruer, S. C. Wilks, J. Woodworth, E. M. Campbell, M. D. Perry, and R. J. Mason, "Ignition and high gain with ultrapowerful lasers," *Physics of Plasmas*, vol. 1, no. 5, pp. 1626–1634, 1994.

[4] R. Kodama, P. Norreys, K. Mima, A. Dangor, R. Evans, H. Fujita, Y. Kitagawa, K. Krushelnick, T. Miyakoshi, N. Miyanaga, *et al.*, "Fast heating of ultrahigh-density plasma as a step towards laser fusion ignition," *Nature*, vol. 412, no. 6849, pp. 798–802, 2001.

[5] J. Green, V. Ovchinnikov, R. Evans, K. Akli, H. Azechi, F. Beg, C. Bellei, R. Freeman, H. Habara, R. Heathcote, *et al.*, "Effect of laser intensity on fast-electron-beam divergence in solid-density plasmas," *Physical review letters*, vol. 100, no. 1, p. 015003, 2008.

[6] K. Lancaster, J. Green, D. Hey, K. Akli, J. Davies, R. Clarke, R. Freeman, H. Habara, M. Key, R. Kodama, *et al.*, "Measurements of energy transport patterns in solid density laser plasma interactions at intensities of 5× 10 20 w cm- 2," *Physical review letters*, vol. 98, no. 12, p. 125002, 2007.

[7] A. Bell and R. Kingham, "Resistive collimation of electron beams in laser-produced plasmas," *Physical review letters*, vol. 91, p. 035003, 08 2003.

[8] A. Robinson and M. Sherlock, "Magnetic collimation of fast electrons produced by ultraintense laser irradiation by structuring the target composition," *Physics of Plasmas*, vol. 14, pp. 083105–083105, 08 2007.

[9] S. Kar, A. Robinson, D. Carroll, O. Lundh, K. Markey, P. McKenna, P. Norreys, and M. Zepf, "Guiding of relativistic electron beams in solid targets by resistively controlled magnetic fields," *Physical review letters*, vol. 102, no. 5, p. 055001, 2009.

[10] B. Ramakrishna, S. Kar, A. Robinson, D. Adams, K. Markey, M. Quinn, X. Yuan, P. McKenna, K. Lancaster, J. Green, *et al.*, "Laser-driven fast electron collimation in targets with resistivity boundary," *Physical review letters*, vol. 105, no. 13, p. 135001, 2010.

[11] A. Robinson, H. Schmitz, and J. Pasley, "Rapid embedded wire heating via resistive guiding of laser-generated fast electrons as a hydrodynamic driver," *Physics of Plasmas*, vol. 20, 12 2013.

[12] A. Robinson, H. Schmitz, J. Green, C. Ridgers, N. Booth, and J. Pasley, "Control of wire heating with resistively guided fast electrons through an inverse conical taper," *Physics of Plasmas*, vol. 22, no. 4, p. 043118, 2015.

[13] A. Robinson, H. Schmitz, J. Green, and C. Ridgers, "Guiding of laser-generated fast electrons by exploiting the resistivity-gradients around a conical guide element," *Plasma Physics and Controlled Fusion*, vol. 57, pp. 1–7, 4 2015.

[14] R. Evans, E. Clark, R. Eagleton, A. Dunne, R. Edwards, W. Garbett, T. Goldsack, S. James, C. Smith, B. Thomas, *et al.*, "Rapid heating of solid density material by a petawatt laser," *Applied Physics Letters*, vol. 86, no. 19, p. 191505, 2005.

[15] K. Lancaster, J. Green, R. Evans, P. Norreys, R. Heathcote, C. Hernandez-Gomez, I. Musgrave, J. Pasley, J. Waugh, N. Woolsey, *et al.*, "Temperature profiles derived from transverse optical shadowgraphy in ultra-intense laser plasma interactions," *Physics of Plasmas*, vol. 16, no. 5, p. 056707, 2009.

[16] M. Nakatsutsumi, J. Davies, R. Kodama, J. Green, K. Lancaster, K. Akli, F. Beg, S. Chen, D. Clark, R. Freeman, *et al.*, "Space and time resolved measurements of the heating of solids to ten million kelvin by a petawatt laser," *New Journal of Physics*, vol. 10, no. 4, p. 043046, 2008.

[17] P. Mora, "Plasma expansion into a vacuum," *Physical Review Letters*, vol. 90, no. 18, p. 185002, 2003.

[18] J. Santos, A. Debayle, P. Nicolaï, V. Tikhonchuk, M. Manclossi, D. Batani, A. Guemnie-Tafo, J. Faure, V. Malka, and J. Honrubia, "Fast-electron transport and induced heating in aluminum foils," *Physics of plasmas*, vol. 14, no. 10, p. 103107, 2007.

[19] S. Baton, J. Santos, F. Amiranoff, H. Popescu, L. Gremillet, M. Koenig, E. Martinolli, O. Guilbaud, C. Rousseaux, M. R. Le Gloahec, *et al.*, "Evidence of ultrashort electron bunches in laser-plasma interactions at relativistic intensities," *Physical review letters*, vol. 91, no. 10, p. 105001, 2003.

[20] M. Streeter, P. Foster, F. Cameron, M. Borghesi, C. Brenner, D. Carroll, E. Divall, N. Dover, B. Dromey, P. Gallegos, *et al.*, "Relativistic plasma surfaces as an efficient second harmonic generator," *New Journal of Physics*, vol. 13, no. 2, p. 023041, 2011.

[21] F. Quéré, C. Thaury, P. Monot, S. Dobosz, P. Martin, J.-P. Geindre, and P. Audebert, "Coherent wake emission of high-order harmonics from overdense plasmas," *Physical review letters*, vol. 96, no. 12, p. 125004, 2006.

[22] B. Dromey, S. Rykovanov, D. Adams, R. Hörlein, Y. Nomura, D. Carroll, P. Foster, S. Kar, K. Markey, P. McKenna, *et al.*, "Tunable enhancement of high harmonic emission from laser solid interactions," *Physical review letters*, vol. 102, no. 22, p. 225002, 2009.

[23] A. Tarasevitch, K. Lobov, C. Wünsche, and D. von der Linde, "Transition to the relativistic regime in high order harmonic generation," *Physical review letters*, vol. 98, no. 10, p. 103902, 2007.

[24] P. McKenna, D. Neely, R. Bingham, and D. Jaroszynski, *Laser-Plasma Interactions and Applications*. Springer, 2013.

[25] E. Stenson, J. Horn-Stanja, M. Stoneking, and T. S. Pedersen, "Debye length and plasma skin depth: two length scales of interest in the creation and diagnosis of laboratory pair plasmas," *Journal of Plasma Physics*, vol. 83, no. 1, 2017.

[26] D. Bauer and P. Mulser, "Vacuum heating versus skin layer absorption of intense femtosecond laser pulses," *Physics of plasmas*, vol. 14, no. 2, p. 023301, 2007.

[27] Z. Ge, W. Yu, H. Zhuo, C. Zhou, Y. Ma, X. Yang, T. Yu, D. Zou, S. Luan, Y. Yin, *et al.*, "Resonant absorption and not-so-resonant absorption in short, intense laser irradiated plasma," *Physics of Plasmas*, vol. 20, no. 7, p. 073301, 2013.

[28] D. R. Rusby, *Study of Escaping Electron Dynamics and Applications for High-Power Laser-Plasma Interactions*. PhD thesis, University of Strathclyde, 16 Richmond St, Glasgow G1 1XQ, 2017.

[29] A. Higginson, *Optimisation and Control of Ion Acceleration in Intense Laser-Foil Interactions*. PhD thesis, University of Strathclyde, 16 Richmond St, Glasgow G1 1XQ, 2018.

[30] F. Brunel, "Not-so-resonant, resonant absorption," *Physical Review Letters*, vol. 59, no. 1, p. 52, 1987.

[31] W. Kruer and K. Estabrook, "J× b heating by very intense laser light," *The Physics of fluids*, vol. 28, no. 1, pp. 430–432, 1985.

[32] H. Alfvén, "On the motion of cosmic rays in interstellar space," *Physical Review*, vol. 55, no. 5, p. 425, 1939.

[33] A. Bell, J. Davies, S. Guerin, and H. Ruhl, "Fast-electron transport in high-intensity short-pulse laser-solid experiments," *Plasma physics and controlled fusion*, vol. 39, no. 5, p. 653, 1997.

[34] W. Kruer, *The physics of laser plasma interactions*. CRC Press, 2018.

[35] L. Spitzer Jr and R. Härm, "Transport phenomena in a completely ionized gas," *Physical Review*, vol. 89, no. 5, p. 977, 1953.

[36] P. McKenna, D. MacLellan, N. Butler, R. Dance, R. Gray, A. Robinson, D. Neely, and M. Desjarlais, "Influence of low-temperature resistivity on fast electron transport in solids: scaling to fast ignition electron beam parameters," *Plasma Physics and Controlled Fusion*, vol. 57, no. 6, p. 064001, 2015.

[37] D. MacLellan, D. Carroll, R. Gray, N. Booth, M. Burza, M. Desjarlais, F. Du, B. Gonzalez-Izquierdo, D. Neely, H. Powell, *et al.*, "Annular fast electron transport in silicon arising from low-temperature resistivity," *Physical review letters*, vol. 111, no. 9, p. 095001, 2013.

[38] E. S. Weibel, "Spontaneously growing transverse waves in a plasma due to an anisotropic velocity distribution," *Physical Review Letters*, vol. 2, no. 3, p. 83, 1959.

[39] M. Wei, F. Beg, A. Dangor, A. Gopal, M. Tatarakis, K. Krushelnick, E. Clark, P. Norreys, R. Clarke, K. Lancaster, *et al.*, "Experimental observations of the weibel instability in high intensity laser solid interactions," *Annual Report of Central Laser Facility, Rutherford Appleton Laboratory*, pp. 7–9, 2001.

[40] A. Robinson, R. Kingham, C. Ridgers, and M. Sherlock, "Effect of transverse density modulations on fast electron transport in dense plasmas," *Plasma Physics and Controlled Fusion*, vol. 50, no. 6, p. 065019, 2008.

[41] A. Bret and C. Deutsch, "Hierarchy of beam plasma instabilities up to high beam densities for fast ignition scenario," *Physics of plasmas*, vol. 12, no. 8, p. 082704, 2005.

[42] A. Bret, M.-C. Firpo, and C. Deutsch, "Characterization of the initial filamentation of a relativistic electron beam passing through a plasma," *Physical review letters*, vol. 94, no. 11, p. 115002, 2005.

[43] A. Debayle, J. Honrubia, E. d'Humieres, and V. Tikhonchuk, "Divergence of laser-driven relativistic electron beams," *Physical Review E*, vol. 82, no. 3, p. 036405, 2010.

[44] R. Scott, C. Beaucourt, H.-P. Schlenvoigt, K. Markey, K. Lancaster, C. Ridgers, C. Brenner, J. Pasley, R. Gray, I. Musgrave, *et al.*, "Controlling fast-electron-beam divergence using two laser pulses," *Physical review letters*, vol. 109, no. 1, p. 015001, 2012.

[45] R. Campbell, J. DeGroot, T. Mehlhorn, D. Welch, and B. Oliver, "Collimation of petawatt laser-generated relativistic electron beams propagating through solid matter," *Physics of Plasmas*, vol. 10, no. 10, pp. 4169–4172, 2003.

[46] A. Robinson and H. Schmitz, "Elliptical magnetic mirror generated via resistivity gradients for fast ignition inertial confinement fusion," *Physics of Plasmas*, vol. 20, no. 6, p. 062704, 2013.

[47] T. Esirkepov, M. Borghesi, S. Bulanov, G. Mourou, and T. Tajima, "Highly efficient relativistic-ion generation in the laser-piston regime," *Physical review letters*, vol. 92, no. 17, p. 175003, 2004.

[48] C. Danson, P. Brummitt, R. Clarke, J. Collier, B. Fell, A. Frackiewicz, S. Hancock, S. Hawkes, C. Hernandez-Gomez, P. Holligan, M. Hutchinson, A. Kidd, W. Lester, I. Musgrave, D. Neely, D. Neville, P. Norreys, D. Pepler, C. Reason, W. Shaikh, T. Winstone, R. Wyatt, and B. Wyborn, "Vulcan petawatt—an ultra-high-intensity interaction facility," *Nuclear Fusion*, vol. 44, no. 12, p. S239, 2004.

[49] M. Roth and M. Schollmeier, "Ion acceleration-target normal sheath acceleration," *arXiv preprint arXiv:1705.10569*, 2017.

[50] A. Macchi, M. Borghesi, and M. Passoni, "Ion acceleration by superintense laser-plasma interaction," *Reviews of Modern Physics*, vol. 85, no. 2, p. 751, 2013.

[51] M. Allen, P. K. Patel, A. Mackinnon, D. Price, S. Wilks, and E. Morse, "Direct experimental evidence of back-surface ion acceleration from laser-irradiated gold foils," *Physical review letters*, vol. 93, no. 26, p. 265004, 2004.

[52] M. Borghesi, J. Fuchs, S. Bulanov, A. Mackinnon, P. Patel, and M. Roth, "Fast ion generation by high-intensity laser irradiation of solid targets and applications," *Fusion Science and Technology*, vol. 49, no. 3, pp. 412–439, 2006.

[53] M. Tabak, D. Clark, S. Hatchett, M. Key, B. Lasinski, R. Snavely, S. Wilks, R. Town, R. Stephens, E. Campbell, *et al.*, "Review of progress in fast ignition," *Physics of Plasmas*, vol. 12, no. 5, p. 057305, 2005.

[54] S. Atzeni, "Inertial fusion fast ignitor: Igniting pulse parameter window vs the penetration depth of the heating particles and the density of the precompressed fuel," *Physics of Plasmas*, vol. 6, no. 8, pp. 3316–3326, 1999.

[55] E. Brookner, "Phased-array radars," *Scientific American*, vol. 252, no. 2, pp. 94–103, 1985.

[56] D. Strickland and G. Mourou, "Compression of amplified chirped optical pulses," *Optics Communications*, vol. 55, no. 6, pp. 447 – 449, 1985.

[57] Nobel Media AB, "The nobel prize in physics 2018." https://www.nobelprize.org/prizes/physics/2018/summary/. (Accessed: 02/11/19).

[58] C. Hooker, Y. Tang, O. Chekhlov, J. Collier, E. Divall, K. Ertel, S. Hawkes, B. Parry, and R. Pattathil, "Improving coherent contrast of petawatt laser pulses," *Optics express*, vol. 19, pp. 2193–203, 01 2011.

[59] D. Neely, P. Foster, A. Robinson, F. Lindau, O. Lundh, A. Persson, C.-G. Wahlström, and P. McKenna, "Enhanced proton beams from ultrathin targets driven by high contrast laser pulses," *Applied Physics Letters*, vol. 89, no. 2, p. 021502, 2006.

[60] T. Z. Esirkepov, J. K. Koga, A. Sunahara, T. Morita, M. Nishikino, K. Kageyama, H. Nagatomo, K. Nishihara, A. Sagisaka, H. Kotaki, T. Nakamura, Y. Fukuda, H. Okada, A. S. Pirozhkov, A. Yogo, M. Nishiuchi, H. Kiriyama, K. Kondo, M. Kando, and S. V. Bulanov, "Prepulse and amplified spontaneous emission effects on the interaction of a petawatt class laser with thin solid targets," *Nuclear Instruments and Methods in Physics Research Section A: Accelerators, Spectrometers, Detectors and Associated Equipment*, vol. 745, pp. 150 – 163, 2014.

[61] B. Dromey, S. Kar, M. Zepf, and P. Foster, "The plasma mirror—a subpicosecond optical switch for ultrahigh power lasers," *Review of Scientific Instruments*, vol. 75, no. 3, pp. 645–649, 2004.

[62] C. Ziener, P. Foster, E. Divall, C. Hooker, M. Hutchinson, A. Langley, and D. Neely, "Specular reflectivity of plasma mirrors as a function of intensity, pulse duration, and angle of incidence," *Journal of applied physics*, vol. 93, no. 1, pp. 768–770, 2003.

[63] Manx Precision Optics Ltd. Ballasalla, Isle of Man, IM9 2AP, British Isles.

[64] A. Dubietis, G. Jonušauskas, and A. Piskarskas, "Powerful femtosecond pulse generation by chirped and stretched pulse parametric amplification in bbo crystal," *Optics Communications*, vol. 88, no. 4, pp. 437 – 440, 1992.

[65] I. Ross, P. Matousek, M. Towrie, A. Langley, and J. Collier, "The prospects for ultrashort pulse duration and ultrahigh intensity using optical parametric chirped pulse amplifiers," *Optics Communications*, vol. 144, no. 1, pp. 125 – 133, 1997.

[66] N. M. Kroll, "Parametric amplification in spatially extended media and application to the design of tuneable oscillators at optical frequencies," *Proceedings of the IEEE*, vol. 51, pp. 110–114, Jan 1963.

[67] S. A. Akhmanov and R. V. Khokhlov, "Parametric amplifiers and generators of light," *Soviet Physics Uspekhi*, vol. 9, no. 2, p. 210, 1966.

[68] I. Musgrave, M. Galimberti, A. Boyle, C. Hernandez-Gomez, A. Kidd, B. Parry, D. Pepler, T. Winstone, and J. Collier, "Review of laser diagnostics at the vulcan laser facility," *High Power Laser Science and Engineering*, vol. 3, 01 2015.

[69] C. Hernandez-Gomez, P. Brummitt, D. Canny, R. Clarke, J. Collier, C. Danson, A. Dunne, B. Fell, A. Frackiewicz, S. Hancock, S. Hawkes, R. Heathcote, P. Holligan, M. Hutchinson, A. Kidd, W. Lester, I. Musgrave, D. Neely, D. Neville, and B. Wyborn, "Vulcan petawatt-operation and development," *Journal de Physique IV (Proceedings)*, vol. 133, 06 2006.

[70] J. S. Green, *Fast Electron Energy Transport in High Intensity Laser-Plasma Interactions*. PhD thesis, Imperial College London, Prince Consort Road, London SW7 2BZ, April 2008.

[71] S. Hawkes, J. Collier, C. Hooker, C. Reason, C. Edwards, C. Hernandez-Gomes, C. Danson, and I. Ross, "Adaptive optics trials on vulcan," *Central Laser Facility Annual Report*, pp. 153–155, 2000/2001.

[72] J. Collier, C. Hernandex-Gomez, R. Allott, C. Danson, and A. Hall, "A single-shot third-order autocorrelator for pulse contrast and pulse shape measurements," *Laser and Particle Beams*, vol. 19, no. 2, p. 231–235, 2001.

[73] C. Hernandez-Gomez, E. Thurston, and J. Collier, "Scanning third order autocorrelator for contrast measurement in vulcan," *Central Laser Facility Annual Report*, p. 156, 2000/2001.

[74] I. O. Musgrave, "Vulcan laser update august 2018." Invited Talk at The York Plasma Institute, UK, 2018.

[75] Imagine Optic. 18 rue Charles de Gaulle 91400, Orsay, France.

[76] I. O. Musgrave. Private Correspondance, 2018.

[77] A. Horne, "Design and build of an in situ focal-spot-monitoring diagnostic utilising fundamental and second harmonic emission," Master's thesis, University of York, Heslington, York, Y010 5DD, UK, September 2017.

[78] J. S. Green, R. Heathcote, N. Booth, D. Farley, C. D. Murphy, J. Pasley, W. Trickey, C. Baird, C. Underwood, P. Koester, A. Horne, Z. E. Davidson, R. Gray, and K. L. Lancaster, "A novel in-situ dual channel alignment system for precision alignment of complex targetry," Central Laser Facility Annual Report 2017-2018.

[79] R. Hörlein, B. Dromey, D. Adams, Y. Nomura, S. Kar, K. Markey, P. Foster, D. Neely, F. Krausz, G. D. Tsakiris, and M. Zepf, "High contrast plasma mirror: spatial filtering and second harmonic generation at 1019w cm-2," *New Journal of Physics*, vol. 10, p. 083002, aug 2008.

[80] G. J. Tallents, *An Introduction to the Atomic and Radiation Physics of Plasmas*. Cambridge University Press, 2018.

[81] M. Saylor, T. Tamargo, W. McLaughlin, H. Khan, D. Lewis, and R. Schenfele, "A thin film recording medium for use in food irradiation," *International Journal of Radiation Applications and Instrumentation. Part C. Radiation Physics and Chemistry*, vol. 31, no. 4, pp. 529 – 536, 1988. Special Issue Progress in Radiation Processing.

[82] R. Chu, D. Lewis, K. O'Hara, B. Buckland, F. Dinelle, and G. V. Dyk, "Gafchromictm dosimetry media: A new high dose, thin film routine dosimeter and dose mapping tool," *International Journal of Radiation Applications and Instrumentation. Part C. Radiation Physics and Chemistry*, vol. 35, no. 4, pp. 767 – 773, 1990. Special Issue Radiation Processing: State of the Art.

[83] S. Devic, "Radiochromic film dosimetry: Past, present, and future," *Physica Medica*, vol. 27, no. 3, pp. 122 – 134, 2011.

[84] S. Devic, N. Tomic, and D. Lewis, "Reference radiochromic film dosimetry: Review of technical aspects," *Physica Medica*, vol. 32, no. 4, pp. 541 – 556, 2016.

[85] *GAFCHROMIC HD-V2 FILM SPECIFICATION AND USER GUIDE*.

[86] *EBT3 SPECIFICATION AND USER GUIDE.*

[87] A. Meadowcroft, C. Bentley, and E. Stott, "Evaluation of the sensitivity and fading characteristics of an image plate system for x-ray diagnostics," *Review of Scientific Instruments*, vol. 79, no. 11, p. 113102, 2008.

[88] GE Healthcare Life Sciences, *Imaging accessories: Storage Phosphor Screen BAS-IP.*

[89] B. Maddox, H. Park, B. Remington, N. Izumi, S. Chen, C. Chen, G. Kimminau, Z. Ali, M. Haugh, and Q. Ma, "High-energy x-ray backlighter spectrum measurements using calibrated image plates," *Review of Scientific Instruments*, vol. 82, no. 2, p. 023111, 2011.

[90] T. Bonnet, M. Comet, D. Denis-Petit, F. Gobet, F. Hannachi, M. Tarisien, M. Versteegen, and M. Aléonard, "Response functions of imaging plates to photons, electrons and 4he particles," *Review of Scientific Instruments*, vol. 84, no. 10, p. 103510, 2013.

[91] C. Suzuki, T. Abe, T. Iimoto, and T. Kosako, "Energy response of an imaging plate to low-energy photons for use in dosimetry," *Japanese Journal of Health Physics*, vol. 46, pp. 158–162, 01 2011.

[92] Fuji Photo Film Co. Ltd., *Fluorescent Image Analyzer FLA-5000 Operation Guide*, October 2001.

[93] A. Lakshmanan, N. Murase, T. Yazawa, J. Qiu, T. Mitsuyu, K. Hirao, A. Tomita, and W. Hoffmann, "Luminescence studies in bafbr and bafbr: Eu," *Radiation measurements*, vol. 33, no. 1, pp. 119–127, 2001.

[94] I. J. Paterson, R. J. Clarke, N. C. Woolsey, and G. Gregori, "Image plate response for conditions relevant to laser–plasma interaction experiments," *Measurement Science and Technology*, vol. 19, p. 095301, aug 2008.

[95] V. Ginzburg and I. Frank, "Radiation of a uniformly moving electron due to its transition from one medium into another," *Zh. Eksp. Teor. Fiz.*, vol. 9, pp. 353–362, 1945.

[96] A. Kobzev, "On the radiation mechanism of a uniformly moving charge," *Physics of Particles and Nuclei*, vol. 45, no. 3, pp. 628–653, 2014.

[97] J. Zheng, K. Tanaka, T. Sato, T. Yabuuchi, T. Kurahashi, Y. Kitagawa, R. Kodama, T. Norimatsu, and T. Yamanaka, "Study of hot electrons by measurement of optical emission from the rear surface of a metallic foil irradiated with ultraintense laser pulse," *Physical review letters*, vol. 92, no. 16, p. 165001, 2004.

[98] U. Happek, A. Sievers, and E. Blum, "Observation of coherent transition radiation," *Physical review letters*, vol. 67, no. 21, p. 2962, 1991.

[99] *Hyades User's Guide - 01.11.xx.*

[100] Y. Guo, D. Jou, and M. Wang, "Understanding of flux-limited behaviors of heat transport in nonlinear regime," *Physics Letters A*, vol. 380, no. 3, pp. 452–457, 2016.

[101] A. P. L. Robinson, *"ZEPHYROS User Manual"*, 2014.

[102] J. R. Davies, "How wrong is collisional monte carlo modeling of fast electron transport in high-intensity laser-solid interactions?," *Phys. Rev. E*, vol. 65, p. 026407, Jan 2002.

[103] R. Campbell, J. DeGroot, T. Mehlhorn, D. Welch, and B. Oliver, "Collimation of petawatt laser-generated relativistic electron beams propagating through solid matter," *Physics of Plasmas*, vol. 10, no. 10, pp. 4169–4172, 2003.

[104] R. Kodama, Y. Sentoku, Z. Chen, G. Kumar, S. Hatchett, Y. Toyama, T. Cowan, R. Freeman, J. Fuchs, Y. Izawa, *et al.*, "Plasma devices to guide and collimate a high density of mev electrons," *Nature*, vol. 432, no. 7020, p. 1005, 2004.

[105] The University of York. Heslington, York, YO10 5DD, UK.

[106] P. Rajeev, S. Banerjee, A. S. Sandhu, R. Issac, L. Tribedi, and G. R. Kumar, "Role of surface roughness in hard-x-ray emission from femtosecond-laser-produced copper plasmas," *Physical Review A*, vol. 65, no. 5, p. 052903, 2002.

[107] A. Lübcke, A. A. Andreev, S. Höhm, R. Grunwald, L. Ehrentraut, and M. Schnürer, "Prospects of target nanostructuring for laser proton acceleration," *Scientific reports*, vol. 7, p. 44030, 2017.

[108] Scitech Precision Ltd. STFC Rutherford Appleton Laboratory, Harwell Campus, Didcot, OX11 0QX, UK.

[109] Science and Technology Facilities Council. Polaris House, North Star Avenue, Swindon, SN2 1SZ, UK.

[110] C. Spindloe. Private Correspondance, 2020.

[111] A. Higginson. Private Correspondance, 2018.

[112] J. S. Green. Private Correspondance, 2019.

[113] https://periodictable.com/Elements/014/data.html. Data based upon Wolfram MATHEMATICA ElementData Function. (Accessed: 27/03/19).

[114] J. Diallo, "Effect of resistive boundaries on the properties of laser produced fast electron beams," Master's thesis, University of York, Heslington, York, Y010 5DD, UK, September 2019.

[115] P. McKenna, K. Ledingham, J. Yang, L. Robson, T. McCanny, S. Shimizu, R. Clarke, D. Neely, K. Spohr, R. Chapman, *et al.*, "Characterization of proton and heavier ion acceleration in ultrahigh-intensity laser interactions with heated target foils," *Physical Review E*, vol. 70, no. 3, p. 036405, 2004.

[116] R. Snavely, M. Key, S. Hatchett, T. Cowan, M. Roth, T. Phillips, M. Stoyer, E. Henry, T. Sangster, M. Singh, *et al.*, "Intense high-energy proton beams from petawatt-laser irradiation of solids," *Physical review letters*, vol. 85, no. 14, p. 2945, 2000.

[117] S. Wilks, W. Kruer, M. Tabak, and A. Langdon, "Absorption of ultra-intense laser pulses," *Physical review letters*, vol. 69, no. 9, p. 1383, 1992.

[118] J. Schreiber, F. Bell, F. Grüner, U. Schramm, M. Geissler, M. Schnürer, S. Ter-Avetisyan, B. M. Hegelich, J. Cobble, E. Brambrink, *et al.*, "Analytical model for ion acceleration by high-intensity laser pulses," *Physical review letters*, vol. 97, no. 4, p. 045005, 2006.

[119] J. Fuchs, P. Antici, E. d'Humières, E. Lefebvre, M. Borghesi, E. Brambrink, C. Cecchetti, M. Kaluza, V. Malka, M. Manclossi, *et al.*, "Laser-driven proton scaling laws and new paths towards energy increase," *Nature physics*, vol. 2, no. 1, p. 48, 2006.

[120] H. Schmitz, "Target normal sheath acceleration sheath fields for arbitrary electron energy distribution," *Physics of Plasmas*, vol. 19, no. 8, p. 083115, 2012.

[121] S. Wilks, A. Langdon, T. Cowan, M. Roth, M. Singh, S. Hatchett, M. Key, D. Pennington, A. MacKinnon, and R. Snavely, "Energetic proton generation in ultra-intense laser–solid interactions," *Physics of plasmas*, vol. 8, no. 2, pp. 542–549, 2001.

[122] A. Mackinnon, Y. Sentoku, P. Patel, D. Price, S. Hatchett, M. Key, C. Andersen, R. Snavely, and R. Freeman, "Enhancement of proton acceleration by hot-electron recirculation in thin foils irradiated by ultraintense laser pulses," *Physical review letters*, vol. 88, no. 21, p. 215006, 2002.

[123] Berger, MJ and Coursey, JS and Zucker, MA and Chang, J. (2005). ESTAR, PSTAR, and ASTAR: Computer Programs for Calculating Stopping-Power and Range Tables for Electrons, Protons, and Helium Ions (version 1.2.3), Available: http://physics.nist.gov/Star (2020). National Institute of Standards and Technology, Gaithersburg, MD.

[124] C. Brenner, P. McKenna, and D. Neely, "Modelling the effect of laser focal spot size on sheath-accelerated protons in intense laser–foil interactions," *Plasma Physics and Controlled Fusion*, vol. 56, no. 8, p. 084003, 2014.

[125] L. Romagnani, M. Borghesi, C. Cecchetti, S. Kar, P. Antici, P. Audebert, S. Bandhoupadjay, F. Ceccherini, T. Cowan, J. Fuchs, *et al.*, "Proton probing measurement of electric and magnetic fields generated by ns and ps laser-matter interactions," *Laser and Particle Beams*, vol. 26, no. 2, pp. 241–248, 2008.